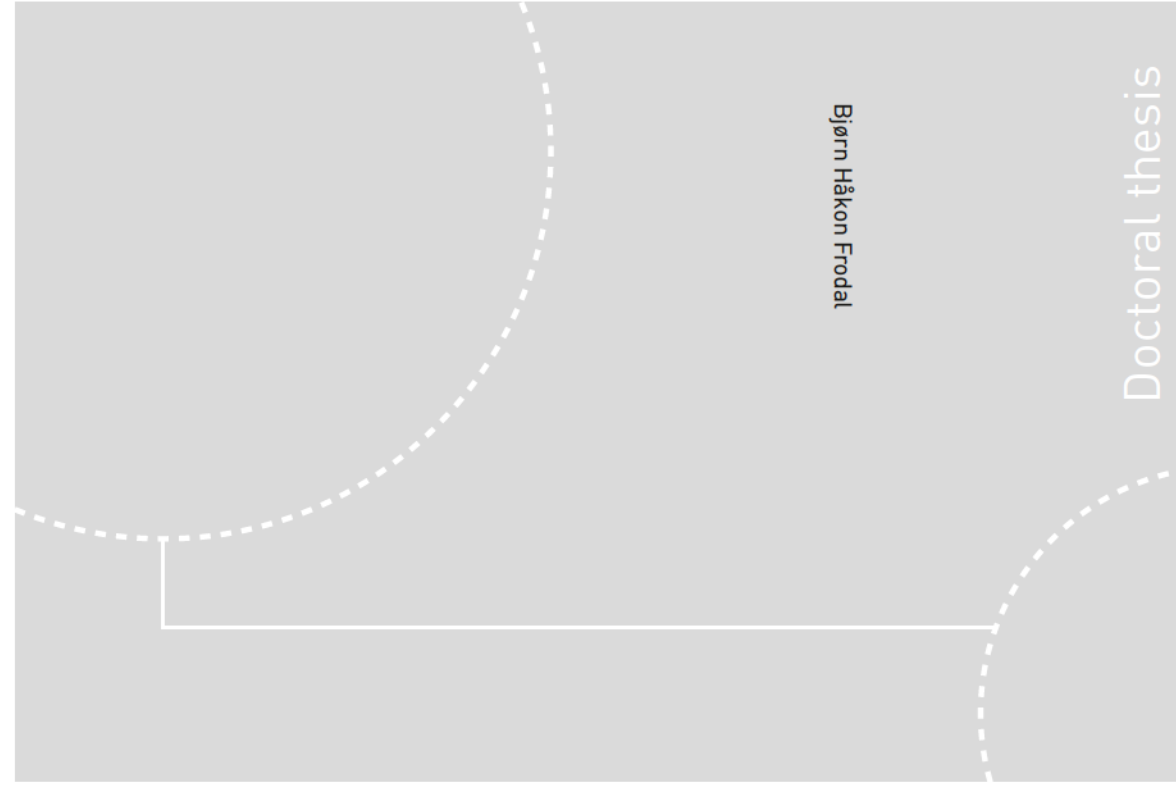


ISBN 978-82-326-4102-4 (printed ver.)  
ISBN 978-82-326-4103-1 (electronic ver.)  
ISSN 1503-8181



Doctoral theses at NTNU, 2019:253

Bjørn Håkon Frodal

# Micromechanical modelling of ductile fracture in aluminium alloys

 **NTNU**  
Norwegian University of  
Science and Technology

 NTNU

Doctoral theses at NTNU, 2019:253

**NTNU**  
Norwegian University of Science and Technology  
Thesis for the Degree of  
Philosophiae Doctor  
Faculty of Engineering  
Department of Structural Engineering

 **NTNU**  
Norwegian University of  
Science and Technology

Bjørn Håkon Frodal

# Micromechanical modelling of ductile fracture in aluminium alloys

Thesis for the Degree of Philosophiae Doctor

Trondheim, October 2019

Norwegian University of Science and Technology  
Faculty of Engineering  
Department of Structural Engineering

 **NTNU**  
Norwegian University of  
Science and Technology

**NTNU**  
Norwegian University of Science and Technology

Thesis for the Degree of Philosophiae Doctor

Faculty of Engineering  
Department of Structural Engineering

© Bjørn Håkon Frodal

ISBN 978-82-326-4102-4 (printed ver.)  
ISBN 978-82-326-4103-1 (electronic ver.)  
ISSN 1503-8181

Doctoral theses at NTNU, 2019:253

Printed by NTNU Grafisk senter

# Preface

This thesis is submitted in partial fulfilment of the requirement for the degree of Philosophiae Doctor (PhD) in Structural Engineering at the Norwegian University of Science and Technology (NTNU). The work has been conducted at the Structural Impact Laboratory (SIMLab) at the Department of Structural Engineering, NTNU. Funding was provided by the Centre for Advanced Structural Analysis (CASA), Centre for Research-Based Innovation, hosted by the Department of Structural Engineering and the SIMLab group. Professor Odd Sture Hopperstad and Professor Tore Børvik supervised the work.

The thesis consists of four parts, which cover separate but related topics. Each part contains a journal article, given in Part 1-4 of this thesis. The journal articles have been published in (Part 1 & 2), submitted to (Part 3), or to be submitted to (Part 4), international peer-reviewed journals. A synopsis binds the individual scientific contributions together.

The first author has been responsible for the experimental work, processing and interpretation of the experimental data, building all numerical models, performing all of the numerical simulations, implementing the single crystal plasticity model and the strain path change model used in Part 2, and preparing the manuscripts that comprise Parts 1-4. The experiments were performed in collaboration with a technician, and in some cases with the assistance of master students. In Part 1, the scanning electron microscopy (SEM), backscattered electron (BSE) micrographs and the electron back-scatter diffraction (EBSD) were performed by a technician. In Part 2, the SEM images were taken by PhD Candidate Susanne Thomesen at SIMLab, and the set of Fortran subroutines used to control the stress state of the unit cell simulations were provided by Dr. Lars Edvard Blystad Dæhli. Associate Professor David Morin provided the Fortran program used to perform the strain localization analyses in Part 3. In Part 4, the SEM and transmission electron microscopy (TEM) were performed by PhD Candidate Emil Christiansen, and the nanostructure model (NaMo) calculations were performed by Adjunct Professor Ole Runar Myhr.

Bjørn Håkon Frodal  
Trondheim, Norway  
July 1, 2019





## Abstract

To predict the behaviour of structural components, engineers often rely on numerical modelling and simulation to describe the mechanical response and failure. For an accurate assessment of the structural response, predictive numerical models are essential. A critical step for better and more physical-based damage and fracture models is improved understanding and quantitative description of the ductile fracture process. Understanding the physical mechanisms at the microscopic scale and the role of the microstructure in metallic materials are thus fundamental. Numerical modelling and simulation on the nano-, micro- and mesoscales assisted by advanced experimental characterization can contribute to a more profound knowledge of the physical phenomena governing damage evolution and ductile failure in materials. As such, this PhD thesis consists of experimental and numerical studies regarding the ductile fracture of aluminium alloys.

Part 1 presents an entirely experimental study, investigating the influence of pre-compression on the strain to failure by reversed loading tests on three aluminium alloys (AA6060, AA6082.25 and AA6082.50) in the peak strength condition (temper T6). The three alloys have different grain structure and crystallographic texture. Diabolo-shaped specimens oriented along the transverse direction of an extruded profile are used and subjected to five different levels of pre-compression (0, 10, 20, 30, 40%) before they are continuously pulled to fracture in tension. It is found that pre-compression has a marked influence on the ductility of the aluminium alloys and that it depends on the microstructure and strength of the material. A fractographic analysis is performed on the reversed loading specimens in order to get a deeper understanding of the ductile fracture mechanisms. In the reversed loading experiments, the tensile ductility is observed to be approximately constant, exhibits a small increase or a large increase, depending on the alloy.

Additional experimental results using reversed loading tests on diabolo-shaped specimens are presented in Part 2. The three aluminium alloys, AA6060, AA6082.25 and AA6082.50 are solution heat-treated and artificially aged to three conditions, namely temper O (annealed), temper T7 (overaged) and temper T6 (peak strength). The reversed loading experiments are performed using five different levels of pre-compression (0, 10, 20, 30, 40%) before the load is reversed and the specimens are pulled to fracture in tension. With an advanced plasticity model accounting for plastic anisotropy, non-associated plastic flow, nonlinear isotropic and kinematic hardening, strength differential effect, and transient and permanent effects of strain path change, the tests are modelled using nonlinear finite element based simulations. The plastic anisotropy is found based on crystal plasticity finite element analyses and unit cell simulations, where the non-proportional loading histories from the reversed loading tests are used to investigate ductile fracture. The strain to coalescence from the unit cell is mapped back to the test specimen, used to determine the failure strain, and compared with the experimental findings.

In Part 3, the effects of plastic anisotropy, strength and work hardening on the ductility of aluminium alloys are investigated using nonlinear finite element simulations and strain localization analyses of tensile tests in different material orientations. The three aluminium alloys (AA6060, AA6082.25 and AA6082.50) are considered in addition to an isotropic material represented by an isotropic high-exponent yield surface. The yield surfaces of these alloys are combined with three flow stress curves representative for the different ageing-treatments in Part 2, resulting in a range of relevant model materials with different plastic anisotropy, strength and work hardening used in the numerical investigations. Finite element simulations are carried out on tensile tests in seven in-plane directions, i.e., 0°, 15°, 30°, 45°, 60°, 75° and 90° to the extrusion direction, and the non-proportional loading histories are used in the subsequent strain localization analyses. In agreement with previous experimental evidence, plastic anisotropy is found to have a marked influence on the tensile ductility and to induce fracture anisotropy. Further, the influence of strength and work hardening is found to depend on the plastic anisotropy.

The role of the quench rate on the plastic flow and ductile fracture of aluminium alloys is investigated in Part 4. The three age hardenable aluminium alloys AA6060, AA6082.25 and AA6082.50 are subjected to different quench rates after the solution heat-treatment (either water quenching or air cooling), and the impact on the precipitate microstructure and the mechanical properties is studied. Tensile tests on smooth and V-notch specimens and Kahn tear tests are performed to study the influence of stress state on plastic flow and fracture. Transmission electron microscopy (TEM) investigations show that the alloys and their precipitation microstructure are differently affected by the quench rate. As a result of the observed lower yield strength and higher work-hardening rate after air cooling, the strain to failure is increased for the smooth and V-notch tensile tests. Depending on the grain structure and plastic anisotropy, the crack propagation energy, calculated from the Kahn tear tests, is differently affected by the quench rate. In addition, finite element simulations of the mechanical tests are performed, using an extension of the Gurson model to high-exponent anisotropic plasticity, for one of the alloys. The anisotropic porous plasticity model is able to precisely capture fracture initiation in all the specimen geometries. On the other hand, the crack propagation energies of the Kahn tear tests are slightly overestimated.

## Acknowledgements

First, I want to thank my supervisors, Professor Odd Sture Hopperstad and Professor Tore Børvik for their excellent guidance and the interesting discussions during the PhD work. Your knowledge, enthusiasm and dedication to the scientific community are truly inspiring. I am grateful for your guidance and could not have asked for better supervisors and scientific mentors.

I would also express my gratitude to the guys in the Lab, Mr. Tore André Kristensen, Mr. Trond Auestad and Mr. Tore Wisth for the help with preparing and performing the tests. Thanks to Dr. Stephane Dumoulin who has provided me with valuable guidance and discussions on the topic of crystal plasticity and for introducing me to the concept of source control. Associate Professor David Morin is gratefully acknowledged for our discussions regarding the strain localization theory and valuable guidance related to numerical implementation. I am grateful to Dr. Lars Edvard Blystad Dæhli for discussions on unit cell simulations and on ductile fracture in general. PhD Candidate Emil Christiansen is thanked for the fruitful discussions and valuable insight on the nano- and micro-scale. I had also the opportunity to supervise several master's students and would like to thank them for their contribution to the project.

The financial support of this work from the Centre for Advanced Structural Analysis (CASA), Centre for Research-based Innovation at the Norwegian University of Science and Technology, is gratefully acknowledged.

Thanks to my colleagues at SIMLab for a great working environment where everyone's door is always open. Special thanks go to PhD Candidate John Fredrick Berntsen for sharing an office in the *basement* (2<sup>nd</sup> floor) for the first part of our PhD work, and our discussions on mathematical, mechanical and numerical dilemmas. PhD Candidates Ole Vestrum and Karoline Osnes are thanked for their enthusiasm, great spirit and for sharing an office for a few months. The gang in the *aquarium* (3<sup>rd</sup> floor office hall), including PhD Candidate Sindre Nordmark Olufsen and all mentioned PhD Candidates is also gratefully acknowledged for casual discussions.

Last but not least, I would like to thank my family and friends for your great support, encouragement and motivation. Thanks to my parents for a safe and healthy upbringing, and always cheering me on in sports. I express my deep gratitude to my fiancée, Susanne Thomesen, for your love, good advice, and for taking some of the scanning electron microscopy (SEM) images for this thesis.



# Contents

<b>Preface</b>	<b>i</b>
<b>Abstract</b>	<b>iv</b>
<b>Acknowledgements</b>	<b>v</b>
<b>Synopsis</b>	<b>1</b>
<b>1 Introduction</b>	<b>1</b>
1.1 Background and motivation . . . . .	1
1.2 Aluminium alloys . . . . .	2
1.2.1 Microstructure . . . . .	3
1.3 Theory of plasticity . . . . .	5
1.3.1 Crystal plasticity . . . . .	6
1.3.2 Phenomenological plasticity . . . . .	7
1.4 Ductile fracture . . . . .	8
1.4.1 Unit cell modelling . . . . .	9
1.4.2 Porous plasticity . . . . .	12
1.4.3 Strain localization theory . . . . .	12
<b>2 Objectives and scope</b>	<b>15</b>
2.1 Objectives . . . . .	15
2.2 Scope . . . . .	16
<b>3 Research methodology</b>	<b>17</b>
3.1 Top-down/bottom-up approach . . . . .	17
3.2 The virtual laboratory . . . . .	18
<b>4 Summary</b>	<b>21</b>
4.1 Part 1 . . . . .	21
4.2 Part 2 . . . . .	22
4.3 Part 3 . . . . .	23
4.4 Part 4 . . . . .	23

<b>5 Concluding remarks and further work</b>	<b>27</b>
<b>References</b>	<b>29</b>
<b>Articles</b>	<b>39</b>
<b>Part 1</b>	
Influence of pre-compression on the ductility of AA6xxx aluminium alloys . . . . .	39
<b>Part 2</b>	
Modelling and simulation of ductile failure in textured aluminium alloys subjected to compression-tension loading . . . . .	61
<b>Part 3</b>	
On the effect of plastic anisotropy, strength and work hardening on the tensile ductility of aluminium alloys . . . . .	97
<b>Part 4</b>	
The role of quench rate on the plastic flow and fracture of three aluminium alloys with different grain structure and texture . . . . .	121
<b>Appendices</b>	<b>153</b>
<b>A Single crystal plasticity model</b>	<b>155</b>

# Synopsis

## 1 Introduction

### 1.1 Background and motivation

Knowledge about the mechanical properties of materials is important in the design of structures. In the past, before the time of Isaac Newton, knowledge about mechanics and mechanical principles was limited, and the design of structures was based on trial and error. It is said that whenever a new bridge was created in ancient Rome, the design engineer was supposedly demanded to stand under the bridge while chariots drove over to test the bridge (Anderson, 2005). This way, the worst engineers were removed from the profession by "natural selection". Today more humane methods are used for testing structures, and numerical simulations and experimental testing of materials and designs are important in validating their structural properties. Progress within the field of mechanics has allowed for more complex structures and better predictions of the structural response.

Due to the high computational cost associated with detailed numerical simulations of large structures and structural components, the industry has relied on simple numerical tools and constitutive models. As costumers, consumers and architects demand cheaper, lighter, stronger, more aesthetic and more durable components and structures, engineers need to utilize more of a material's capacity. With the increase of computational power observed in recent years, more advanced numerical tools, plasticity and failure models can be used by the industry to design safe components and structures.

The need for more accurate plasticity and failure models demands a greater understanding of the underlying physical phenomena governing plastic deformation and damage evolution. Better and more physical-based damage and fracture models have been developed by the research community in more recent years, but there are still mechanisms that are not fully understood. An improved understanding of these physical mechanisms can only be achieved by modelling and simulation on the nano-, micro- and mesoscales assisted by advanced experimental characterization.

For the 6000 series of aluminium alloys, the understanding and knowledge of material properties such as the yield strength, work hardening and plastic flow are quite advanced. For these age hardenable aluminium alloys, the nanostructure model NaMo developed by Myhr et al. (2010) is capable of predicting the yield strength and work hardening based on the chemical composition and thermal history. The model has been extensively tested, verified and validated for structural applications (Johnsen et al., 2013; Holmen et al., 2015; Hoang et al., 2015; Granum et al., 2018).



By combining NaMo with crystal plasticity theory (Khadyko et al., 2016a), the yielding and plastic flow of textured aluminium alloys can be determined. Phenomenological and porous plasticity models can be calibrated utilizing hierarchical modelling schemes involving crystal plasticity analyses and unit cell simulations. These models can then be used in large scale simulations where the ductile fracture properties may be estimated from strain localization theory or unit cell simulations. Utilizing such virtual material testing can reduce the number of experimental tests needed to calibrate a material model, and will aid in the process of designing new structures and alloys.

## 1.2 Aluminium alloys

Aluminium alloys are attractive in several engineering applications, such as in car body panels, aeroplane fuselages, and in load-bearing structural components, due to their high load-bearing capacity and low weight. Superior properties related to formability, corrosion resistance and recycling make them appealing to, e.g., the automotive, aviation, and offshore industry. In recent years, with the development of new alloys, possessing enhanced properties, aluminium alloys have been applied within new areas, commonly replacing preferred structural materials like steel. Utilization of tools like NaMo (Myhr et al., 2010), makes the tailoring of alloys possible, with given properties for a certain structural application.

**Table 1.1:** International Alloy Designation System (IADS) for wrought alloys (Polmear, 2006).

4-digit series	Main alloying elements	Heat-treatable
1xxx	Minimum of 99.00% aluminium	-
2xxx	Copper, Cu	✓
3xxx	Manganese, Mn	-
4xxx	Silicon, Si	-
5xxx	Magnesium, Mg	-
6xxx	Magnesium and Silicon, Mg & Si	✓
7xxx	Zinc, Zn	✓
8xxx	Others (e.g., Lithium, Li)	-

Aluminium alloys are often divided in two principal classifications, namely *wrought* and *cast* alloys. Wrought alloys, used in rolled plates, extruded profiles and drawn wires, are produced as cast ingots or billets before they are worked, whereas cast alloys are typically used when a component is produced by casting. This thesis will focus on wrought aluminium alloys. In 1970, the International Alloy Designation System (IADS) for wrought alloys was introduced. This system is based on the classification system used by the Aluminium Association of the United States and will be used in this thesis. A list of the classification of aluminium alloys and their main alloying elements is given in Table 1.1. Further, aluminium alloys are divided into the categories of *heat-treatable* and *non-heat-treatable* alloys. The 2000, 6000, and 7000 series of aluminium alloys respond to strengthening by heat-treatment and cover the category of heat-treatable alloys.

Aluminium alloys are typically designated with a *temper* suffix letter, indicating its basic treatment and condition. F, O, W, H and T are common temper conditions, indicating: (F) as-fabricated, (O) annealed, (W) solution heat-treated (unstable), (H) cold-worked, and (T) heat-treated to produce stable tempers other than F, O and H. Tempers H and T, typically have suffix digits further specifying their type (see, e.g., Polmear, 2006). The main classification of T tempers are: (T1) annealed and naturally aged, (T2) annealed, cold worked and naturally aged, (T3) solution heat-treated, cold worked and naturally aged, (T4) solution heat-treated and naturally aged to a substantially stable condition, (T5) annealed and artificially aged, (T6) solution heat-treated and artificially aged, (T7) solution heat-treated and artificially overaged, (T8) solution heat-treated, cold-worked and artificially aged, (T9) solution heat-treated, artificially aged and cold-worked, and (T10) annealed, artificially aged and cold-worked.

### 1.2.1 Microstructure

The alloying elements of the different classes of aluminium alloys are added to give strength and to enhance the properties of aluminium. With these alloying elements the low yield strength of pure aluminium, of about 7-11 MPa, can be raised to above 700 MPa (Polmear, 2006). For the non-heat-treatable alloys, high strength is mainly achieved by strain-hardening (cold-working) in association with solid solution hardening and/or dispersion hardening. For the heat-treatable alloys precipitation hardening is also available by natural or artificial ageing. This thesis will mainly focus on age hardenable, i.e., heat-treatable, aluminium alloys.

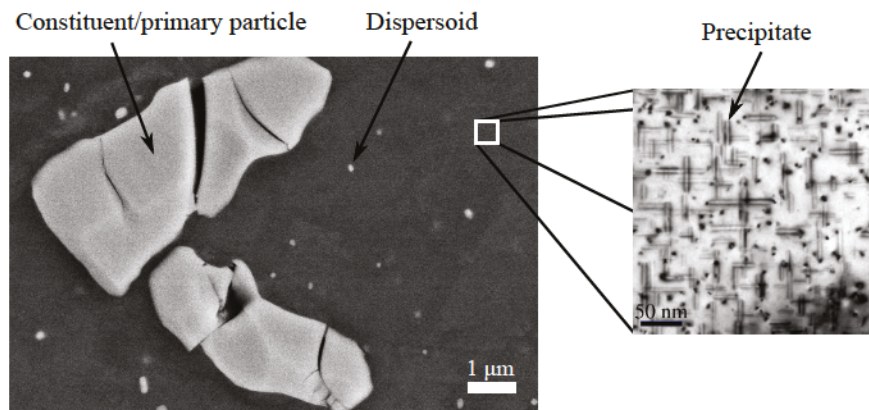


**Figure 1.1:** Different particles found in age hardenable aluminium alloys, from Part 1 and Part 4 of this thesis, using scanning electron microscopy (SEM) and transmission electron microscopy (TEM). Precipitates are visible through the dark strain field in the surrounding aluminium matrix.

Age hardenable aluminium alloys typically contain three main groups of second phase particles. These particles are often called *constituent particles* (or primary particles), *dispersoids* and *precipitates*, see Figure 1.1. The coarse constituent particles typically comprise practically insoluble elements such as iron (Fe). These particles have no practical function and are often detrimental to the fracture properties of an alloy. Due to the difficulty and high cost of

removing these insoluble elements completely, typical commercial aluminium alloys contain coarse constituent particles (Polmear, 2006). The typical size of primary particles in alloys after fabrication, e.g., rolling or extrusion, are in the range of 0.5 – 10  $\mu\text{m}$ . Smaller dispersoids form during homogenization and typically contain the elements: manganese (Mn), chromium (Cr), and zirconium (Zr) (Polmear, 2006). These particles inhibit recrystallization and grain growth by pinning grain boundaries during processing and heat-treatment of the alloys (Remøe et al., 2017). The typical size of dispersoids is in the range of 0.05 – 0.5  $\mu\text{m}$ . During natural or artificial ageing of heat-treatable aluminium alloys, fine precipitates form, consisting of soluble elements. Generally, precipitates have the largest influence on the strength of an alloy, and their size can be up to 0.1  $\mu\text{m}$ .

In all age hardenable aluminium alloys containing precipitates, *precipitate free zones* (PFZs) form around dispersoids and grain boundaries (Unwin et al., 1969; Polmear, 2006). The PFZs lack strengthening precipitates and are thus softer than the rest of the grain interior, but the PFZs typically retain some solute in solid solution (Unwin et al., 1969) and are stronger than pure aluminium. The PFZs form due to vacancy and/or solute depletion close to the dispersoids and grain boundaries as the vacancies and solute atoms diffuse to these locations. Crack initiation and growth can occur more easily in these weaker zones as plastic deformation will localize in the PFZs (Dowling and Martin, 1976; Morgenevner et al., 2008; Chen et al., 2009; Khadyko et al., 2016b). It has been reported that the PFZs can develop significant misorientations relative to their parent grain, due to the localized plastic deformation, which could contribute to the strengthening of PFZs (Christiansen et al., 2018) and delay fracture initiation.

Aluminium alloys have a polycrystalline structure; as such, they are composed of a number of individual crystals or *grains*. Each grain within the polycrystal has a crystallographic orientation relative to the material component which could be, e.g., a rolled plate or an extruded profile. If substantial amounts of grains have preferred crystallographic orientations, the material is said to have a *crystallographic texture*, or simply *texture* (Engler and Randle, 2009). Texture typically forms as a result of mechanical processing of the alloy by, e.g., rolling or extrusion. The mechanical properties of textured aluminium alloys are expected to be anisotropic. In contrast, if grains in a polycrystalline aggregate have a random distribution of orientations the alloy has a random texture and is expected to behave in an isotropic fashion. Properties such as Young's modulus, Poisson's ratio, yield strength, ductility, plastic flow, toughness, electrical conductivity and thermal expansion depend on the crystallographic texture (Engler and Randle, 2009). During plastic deformation, the individual grains can rotate and thus the texture of the polycrystal can evolve.

Textured aluminium alloys experience anisotropic plastic flow which is mostly governed by the crystallographic texture (Engler and Randle, 2009), but also other microstructural features such as the grain morphology (Delannay et al., 2009) and precipitate structure (Khadyko et al., 2017) may have a noticeable effect. In addition to plastic anisotropy, metallic materials may experience fracture anisotropy, meaning that the tensile ductility may vary depending on the loading direction. The main sources of anisotropic fracture in metals are: *plastic anisotropy*, *morphological anisotropy*, and *topological anisotropy*. Morphological anisotropy originates from



the preferred orientation and shape of constituent particles and microscopic voids in the material, whereas topological anisotropy stems from the spatial distribution of constituent particles and voids. For certain aluminium alloys, the fracture anisotropy has been observed experimentally to correlate with the plastic flow anisotropy as expressed by the Lankford coefficients (Fourmeau et al., 2013; Khadyko et al., 2019). Fracture anisotropy has also been observed to depend on the orientation of constituent particles relative to the loading direction, as particles can crack more easily along a specific direction (Agarwal et al., 2002). The arrangement of constituent particles has also an effect on the failure process and can induce fracture anisotropy, even in alloys experiencing nearly isotropic yielding and plastic flow (Hannard et al., 2018). For a further discussion and treatment of fracture anisotropy in aluminium alloys, the reader is referred to Part 3 of the thesis.

By changing the chemical composition, heat treatment and mechanical processing of aluminium alloys, material scientists are able to design alloys with attractive properties. They can influence material characteristics such as the grain structure, crystallographic texture and precipitate structure by controlling the thermo-mechanical processing, and thus engineer materials with, e.g., the appropriate yield strength and ductility. While this flexibility is desired, it can also lead to processing related issues such as *quench sensitivity*. During quenching of an alloy after homogenization or the solution heat-treatment, the hardening capability may be reduced if the quench rate is too low (Dons and Lohne, 1983). Quench sensitivity primarily stems from the precipitation of non-hardening phases on dispersoids and at grain boundaries during cooling (Dons and Lohne, 1983). As a result, the age hardenable aluminium alloy experiences a solute loss, and this solute can no longer contribute to the age hardening of the alloy by forming strengthening precipitates in the subsequent artificial ageing. Alloys with few or none dispersoids can also be quench-sensitive (Milkereit et al., 2010; Strobel et al., 2011, 2016) and this is linked to the supersaturation of vacancies. The high number density of vacancies after a fast quench is favourable for precipitate formation during artificial ageing (Evancho and Staley, 1974; Deschamps et al., 2009; Seyedrezai et al., 2009; Falahati et al., 2012), and with lower quench rates the number of vacancies is reduced. The vacancy concentration has also been found to affect quench sensitivity in alloys with a high content of dispersoids (Strobel et al., 2019). Due to the reduction of vacancies and solute after a slow quench, the PFZs around dispersoids and grain boundaries are wider. This will, in turn, promote plastic localization and fracture initiation in the PFZs, and a decreased fracture toughness (De Haas and De Hosson, 2002; Dumont et al., 2003, 2004a,b; Morgeneyer et al., 2008). For a further discussion and treatment of quench sensitivity and its impact on plastic flow and fracture of aluminium alloys, the reader is referred to Part 4 of this thesis.

### **1.3 Theory of plasticity**

Before our attention can be directed towards ductile fracture, a vital part of a ductile material's response, namely its plastic deformation, needs to be elaborated, as the stress state and the loading path of a material have a marked influence on the fracture behaviour (Benzerga and Leblond, 2010; Pineau et al., 2016). The fundamental goal of the theory of plasticity is to serve as a mathematical

and physical foundation for which the plastic deformation of materials under complex loading conditions can be formulated and described. The first works on the theory of plasticity date back to the 1860s when Tresca published his now renowned yield criterion based on experimental results (Khan and Huang, 1995). In the years to come, pioneering researchers such as Saint-Venant, Levy, von Mises, Hencky, Prandtl, and Taylor developed fundamental concepts which are still applied and further developed today.

The theories of plasticity can be categorized into two main groups (Khan and Huang, 1995). The first category, comprised of physical theories of plasticity, tries to describe the mechanisms of plastic deformation on the microscopic scale. The mechanisms are usually formulated on a crystal scale and the detailed deformation of crystals/grains are important aspects. An essential part of the physical theories of plasticity is *crystal plasticity*. The second category consists of mathematical theories developed to describe experimental observations on a macroscopic or continuum scale. This group of plasticity models is typically based on assumptions and hypotheses from experimental observations. Albeit they do not require any deep knowledge of the physical mechanisms of plastic deformation, this knowledge is typically used in order to formulate reasonable assumptions and hypotheses. Due to their phenomenological nature, these models are often referred to as *phenomenological plasticity* models. Phenomenological plasticity models typically contain variables and parameters that can be measured and calibrated by performing experiments on the macroscopic scale, whereas physical models may contain parameters encompassing information of the microstructure and are thus harder to quantify.

### 1.3.1 Crystal plasticity

In the early 1900s, the foundation for single crystal plasticity was established by the works of Ewing and Rosenhain (1900), Taylor and Elam (1923, 1925), Schmid (1924), and Taylor (1934a, 1934b). Later, the mathematical formulation based on the physical mechanisms responsible for plastic deformation in single crystals was pioneered by Taylor (1938). In the years to come, Hill (1966), Hill and Rice (1972), Asaro and Rice (1977), and Hill and Havner (1982) developed more rigorous formulations of single crystal plasticity.

The fundamental phenomenon of plastic deformation is plastic slip, which occurs on certain crystallographic slip systems defined by slip normals and slip directions. For a given crystal structure, e.g., a face-centred-cubic (FCC) lattice in aluminium, the number of slip systems is known due to the pioneering research of Taylor and co-workers. For FCC metals plastic slip develops on  $\{111\}$  planes in  $\langle 110 \rangle$  directions, making a total of 12 slip systems. A central principle within crystal plasticity is *Schmid's law*, which states that plastic slip will occur on a certain slip system when the magnitude of the resolved shear stress on that slip plane, along a slip direction, reaches a critical value. Albeit some micromechanical phenomena exist which give rise to non-Schmid effects, Schmid's law is readily accepted for metals and typically gives good predictions of the single crystal response. For further discussions and theory of single crystal plasticity, the reader is referred to the textbook of Khan and Huang (1995) and the review paper of

Roters et al. (2010). See also Appendix A for the theory, algorithm and implementation of the single crystal plasticity model used in Part 2 of the thesis.

As stated above, in Section 1.2.1, aluminium alloys and metals in general, are materials made up of a polycrystalline structure. Thus, to describe their mechanical response a polycrystal plasticity theory is needed. In order to formulate such a theory, the single crystal plasticity theory is often used in combination with some homogenization scheme. The framework proposed by Sachs (1928), assumes that all grains within a polycrystal experience the same state of stress. As a result, equilibrium across grains is fulfilled, but compatibility is violated. The full-constraint Taylor model (Taylor, 1938; Bishop and Hill, 1951a, 1951b) is based on the assumption that all grains experience the same deformation, and so in contrast to the model of Sachs (1928), compatibility is fulfilled but stress equilibrium is violated. In order to develop a more realistic description of polycrystals, different approaches have been proposed such as relaxed-constraint Taylor models (Kocks and Chandra, 1982; Van Houtte, 1982, 1988; Van Houtte et al., 2002), and visco-plastic self-consistent (VPSC) models (Hutchinson, 1976; Molinari et al., 1987; Lebensohn and Tomé, 1993, 1994).

With the increase in computational power observed in recent years, the full-field micromechanical approaches have become more popular. Here the single crystal plasticity theory is usually combined with the finite element method (CP-FEM) (Raabe and Roters, 2004; Kanjarla et al., 2010; Saai et al., 2013; Zhang et al., 2015) or a spectral method using fast Fourier transformation (FFT) (Lebensohn et al., 2012; Eisenlohr et al., 2013; Zhang et al., 2016) to account for both stress equilibrium and compatibility. In addition, the complex grain morphology, local interactions and inhomogeneities of the mechanical fields of polycrystalline materials can be represented. Recently, hierarchical modelling approaches have been utilized (Zhang et al., 2015; Zhang et al., 2016) with, e.g., CP-FEM to reduce the number of experimental tests needed to calibrate phenomenological plasticity models. For further treatments on the field of crystal plasticity and their use in hierarchical modelling approaches, the reader is referred to Part 2 of the thesis and the references therein.

### **1.3.2 Phenomenological plasticity**

Phenomenological plasticity theory was established before scientists and engineers knew about the physical phenomena governing plastic deformation. Due to their computational efficiency, phenomenological plasticity models are still widely used today and are used in the majority of numerical simulations involving plastic deformation in industry. For metals, the early models developed by Tresca and von Mises are still used, even though more advanced and sophisticated models are available. These first models developed for plastic deformation describes isotropic material behaviour. For aluminium alloys exhibiting isotropic behaviour, the yield criteria by Tresca and von Mises give less accurate results. As a result, a high-exponent yield criterion was developed by Hershey (1954) and Hosford (1972), which gives good predictions for isotropic alloys (Hosford, 1972; Hosford, 1996; Lian and Chen, 1991).

Due to the thermo-mechanical processing of aluminium alloys, the plastic behaviour of, e.g., rolled



plates and extruded profiles is likely anisotropic, and for such materials, the yielding and plastic flow should be described using an anisotropic yield criterion. One of the first anisotropic yield criteria proposed is the one by Hill (1948) for orthotropic materials. The quadratic yield function of Hill (1948) gives less accurate estimates of the yield surface for aluminium alloys (Woodthorpe and Pearce, 1970; Stout et al., 1983; Iadicola et al., 2008), but give reasonable estimates for, e.g., steels. Inspired by the non-quadratic yield function of Hershey (1954) and Hosford (1972), Barlat et al. (1991) proposed a criterion for orthotropic materials based on linear transformation of the stress tensor. Later, Karafillis and Boyce (1993) generalized the theory of linear transformation, and proposed a more flexible criterion capable of accounting for other material symmetries as well. This criterion was later extended by Bron and Besson (2004) to include an additional linear transformation to further increase its flexibility. Similarly, Barlat et al. (2005) used two linear transformations of the stress tensor and proposed a new yield function based on the non-quadratic yield criterion by Barlat et al. (1991). Yield criteria including more linear transformations of the stress tensor have also been proposed (Aretz et al., 2010; Aretz and Barlat, 2013), and linear transformation has been used to extend criteria based on stress tensor invariants (e.g., Cazacu and Barlat, 2001; Yoshida et al., 2013; Lou and Yoon, 2018).

As the number of linear transformations and anisotropy parameters increase, the calibration process becomes more and more challenging, and the process of experimental testing to determine the yield criterion for a material becomes expensive and time-consuming. To reduce the number of experimental tests needed to calibrate the yield surface of a material, virtual material testing based on micromechanical approaches such as crystal plasticity theory can be utilised. For further discussions and treatments of plastic anisotropy and virtual material testing, the reader is referred to Part 2 of the thesis.

One of the drawbacks of phenomenological plasticity models, compared with crystal plasticity models, is their inability to describe anisotropic hardening such as the evolution of the yield surface due to changes in the crystallographic texture. More recently, frameworks have been proposed in order to accommodate anisotropic hardening. The most promising frameworks are those proposed by Gawad et al. (2015) and Kohar et al. (2019). The hierarchical multi-scale framework of Gawad et al. (2015) systematically recalibrates the yield surface based on data provided by a crystal plasticity virtual experiment framework. The model of Kohar et al. (2019) introduces the plastic spin into the plasticity model, and the evolution of the plastic spin is calibrated based on crystal plasticity.

## 1.4 Ductile fracture

Ductile fracture in metallic materials is governed by *nucleation*, *growth* and *coalescence* of microscopic voids (Benzerga and Leblond, 2010; Besson, 2010; Pineau et al., 2016; Benzerga et al., 2016). Voids may nucleate at constituent particles or inclusions either by decohesion or by particle cracking (Maire et al., 2011), or voids may pre-exist in the material (Toda et al., 2013). Tipper (1949) was the first to establish that materials would fail in a ductile manner due to void

formation at constituent particles. Later, this could be confirmed by fractography investigations of fracture surfaces utilizing scanning electron microscopy (SEM), as first documented by Plateau et al. (1957). More recently, *in situ* experiments utilizing X-ray tomography have been used to further study the ductile failure process (Maire et al., 2011).

After void nucleation, voids will grow in the material due to plastic straining and finally, coalesce as the inter-void ligaments are subjected to plastic flow localization. The three essential types of void coalescence are (Benzerga and Leblond, 2010; Pineau et al., 2016): (i) coalescence in layers by *internal necking*, (ii) *void-sheet coalescence* in a micro-shear band, and (iii) coalescence in columns or *necklace coalescence*. The mode of coalescence typically varies depending on the underlying microstructure, and the stress state or the subjected loading path of the material. In general, void-sheeting and necklace coalescence are usually observed for low stress triaxiality ratios, whereas internal necking is dominant in the intermediate and high stress triaxiality regime.

Ductile fracture modelling can be categorized, like plasticity, into (i) phenomenological, and (ii) physically based models. Uncoupled damage and fracture models can be classified as purely phenomenological. In these models, the evolution of damage does not affect the mechanical response of the material and is merely an indicator for ductile failure. In contrast, coupled damage and fracture models, such as porous plasticity models, are typically based on the underlying physical mechanisms at the microscopic level, and the constitutive equations are coupled so that damage evolution typically affects yielding and plastic flow. See Section 1.4.2 for further treatments of porous plasticity models.

Phenomenological models, as previously discussed in Section 1.3 for plasticity models, are typically less computationally demanding, and easier to calibrate than physically based models. As a result, uncoupled fracture models are widely used by both scientists and engineers to model structural failure. Some of the most renowned models include the original and modified Cockcroft-Latham criterion (Cockcroft and Latham, 1968; Gruben et al., 2012), the original and modified Johnson-Cook criterion (Johnson and Cook, 1985; Børvik et al., 2001), the original and modified Mohr-Coulomb criterion (Bai and Wierzbicki, 2010), and the Hosford-Coulomb criterion (Mohr and Marcadet, 2015). For further treatments of uncoupled damage models, the reader is referred to the review by Pineau et al. (2016).

#### **1.4.1 Unit cell modelling**

The first studies of ductile failure, employing micromechanical modelling strategies, were those of McClintock (1968) and Rice and Tracey (1969), who investigated void growth in an infinite elastic-plastic material consisting of a single void. McClintock (1968) considered a cylindrical void, whereas Rice and Tracey (1969) investigated the response of a spherical void. A few years later, Needleman (1972) used unit cell analyses for the first time studying void growth in an elastic-plastic material. This study presented a framework consisting of a periodic array of circular cylindrical voids, which allowed for studying the interaction between neighbouring voids. A unit cell model was employed, i.e., a representative volume element, containing a single void with



appropriate boundary conditions applied to the cell periphery as to represent the whole material volume, see Figure 1.2. Since then, a large number of studies has employed unit cell analyses in the quest of elucidating the physical mechanisms of ductile fracture at the microscopic scale (see, e.g., Tvergaard, 1981, 1982a, 1982b; Thomson and Hancock, 1984; Needleman, 1987; Koplik and Needleman, 1988; Becker et al., 1989; Fleck et al., 1989; Tvergaard, 1996; Kuna and Sun, 1996; Zhang et al., 2001; Benzerga and Besson, 2001; Kim et al., 2004; Potirniche et al., 2006; Barsoum and Faleskog, 2007, 2011; Yerra et al., 2010; Zhang and Skallerud, 2010; Steglich et al., 2010; Keralavarma and Benzerga, 2010; Keralavarma et al., 2011; Benzerga et al., 2012; Srivastava and Srivastava, 2013; Dunand and Mohr, 2014; Wong and Guo, 2015; Tekoğlu et al., 2015; Kristoffersen et al., 2016; Dæhli et al., 2016, 2017a, 2017b; Legarth and Tvergaard, 2018; Guo and Wong, 2018; Frodal et al., 2019).

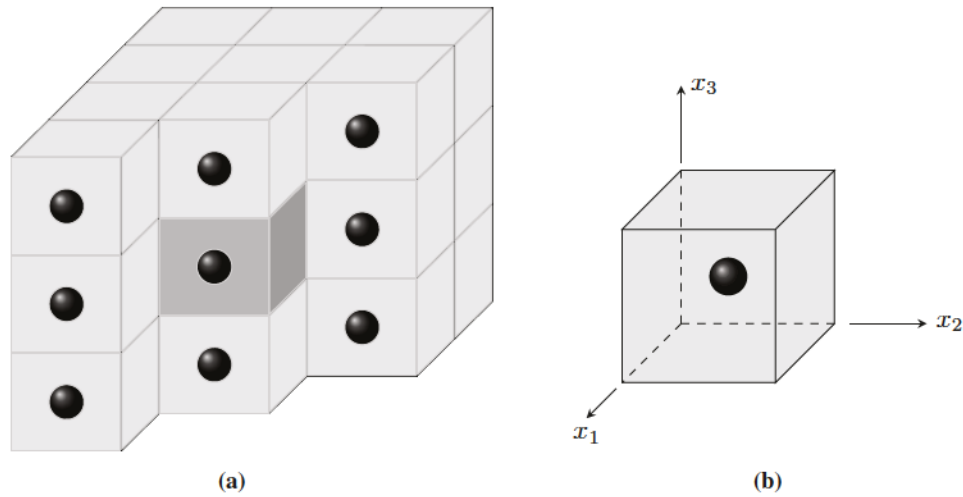


**Figure 1.2:** A representative volume element of an aluminium alloy: (a) an idealized microstructure consisting of a periodic array, where particles or voids with equal size and shape are evenly distributed, and (b) the fundamental building block, namely the unit cell model.

Unit cell simulation is an attractive way of studying the mechanisms of ductile fracture, as information of the local deformation fields can be employed to get a more profound understanding of the growth and coalescence of voids. The framework has been used to study the influence of the stress state on the growth of voids, and more recently the effect of the Lode parameter has been extensively investigated (see, e.g., Zhang et al., 2001; Kim et al., 2004; Barsoum and Faleskog, 2007, 2011; Dunand and Mohr, 2014; Wong and Guo, 2015). The effect of anisotropy has also been examined using unit cells and was first accounted for by Benzerga and Besson (2001). They used a Hill (1948) matrix formulation in order to describe the anisotropic material behaviour. Steglich et al. (2010) used the anisotropic yield criterion of Bron and Besson (2004) in the assessment of an aluminium alloy. Dæhli et al. (2017a) utilized the FC-Taylor method to determine the yield surfaces for typical crystallographic textures encountered in aluminium

alloys, and calibrated the anisotropic yield criterion of Barlat et al. (2005). Further, studies have been devoted to the interaction of plastic anisotropy, initial void shape, and void spacing on void growth (Keralavarma and Benzerga, 2010; Keralavarma et al., 2011; Legarth and Tvergaard, 2018). Void growth has also been investigated for single crystals utilizing crystal plasticity in the matrix material (Potirniche et al., 2006; Yerra et al., 2010; Srivastava and Srivastava, 2013).

Most of the ductile failure assessments employing unit cell simulations have consisted of studies involving proportional loading, whereas the loading conditions in advanced structural components are usually non-proportional. As a result, the important impact of non-proportional loading has been investigated in more recent years (see, e.g., Zhang and Skallerud, 2010; Benzerga et al., 2012; Dæhli et al., 2016; Kristoffersen et al., 2016; Frodal et al., 2019). Comparisons made between non-proportional loading paths and the proportional loading paths given by, e.g., the strain-average triaxiality to material failure (Benzerga et al., 2012; Dæhli et al., 2016), clearly demonstrate the importance of accounting for non-proportional loading in the context of ductile fracture. For further discussion and treatment of plastic anisotropy and non-proportional loading, the reader is referred to Part 2 and Part 3 of the thesis.

Only a few unit cell studies have been devoted to void nucleation. Some have investigated the effect of the cohesive separation at the particle-matrix interface (see, e.g., Needleman, 1987). Others have examined the stress and strain distributions, assuming that the particle and matrix are inseparable such as in the study by Thomson and Hancock (1984). Studies have also been devoted to the void-particle interaction effects by assuming no bonding between the particle and the matrix (see, e.g., Fleck et al., 1989). More intricate studies of void nucleation need information of the local properties of particles and at the particle-matrix interface that are difficult to obtain.

In the unit cell modelling framework, ductile failure is usually assumed to correspond to the onset of void coalescence and determined from the global kinematic quantities (Koplik and Needleman, 1988). However, strain localization is often a strong indicator for imminent ductile failure, as plastic deformation and damage evolution localize in a narrow region prior to failure initiation, see Section 1.4.3. Based on unit cell simulations, Tekoğlu et al. (2015) showed that depending on the stress triaxiality, strain localization occurs simultaneously or just before void coalescence.

Whereas several studies have used unit cell simulations to investigate void growth and coalescence in anisotropic materials, localization analyses with finite element-based unit cells have so far only been performed for isotropic materials (Barsoum and Faleskog, 2007, 2011; Dunand and Mohr, 2014; Dæhli et al., 2017b; Guo and Wong, 2018). Using these computationally expensive finite element models to perform strain localization analyses for anisotropic solids is still difficult even with modern computers. A large number of localization band orientations has to be investigated within a three-dimensional setup for each load case and results in prohibitive computational times. See Section 1.4.3 and Part 3 of the thesis for further assessment of strain localization. For further details on unit cell modelling, the reader is referred to Benzerga and Leblond (2010), Besson (2010), Pineau et al. (2016), and Benzerga et al. (2016).

### 1.4.2 Porous plasticity

Modelling of ductile materials is often done using micromechanically motivated homogenized material models such as porous plasticity models. In these models, the evolution of microstructural variables is included to describe effects such as material softening due to damage evolution. These variables typically account for physical phenomena occurring at the lower scales of ductile failure by nucleation, growth and coalescence of voids. The first model based on this micromechanical framework is the now renowned model by Gurson (1977). He derived a flow potential based on the limit-analysis of a hollow sphere consisting of a rigid-perfectly plastic material obeying the von Mises yield criterion and the associated flow rule. He further showed that the normality of the plastic flow was preserved in the homogenization procedure. This model is attractive due to its simple formulation, incorporating only a single microstructural parameter through the volume fraction of microscopic voids.

As the original model was developed by considering a rigid-perfectly plastic von Mises material, several extensions have been made to further enhance the model. The first heuristic extension was made by Gurson himself, by adding work hardening to the matrix material. Later, Chu and Needleman (1980) introduced void nucleation in the model, and Tvergaard and Needleman (1984) introduced an accelerated void growth term as to phenomenologically account for void coalescence. Tvergaard (1981) introduced three additional parameters in the yield criterion of Gurson (1977) to give better agreement with unit cell analyses. This version of the model is frequently called the Gurson-Tvergaard-Needleman (GTN) model. Extensions and enhancements have also been made to this framework to incorporate, e.g., kinematic hardening (Mear and Hutchinson, 1985), void shape effects (Gologanu et al., 1993, 1994; Monchiet et al., 2008; Madou and Leblond, 2012), plastic anisotropy of the matrix material (Benzerga and Besson, 2001; Monchiet et al., 2008; Keralavarma and Benzerga, 2010; Morin et al., 2015; Dæhli et al., 2017a), void size effects (Wen et al., 2005; Monchiet and Bonnet, 2013), damage due to void shearing (Nahshon and Hutchinson, 2008), and single crystal plasticity (Han et al., 2013; Paux et al., 2015; Ling et al., 2016). For further elaborations of porous plasticity models, the reader is referred to Benzerga et al. (2016).

### 1.4.3 Strain localization theory

There are two types of strain localization approaches: (i) bifurcation analyses and (ii) imperfection analyses. The principle behind the bifurcation analyses is that an instability in the constitutive equations leads to a bifurcation under homogeneous deformation, which is associated with loss of ellipticity of the governing partial differential equations. In the imperfection analyses, a planar imperfection band is introduced that eventually will trigger loss of ellipticity. In the following, the focus will be on imperfection band analyses, and the reader is referred to Part 3 of the thesis and the references therein for further treatments beyond this section, see also Figure 1.3.

The imperfection band approach to localization analysis, first proposed by Marciniak and Kuczyński (1967) for plane stress states, and later extended by Rice (1976) to a general and rigorous formulation,

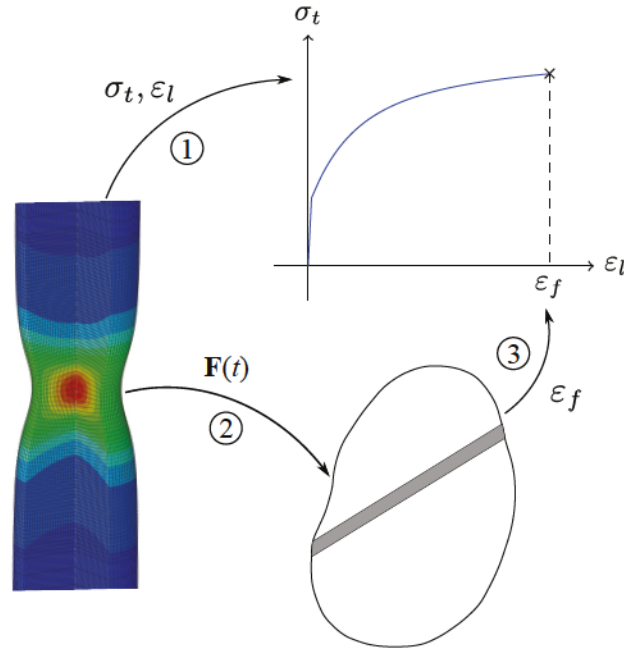


**Figure 1.3:** Methodology of the localization analyses used in Part 3 of the thesis: ① the true stress-strain ( $\sigma_t - \varepsilon_l$ ) curve is extracted from a finite element simulation, ② the deformation gradient  $\mathbf{F}(t)$  of each element within the neck is used in imperfection band analyses, and ③ the failure strain  $\varepsilon_f$  of the test is predicted.

can be applied to study and predict the initiation of ductile failure. A material with an imperfection is considered where the properties are slightly different inside the imperfection compared to the rest of the material. When the material is subjected to loading, deformation tends to concentrate inside the imperfection and this tendency promotes localization of deformation in the material. The imperfection is taken in the form of a planar band, and the stress and strain fields inside and outside of the band are homogeneous but may differ. Localization by loss of ellipticity occurs when the strain rate becomes infinite inside the imperfection band. To trigger loss of ellipticity, the imperfection band must incorporate a softening mechanism (Rudnicki and Rice, 1975) in the case of associated plastic flow, and this is usually achieved by the use of a porous plasticity model describing the constitutive behaviour inside the band, see Section 1.4.2. The material outside the band is described either by metal plasticity or porous plasticity. The imperfection band approach has recently been used in several studies, and good quantitative agreement is observed both with unit cell simulations (Morin et al., 2018a, 2019) and experimental tests (Gruben et al., 2017; Morin et al., 2018b; Morin et al., 2019).

For further discussions and treatments of ductile fracture in general, the reader is referred to the review papers by Benzerga and Leblond (2010), Besson (2010), Pineau et al. (2016), and Benzerga et al. (2016).





## 2 Objectives and scope

### 2.1 Objectives

The primary objectives of this PhD thesis are to acquire a better understanding of the plastic deformation and the ductile fracture mechanisms in aluminium alloys subjected to non-proportional loading by the use of micromechanical modelling. In this work, reversed loading tests are used to unravel the properties of aluminium alloys after compression-tension loading. Different specimen types are used in the experimental and numerical work, as to account for different stress states and loading paths. The effect of different processing routes, such as different quench rates and artificial ageing are used and their influence on the ductile fracture process investigated. Specific objectives are summarized as follows:

- To perform experimental tests to investigate the physical mechanisms governing ductile fracture in aluminium alloys subjected to non-proportional loading histories, such as reversed loading.
- To identify and investigate micromechanical mechanisms relevant to the mechanical response and ductile failure of aluminium alloys.
- To use crystal and phenomenological plasticity models to account for material anisotropy in the context of ductile fracture.
- To explore the capabilities of hierarchical modelling tools in studies of ductile fracture.
- To use and validate phenomenological plasticity models incorporating the strength differential effect, and effects after a strain path change such as work-hardening stagnation, permanent softening and the Bauschinger effect.
- To use and validate a heuristic extension of the Gurson model for anisotropic porous ductile solids with experimental tests and finite element based simulations
- To investigate mechanisms related to the processing of aluminium alloys, such as fracture anisotropy and quench sensitivity, and their impact on ductile fracture.
- To investigate the effect of plastic anisotropy, strength and work hardening on the ductility of aluminium alloys and how plastic anisotropy relates to fracture anisotropy by use of the strain localization theory.
- To investigate the role of grain structure, grain size and crystallographic texture on ductile fracture of aluminium alloys.

## 2.2 Scope

The current study focuses on the behaviour and modelling of aluminium alloys by use of experimental tests and numerical simulations utilizing physically based micromechanical models. The experimental tests are performed on extruded aluminium alloys involving the 6000 series of age hardenable alloys. Smooth, diabolo-shaped and V-notch axisymmetric tensile tests in addition to Kahn tear tests were performed at ambient temperature, under quasi-static loading conditions. Microstructural information was obtained by optical microscopy, scanning electron microscopy (SEM), and transmission electron microscopy (TEM).

Effects that are considered important, but not focused on in the current work are:

- The effect of grain morphology and precipitate structure on the plastic anisotropy by use of crystal plasticity.
- Dynamic loading and rate sensitivity.
- Heterogeneous, spatial distributions of particles and voids, non-spherical particles and voids, pre-cracked particles and void nucleation in the unit cell framework.
- Crystal plasticity in the matrix material of the unit cell model as the constituent particles which are important in the ductile fracture process typically resides inside a grain or on the grain boundary between grains, where the plastic behaviour is well described by the crystal plasticity theory.
- Void nucleation and more general void shapes within the porous plasticity framework.
- Size effects by considering strain gradient plasticity.
- Non-local approaches to ductile fracture.
- Effect of intercrystalline fracture, and the competition between intercrystalline and transcrystalline fracture in numerical models.

### 3 Research methodology

#### 3.1 Top-down/bottom-up approach

A key objective and research goal for the Centre for Advanced Structural Analysis (CASA), which this thesis is part of, is to adopt a research method based on multi- and interdisciplinary research. Thus, to understand mechanisms governing the response of structural components, scientists and engineers need to go down in scale. Experimental techniques or numerical methods at a lower scale can be applied. With newfound knowledge of the physical mechanisms at the microscale, the models on the meso- and macroscopic levels can be improved, and information of several length scales can be combined to give reliable predictions of the component or structural response by a top-down/bottom-up approach, see Figure 3.1.

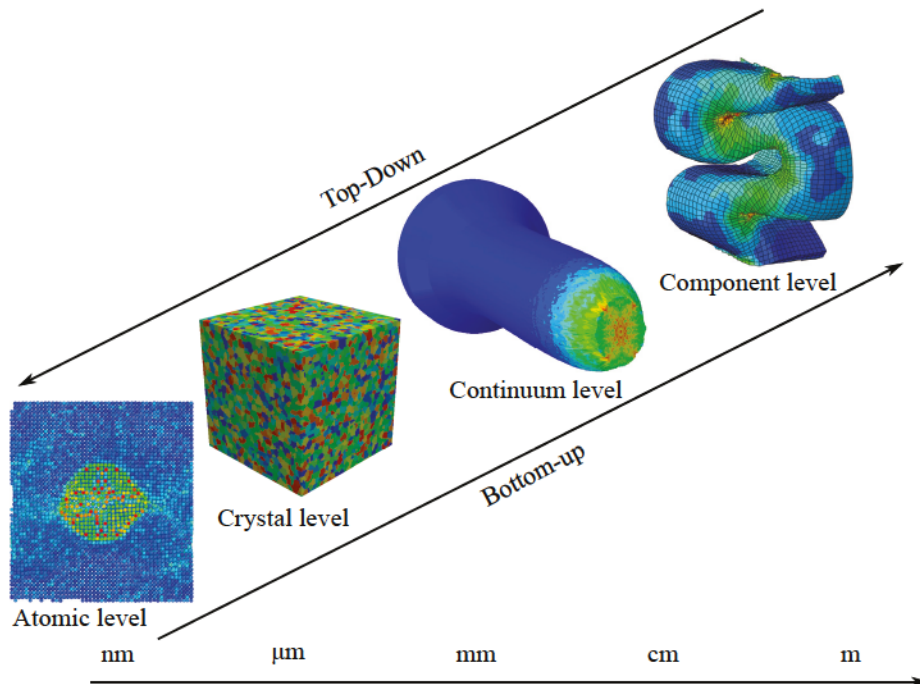
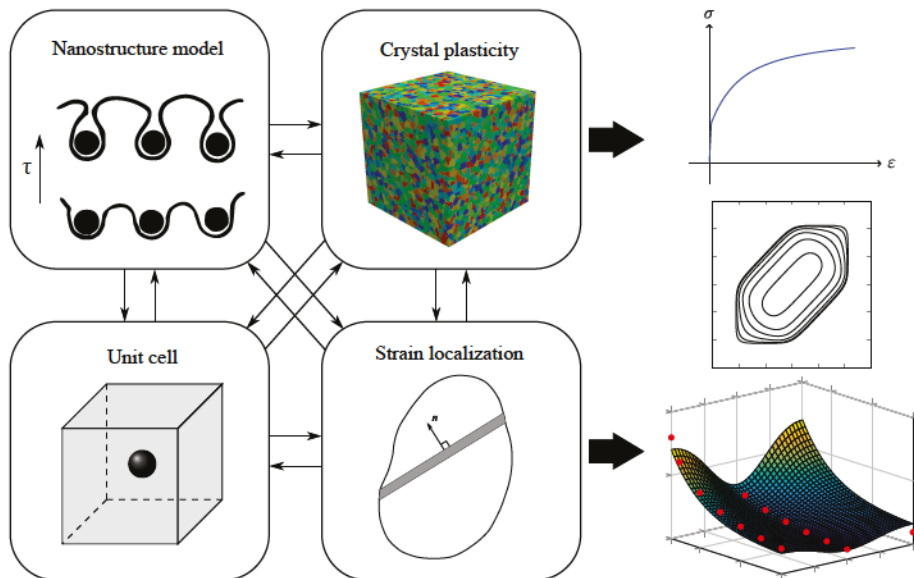


Figure 3.1: Research methodology, the top-down/bottom-up approach.



### 3.2 The virtual laboratory

Through several years at the SIMLab group, it has been worked on and utilized approaches which can predict parts of the mechanical behaviour of metallic materials based on physically based models. Recently, microstructure-based modelling approaches have allowed for good estimates of physical phenomena, and a long-term objective of the SIMLab group is to establish a virtual laboratory for the design of structures consisting of aluminium alloys and other materials. By use of a top-down/bottom-up approach the virtual laboratory can be further improved. Within this thesis, some of the approaches and techniques of the virtual laboratory have been utilized to investigate their potential and predictive capability. In addition, components such as the unit cell modelling framework have been extensively used in the literature for years to investigate mechanisms of ductile fracture.



**Figure 3.2:** The virtual laboratory and its core features used in this thesis.

The primary goal of the virtual laboratory is foremost to aid engineers in the design phase of products and structures by reducing the amount of physical testing needed to calibrate a material model used for early development. The industry will probably rely on experimental testing for final validation in many years to come, but by use of a virtual laboratory, the early design phase can be made more efficient and the cost of extensive material test programmes can be reduced. Knowing which material properties that are needed for a specific design or structural application, material scientists can tailor aluminium alloys and other materials to the desired specification.

The microstructure-based virtual laboratory consists of separate modules that can either be (i) used independently and combined with experimental testing or (ii) combined to predict the material properties without the need for physical experiments. The separate modules require inputs which the engineer can obtain from other modules, experiments or both. Then the current module is

run and outputs information of the particular module. The output typically contains relevant parameters useful for other modules. Some of the modules can also be used directly in nonlinear finite element analyses of structural components. The virtual laboratory framework is illustrated in Figure 3.2.



## 4 Summary

### 4.1 Part 1

- [1] Frodal, B. H., Pedersen, K. O., Børvik, T., Hopperstad, O. S. (2017). *Influence of pre-compression on the ductility of AA6xxx aluminium alloys*. International Journal of Fracture 206, 131-149.

Part 1 presents an entirely experimental study, investigating the influence of pre-compression on the strain to failure by reversed loading tests on three aluminium alloys in the peak strength condition (temper T6). Diabolo-shaped specimens were machined from extruded profiles of the three alloys (AA6060, AA6082.25 and AA6082.50), solution heat-treated and artificially aged. The three alloys had different grain structure and crystallographic texture, including recrystallized (AA6060) and non-recrystallized (AA6082.25) grain structures with typical recrystallization and deformation texture, respectively. In addition, one of the alloys (AA6082.50) had abnormally large grains with a rotated cube texture, which was a result of recrystallization and grain growth subsequent to the solution heat treatment. Typical of extruded alloys, the constituent particles were lined up in stringers along the extrusion direction (ED) and the distribution was reasonably similar for the three alloys.

Specimens oriented along the transverse direction (TD) of the extruded profile were used and subjected to five different levels of pre-compression (0, 10, 20, 30, 40%) before they were pulled to fracture in tension. During testing, the force and the minimum diameters of the specimen along ED and the normal direction (ND) were continuously measured. From these experimental tests, it was found that pre-compression has a marked influence on the ductility of the aluminium alloys and that it depends on the microstructure and the strength of the alloy. For the three alloys tested, three different effects were seen from pre-compression. For the AA6060 alloy, the tensile ductility was observed to drastically increase. After 40% pre-compression, the strain to failure measured from the compressed configuration was doubled compared to the tests in monotonic tension. A more moderate increase in the strain to failure with pre-compression was observed for the AA6082.25 alloy. In contrast, the tensile ductility of the AA6082.50 alloy was observed to be approximately constant.

From the microstructural investigations performed on fractured specimens and specimens stopped during the compression-tension loading cycle, it was found that fracture was mainly transcrystalline with some areas of intercrystalline fracture for the AA6060 and AA6082.25 alloys. A larger amount of intercrystalline fracture was found for the AA6082.50 alloy, caused by the large grains which reduced the ductility of the alloy. With increasing pre-compression, the amount of intercrystalline

fracture was seen to decrease for the AA6060 alloy, which could be caused by strengthening of the precipitate free zones (PFZs), contributing to an increased tensile ductility after pre-compression. Due to much wider PFZs in the AA6060 alloy, strengthening of the PFZs was considered more favourable for this alloy. Another reasonable conjecture which explains the observed differences in ductility is that for the lean AA6060 alloy damage is mainly due to the growth of existing voids in the vicinity of primary particles, while for the two AA6082 alloys the stress level is sufficiently high to make void nucleation a more favourable mechanism for damage evolution. See Part 1 for a discussion.

## 4.2 Part 2

- [2] Frodal, B. H., Dæhli, L. E. B., Børvik, T., Hopperstad, O. S. (2019). *Modelling and simulation of ductile failure in textured aluminium alloys subjected to compression-tension loading*. International Journal of Plasticity 118, 36-69.

In Part 2, additional experimental tests on the same aluminium alloys presented in Part 1 (AA6060, AA6082.25 and AA6082.50) were conducted, including diabolo-shaped specimens subjected to different artificial ageing, leading to three different conditions, namely temper O (annealed), temper T7 (overaged) and temper T6 (peak strength). The reversed loading experiments were also here conducted using five different pre-compression levels (0, 10, 20, 30, 40%) before they were reloaded to fracture in tension. The strength, work hardening, plastic anisotropy and microstructural differences after artificial ageing were observed to impact the tensile ductility of the aluminium alloys differently.

The materials were modelled with an advanced plasticity model accounting for plastic anisotropy, non-associated plastic flow, nonlinear isotropic and kinematic hardening, strength differential effect, and transient and permanent effects of strain path change. A hierarchical modelling framework utilizing virtual material tests with crystal plasticity finite element analyses were performed to calibrate an anisotropic yield surface for each material. The work-hardening response was calibrated from experimental data. Non-proportional loading histories from finite element simulations of the reversed loading tests were then used in unit cell simulations to investigate the mechanisms of ductile fracture at the microscopic scale after a strain path change. The strain to coalescence of the unit cell was mapped back to the numerical simulation of the diabolo-shaped specimen and compared to the experiments.

The unit cell model predicted an approximately constant tensile ductility with pre-compression for the different aluminium alloys, whereas the response of the unit cell was clearly affected by variations in the strength, work hardening and plastic anisotropy depending on the temper-alloy combination. The prediction of a constant tensile ductility with pre-compression matched the experimental observations for some of the materials. In addition, other physical mechanisms not accounted for in the unit cell model can affect the ductile fracture process, see Part 2 for further details.

### 4.3 Part 3

- [3] Frodal, B. H., Morin, D., Børvik, T., Hopperstad, O. S. (2019). *On the effect of plastic anisotropy, strength and work hardening on the tensile ductility of aluminium alloys*. Submitted for possible journal publication.

Part 3 mainly presents a numerical study investigating the relationship between plastic anisotropy and fracture anisotropy, but also effects of strength and work hardening on the tensile ductility of aluminium alloys were considered. The aluminium alloys presented in Part 1 and Part 2 were investigated here as well, and the yield surfaces calibrated from crystal plasticity finite element analyses in Part 2 were used. In addition, an isotropic alloy was included, and by combining the yield surfaces from the four alloys with three flow stress curves representative for the different ageing heat-treatments in Part 2, a set of 12 model materials was constructed.

The influence of plastic anisotropy, strength and work hardening on ductile failure was studied by nonlinear finite element simulations and strain localization analyses using the imperfection band approach on smooth axisymmetric tensile specimens in different material orientations. A total of seven in-plane directions were tested, at  $0^\circ$ ,  $15^\circ$ ,  $30^\circ$ ,  $45^\circ$ ,  $60^\circ$ ,  $75^\circ$  and  $90^\circ$  to the reference direction, i.e., extrusion direction. From these finite element simulations, the non-proportional loading histories were then used in imperfection band analyses to predict the failure strain of the tensile tests.

Plastic anisotropy was found to have a marked influence on the tensile ductility and to induce fracture anisotropy. In agreement with previous experimental evidence, the imperfection band analyses predicted a variation of the failure strain with the tensile direction that correlated with the variation of the Lankford coefficient. This indicates that the fracture anisotropy is closely linked to the plastic anisotropy for certain aluminium alloys. Due to the redistribution of the plastic deformation and a stress state with a lower stress triaxiality in the neck, which was observed for the materials with a lower strength and higher work hardening, the failure strain predicted by the strain localization analyses was higher for these materials. Thus, the materials were observed to be less prone to localization and ductile failure due to a high work-hardening rate. The influence of strength and work hardening was also found to depend on the plastic anisotropy, see Part 3.

### 4.4 Part 4

- [4] Frodal, B. H., Christiansen, E., Myhr, O. R., Hopperstad, O. S. (2019). *The role of quench rate on the plastic flow and fracture of three aluminium alloys with different grain structure and texture*. To be submitted for journal publication.

In Part 4, additional experimental tests were performed on smooth, V-notch axisymmetric tensile specimens and on Kahn tear test specimens. These experiments were used to investigate the



influence of process related issues, such as quench sensitivity and the role of quench rate on the plastic flow and fracture of aluminium alloys. The three aluminium alloys used in Part 1 and Part 2 were subjected to two different processing routes, i.e., two different thermal histories, using either air-cooling or water-quenching after the solution heat-treatment. The three alloys AA6060, AA6082.25 and AA6082.50 were subjected to the solution heat-treatment, then they were either air-cooled or water-quenched and artificially aged to temper T6 (peak strength). Thus a total of six materials with different precipitate microstructure and mechanical properties, such as yield strength, work hardening and ductility, were considered.

Transmission electron microscopy (TEM) investigations were used to investigate the precipitate microstructure after the thermal processing. The alloys and their precipitation microstructure were differently affected by the quench rate. Common for all the alloys was that after air-cooling, the precipitate free zones around dispersoids and grain boundaries became larger than after water-quenching. In agreement with changes in the precipitate structure, the yield strength of the alloys became lower and the work-hardening rate higher after the air-cooling compared to the water-quench. Due to this change, the failure strain was increased for the tensile tests on smooth and V-notch specimens after air-cooling. Also, the crack propagation energy, calculated from the Kahn tear tests, was markedly affected by the quench rate and the effect was different depending on the grain structure and plastic anisotropy.

From the fractographic analysis, in the SEM, the amount of intercrystalline fracture was observed to vary depending on the grain structure, crystallographic texture, precipitate structure and loading direction. The crack propagation energies were found to correlate with the amount of intercrystalline fracture observed on the fracture surfaces of the Kahn tear tests.

The physically-based nanostructure model NaMo was used to predict the effect of the different cooling rates on the mechanical properties of the alloys. Based on the chemical composition and the thermo-mechanical processing of the alloys, the evolution of the precipitate structure was estimated together with their yield strength after different quench rates. The agreement between simulation results and experimental measurements was good, and NaMo appeared to capture the effects of alloy composition, grain structure, PFZ widths and cooling rate on the resulting yield stress with good accuracy.

Finite element simulations of the mechanical tests were performed for the AA6082.25 alloy to investigate the predictive capabilities of an extension of the Gurson (1977) model to high-exponent anisotropic plasticity. The anisotropic yield surface calibrated in Part 2 was utilized. The anisotropic porous plasticity model used was able to precisely capture the fracture initiation in all the specimen geometries, whereas the crack propagation energies of the Kahn tear tests were slightly overestimated. For the crack propagation problem, the porous plasticity model tended to predict a too ductile failure mode, and the dissipated energy due to plastic dissipation was slightly overestimated.

## Other contributions

*Contributions related to, but not included in, this thesis.*

The following studies have been conducted in parallel with the work on the thesis, but have not been included.

## Other journal publications

- [5] Holmen, J. K., Frodal, B. H., Hopperstad, O. S., Børvik, T. (2017). *Strength differential effect in age hardened aluminum alloys*. International Journal of Plasticity 99, 144-161.

## Conference contributions

- [6] Frodal, B. H., Pedersen, K. O., Børvik, T., Hopperstad, O. S. (2016). *Effect of Pre-Compression on Ductile Fracture of Aluminium Alloys*. Presented at the 15th European Mechanics of Materials Conference, EMMC15, Brussel, Belgium.
- [7] Frodal, B. H., Dæhli, L. E. B., Børvik, T., Hopperstad, O. S. (2018). *Ductile failure of textured aluminium alloys under compression-tension loading: experiments, modelling and simulations*. Presented at Topics in Ductile Fracture of Metals, Trondheim, Norway.
- [8] Christiansen, E., Sævareid, S., Frodal, B. H., Marioara, C. D., Hopperstad, O. S., Holmestad, R. (2018) *Precipitate Free Zones and Crack Propagation in Al-Mg-Si Alloys*. At the 16th International Conference on Aluminium Alloys, ICAA16, Montreal, Canada.
- [9] Frodal, B. H., Morin, D., Børvik, T., Hopperstad, O. S. (2019). *On the effect of plastic anisotropy, strength and work hardening on the tensile ductility of aluminium alloys*. Poster at the Aluminium Innovation Workshop, Trondheim, Norway.





## 5 Concluding remarks and further work

By use of experimental investigations on the macro-, micro- and nanoscopic scales assisted by advanced numerical simulations, this thesis has revealed some of the underlying physical phenomena of yielding, plastic flow and ductile fracture of aluminium alloys. An emphasis has been on the effects of non-proportional loading on ductile fracture through reversed loading tests, and the use of micromechanical modelling tools based on crystal plasticity, porous plasticity, strain localization and unit cell frameworks. In addition, the influence of plastic anisotropy, strength, work hardening and process related issues in connection with the role of microstructural properties such as grain structure, grain size and crystallographic texture have been investigated.

Albeit overall precise results can be obtained from micromechanical modelling of ductile fracture, it is necessary to be able to predict also when the current models yield less optimal results. Typically, when the failure mode is governed by substantial void growth, the current models of ductile fracture are able to give good estimates of the strain to failure. If the failure mode is less ductile, the predictive capabilities of the models become less accurate.

The current state of micromechanical modelling and simulations of aluminium alloys is quite advanced and the use of hierarchical modelling frameworks in a virtual laboratory is promising. These models and frameworks will continue to flourish as new understanding of microstructural mechanisms is achieved along with improvements of the methods, models and advances of computing resources.

Based on the work and findings presented in this thesis, the following is suggested as further work.

- The reversed loading tests performed in this thesis (Part 1 & Part 2) were all subjected to loading along the transverse direction (TD). In Part 3, the influence of plastic anisotropy on the tensile ductility and the fracture anisotropy was investigated, and the tensile ductility was observed to vary with tensile direction and plastic anisotropy. It would be interesting also to investigate if the effect of pre-compression would be affected by loading direction, and how it would relate to the results observed in Part 3. As such, reversed loading tests should be performed in  $0^\circ$ ,  $15^\circ$ ,  $30^\circ$ ,  $45^\circ$ ,  $60^\circ$  and  $75^\circ$  to the extrusion direction (ED) to supplement those performed in the  $90^\circ$ -direction (TD).
- In Part 1 & Part 2, the amount of intercrystalline fracture was observed to decrease with increasing pre-compression for the AA6060 alloy in temper T7 and T6, and a probable cause for this is strengthening of the precipitate free zones (PFZs) around grain boundaries. To further study the impact of PFZs, the same material processing as in Part 4 can be used to examine the effect of different quench rates on the influence of pre-compression. After

air-cooling, the PFZs became wider (Part 4) than after water-quenching, and it would be interesting to see how this would affect the ductility after pre-compression.

- In Part 2, a simple representation of the grain morphology were used in the crystal plasticity calculations and calibration of the yield surfaces. In the future, it would be interesting to do full field micromechanical crystal plasticity simulations including the effects of grain morphology and to utilize a more advanced and physically based crystal plasticity hardening model with a more advanced latent hardening formulation, instead of the extended Voce hardening rule with a single non-diagonal parameter in the latent hardening matrix. In Part 2, the crystal plasticity framework was only used to determine the instance of initial yielding, and the extended Voce hardening model should suffice.
- The yield surfaces calibrated in Part 2 are only initial ones. During plastic deformation, the crystallographic texture will evolve and the shape of the yield surfaces with it. In the future, it would be interesting to investigate the effect of an evolving yield surface in simulations of ductile fracture and how, e.g., texture evolution might affect ductile fracture properties. Evolution of the yield surface in a phenomenological framework could be accounted for by introduction of the plastic spin, as done by Kohar et al. (2019). Another approach could be to include crystal plasticity directly in the numerical simulations of structural components.
- A strength differential (SD) effect was observed for the aluminium alloys investigated in this thesis (Part 1 & Part 2). The physical origin of this effect has not been established. To further investigate the physical origin, experiments under superposed hydrostatic pressure could be used to confirm or refute the hypothesis of Spitzig and Richmond (1984) that it is linked to the effect of hydrostatic pressure on dislocation motion.
- Typical uncoupled damage models proposed in the literature predict either no damage accumulation or lower damage accumulation when the material is subjected to compression compared to tension. As a result, these models will either predict a constant or reduced tensile ductility after pre-compression and be unable to describe an increase in tensile ductility after pre-compression, as was observed for some of the materials tested in this thesis. Thus, an uncoupled damage model capable of predicting an increased, decreased and constant tensile ductility after a strain path change should be developed for use in large scale simulations where the structure is subjected to substantial pre-deformations.
- In Part 4, the prediction of the crack propagation in the Kahn tear tests was observed to be highly mesh-size dependent. To reduce this dependency, a non-local approach to ductile fracture should be used and is currently being developed at SIMLab.
- As stated above, it is important to know when the ductile fracture models are not able to estimate the correct ductility due to, e.g., intercrystalline fracture. An effort should, therefore, be made to further investigate mechanisms of intercrystalline fracture and develop models capable to account for the presence of PFZs and less ductile fracture modes in aluminium alloys.

## References

- Agarwal, H., Gokhale, A. M., Graham, S., and Horstemeyer, M. F. (2002). "Anisotropy of intermetallic particle cracking damage evolution in an Al-Mg-Si base wrought aluminum alloy under uniaxial compression". *Metallurgical and Materials Transactions A* 33, pp. 3443–3448.
- Anderson, T. L. (2005). *Fracture Mechanics: Fundamentals and Applications*. Third edition. CRC press, Taylor & Francis Group.
- Aretz, H. and Barlat, F. (2013). "New convex yield functions for orthotropic metal plasticity". *International Journal of Non-Linear Mechanics* 51, pp. 97–111.
- Aretz, H., Aegerter, J., and Engler, O. (2010). "Analysis of Earing in Deep Drawn Cups". *AIP Conference Proceedings* 1252, pp. 417–424.
- Asaro, R. J. and Rice, J. R. (1977). "Strain localization in ductile single crystals". *Journal of the Mechanics and Physics of Solids* 25, pp. 309–338.
- Bai, Y. and Wierzbicki, T. (2010). "Application of extended Mohr–Coulomb criterion to ductile fracture". *International Journal of Fracture* 161, pp. 1–20.
- Barlat, F., Aretz, H., Yoon, J. W., Karabin, M. E., Brem, J. C., and Dick, R. E. (2005). "Linear transformation-based anisotropic yield functions". *International Journal of Plasticity* 21, pp. 1009–1039.
- Barlat, F., Lege, D. J., and Brem, J. C. (1991). "A six-component yield function for anisotropic materials". *International Journal of Plasticity* 7, pp. 693–712.
- Barsoum, I. and Faleskog, J. (2007). "Rupture mechanisms in combined tension and shear-Micromechanics". *International Journal of Solids and Structures* 44, pp. 5481–5498.
- Barsoum, I. and Faleskog, J. (2011). "Micromechanical analysis on the influence of the Lode parameter on void growth and coalescence". *International Journal of Solids and Structures* 48, pp. 925–938.
- Becker, R., Smelser, R. E., Richmond, O., and Appleby, E. J. (1989). "The effect of void shape on void growth and ductility in axisymmetric tension tests". *Metallurgical Transactions A* 20, pp. 853–861.
- Benzerga, A. A., Surovik, D., and Keralavarma, S. M. (2012). "On the path-dependence of the fracture locus in ductile materials – Analysis". *International Journal of Plasticity* 37, pp. 157–170.
- Benzerga, A. A. and Leblond, J.-B. (2010). "Ductile Fracture by Void Growth to Coalescence". *Advances in Applied Mechanics* 44, pp. 169–305.
- Benzerga, A. A. and Besson, J. (2001). "Plastic potentials for anisotropic porous solids". *European Journal of Mechanics - A/Solids* 20, pp. 397–434.
- Benzerga, A. A., Leblond, J.-B., Needleman, A., and Tvergaard, V. (2016). "Ductile failure modeling". *International Journal of Fracture* 201, pp. 29–80.

- Besson, J. (2010). "Continuum Models of Ductile Fracture: A Review". *International Journal of Damage Mechanics* 19, pp. 3–52.
- Bishop, J. F. W. and Hill, R. (1951a). "A theory of the plastic distortion of a polycrystalline aggregate under combined stresses". *Philosophical Magazine* 42, pp. 414–427.
- Bishop, J. F. W. and Hill, R. (1951b). "A theoretical derivation of the plastic properties of a polycrystalline face-centred metal". *Philosophical Magazine* 42, pp. 1298–1307.
- Bron, F. and Besson, J. (2004). "A yield function for anisotropic materials Application to aluminum alloys". *International Journal of Plasticity* 20, pp. 937–963.
- Børvik, T., Hopperstad, O. S., Berstad, T., and Langseth, M. (2001). "A computational model of viscoplasticity and ductile damage for impact and penetration". *European Journal of Mechanics - A/Solids* 20, pp. 685–712.
- Cazacu, O. and Barlat, F. (2001). "Generalization of Drucker's Yield Criterion to Orthotropy". *Mathematics and Mechanics of Solids* 6, pp. 613–630.
- Chen, Y., Pedersen, K. O., Clausen, A. H., and Hopperstad, O. S. (2009). "An experimental study on the dynamic fracture of extruded AA6xxx and AA7xxx aluminium alloys". *Materials Science and Engineering: A* 523, pp. 253–262.
- Christiansen, E., Marioara, C. D., Marthinsen, K., Hopperstad, O. S., and Holmestad, R. (2018). "Lattice rotations in precipitate free zones in an Al-Mg-Si alloy". *Materials Characterization* 144, pp. 522–531.
- Chu, C. C. and Needleman, A. (1980). "Void nucleation effects in biaxially stretched sheets". *Journal of engineering materials and technology* 102, pp. 249–256.
- Cockcroft, M. G. and Latham, D. J. (1968). "Ductility and the workability of metals". *Journal of the Institute of Metals* 96, pp. 33–39.
- De Haas, M. and De Hosson, J. T. M. (2002). "On the effects of thermomechanical processing on failure mode in precipitation-hardened aluminium alloys". *Journal of Materials Science* 37, pp. 5065–5073.
- Delannay, L., Melchior, M. A., Signorelli, J. W., Remacle, J. F., and Kuwabara, T. (2009). "Influence of grain shape on the planar anisotropy of rolled steel sheets – evaluation of three models". *Computational Materials Science* 45, pp. 739–743.
- Deschamps, A., Texier, G., Ringeval, S., and Delfaut-Durut, L. (2009). "Influence of cooling rate on the precipitation microstructure in a medium strength Al-Zn-Mg alloy". *Materials Science and Engineering: A* 501, pp. 133–139.
- Dæhli, L. E. B., Børvik, T., and Hopperstad, O. S. (2016). "Influence of loading path on ductile fracture of tensile specimens made from aluminium alloys". *International Journal of Solids and Structures* 88, pp. 17–34.
- Dæhli, L. E. B., Faleskog, J., Børvik, T., and Hopperstad, O. S. (2017a). "Unit cell simulations and porous plasticity modelling for strongly anisotropic FCC metals". *European Journal of Mechanics - A/Solids* 65, pp. 360–383.
- Dæhli, L. E. B., Morin, D., Børvik, T., and Hopperstad, O. S. (2017b). "Influence of yield surface curvature on the macroscopic yielding and ductile failure of isotropic porous plastic materials". *Journal of the Mechanics and Physics of Solids* 107, pp. 253–283.
- Dons, A. L. and Lohne, O. (1983). "Quench Sensitivity of AlMgSi-Alloys Containing Mn or Cr". *MRS Proceedings* 21, p. 723.



- Dowling, J. M. and Martin, J. W. (1976). "The influence of MN additions on the deformation behaviour of an Al-Mg-Si alloy". *Acta Metallurgica* 24, pp. 1147–1153.
- Dumont, D., Deschamps, A., and Brechet, Y. (2003). "On the relationship between microstructure, strength and toughness in AA7050 aluminum alloy". *Materials Science and Engineering: A* 356, pp. 326–336.
- Dumont, D., Deschamps, A., and Brechet, Y. (2004a). "A model for predicting fracture mode and toughness in 7000 series aluminium alloys". *Acta Materialia* 52, pp. 2529–2540.
- Dumont, D., Deschamps, A., Bréchet, Y., Sigli, C., and Ehrström, J. C. (2004b). "Characterisation of precipitation microstructures in aluminium alloys 7040 and 7050 and their relationship to mechanical behaviour". *Materials Science and Technology* 20, pp. 567–576.
- Dunand, M. and Mohr, D. (2014). "Effect of Lode parameter on plastic flow localization after proportional loading at low stress triaxialities". *Journal of the Mechanics and Physics of Solids* 66, pp. 133–153.
- Eisenlohr, P., Diehl, M., Lebensohn, R. A., and Roters, F. (2013). "A spectral method solution to crystal elasto-viscoplasticity at finite strains". *International Journal of Plasticity* 46, pp. 37–53.
- Engler, O. and Randle, V. (2009). *Introduction to texture analysis: macrotecture, microtexture, and orientation mapping*. Second edition. CRC press, Taylor & Francis Group.
- Evancho, J. W. and Staley, J. T. (1974). "Kinetics of precipitation in aluminum alloys during continuous cooling". *Metallurgical Transactions* 5, p. 43.
- Ewing, J. A. and Rosenhain, W. (1900). "The crystalline structure of metals". *Proceedings of the Royal Society of London* 67, pp. 112–117.
- Falahati, A., Lang, P., and Kozeschnik, E. (2012). "Precipitation in Al-Alloy 6016 – The Role of Excess Vacancies". *Materials Science Forum* 706. Trans Tech Publications, pp. 317–322.
- Fleck, N. A., Hutchinson, J. W., and Tvergaard, V. (1989). "Softening by void nucleation and growth in tension and shear". *Journal of the Mechanics and Physics of Solids* 37, pp. 515–540.
- Fourmeau, M., Børvik, T., Benallal, A., and Hopperstad, O. S. (2013). "Anisotropic failure modes of high-strength aluminium alloy under various stress states". *International Journal of Plasticity* 48, pp. 34–53.
- Frodal, B. H., Dæhli, L. E. B., Børvik, T., and Hopperstad, O. S. (2019). "Modelling and simulation of ductile failure in textured aluminium alloys subjected to compression-tension loading". *International Journal of Plasticity* 118, pp. 36–69.
- Gawad, J., Banabic, D., Bael, A. V., Comsa, D. S., Gologanu, M., Eyckens, P., Houtte, P. V., and Roose, D. (2015). "An evolving plane stress yield criterion based on crystal plasticity virtual experiments". *International Journal of Plasticity* 75, pp. 141–169.
- Gologanu, M., Leblond, J.-B., and Devaux, J. (1993). "Approximate models for ductile metals containing non-spherical voids—Case of axisymmetric prolate ellipsoidal cavities". *Journal of the Mechanics and Physics of Solids* 41, pp. 1723–1754.
- Gologanu, M., Leblond, J.-B., and Devaux, J. (1994). "Approximate models for ductile metals containing nonspherical voids—Case of axisymmetric oblate ellipsoidal cavities". *Journal of Engineering Materials and Technology* 116, pp. 290–297.

- Granum, H., Myhr, O. R., Børvik, T., and Hopperstad, O. S. (2018). “Nanostructure-based finite element analyses of aluminium profiles subjected to quasi-static axial crushing”. *Thin-Walled Structures* 131, pp. 769–781.
- Gruben, G., Hopperstad, O. S., and Børvik, T. (2012). “Evaluation of uncoupled ductile fracture criteria for the dual-phase steel Docol 600DL”. *International Journal of Mechanical Sciences* 62, pp. 133–146.
- Gruben, G., Morin, D., Langseth, M., and Hopperstad, O. S. (2017). “Strain localization and ductile fracture in advanced high-strength steel sheets”. *European Journal of Mechanics - A/Solids* 61, pp. 315–329.
- Guo, T. F. and Wong, W. H. (2018). “Void-sheet analysis on macroscopic strain localization and void coalescence”. *Journal of the Mechanics and Physics of Solids* 118, pp. 172–203.
- Gurson, A. L. (1977). “Continuum theory of ductile rupture by void nucleation and growth: Part I—Yield criteria and flow rules for porous ductile media”. *Journal of Engineering Materials and Technology* 99, pp. 2–15.
- Han, X., Besson, J., Forest, S., Tanguy, B., and Bugat, S. (2013). “A yield function for single crystals containing voids”. *International Journal of Solids and Structures* 50, pp. 2115–2131.
- Hannard, F., Simar, A., Maire, E., and Pardoën, T. (2018). “Quantitative assessment of the impact of second phase particle arrangement on damage and fracture anisotropy”. *Acta Materialia* 148, pp. 456–466.
- Hershey, A. V. (1954). “The plasticity of an isotropic aggregate of anisotropic face-centered cubic crystals”. *Journal of Applied Mechanics* 21, pp. 241–249.
- Hill, R. (1948). “A theory of the yielding and plastic flow of anisotropic metals”. *Proceedings of the Royal Society of London A: Mathematical, Physical and Engineering Sciences* 193, pp. 281–297.
- Hill, R. (1966). “Generalized constitutive relations for incremental deformation of metal crystals by multislip”. *Journal of the Mechanics and Physics of Solids* 14, pp. 95–102.
- Hill, R. and Havner, K. S. (1982). “Perspectives in the mechanics of elastoplastic crystals”. *Journal of the Mechanics and Physics of Solids* 30, pp. 5–22.
- Hill, R. and Rice, J. R. (1972). “Constitutive analysis of elastic-plastic crystals at arbitrary strain”. *Journal of the Mechanics and Physics of Solids* 20, pp. 401–413.
- Hoang, N.-H., Hopperstad, O. S., Myhr, O. R., Marioara, C., and Langseth, M. (2015). “An improved nano-scale material model applied in axial-crushing analyses of square hollow section aluminium profiles”. *Thin-Walled Structures* 92, pp. 93–103.
- Holmen, J. K., Børvik, T., Myhr, O. R., Fjær, H. G., and Hopperstad, O. S. (2015). “Perforation of welded aluminum components: Microstructure-based modeling and experimental validation”. *International Journal of Impact Engineering* 84, pp. 96–107.
- Hosford, W. F. (1972). “A generalized isotropic yield criterion”. *Journal of Applied Mechanics* 39, pp. 607–609.
- Hosford, W. F. (1996). “On the crystallographic basis of yield criteria”. *Textures and Microstructures* 26, pp. 479–493.
- Hutchinson, J. W. (1976). “Bounds and self-consistent estimates for creep of polycrystalline materials”. *Proceedings of the Royal Society of London A: Mathematical, Physical and Engineering Sciences* 348, pp. 101–127.



- Iadicola, M. A., Foecke, T., and Banovic, S. W. (2008). “Experimental observations of evolving yield loci in biaxially strained AA5754-O”. *International Journal of Plasticity* 24, pp. 2084–2101.
- Johnsen, J., Holmen, J. K., Myhr, O. R., Hopperstad, O. S., and Børvik, T. (2013). “A nano-scale material model applied in finite element analysis of aluminium plates under impact loading”. *Computational Materials Science* 79, pp. 724–735.
- Johnson, G. R. and Cook, W. H. (1985). “Fracture characteristics of three metals subjected to various strains, strain rates, temperatures and pressures”. *Engineering Fracture Mechanics* 21, pp. 31–48.
- Kanjarla, A. K., Van Houtte, P., and Delannay, L. (2010). “Assessment of plastic heterogeneity in grain interaction models using crystal plasticity finite element method”. *International Journal of Plasticity* 26, pp. 1220–1233.
- Karafillis, A. P. and Boyce, M. C. (1993). “A general anisotropic yield criterion using bounds and a transformation weighting tensor”. *Journal of the Mechanics and Physics of Solids* 41, pp. 1859–1886.
- Keralavarma, S. M. and Benzerga, A. A. (2010). “A constitutive model for plastically anisotropic solids with non-spherical voids”. *Journal of the Mechanics and Physics of Solids* 58, pp. 874–901.
- Keralavarma, S. M., Hoelscher, S., and Benzerga, A. A. (2011). “Void growth and coalescence in anisotropic plastic solids”. *International Journal of Solids and Structures* 48, pp. 1696–1710.
- Khadyko, M., Myhr, O. R., Dumoulin, S., and Hopperstad, O. S. (2016a). “A microstructure-based yield stress and work-hardening model for textured 6xxx aluminium alloys”. *Philosophical Magazine* 96, pp. 1047–1072.
- Khadyko, M., Marioara, C. D., Ringdalen, I. G., Dumoulin, S., and Hopperstad, O. S. (2016b). “Deformation and strain localization in polycrystals with plastically heterogeneous grains”. *International Journal of Plasticity* 86, pp. 128–150.
- Khadyko, M., Marioara, C. D., Dumoulin, S., Børvik, T., and Hopperstad, O. S. (2017). “Effects of heat-treatment on the plastic anisotropy of extruded aluminium alloy AA6063”. *Materials Science and Engineering: A* 708, pp. 208–221.
- Khadyko, M., Morin, D., Børvik, T., and Hopperstad, O. S. (2019). “Tensile ductility of extruded aluminium alloy AA6063 in different tempers”. *Materials Science and Engineering: A* 744, pp. 500–511.
- Khan, A. S. and Huang, S. (1995). *Continuum theory of plasticity*. John Wiley & Sons.
- Kim, J., Gao, X., and Srivatsan, T. S. (2004). “Modeling of void growth in ductile solids: effects of stress triaxiality and initial porosity”. *Engineering Fracture Mechanics* 71, pp. 379–400.
- Kocks, U. F. and Chandra, H. (1982). “Slip geometry in partially constrained deformation”. *Acta Metallurgica* 30, pp. 695–709.
- Kohar, C. P., Bassani, J. L., Brahme, A., Muhammad, W., Mishra, R. K., and Inal, K. (2019). “A new multi-scale framework to incorporate microstructure evolution in phenomenological plasticity: Theory, explicit finite element formulation, implementation and validation”. *International Journal of Plasticity* 117, pp. 122–156.
- Koplik, J. and Needleman, A. (1988). “Void growth and coalescence in porous plastic solids”. *International Journal of Solids and Structures* 24, pp. 835–853.

- Kristoffersen, M., Børvik, T., and Hopperstad, O. S. (2016). "Using unit cell simulations to investigate fracture due to compression–tension loading". *Engineering Fracture Mechanics* 162, pp. 269–289.
- Kuna, M. and Sun, D. Z. (1996). "Three-dimensional cell model analyses of void growth in ductile materials". *International Journal of Fracture* 81, pp. 235–258.
- Lebensohn, R. A. and Tomé, C. N. (1993). "A self-consistent anisotropic approach for the simulation of plastic deformation and texture development of polycrystals: Application to zirconium alloys". *Acta Metallurgica et Materialia* 41, pp. 2611–2624.
- Lebensohn, R. A. and Tomé, C. N. (1994). "A self-consistent viscoplastic model: prediction of rolling textures of anisotropic polycrystals". *Materials Science and Engineering: A* 175, pp. 71–82.
- Lebensohn, R. A., Kanjarla, A. K., and Eisenlohr, P. (2012). "An elasto-viscoplastic formulation based on fast Fourier transforms for the prediction of micromechanical fields in polycrystalline materials". *International Journal of Plasticity* 32-33, pp. 59–69.
- Legarth, B. N. and Tvergaard, V. (2018). "Effects of Plastic Anisotropy and Void Shape on Full Three-Dimensional Void Growth". *Journal of Applied Mechanics* 85, p. 051007.
- Lian, J. and Chen, J. (1991). "Isotropic polycrystal yield surfaces of B.C.C. and F.C.C. metals: crystallographic and continuum mechanics approaches". *Acta Metallurgica et Materialia* 39, pp. 2285–2294.
- Ling, C., Besson, J., Forest, S., Tanguy, B., Latourte, F., and Bosso, E. (2016). "An elastoviscoplastic model for porous single crystals at finite strains and its assessment based on unit cell simulations". *International Journal of Plasticity* 84, pp. 58–87.
- Lou, Y. and Yoon, J. W. (2018). "Anisotropic yield function based on stress invariants for BCC and FCC metals and its extension to ductile fracture criterion". *International Journal of Plasticity* 101, pp. 125–155.
- Madou, K. and Leblond, J.-B. (2012). "A Gurson-type criterion for porous ductile solids containing arbitrary ellipsoidal voids—I: Limit-analysis of some representative cell". *Journal of the Mechanics and Physics of Solids* 60, pp. 1020–1036.
- Maire, E., Zhou, S., Adrien, J., and Dimichiel, M. (2011). "Damage quantification in aluminium alloys using in situ tensile tests in X-ray tomography". *Engineering Fracture Mechanics* 78, pp. 2679–2690.
- Marciniak, Z. and Kuczyński, K. (1967). "Limit strains in the processes of stretch-forming sheet metal". *International Journal of Mechanical Sciences* 9, pp. 609–620.
- McClintock, F. A. (1968). "A criterion for ductile fracture by the growth of holes". *Journal of applied mechanics* 35, pp. 363–371.
- Mear, M. E. and Hutchinson, J. W. (1985). "Influence of yield surface curvature on flow localization in dilatant plasticity". *Mechanics of Materials* 4, pp. 395–407.
- Milkereit, B., Schick, C., and Kessler, O. (2010). "Continuous cooling precipitation diagrams depending on the composition of aluminum-magnesium-silicon alloys". *Proceedings of the 12th International Conference on Aluminium Alloys, Yokohama, Japan*, pp. 407–412.
- Mohr, D. and Marcadet, S. J. (2015). "Micromechanically-motivated phenomenological Hosford–Coulomb model for predicting ductile fracture initiation at low stress triaxialities". *International Journal of Solids and Structures* 67-68, pp. 40–55.

- Molinari, A., Canova, G. R., and Ahzi, S. (1987). "A self consistent approach of the large deformation polycrystal viscoplasticity". *Acta Metallurgica* 35, pp. 2983–2994.
- Monchiet, V. and Bonnet, G. (2013). "A Gurson-type model accounting for void size effects". *International Journal of Solids and Structures* 50, pp. 320–327.
- Monchiet, V., Cazacu, O., Charkaluk, E., and Kondo, D. (2008). "Macroscopic yield criteria for plastic anisotropic materials containing spheroidal voids". *International Journal of Plasticity* 24, pp. 1158–1189.
- Morgeneyer, T. F., Starink, M. J., Wang, S. C., and Sinclair, I. (2008). "Quench sensitivity of toughness in an Al alloy: Direct observation and analysis of failure initiation at the precipitate-free zone". *Acta Materialia* 56, pp. 2872–2884.
- Morin, D., Fourmeau, M., Børvik, T., Benallal, A., and Hopperstad, O. S. (2018b). "Anisotropic tensile failure of metals by the strain localization theory: An application to a high-strength aluminium alloy". *European Journal of Mechanics - A/Solids* 69, pp. 99–112.
- Morin, D., Hopperstad, O. S., and Benallal, A. (2018a). "On the description of ductile fracture in metals by the strain localization theory". *International Journal of Fracture* 209, pp. 27–51.
- Morin, D., Dæhli, L. E. B., Børvik, T., Benallal, A., and Hopperstad, O. S. (2019). "Numerical study of ductile failure under non-proportional loading". *European Journal of Mechanics - A/Solids* 74, pp. 221–241.
- Morin, L., Leblond, J.-B., and Kondo, D. (2015). "A Gurson-type criterion for plastically anisotropic solids containing arbitrary ellipsoidal voids". *International Journal of Solids and Structures* 77, pp. 86–101.
- Myhr, O. R., Grong, Ø., and Pedersen, K. O. (2010). "A Combined Precipitation, Yield Strength, and Work Hardening Model for Al-Mg-Si Alloys". *Metallurgical and Materials Transactions A* 41, pp. 2276–2289.
- Nahshon, K. and Hutchinson, J. W. (2008). "Modification of the Gurson Model for shear failure". *European Journal of Mechanics - A/Solids* 27, pp. 1–17.
- Needleman, A. (1972). "Void growth in an elastic-plastic medium". *Journal of Applied Mechanics* 39, pp. 964–970.
- Needleman, A. (1987). "A continuum model for void nucleation by inclusion debonding". *Journal of applied mechanics* 54, pp. 525–531.
- Paux, J., Morin, L., Brenner, R., and Kondo, D. (2015). "An approximate yield criterion for porous single crystals". *European Journal of Mechanics - A/Solids* 51, pp. 1–10.
- Pineau, A., Benzerga, A. A., and Pardoën, T. (2016). "Failure of metals I: Brittle and ductile fracture". *Acta Materialia* 107, pp. 424–483.
- Plateau, J., Henry, G., and Crussard, C. (1957). "Quelques nouvelles applications de la microfractographie". *Revue de metallurgie* 54, pp. 200–216.
- Polmear, I. (2006). *Light Alloys: From Traditional Alloys to Nanocrystals*. Fourth edition. Elsevier.
- Potirniche, G. P., Hearndon, J. L., Horstemeyer, M. F., and Ling, X. W. (2006). "Lattice orientation effects on void growth and coalescence in fcc single crystals". *International Journal of Plasticity* 22, pp. 921–942.
- Raabe, D. and Roters, F. (2004). "Using texture components in crystal plasticity finite element simulations". *International Journal of Plasticity* 20, pp. 339–361.



- Remøe, M. S., Marthinsen, K., Westermann, I., Pedersen, K., Røyset, J., and Marioara, C. (2017). “The effect of alloying elements on the ductility of Al-Mg-Si alloys”. *Materials Science and Engineering: A* 693, pp. 60–72.
- Rice, J. R. (1976). “Localization of plastic deformation”. In: *14th International Congress of Theoretical and Applied Mechanics*, pp. 207–220.
- Rice, J. R. and Tracey, D. M. (1969). “On the ductile enlargement of voids in triaxial stress fields”. *Journal of the Mechanics and Physics of Solids* 17, pp. 201–217.
- Roters, F., Eisenlohr, P., Hantcherli, L., Tjahjanto, D. D., Bieler, T. R., and Raabe, D. (2010). “Overview of constitutive laws, kinematics, homogenization and multiscale methods in crystal plasticity finite-element modeling: Theory, experiments, applications”. *Acta Materialia* 58, pp. 1152–1211.
- Rudnicki, J. W. and Rice, J. R. (1975). “Conditions for the localization of deformation in pressure-sensitive dilatant materials”. *Journal of the Mechanics and Physics of Solids* 23, pp. 371–394.
- Saai, A., Dumoulin, S., Hopperstad, O. S., and Lademo, O.-G. (2013). “Simulation of yield surfaces for aluminium sheets with rolling and recrystallization textures”. *Computational Materials Science* 67, pp. 424–433.
- Sachs, G. (1928). “Zur ableitung einer fleissbedingung”. *Z VDI* 72, p. 734.
- Schmid, E. (1924). “Neuere untersuchungen an metallkristallen”. *Proceedings of the International Congress on Applied Mechanics*, pp. 342–353.
- Seyedrezai, H., Grebennikov, D., Mascher, P., and Zurob, H. S. (2009). “Study of the early stages of clustering in Al-Mg-Si alloys using the electrical resistivity measurements”. *Materials Science and Engineering: A* 525, pp. 186–191.
- Spitzig, W. A. and Richmond, O. (1984). “The effect of pressure on the flow stress of metals”. *Acta Metallurgica* 32, pp. 457–463.
- Srivastava, A. and Srivastava, A. (2013). “Void growth versus void collapse in a creeping single crystal”. *Journal of the Mechanics and Physics of Solids* 61, pp. 1169–1184.
- Steglich, D., Wafai, H., and Besson, J. (2010). “Interaction between anisotropic plastic deformation and damage evolution in Al 2198 sheet metal”. *Engineering Fracture Mechanics* 77, pp. 3501–3518.
- Stout, M. G., Hecker, S. S., and Bourcier, R. (1983). “An evaluation of anisotropic effective stress-strain criteria for the biaxial yield and flow of 2024 aluminum tubes”. *Journal of Engineering Materials and Technology* 105, pp. 242–249.
- Strobel, K., Easton, M. A., Sweet, L., Couper, M. J., and Nie, J.-F. (2011). “Relating Quench Sensitivity to Microstructure in 6000 Series Aluminium Alloys”. *Materials Transactions* 52, pp. 914–919.
- Strobel, K., Lay, M. D. H., Easton, M. A., Sweet, L., Zhu, S., Parson, N. C., and Hill, A. J. (2016). “Effects of quench rate and natural ageing on the age hardening behaviour of aluminium alloy AA6060”. *Materials Characterization* 111, pp. 43–52.
- Strobel, K., Easton, M. A., Lay, M. D. H., Rometsch, P. A., Zhu, S., Sweet, L., Parson, N. C., and Hill, A. J. (2019). “Quench Sensitivity in a Dispersoid-Containing Al-Mg-Si Alloy”. *Metallurgical and Materials Transactions A* 50, pp. 1957–1969.

- Taylor, G. I. (1934a). "The mechanism of plastic deformation of crystals. Part I.—Theoretical". *Proceedings of the Royal Society of London* 145, pp. 362–387.
- Taylor, G. I. (1934b). "The mechanism of plastic deformation of crystals. Part II.—Comparison with observations". *Proceedings of the Royal Society of London* 145, pp. 388–404.
- Taylor, G. I. (1938). "Plastic strain in metals". *J. Inst. Metals* 62, pp. 307–324.
- Taylor, G. I. and Elam, C. F. (1923). "The distortion of an aluminium crystal during a tensile test". *Proceedings of the Royal Society of London* 102, pp. 643–667.
- Taylor, G. I. and Elam, C. F. (1925). "The plastic extension and fracture of aluminium crystals". *Proceedings of the Royal Society of London* 108, pp. 28–51.
- Tekoğlu, C., Hutchinson, J. W., and Pardoën, T. (2015). "On localization and void coalescence as a precursor to ductile fracture". *Philosophical Transactions of the Royal Society A: Mathematical, Physical and Engineering Sciences* 373, p. 20140121.
- Thomson, R. D. and Hancock, J. W. (1984). "Local stress and strain fields near a spherical elastic inclusion in a plastically deforming matrix". *International Journal of Fracture* 24, pp. 209–228.
- Tipper, C. F. (1949). "The fracture of metals". *Metallurgia* 39, pp. 133–137.
- Toda, H., Oogo, H., Horikawa, K., Uesugi, K., Takeuchi, A., Suzuki, Y., Nakazawa, M., Aoki, Y., and Kobayashi, M. (2013). "The True Origin of Ductile Fracture in Aluminum Alloys". *Metallurgical and Materials Transactions A* 45, pp. 765–776.
- Tvergaard, V. and Needleman, A. (1984). "Analysis of the cup-cone fracture in a round tensile bar". *Acta Metallurgica* 32, pp. 157–169.
- Tvergaard, V. (1981). "Influence of voids on shear band instabilities under plane strain conditions". *International Journal of Fracture* 17, pp. 389–407.
- Tvergaard, V. (1982a). "Ductile fracture by cavity nucleation between larger voids". *Journal of the Mechanics and Physics of Solids* 30, pp. 265–286.
- Tvergaard, V. (1982b). "On localization in ductile materials containing spherical voids". *International Journal of Fracture* 18, pp. 237–252.
- Tvergaard, V. (1996). "Effect of void size difference on growth and cavitation instabilities". *Journal of the Mechanics and Physics of Solids* 44, pp. 1237–1253.
- Unwin, P. N. T., Lorimer, G. W., and Nicholson, R. B. (1969). "The origin of the grain boundary precipitate free zone". *Acta Metallurgica* 17, pp. 1363–1377.
- Van Houtte, P. (1982). "On the equivalence of the relaxed Taylor theory and the Bishop-Hill theory for partially constrained plastic deformation of crystals". *Materials Science and Engineering* 55, pp. 69–77.
- Van Houtte, P. (1988). "A comprehensive mathematical formulation of an extended Taylor-Bishop-Hill model featuring relaxed constraints, the Renouard-Wintenberger theory and a strain rate sensitivity model". *Texture, Stress, and Microstructure* 8, pp. 313–350.
- Van Houtte, P., Delannay, L., and Kalidindi, S. R. (2002). "Comparison of two grain interaction models for polycrystal plasticity and deformation texture prediction". *International Journal of Plasticity* 18, pp. 359–377.
- Wen, J., Huang, Y., Hwang, K. C., Liu, C., and Li, M. (2005). "The modified Gurson model accounting for the void size effect". *International Journal of Plasticity* 21, pp. 381–395.
- Wong, W. H. and Guo, T. F. (2015). "On the energetics of tensile and shear void coalescences". *Journal of the Mechanics and Physics of Solids* 82, pp. 259–286.

- Woodthorpe, J. and Pearce, R. (1970). "The anomalous behaviour of aluminium sheet under balanced biaxial tension". *International Journal of Mechanical Sciences* 12, pp. 341–347.
- Yerra, S. K., Tekoglu, C., Scheyvaerts, F., Delannay, L., Van Houtte, P., and Pardoën, T. (2010). "Void growth and coalescence in single crystals". *International Journal of Solids and Structures* 47, pp. 1016–1029.
- Yoshida, F., Hamasaki, H., and Uemori, T. (2013). "A user-friendly 3D yield function to describe anisotropy of steel sheets". *International Journal of Plasticity* 45, pp. 119–139.
- Zhang, H., Diehl, M., Roters, F., and Raabe, D. (2016). "A virtual laboratory using high resolution crystal plasticity simulations to determine the initial yield surface for sheet metal forming operations". *International Journal of Plasticity* 80, pp. 111–138.
- Zhang, K., Holmedal, B., Hopperstad, O. S., Dumoulin, S., Gawad, J., Van Bael, A., and Van Houtte, P. (2015). "Multi-level modelling of mechanical anisotropy of commercial pure aluminium plate: Crystal plasticity models, advanced yield functions and parameter identification". *International Journal of Plasticity* 66, pp. 3–30.
- Zhang, K. S., Bai, J. B., and François, D. (2001). "Numerical analysis of the influence of the Lode parameter on void growth". *International Journal of Solids and Structures* 38, pp. 5847–5856.
- Zhang, Z. L. and Skallerud, B. (2010). "Void Coalescence With and Without Prestrain History". *International Journal of Damage Mechanics* 19, pp. 153–174.

# PART 1

Bjørn Håkon Frodal, Ketill Olav Pedersen, Tore Børvik,  
Odd Sture Hopperstad

## **Influence of pre-compression on the ductility of AA6xxx aluminium alloys**

International Journal of Fracture 206 (2017) 131-149.  
<https://doi.org/10.1007/s10704-017-0204-4>



Is not included due to copyright  
available in  
International Journal of Fracture 206 (2017) 131-149  
<https://doi.org/10.1007/s10704-017-0204-4>



## PART 2

Bjørn Håkon Frodal, Lars Edvard Blystad Dæhli, Tore Børvik,  
Odd Sture Hopperstad

**Modelling and simulation of ductile failure in  
textured aluminium alloys subjected to  
compression-tension loading**

International Journal of Plasticity 118 (2019) 36-69.  
<https://doi.org/10.1016/j.ijplas.2019.01.008>





Contents lists available at ScienceDirect

## International Journal of Plasticity

journal homepage: [www.elsevier.com/locate/ijplas](http://www.elsevier.com/locate/ijplas)

## Modelling and simulation of ductile failure in textured aluminium alloys subjected to compression-tension loading



Bjørn Håkon Frodal<sup>a,b,\*</sup>, Lars Edvard Blystad Dæhli<sup>a</sup>, Tore Børvik<sup>a,b</sup>,  
Odd Sture Hopperstad<sup>a,b</sup>

<sup>a</sup> Structural Impact Laboratory (SIMLab), Department of Structural Engineering, Norwegian University of Science and Technology (NTNU), NO-7491, Trondheim, Norway

<sup>b</sup> Centre for Advanced Structural Analysis (CASA), NTNU, NO-7491, Trondheim, Norway

## ARTICLE INFO

**Keywords:**

Ductility  
Fracture  
Crystal plasticity  
Finite elements  
Unit cell modelling

## ABSTRACT

The effects of strain path change on the ductile failure process of textured aluminium alloys are investigated through reversed loading experiments and finite element-based unit cell simulations. Three extruded aluminium alloys (AA6060, AA6082.25 and AA6082.50) are solution heat-treated and artificially aged to three different conditions, namely temper O (annealed), temper T7 (overaged) and temper T6 (peak strength). Compression-tension experiments on diabol-shaped specimens are conducted including five different pre-compression levels (0, 10, 20, 30, 40%), i.e., the specimens are first compressed to a prescribed strain and then reloaded to fracture in tension. The materials are modelled with an advanced plasticity model accounting for plastic anisotropy, non-associated plastic flow, nonlinear isotropic and kinematic hardening, strength differential effect, and transient and permanent effects of strain path change. Crystal plasticity finite element analyses are performed to determine the plastic anisotropy of the materials and then used to calibrate the anisotropic yield surfaces, whereas the work-hardening response is calibrated from the experimental data. The effects of grain morphology and precipitate structure on the plastic anisotropy are neglected. Finite element simulations of all the reversed loading tests are performed and the non-proportional loading history from the centre of the specimen is extracted. These non-proportional loading histories are imposed to a unit cell model with a central spherical particle to study the effect of pre-compression on the ductile failure process, where the initial plastic anisotropy and the work-hardening behaviour after strain path change are accounted for. The strain to coalescence of the three-dimensional unit cell is mapped back to the reversed loading tests to determine the logarithmic strain to failure after the strain path change, and the numerical results are compared with the experimental data. The unit cell model predicts an approximately constant tensile ductility with pre-compression for the different materials. Variations are observed between the materials as the strength, work hardening and anisotropy are found to influence the response of the unit cell differently and affect the tensile ductility after the pre-deformation. In the experiments, the tensile ductility is largely constant or exhibits a small increase for the majority of the materials, but for some alloy-temper combinations a larger increase is observed, which is not captured in the unit cell computations.

\* Corresponding author. Structural Impact Laboratory (SIMLab), Department of Structural Engineering, Norwegian University of Science and Technology (NTNU), NO-7491, Trondheim, Norway.

E-mail address: [bjorn.h.frodal@ntnu.no](mailto:bjorn.h.frodal@ntnu.no) (B.H. Frodal).

<https://doi.org/10.1016/j.ijplas.2019.01.008>

Received 12 September 2018; Received in revised form 14 January 2019; Accepted 16 January 2019

Available online 31 January 2019

0749-6419/ © 2019 Elsevier Ltd. All rights reserved.

## 1. Introduction

The different microstructural characteristics of metals, such as grain structure and crystallographic texture, determine their plastic behaviour. Rolled plates and extruded profiles typically exhibit plastic anisotropy, which should be modelled by an anisotropic yield criterion. Numerous anisotropic yield criteria have been proposed in the literature. Hill (1948) proposed a quadratic yield function for orthotropic materials, which gives reasonable predictions for traditional steels. For aluminium alloys, the Hill yield criterion has been found to provide less accurate estimates of the yield surface (Woodthorpe and Pearce, 1970; Stout et al., 1983; Iadicola et al., 2008). Barlat et al. (1991) proposed a yield criterion for orthotropic materials, using linear transformation of the stress tensor. This criterion was based on the non-quadratic yield function of Hershey (1954) and Hosford (1972), which gives good prediction of the yield surface for isotropic materials. Karafillis and Boyce (1993) further generalised the theory of linear transformations to describe a more universal anisotropic yield function, as to also accommodate other material symmetries. Later, Bron and Besson (2004) introduced an additional linear transformation in the yield criterion of Karafillis and Boyce (1993) to increase the number of anisotropy coefficients and the degree of flexibility. Barlat et al. (2005) proposed a new criterion based on the non-quadratic yield criterion of Barlat et al. (1991) using two linear transformations, consisting of 16 independent anisotropy coefficients (Van Den Boogaard et al., 2016) for the most general formulation. More recently, anisotropic yield criteria including even more linear transformations have been introduced (Aretz et al., 2010; Aretz and Barlat, 2013). Yield criteria based on invariants of the stress tensor have also been extended to anisotropy by implementing linear transformations of the stress tensor (e.g., Cazacu and Barlat, 2001; Yoshida et al., 2013; Lou and Yoon, 2018).

The improved flexibility and accuracy of these yield functions come at the cost of more anisotropy coefficients that have to be determined. The calibration process then becomes challenging as more experimental tests are required. It is therefore desirable to determine the material behaviour of complex materials without performing extensive experimental testing, which is both expensive and time consuming. To reduce the number of experimental tests needed to calibrate the yield surface of a material, virtual material testing based on crystal plasticity theory can be utilised. This can be done in two ways. The first approach is to use virtual testing in combination with experiments to provide data for deformation modes that are difficult to obtain experimentally (Barlat et al., 2005; Grytten et al., 2008; Zhang et al., 2015). In the second approach, only virtual testing is used to determine the yield surface of a material (Saai et al., 2013; K. Zhang et al., 2015; H. Zhang et al., 2016). The accuracy of such methods relies on the capability of the crystal plasticity theory to incorporate the important microstructural effects and also the flexibility of the phenomenological yield function.

The full-constraint Taylor model (Taylor, 1938; Bishop and Hill, 1951a, b) is one of the most used representations to describe the response of polycrystals. This approach is based on the assumption that all grains in an aggregate experience the same deformation; thus, compatibility is fulfilled but stress equilibrium is violated. Owing to this violation, several relaxed-constraint Taylor models have been proposed in an attempt to develop a more realistic description of polycrystals, while keeping the simplicity of the full-constraint Taylor model (Kocks and Chandra, 1982; Van Houtte, 1982, 1988; Van Houtte et al., 2002). Another way of representing a polycrystalline aggregate is by so-called self-consistent models. In these models, each grain is represented by an ellipsoidal inclusion surrounded by a homogeneous equivalent medium. The most popular version of the self-consistent models seems to be the viscoplastic self-consistent (VPSC) model (Hutchinson, 1976; Molinari et al., 1987; Lebensohn and Tomé, 1993, 1994). Unlike the Taylor model, the self-consistent models satisfy both stress equilibrium and deformation compatibility. In contrast, the shape of grains, their local interaction and inhomogeneities of the mechanical fields within grains are not accounted for (Lebensohn et al., 2012; Zhang et al., 2016).

More recently, full-field micromechanical approaches such as the combination of crystal plasticity with the finite element method (CP-FEM) (Raabe and Roters, 2004; Kanjarla et al., 2010; Saai et al., 2013; Zhang et al., 2015) or a spectral method using fast Fourier transformation (FFT) (Lebensohn et al., 2012; Eisenlohr et al., 2013; Zhang et al., 2016) have become increasingly popular with the advances in computer technology. These methods typically require more computational resources than the various Taylor and self-consistent models, but are capable of accounting for stress equilibrium and compatibility across grain boundaries, local interaction and inhomogeneities of the mechanical fields within grains, and resolving the complex grain morphology of polycrystalline materials. The FFT is more computationally efficient in solving the mechanical problem, but is limited to periodic boundary conditions (Zhang et al., 2016). In contrast, CP-FEM requires more computational resources, but can be used to solve the mechanical response of a polycrystalline material with any geometry and boundary conditions. Currently, the CP-FEM framework is restricted to the mesoscopic scale as numerical simulations of structural components and full structures are too computationally demanding, and for such large-scale problems phenomenological plasticity models are still preferred.

By utilising hierarchical modelling schemes, it is possible to combine the accuracy of the polycrystal plasticity models with the computational efficiency of the phenomenological plasticity models. Barlat et al. (2005) combined experimental data and results obtained with the VPSC model to calibrate the Yld2004–18p yield surface for an aluminium sheet material. Grytten et al. (2008) determined the parameters of the same yield function using (i) only experimental data, (ii) only virtual data obtained with the full-constraint Taylor model, and (iii) a combination of these two methods. They found that the full-constraint Taylor model was not capable of reproducing the experimental results, and that the yield surface determined from experimental data only was favourable. Saai et al. (2013) compared the full-constraint Taylor model to CP-FEM simulations utilising the hierarchical modelling framework. They found that the yield surface calibrated solely from CP-FEM predicted the experimental data quite accurately, while the full-constraint Taylor model gave less accurate results. Zhang et al. (2015) compared five different homogenisation models, including full-constraint and relaxed-constraint Taylor models, the VPSC model and CP-FEM, and concluded that CP-FEM was one of the methods that gave the best agreement with the experimental data. These identification methods have also been used to calibrate different yield



functions, or used with different crystal plasticity models (Inal et al., 2010; An et al., 2011; Zhang et al., 2016).

One of the advantages of the crystal plasticity theory is its ability to predict the change of plastic anisotropy by evolving the crystallographic texture, and it can thus account for anisotropic hardening. Anisotropic hardening has also been introduced in phenomenological yield criteria. The first attempts to include this feature were made by introducing an interpolation method to determine the evolution of the yield surface with plastic deformation (Plunkett et al., 2007; Aretz, 2008). Gawad et al. (2015) presented a hierarchical multi-scale framework that accounts for evolution of the plastic anisotropy by systematically recalibrating the yield surface to data provided by the crystal plasticity virtual experiment framework. Kohar et al. (2017) accounted for microstructure evolution by introducing the plastic spin into the phenomenological plasticity framework, where the evolution of the plastic spin was calibrated based on crystal plasticity. Lee et al. (2017) proposed a model describing the evolution of the yield surface by coupling quadratic and non-quadratic yield functions with a non-associated flow rule.

After a strain path change, materials typically experience a transient response. The Bauschinger effect (Bauschinger, 1881) is often observed after reversed loading, where the re-yielding stress after the strain path change is lower than the flow stress prior to unloading, and the subsequent work-hardening rate is, in general, much higher than under monotonic loading. Another transient effect is work-hardening stagnation, which is observed after the first transient phase. The work-hardening rate temporarily decreases, making a plateau in the flow stress curve, before it increases again with straining. These transient effects will commonly vanish after a certain plastic strain, and the flow stress curve after the strain path change coalesces with the flow stress curve for monotonic loading (Ha et al., 2013). In contrast, some materials experience permanent softening after the strain path change. In this case, the flow stress curve after strain path change remains lower than the monotonic flow stress curve, although the work-hardening rate may reach the same level as under monotonic loading (Li and Bate, 1991; Mánik et al., 2015).

Two main approaches exist for including the effects of strain path change in phenomenological plasticity models. The first approach relies on combined isotropic and kinematic hardening, incorporating internal variables with a fading memory of the strain path. The yield surface of the material translates, expands and shrinks with plastic deformation, whereas its shape is invariant. This approach was first proposed by Teodosiu and Hu (1995), and their model applies second and fourth order tensors to describe the transient response. More recently, Mánik et al. (2015) proposed a model including only second order tensors to describe the behaviour after strain path change. This model, denoted the MHH model, is not only capable of describing the transients, but also the permanent softening unlike the model of Teodosiu and Hu (1995). In the second approach, the effects of strain path changes are accounted for by distortion of the yield surface. This yield surface distortion has been observed experimentally during both proportional and non-proportional loading paths (Khan et al., 2009, 2010a; 2010b; Pandey et al., 2013). François (2001) introduced a “distorted stress” tensor into the yield function to describe an egg-shaped distortion of the yield surface. Based on two-dimensional rheological ideas, Shutov et al. (2011), and Shutov and Ihlmann (2012) proposed models that account for yield surface distortion. Freund et al. (2012) introduced a model based on one-dimensional constitutive equations with only scalar variables to describe the distortion of the yield surface. A general model, called the Homogeneous Anisotropic Hardening (HAH) model, capable of distorting any homogeneous yield surface was proposed by Barlat et al. (2011). This model accounts for the Bauschinger effect without the use of kinematic hardening. Later, several extensions and enhancements have been made to this model to account for more complex effects of strain path changes (Barlat et al., 2013, 2014; Ha et al., 2013; Lee et al., 2015; Qin et al., 2017). An evaluation of the HAH and MHH models was recently performed by Qin et al. (2017). They observed that for one of the materials investigated, the MHH model gave better agreement with experimental data after a single strain path change for large pre-strains, while the HAH model gave better agreement after a double strain path change. Recently, Qin et al. (2018) proposed a distortional yield surface model that combines some of the features of the HAH model with the MHH model. Strain path change models have also been proposed and used within the crystal plasticity framework (e.g., Holmedal et al., 2008; Kitayama et al., 2013; Wen et al., 2015, 2016).

For certain metallic materials, a strength differential effect, i.e., a higher flow stress in compression than in tension, can be observed. Several studies have observed the strength differential effect in aluminium alloys (e.g., Spitzig and Richmond, 1984; Bai and Wierzbicki, 2008; Luo and Rousselier, 2014; Holmen et al., 2017). Spitzig and Richmond (1984) suggested that the strength differential effect and the pressure sensitivity they observed for aluminium were linked to the effect of hydrostatic pressure on dislocation motion. Bulatov et al. (1999) performed atomistic simulations of aluminium, and examined the lattice resistance to dislocation motion under pressure. The results support the conclusion by Spitzig and Richmond (1984) suggesting that pressure-dependent slip in aluminium is caused by the interaction of a transient activation dilatancy of the moving dislocations with pressure. Along with pressure sensitivity, Bai and Wierzbicki (2008) explicitly included the influence of the third deviatoric stress invariant in simulations of an AA2024-T351 aluminium alloy. More recently, Luo and Rousselier (2014) accounted for the strength differential effect of an extruded aluminium alloy by introducing initial backstresses on the slip system level utilising crystal plasticity. A strength differential effect was observed along the transverse direction of the extruded profile, whereas the tensile and compressive yield stresses were identical along the extrusion direction. Holmen et al. (2017) investigated four aluminium alloys in several different tempers exhibiting the strength differential effect. Based on the work by Spitzig and Richmond (1984), a pressure dependent non-associative Drucker and Prager (1952) plasticity model was calibrated, and good agreement was found between the numerical and experimental data. For more elaborate discussions regarding the strength differential effect in aluminium alloys the reader is referred to, e.g., Luo and Rousselier (2014) and Holmen et al. (2017).

Research on ductile fracture has mainly addressed proportional loading conditions, whereas ductile failure in real applications is typically preceded by a non-proportional loading path. Recently, the important influence of non-proportional loading has been investigated both experimentally (Bao and Treitler, 2004; Kristoffersen et al., 2013; Papasidero et al., 2015; Marcadet and Mohr, 2015; Basu and Benzerga, 2015; Frodal et al., 2017) and numerically using unit cells (Zhang and Skallerud, 2010; Benzerga et al., 2012; Kristoffersen et al., 2016; Dæhli et al., 2016a). During non-proportional loading, the transient and permanent effects of strain



path change are essential to the description and prediction of ductile failure. Effects such as work-hardening stagnation may lead to an earlier localisation of plastic deformation and can have a detrimental effect on ductility.

Reversed loading is an important type of non-proportional loading, and has been studied in more recent years in the context of ductile failure (Bao and Treitler, 2004; Kristoffersen et al., 2013; Papasidero et al., 2015; Marcadet and Mohr, 2015; Frodal et al., 2017). Kristoffersen et al. (2013) investigated the effect of pre-compression on the ductility of an X65 steel used in offshore pipelines. They used diabolo-shaped specimens and performed experimental tests with pre-compression of up to 100%. For a pre-compression of 10% the tensile ductility increased compared to monotonic tension, whereas for higher levels the ductility decreased with pre-compression. Marcadet and Mohr (2015) evaluated the response of a dual phase steel sheet, using reversed loading experiments and numerical simulations of the tests. In the finite element simulations, they included the effects of transients such as the Bauschinger effect and work-hardening stagnation, and observed that the local thickening of the sheet during compression delayed the formation of a neck and the consequent increase in stress triaxiality. The experiments performed on notched flat specimens using a floating anti-buckling device showed that the strain to failure increased with pre-compression. For an aluminium alloy, Bao and Treitler (2004) performed reversed loading experiments on diabolo-shaped specimens. They used three different specimen geometries to account for different triaxiality levels during the reversed loading tests, and found that the tensile ductility of the material decreased with pre-compression in all the tests. The reduced tensile ductility was attributed to particle fracture and an increased dislocation density after the pre-loading, which accelerated the nucleation, growth and coalescence of voids in the succeeding tension stage. Papasidero et al. (2015) performed experiments on tubular specimens involving torsion, compression and tension tests in different combinations to study the effect of stress state and loading path on the onset of ductile fracture in aluminium. The experiments with non-proportional loading paths showed a pronounced effect of the loading path on the strain to failure. Frodal et al. (2017) investigated the influence of pre-compression on three extruded aluminium alloys with different microstructure and strength. Reversed loading experiments conducted on diabolo-shaped specimens showed that pre-compression had a marked influence on the ductility of the alloys, and the effect was significantly different between them.

Unit cell modelling is an important tool for studying ductile failure, either by proportional or non-proportional loading. Zhang and Skallerud (2010) investigated the effects of pre-strain on void coalescence using axisymmetric unit cell analyses. They imposed non-proportional loading histories on the unit cell consisting of a pre-strain stage in uniaxial tension, before a tensile stage with an elevated stress triaxiality ratio was applied and compared with results for proportional loading paths. Benzerga et al. (2012) performed analyses of an axisymmetric unit cell subjected to different proportional and non-proportional loading paths. Dæhli et al. (2016a) extracted the non-proportional loading paths from smooth axisymmetric tensile tests and applied them in analyses using an axisymmetric unit cell. These simulations were compared with analyses using proportional loading paths, given by the strain-average triaxiality to material failure. Results from these studies clearly demonstrate the importance of non-proportional loading in the context of ductile failure predictions. Kristoffersen et al. (2016) used axisymmetric unit cell analyses of reversed loading tests with diabolo-shaped specimens. A non-proportional loading path was created by two proportional loading steps, one in compression and one in the subsequent tension stage.

The effect of plastic anisotropy on ductile failure has also been studied with unit cell calculations. Benzerga and Besson (2001) were the first to account for anisotropy in terms of a Hill (1948) matrix formulation under proportional loading. Chien et al. (2001) and Wang et al. (2004) carried out three-dimensional (3D) unit cell simulations with the same anisotropic yield criterion. Steglich et al. (2010) assessed the ductile failure properties of an aluminium alloy using 3D unit cell calculations, where the yield criterion of Bron and Besson (2004) was employed. The individual and coupled effects of void shape and material anisotropy were studied by Keralavarma and Benzerga (2010) and Keralavarma et al. (2011) using axisymmetric unit cells. Recently, Dæhli et al. (2017) performed 3D unit cell analyses for a wide range of stress states applying the yield criterion of Barlat et al. (2005) for the matrix material. The full-constraint Taylor method was used to determine the yield surfaces representing typical crystallographic textures for face centred cubic (FCC) metals. Legarth and Tvergaard (2018) studied the interaction between plastic anisotropy, initial void shape and void spacing and their effect on void growth applying 3D unit cell simulations.

The aim of the present paper is to study the ductile failure process of textured aluminium alloys during reversed loading by experimental tests and three-dimensional unit cell simulations. First, an experimental programme is presented involving reversed loading tests of diabolo-shaped specimens on three aluminium alloys (AA6060, AA6082.25 and AA6082.50) solution heat-treated and artificially aged to three conditions, namely temper O (annealed), temper T7 (overaged) and temper T6 (peak strength). Second, finite element simulations of all the tests are conducted, using an advanced plasticity model to describe the material behaviour as outlined below. Third, unit cell simulations are carried out to study the ductile failure mechanisms numerically, where the non-proportional loading history is obtained from the finite element simulations of the tests. The results from the unit cell simulations are further mapped back to the reversed loading tests of the diabolo-shaped specimen, and compared to the experimental results. In order to incorporate the plastic anisotropy of the materials, the anisotropic yield criterion Yld2004–18p (Barlat et al., 2005) is applied in all simulations. CP-FEM calculations are used to determine the shape of the yield surface, incorporating the effect of the work-hardening behaviour of each material. The strength differential effect observed in the experimental tests is accounted for by using a pressure-dependent version of the Yld2004–18p yield criterion and a non-associated flow rule to retain isochoric plastic flow. The work hardening is described by combined isotropic and kinematic hardening, while additional internal variables are used to account for transient and permanent effects of strain path change (Mánik et al., 2015). A two-step process is adopted to calibrate the work-hardening rules based on experimental data from selected tests.

**Table 1**  
Chemical compositions of the aluminium alloys in wt%.

Alloy	Fe	Si	Mg	Mn	Cr	Cu	Zn	Ti	Al
AA6060	0.193	0.422	0.468	0.015	0.000	0.002	0.005	0.008	Bal.
AA6082.25	0.180	0.880	0.600	0.530	0.150	0.020	0.005	0.011	Bal.
AA6082.50	0.200	1.020	0.670	0.540	0.001	0.003	0.005	0.010	Bal.

## 2. Materials

In this paper, the three aluminium alloys AA6060, AA6082.25 and AA6082.50 are investigated. The chemical composition of the alloys is given in Table 1. These alloys were provided by Hydro Aluminium as extruded rectangular profiles with a thickness of 10 mm and a width of 83 mm. Prior to the solution heat-treatment, diabolo-shaped specimens were machined from the extruded profiles (Frodal et al., 2017). The specimens were then solution heat-treated and artificially aged to three different tempers, namely temper O (annealed), temper T7 (overaged) and temper T6 (peak strength).

The heat-treatment was performed in five stages. Stage 1–3 consisted of keeping the specimens in a salt bath at 540 °C for 15 min, water quenching, and storage in room temperature for 15 min. In stage 4, the specimens were kept in an oil bath at 185 °C for either five hours to achieve temper T6, or for one week to achieve temper T7. To attain temper O, the specimens were kept in a salt bath at 350 °C for 24 h. Stage 5 consisted of air-cooling to room temperature.

The three aluminium alloys have different grain structure and texture. The AA6060 alloy has a recrystallised grain structure comprising equi-axed grains, and exhibits a cube texture with a minor Goss component. A typical fibrous, non-recrystallised grain structure is observed for the AA6082.25 alloy, which has a cube texture with orientations along the  $\beta$ -fibre. The AA6082.50 alloy has recrystallised grain structure with large elongated grains and a rotated cube texture. For further details about the materials, the reader is referred to Khadyko et al. (2014) and Frodal et al. (2017).

## 3. Experiments

### 3.1. Experimental procedures

Reversed loading tests were performed to study the influence of pre-compression on the ductility of the three alloys in different tempers. Diabolo-shaped specimens were used in the tests, with a minimum diameter of 6.4 mm and a notch radius of 3.6 mm. The specimens were machined from the extruded profiles, oriented along the transverse direction (TD).

A displacement-controlled test machine with a constant cross-head velocity of 0.50 mm/min was used to perform the tests. Using an in-house measuring system, the minimum diameters along the extrusion direction (ED) and thickness direction (ND) of the specimens were continuously measured until fracture (Frodal et al., 2017).

The current area of the minimum cross-section can be estimated as an elliptical area by

$$A = \frac{\pi}{4} D_1 D_3 \quad (1)$$

where  $D_1$  and  $D_3$  are the measured diameters in ED and ND, respectively. The true stress over the minimum cross-section area is then

$$\sigma_t = \frac{F}{A} \quad (2)$$

where  $F$  is the measured force. Assuming plastic incompressibility and negligible elastic strains, the logarithmic strain is given by

$$\varepsilon_t = \ln\left(\frac{A_0}{A}\right) \quad (3)$$

where  $A_0$  is the initial cross-section area of the specimen. It is important to note that  $\sigma_t$  and  $\varepsilon_t$  represent average values over the minimum cross-section area of the specimen. Note also that close to failure this strain measure, based on the assumption of plastic incompressibility, becomes less accurate due to damage-induced increase of the porosity.

For each alloy and temper, the specimens were subjected to five different levels of pre-compression. The specimens were first compressed to a predefined strain level of either 0, 10, 20, 30 or 40% pre-compression, and then pulled to fracture in tension. Two or three tests were conducted for each pre-compression level. Fracture surfaces of the failed specimens were investigated in a Zeiss Gemini Supra 55VP FESEM operated at 20 kV.

Note that the test results for the three alloys in temper T6 have previously been presented in Frodal et al. (2017) and are included here for completeness. For further details about the experimental setup, the reader is referred to Frodal et al. (2017).

### 3.2. Experimental results

#### 3.2.1. Stress-strain curves

Fig. 1 presents the stress-strain curves from the reversed loading tests in terms of true stress and logarithmic strain. The point of

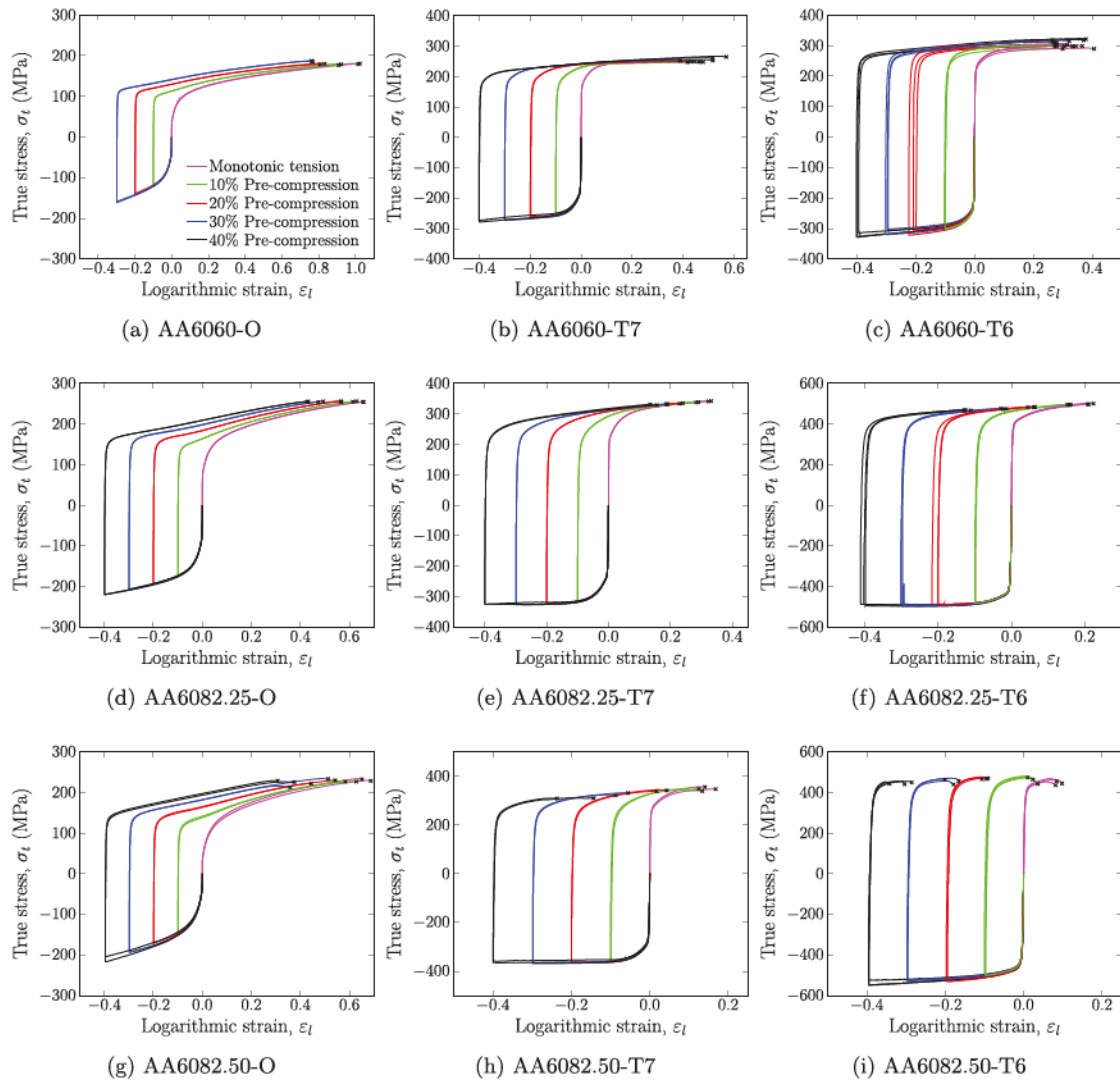


Fig. 1. Stress-strain curves for the three alloys in different tempers. The point of failure is indicated with a cross.

failure is indicated by a cross for each stress-strain curve. This is defined as either the point where a marked drop in the load level occurs, or where a distinct change in the slope of the stress-strain curve is observed. In the tests of the AA6060 alloy in temper O subjected to 40% pre-compression, failure occurred in the threaded section of the specimen due to severe work hardening in the notch during compression, and the results from these tests are omitted.

Table 2 presents the yield stress at 0.2% plastic strain in tension and compression, in addition to the re-yielding stress after load reversal. Note that the stress level is amplified by the triaxial stress field in the notched area of the specimen. For the three alloys in temper T7 and T6, the re-yielding stresses are lower than the initial yield stress, whereas for temper O the re-yielding stresses are higher than the initial yield stress. The re-yielding stress increases with increasing pre-compression for the AA6060 and AA6082.50 alloys in all tempers, as well as for the AA6082.25 alloy in temper O. In contrast, the AA6082.25 alloy in temper T7 and T6 has an almost constant re-yielding stress with increasing pre-compression.

For all the materials, a strength differential effect is observed, i.e., the initial yield stress and the flow stress at small plastic strains are markedly higher in compression than in tension, see Table 2. A more comprehensive investigation of the strength differential effect for the materials used in the present study can be found in Holmen et al. (2017).

After load reversal, the Bauschinger effect is observed, see Fig. 1, and is seen to be largest in the tests subjected to 10% pre-compression for all the materials. At larger pre-compression levels, the Bauschinger effect decreases with increasing pre-compression. The materials also exhibit permanent softening after load reversal, as the magnitude of the flow stress is substantially reduced.



Table 2

Yield stresses at 0.2% plastic strain,  $\sigma_{0.2}$ , and re-yielding stresses after pre-compression, with standard deviations.

Material	Tension (MPa)	Compression (MPa)	Re-yielding after 10% pre-compression (MPa)	Re-yielding after 20% pre-compression (MPa)	Re-yielding after 30% pre-compression (MPa)	Re-yielding after 40% pre-compression (MPa)
AA6060-O	42.5 ± 0.9	− 44.2 ± 1.4	82.5 ± 1.9	89.2 ± 0.4	94.0 ± 0.5	–
AA6060-T7	162.7 ± 1.3	− 169.8 ± 2.0	136.5 ± 0.2	144.9 ± 1.6	148.2 ± 1.8	148.3 ± 0.8
AA6060-T6	207.0 ± 4.7	− 221.4 ± 5.8	184.7 ± 5.6	187.6 ± 9.2	195.4 ± 5.5	201.8 ± 4.3
AA6082.25-O	81.0 ± 0.1	− 83.3 ± 0.7	107.3 ± 0.6	115.7 ± 0.8	117.5 ± 0.2	117.8 ± 0.8
AA6082.25-T7	216.0 ± 1.8	− 217.7 ± 2.4	163.3 ± 1.5	166.2 ± 0.7	167.0 ± 2.0	169.7 ± 1.0
AA6082.25-T6	362.7 ± 10.2	− 381.6 ± 7.0	272.9 ± 3.5	269.2 ± 6.4	269.6 ± 3.9	269.1 ± 6.1
AA6082.50-O	41.7 ± 1.4	− 46.9 ± 1.4	86.0 ± 1.4	94.6 ± 2.0	101.3 ± 0.6	111.2 ± 6.9
AA6082.50-T7	248.7 ± 2.2	− 262.3 ± 5.8	179.0 ± 0.5	183.2 ± 1.4	189.1 ± 4.0	189.2 ± 0.6
AA6082.50-T6	356.3 ± 13.5	− 391.6 ± 8.9	283.7 ± 1.2	305.1 ± 2.8	315.1 ± 5.7	315.8 ± 8.1

Permanent softening is discussed in further detail in Section 5.3. Work-hardening stagnation is observed after re-yielding for the three alloys in temper O. The effect is greatest for the tests subjected to 10% pre-compression, and then it decreases with increasing pre-compression and almost disappears after 40% pre-compression. The work-hardening stagnation can be explained by the pile-up of dislocations around obstacles during plastic deformation, which experience less resistance when travelling in the opposite direction after load reversal (Hasegawa et al., 1986). The reason why work-hardening stagnation is observed for the O temper and not for the others is probably the large non-shearable precipitates present in this temper.

The measured Lankford coefficients in tension, compression and in tension after load reversal are presented in Table 3. These coefficients give the ratio between the incremental strain in ED and ND, and thus the evolution of the cross-section of the specimen. The Lankford coefficients are different in tension and compression as well as between the different alloys and tempers. For the AA6060 and AA6082.50 alloys, the Lankford coefficients are greater in compression than in tension, while they are similar and closer to unity for the AA6082.25 alloy. Small variations are observed between different tempers. In tension after pre-compression, a small difference and evolution of the Lankford coefficients with pre-compression is observed. In general, the coefficients for the AA6060 and AA6082.25 alloys suggest that the materials become more anisotropic with increasing pre-compression, although this effect is modest, while for the AA6082.50 alloy the evolution of the Lankford coefficient is more irregular.

### 3.2.2. Effect of pre-compression on ductility

Fig. 2 presents the failure strain,  $\epsilon_f$ , and the relative failure strain,  $\epsilon_r$ , versus pre-compression level, where the relative failure strain is defined as  $\epsilon_r = \epsilon_f - \epsilon_0$  and  $\epsilon_0$  is the strain at load reversal. The failure strain  $\epsilon_f$  is seen to decrease with increasing pre-compression for most of the materials. For the AA6060 alloy in temper T7 and T6, the point of failure occurred within a narrow range of strain values for different levels of pre-compression, and the failure strain is approximately constant.

The tensile ductility is here defined as the deformation capability of the material subsequent to the pre-deformation, i.e., tensile ductility is defined in terms of the relative failure strain,  $\epsilon_r$ . Fig. 2 shows that the AA6060 alloy in temper T7 and T6 and the AA6082.25 alloy in temper T7 exhibit a marked increase in tensile ductility with increasing pre-compression level. The relative failure strain is almost doubled after 40% pre-compression compared to monotonic tension for these materials. The AA6082.25 in temper O is also seen to have a relatively large increase in tensile ductility with increasing pre-compression level. The remaining materials either display a small increase in the tensile ductility or a largely constant tensile ductility with increasing pre-compression level.

It is apparent that the magnitude of the failure strain varies between the materials, and that the strength of the material plays an important role. Fig. 3 shows the failure strain in monotonic tension versus the initial yield stress at 0.2% plastic strain, and it is evident that the failure strain decreases with increasing yield strength. In previous studies on various aluminium alloys, it has also been found that the failure strain tends to decrease linearly with increasing strength for similar microstructures (e.g., Lloyd, 2003; Westermann et al., 2014; Pedersen et al., 2015; Hannard et al., 2016).

Table 3

Measured Lankford coefficients in tension, compression and in tension after pre-compression, with standard deviations.

Material	Tension	Compression	In tension after 10% pre-compression	In tension after 20% pre-compression	In tension after 30% pre-compression	In tension after 40% pre-compression
AA6060-O	1.24 ± 0.01	1.40 ± 0.06	1.35 ± 0.03	1.48 ± 0.01	1.63 ± 0.03	–
AA6060-T7	1.24 ± 0.01	1.27 ± 0.09	1.32 ± 0.01	1.35 ± 0.01	1.43 ± 0.02	1.47 ± 0.01
AA6060-T6	1.27 ± 0.01	1.36 ± 0.10	1.35 ± 0.01	1.37 ± 0.04	1.43 ± 0.05	1.50 ± 0.13
AA6082.25-O	0.82 ± 0.01	0.85 ± 0.03	0.82 ± 0.00	0.80 ± 0.01	0.78 ± 0.01	0.74 ± 0.01
AA6082.25-T7	0.85 ± 0.01	0.83 ± 0.02	0.84 ± 0.01	0.84 ± 0.01	0.83 ± 0.01	0.81 ± 0.01
AA6082.25-T6	0.97 ± 0.01	0.95 ± 0.02	0.96 ± 0.01	0.94 ± 0.01	0.93 ± 0.00	0.91 ± 0.01
AA6082.50-O	0.45 ± 0.05	0.51 ± 0.07	0.41 ± 0.05	0.33 ± 0.04	0.36 ± 0.02	0.26 ± 0.03
AA6082.50-T7	0.41 ± 0.06	0.59 ± 0.09	0.37 ± 0.05	0.46 ± 0.03	0.39 ± 0.01	0.43 ± 0.01
AA6082.50-T6	0.36 ± 0.05	0.55 ± 0.05	0.45 ± 0.04	0.45 ± 0.05	0.38 ± 0.05	0.42 ± 0.08

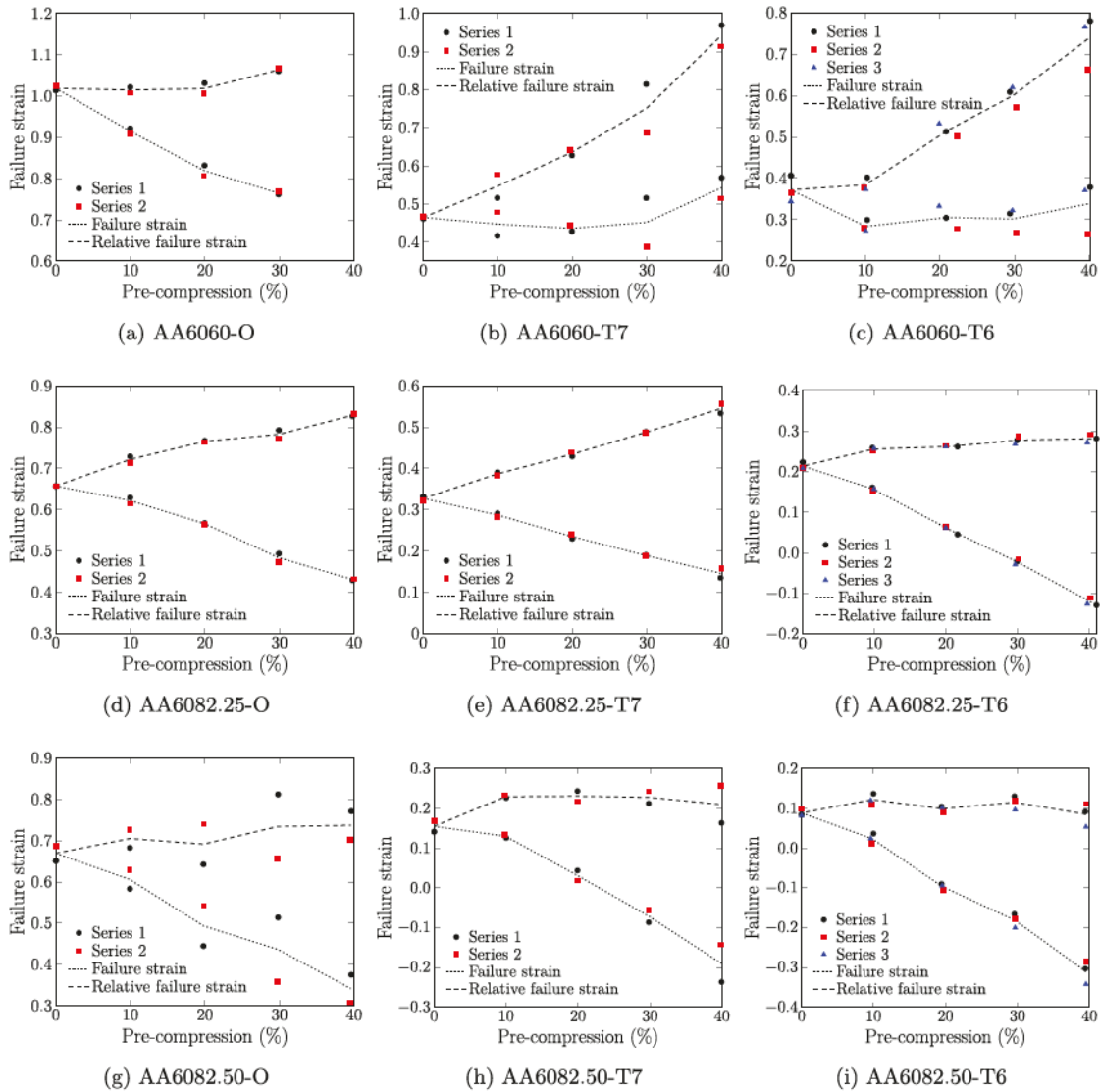


Fig. 2. Failure strain,  $\epsilon_f$ , and relative failure strain,  $\epsilon_r$ , versus pre-compression level for the three alloys in different tempers. The relative failure strain is the strain to failure measured with respect to the compressed configuration.

### 3.2.3. Fracture surfaces

Fig. 4 presents a selection of the most interesting fracture surfaces, namely the fracture surfaces of the AA6060 and AA6082.50 alloys in tempers O and T7 subjected to monotonic tension, whereas the fracture surfaces of the three alloys in temper T6 can be found in Frodal et al. (2017). In general, the fracture surfaces of specimens in tempers T7 and T6 for a given alloy are similar, while specimens in temper O exhibit a different fracture surface. For all tempers, the specimens of the AA6060 alloy display diamond-shaped cup-and-cone fracture surfaces. The diamond shape observed for tempers T7 and T6 is similar, but is sharper than for temper O. The specimens of the AA6082.25 alloy have typical circular cup-and-cone fracture surfaces similar for all tempers. The specimens of the AA6082.50 alloy in temper O exhibit an elliptical cup-and-cone fracture surface, while in tempers T7 and T6 a shear failure mode is found for this alloy. Note that the area calculation in Equation (1) is based on an elliptical shape of the minimum cross-section area, and thus errors will be introduced at large strains for the AA6060 alloy due to the diamond-shaped minimum cross-section area. A detailed discussion of this issue can be found in Frodal et al. (2017).

The general trend is that the same failure modes and fracture surface shapes are observed with increasing pre-compression as for monotonic tension. The fracture areas become larger with increasing pre-compression in agreement with a lower failure strain. The only exception is the AA6060 alloy in temper T7 and T6. As the pre-compression increases, the fracture surfaces for these materials



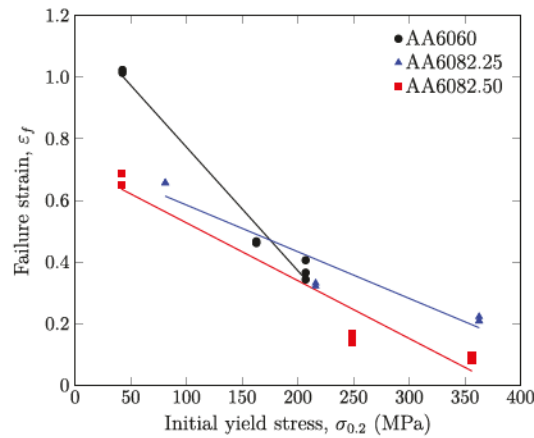


Fig. 3. Failure strain,  $\epsilon_f$ , versus initial yield stress,  $\sigma_{0.2}$ , for the three alloys in different tempers subjected to monotonic tension. Lines represent a linear least-square fit to the experimental data.

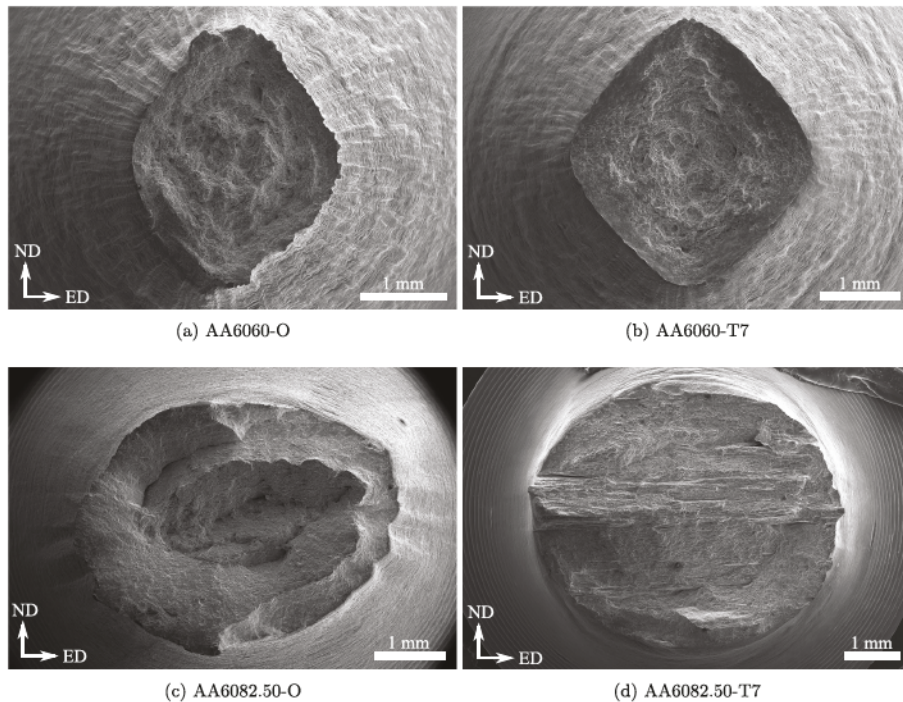


Fig. 4. Fracture surfaces of the AA6060 and AA6082.50 alloys in temper O and T7, subjected to monotonic tension.

become more elliptical than the clear diamond shape observed for monotonic tension, and the area of the fracture surface is almost unchanged.

For the AA6060 alloy in temper T6, Frodal et al. (2017) observed some areas of intercrystalline fracture, and the amount was seen to decrease with increasing pre-compression. The same trend is also observed for temper T7, but fewer areas are seen than for temper T6. In contrast, intercrystalline fracture is not observed for temper O.

#### 4. Constitutive modelling

In the finite element simulations of the material tests and in the subsequent unit cell simulations, an advanced plasticity model is applied. The anisotropic yield criterion of the plasticity model is calibrated based on polycrystal plasticity calculations. In the

following, the crystal plasticity model is described first and then the phenomenological plasticity model is outlined.

#### 4.1. Crystal plasticity

##### 4.1.1. Single crystal plasticity

A rate-dependent crystal plasticity formulation is adopted where plastic deformation is assumed to occur by plastic slip on certain crystallographic slip systems, determined by the crystal structure. It is further assumed that the elastic deformations are infinitesimal, while the plastic deformations and rotations may be finite. For details beyond this section on general theory of single crystal plasticity, the reader is referred to the textbook of Khan and Huang (1995).

The velocity gradient  $L$  is additively decomposed into a symmetric and a skew-symmetric part

$$L_{ij} = D_{ij} + W_{ij} \quad (4)$$

where  $D$  is the symmetric rate of deformation tensor and  $W$  is the skew-symmetric spin tensor. These tensors are additively decomposed into elastic and plastic parts

$$D_{ij} = D_{ij}^e + D_{ij}^p, \quad W_{ij} = W_{ij}^e + W_{ij}^p \quad (5)$$

where  $D^e$  and  $D^p$  are the elastic and plastic rate of deformation tensors, respectively. The elastic spin tensor  $W^e$  consists of an infinitesimal elastic contribution and rigid spin of the crystal lattice, whereas  $W^p$  is the plastic spin tensor caused by plastic slip. Plastic slip occurs on certain crystallographic slip systems, and the plastic parts of the rate of deformation and spin tensors are given by

$$D_{ij}^p = \frac{1}{2} \sum_{\alpha=1}^N \dot{\gamma}^{(\alpha)} (S_{ij}^{(\alpha)} + S_{ji}^{(\alpha)}) \quad (6)$$

$$W_{ij}^p = \frac{1}{2} \sum_{\alpha=1}^N \dot{\gamma}^{(\alpha)} (S_{ij}^{(\alpha)} - S_{ji}^{(\alpha)}) \quad (7)$$

where  $N$  is the number of slip systems and  $\dot{\gamma}^{(\alpha)}$  is the plastic slip rate on slip system  $\alpha$ . Further,  $S^{(\alpha)} = \mathbf{m}^{(\alpha)} \otimes \mathbf{n}^{(\alpha)}$  is the Schmid tensor, where  $\mathbf{m}^{(\alpha)}$  and  $\mathbf{n}^{(\alpha)}$  are unit vectors defining the slip direction and slip plane normal, respectively.

Let  $\mathbf{e}_i$  ( $i = 1,2,3$ ) denote the basis for the global coordinate system, and  $\hat{\mathbf{e}}_i$  the basis for a co-rotated coordinate system that rotates with the crystal lattice. The rotation of the lattice is given by the orthogonal rotation tensor  $\mathfrak{R}$ , that evolves according to the differential equations

$$\dot{\mathfrak{R}}_{ij} = W_{ik}^e \mathfrak{R}_{kj} \quad (8)$$

The unit vectors  $\mathbf{m}^{(\alpha)}$  and  $\mathbf{n}^{(\alpha)}$  are not affected by the crystallographic slip and are given by

$$m_i^{(\alpha)} = \mathfrak{R}_{ij} \hat{m}_j^{(\alpha)}, \quad n_i^{(\alpha)} = \mathfrak{R}_{ij} \hat{n}_j^{(\alpha)} \quad (9)$$

where the vector components  $\hat{m}_i^{(\alpha)}$  and  $\hat{n}_i^{(\alpha)}$  in the co-rotational coordinate system are constant and defined by the crystal structure.

In the co-rotated coordinate system, the rate form of the generalised Hooke's law can be expressed as

$$\dot{\hat{\sigma}}_{ij} = \hat{C}_{ijkl} \hat{D}_{kl}^e \quad (10)$$

where  $\hat{\sigma}$  is the Cauchy stress tensor, and the fourth-order elasticity tensor  $C$  is assumed invariant of plastic deformation and constant in the co-rotational lattice frame. The elasticity tensor accounts for the elastic anisotropy of the crystal, and is defined by the three independent elastic constants  $\hat{c}_{11}$ ,  $\hat{c}_{12}$  and  $\hat{c}_{44}$ . In this case, Equation (10) can be written on matrix form as

$$\begin{bmatrix} \dot{\hat{\sigma}}_{11} \\ \dot{\hat{\sigma}}_{22} \\ \dot{\hat{\sigma}}_{33} \\ \dot{\hat{\sigma}}_{12} \\ \dot{\hat{\sigma}}_{23} \\ \dot{\hat{\sigma}}_{31} \end{bmatrix} = \begin{bmatrix} \hat{c}_{11} & \hat{c}_{12} & \hat{c}_{12} & 0 & 0 & 0 \\ \hat{c}_{12} & \hat{c}_{11} & \hat{c}_{12} & 0 & 0 & 0 \\ \hat{c}_{12} & \hat{c}_{12} & \hat{c}_{11} & 0 & 0 & 0 \\ 0 & 0 & 0 & \hat{c}_{44} & 0 & 0 \\ 0 & 0 & 0 & 0 & \hat{c}_{44} & 0 \\ 0 & 0 & 0 & 0 & 0 & \hat{c}_{44} \end{bmatrix} \begin{bmatrix} \hat{D}_{11}^e \\ \hat{D}_{22}^e \\ \hat{D}_{33}^e \\ 2\hat{D}_{12}^e \\ 2\hat{D}_{23}^e \\ 2\hat{D}_{31}^e \end{bmatrix} \quad (11)$$

The plastic power per unit volume is defined as

$$\dot{w}^p = \sigma_{ij} D_{ij}^p = \hat{\sigma}_{ij} \hat{D}_{ij}^p = \sum_{\alpha=1}^N \tau^{(\alpha)} \dot{\gamma}^{(\alpha)} \quad (12)$$

where the resolved shear stress  $\tau^{(\alpha)}$  acting on slip system  $\alpha$  is defined as power conjugate to the plastic slip rate  $\dot{\gamma}^{(\alpha)}$ . The resolved shear stresses are here defined by

$$\tau^{(\alpha)} = \sigma_{ij} S_{ij}^{(\alpha)} = \hat{\sigma}_{ij} \hat{S}_{ij}^{(\alpha)} \quad (13)$$

In this work, the plastic flow is described by the rate-dependent constitutive relation (Hutchinson, 1976)

$$\dot{\gamma}^{(\alpha)} = \dot{\gamma}_0 \left| \frac{\tau^{(\alpha)}}{\tau_c^{(\alpha)}} \right|^{\frac{1}{m}} \text{sgn}(\tau^{(\alpha)}) \quad (14)$$

where  $\dot{\gamma}_0$  is the reference shearing rate,  $m$  is the instantaneous strain rate sensitivity, and  $\tau_c^{(\alpha)}$  is the critical resolved shear stress on slip system  $\alpha$ . The critical resolved shear stresses, with initial value  $\tau_0$ , evolve according to (Saai et al., 2013)

$$\dot{\tau}_c^{(\alpha)} = \theta(\Gamma) \sum_{\beta=1}^N q_{\alpha\beta} |\dot{\gamma}^{(\beta)}| \quad (15)$$

where  $q_{\alpha\beta}$  is the latent hardening matrix, and  $\theta(\Gamma)$  is the work-hardening rate; a function of the accumulated plastic shear strain,  $\Gamma$ , defined as

$$\Gamma = \int_0^t \sum_{\alpha=1}^N |\dot{\gamma}^{(\alpha)}| dt \quad (16)$$

The work-hardening rate is given by (Saai et al., 2013)

$$\theta(\Gamma) = \sum_{k=1}^{N_r} \theta_{rk} \exp\left(-\frac{\theta_{rk}}{\tau_k} \Gamma\right) \quad (17)$$

where  $N_r$  is the number of hardening terms, and  $\theta_{rk}$  and  $\tau_k$  are the initial hardening rate and saturated value of hardening term  $k$ , respectively.

#### 4.1.2. Polycrystal plasticity

In this work, the crystal plasticity finite element method (CP-FEM) is used to model the material anisotropy. The material is represented by a representative volume element (RVE), see Section 5.1, where each grain is explicitly modelled and behaves according to the single crystal plasticity model, described in Section 4.1.1. Thus, stress equilibrium and compatibility across grain boundaries are fulfilled. Every grain is given an initial orientation based on the crystallographic texture of the aluminium alloys, see Frodal et al. (2017) for the orientation distribution functions (ODFs).

The volume-average Cauchy stress tensor,  $\bar{\sigma}$ , and the volume-average plastic power per unit volume,  $\bar{w}^p$ , of the RVE are defined as

$$\bar{\sigma} = \sum_{k=1}^{N_{\text{int}}} v_k \sigma_k, \quad \bar{w}^p = \sum_{k=1}^{N_{\text{int}}} v_k w_k^p \quad (18)$$

where  $v_k$  is the volume fraction,  $\sigma_k$  is the Cauchy stress tensor, and  $w_k^p$  is the plastic power per unit volume of integration point  $k$ . The total number of integration points is  $N_{\text{int}}$ . When the initial volume of each integration point is equal, and under the assumption of infinitesimal elastic strains, the volume fraction of every integration point can be approximated by  $v_k = 1/N_{\text{int}}$ .

#### 4.2. Phenomenological plasticity

In this section, the constitutive relations of the phenomenological plasticity model are outlined. The plasticity model consists of a pressure-sensitive version of the anisotropic yield criterion Yld2004–18p (Barlat et al., 2005) to describe plastic anisotropy and the strength differential effect, a non-associated flow rule to ensure isochoric plastic flow, nonlinear isotropic and kinematic work-hardening rules, and internal variables to account for the effects of strain path changes (Mánik et al., 2015).

Again a co-rotational formulation is used, analogous to Equation (8), but under the assumption of zero plastic spin. The co-rotated Cauchy stress rate and the elastic rate of deformation tensors are related by the generalised Hooke's law, Equation (10). Elastic isotropy is assumed, and the fourth-order elasticity tensor  $C$  contains only two independent parameters, i.e., Young's modulus  $E$  and Poisson's ratio  $\nu$ .

To describe the strength differential effect observed in the experimental tests, we formulate a pressure-sensitive yield criterion valid for plastic anisotropy. To this end, the Drucker and Prager (1952) yield criterion is adopted with the equivalent stress defined by the Yld2004–18p yield function (Barlat et al., 2005). Note that the pressure sensitivity is assumed to be weak. Thus, the yield criterion is formulated as

$$\Phi(\eta, p) \equiv \phi(\eta) - \sigma_y(p) = 0, \quad \phi(\eta) = \frac{\varphi(\eta) + \alpha\eta \cdot I}{1 + \alpha} \quad (19)$$

where  $\eta = \sigma - \chi$  is the effective stress tensor,  $\chi$  is the backstress tensor,  $I$  is the second-order identity tensor,  $\sigma_y(p)$  controls the size of the elastic domain,  $p$  is the accumulated plastic strain,  $\varphi(\eta)$  is the equivalent stress with respect to the effective stress defined by the Yld2004–18p yield function, and  $\alpha$  governs the pressure sensitivity. For  $\alpha = 0$  the yield criterion reduces to the pressure independent Yld2004–18p yield criterion.

The equivalent stress of the anisotropic Yld2004–18p yield function is given by (Barlat et al., 2005)

$$\varphi(\boldsymbol{\eta}) = \left( \frac{1}{4} \sum_{k=1}^3 \sum_{l=1}^3 |S'_k - S''_l|^a \right)^{\frac{1}{a}} \tag{20}$$

where  $a$  is an exponent determining the curvature of the yield surface, and  $S'_k$  and  $S''_l$  are the principal values of the tensors  $s'$  and  $s''$ , respectively. The tensors  $s'$  and  $s''$  are determined by the linear transformations

$$\hat{s}'_{ij} = \hat{C}'_{ijkl} \hat{s}_{kl}, \quad \hat{s}''_{ij} = \hat{C}''_{ijkl} \hat{s}_{kl} \tag{21}$$

where the fourth-order tensors  $C'$  and  $C''$  contain coefficients describing the plastic anisotropy, and  $s$  is the deviatoric part of the effective stress tensor given as

$$\hat{s}_{ij} = \hat{\eta}_{ij} - \frac{1}{3} \hat{\eta}_{kk} \delta_{ij} \tag{22}$$

where  $\delta_{ij}$  is the Kronecker delta. For an orthotropic material, Equation (21) can be written on matrix form as

$$\begin{bmatrix} \hat{s}'_{11} \\ \hat{s}'_{22} \\ \hat{s}'_{33} \\ \hat{s}'_{12} \\ \hat{s}'_{23} \\ \hat{s}'_{31} \end{bmatrix} = \begin{bmatrix} 0 & -\hat{c}'_{12} & -\hat{c}'_{13} & 0 & 0 & 0 \\ -\hat{c}'_{21} & 0 & -\hat{c}'_{23} & 0 & 0 & 0 \\ -\hat{c}'_{31} & -\hat{c}'_{32} & 0 & 0 & 0 & 0 \\ 0 & 0 & 0 & \hat{c}'_{44} & 0 & 0 \\ 0 & 0 & 0 & 0 & \hat{c}'_{55} & 0 \\ 0 & 0 & 0 & 0 & 0 & \hat{c}'_{66} \end{bmatrix} \begin{bmatrix} \hat{s}_{11} \\ \hat{s}_{22} \\ \hat{s}_{33} \\ \hat{s}_{12} \\ \hat{s}_{23} \\ \hat{s}_{31} \end{bmatrix} \tag{23}$$

$$\begin{bmatrix} \hat{s}''_{11} \\ \hat{s}''_{22} \\ \hat{s}''_{33} \\ \hat{s}''_{12} \\ \hat{s}''_{23} \\ \hat{s}''_{31} \end{bmatrix} = \begin{bmatrix} 0 & -\hat{c}''_{12} & -\hat{c}''_{13} & 0 & 0 & 0 \\ -\hat{c}''_{21} & 0 & -\hat{c}''_{23} & 0 & 0 & 0 \\ -\hat{c}''_{31} & -\hat{c}''_{32} & 0 & 0 & 0 & 0 \\ 0 & 0 & 0 & \hat{c}''_{44} & 0 & 0 \\ 0 & 0 & 0 & 0 & \hat{c}''_{55} & 0 \\ 0 & 0 & 0 & 0 & 0 & \hat{c}''_{66} \end{bmatrix} \begin{bmatrix} \hat{s}_{11} \\ \hat{s}_{22} \\ \hat{s}_{33} \\ \hat{s}_{12} \\ \hat{s}_{23} \\ \hat{s}_{31} \end{bmatrix} \tag{24}$$

where the 18 anisotropy parameters  $\hat{c}'_{ij}$  and  $\hat{c}''_{ij}$  together with the exponent  $a$  determine the shape of the yield surface in stress space. Recently, Van Den Boogaard et al. (2016) showed that the 18 anisotropy parameters can be reduced to 16 independent ones. Thus, we will select  $\hat{c}'_{12} = \hat{c}'_{13} = 1$ . Any other choice will give equivalent results, but for an isotropic material these selected values will result in that all  $\hat{c}'_{ij}$  and  $\hat{c}''_{ij}$  become equal to one.

By studying the strength differential effect and pressure sensitivity in aluminium, Spitzig and Richmond (1984) found that the plastic dilatancy described by the associated flow rule for a pressure sensitive yield criterion greatly overestimated their experimental findings and that the plastic volume changes were negligible in comparison. Following their work, the flow rule is assumed to be non-associated and given by

$$\dot{D}^p_{ij} = \dot{\lambda} \frac{\partial \varphi}{\partial \hat{\eta}_{ij}} \tag{25}$$

where  $\dot{\lambda}$  is the plastic multiplier. The equivalent plastic strain rate is defined by the plastic power, where  $\varphi(\boldsymbol{\eta})$  is taken to be power conjugate to  $\dot{p}$ , so that

$$\dot{p} \equiv \frac{\hat{\eta}_{ij} \dot{D}^p_{ij}}{\varphi(\boldsymbol{\eta})} = \dot{\lambda} \tag{26}$$

To obtain the latter equality, it was used that  $\varphi(\boldsymbol{\eta})$  is a homogeneous function of order one with respect to the effective stress. The backstress tensor  $\boldsymbol{\chi}$  is defined as a sum of  $N_\chi$  kinematic hardening terms, viz.

$$\hat{\chi}_{ij} = \sum_{k=1}^{N_\chi} \hat{\chi}^{(k)}_{ij} \tag{27}$$

Each partial hardening term  $\boldsymbol{\chi}^{(k)}$  evolves according to (Armstrong and Frederick, 1966; Frederick and Armstrong, 2007)

$$\dot{\hat{\chi}}^{(k)}_{ij} = \theta_{\chi k} \left( \frac{\hat{\eta}_{ij}}{\varphi(\boldsymbol{\eta})} - \frac{\hat{\chi}^{(k)}_{ij}}{Q_{\chi k}} \right) \dot{p} \tag{28}$$

where  $\theta_{\chi k}$  and  $Q_{\chi k}$  are parameters governing the kinematic hardening of the material.

The size of the elastic domain is given by

$$\sigma_y(p) = \sigma_0 + R(p) + R_r(p) + S_r(p) \tag{29}$$

where  $\sigma_0$  is the initial yield stress,  $R(p)$  is the isotropic hardening contribution for monotonic loading,  $R_r(p)$  accounts for permanent



softening after load reversal, and  $S_r(p)$  represents the extra strength contribution due to the built-up microstructure anisotropy during straining before load reversal. The isotropic hardening contribution for monotonic loading is given by the extended Voce hardening rule (Voce, 1948)

$$R(p) = \sum_{k=1}^{N_V} Q_{Rk} \left( 1 - \exp\left(-\frac{\theta_{Rk}}{Q_{Rk}} p\right) \right) \quad (30)$$

where  $N_V$  is the number of hardening terms, and  $Q_{Rk}$  and  $\theta_{Rk}$  are parameters controlling the shape of the isotropic hardening curve for monotonic loading. The evolution equations for the internal variables  $R_r$  and  $S_r$  are given by (Mánik et al., 2015)

$$\dot{R}_r = k_r \min(\hat{P}_{ij} \hat{N}_{ij}, 0) \dot{p} \quad (31)$$

$$\dot{S}_r = -c_r [S_r + q_r (\sigma_0 + R + R_r) \min(\hat{P}_{ij} \hat{N}_{ij}, 0)] \dot{p} \quad (32)$$

where  $k_r$  is a parameter controlling the permanent softening,  $P$  is the “delayed pointer”,  $N$  is the direction of the plastic rate of deformation, and  $c_r$  and  $q_r$  are parameters controlling the extra strength contributions represented by  $S_r$ . The “delayed pointer” evolves according to

$$\dot{\hat{P}}_{ij} = c_p (\hat{N}_{ij} - \hat{P}_{ij}) \dot{p} \quad , \quad \hat{N}_{ij} = \frac{\hat{D}_{ij}^p}{\sqrt{\hat{D}_{ki}^p \hat{D}_{ki}^p}} \quad (33)$$

where  $c_p$  is a parameter controlling its evolution. The “delayed pointer” is initially assumed to be equal to the zero tensor, which is the case for well-annealed materials (Mánik et al., 2015). This is not necessarily true for our materials, but since the pre-straining in the present study is quite large, the “delayed pointer” at load reversal is similar to its true quantity and thus this is an appropriate simplification. The strain path change variables  $R_r$  and  $S_r$  are also assumed to be zero initially. It should be noted that the effect of orthogonal strain path changes, which is accounted for in the model by Mánik et al. (2015), has been neglected in the above equations as we are only simulating load reversal tests.

Finally, the loading/unloading conditions of plasticity are given in Kuhn-Tucker form as

$$\Phi \leq 0, \quad \dot{\lambda} \geq 0, \quad \dot{\lambda} \Phi = 0 \quad (34)$$

whereas the consistency condition, used to determine the plastic multiplier  $\dot{\lambda}$  in the plastic domain, is expressed by

$$\dot{\lambda} \Phi = 0 \quad (35)$$

The reader is referred to Mánik et al. (2015) for a more detailed description and interpretation of the constitutive relations accounting for the effects of strain path change.

## 5. Numerical simulations

### 5.1. Crystal plasticity and calibration of yield surfaces

In this section, the yield surface of the materials is calibrated using the crystal plasticity model described in Section 4.1. The parameters controlling the shape of the Yld2004–18p yield surface are typically determined from a large number of experimental tests (see, e.g., Fourmeau et al., 2011). It is, however, desirable to determine the behaviour of complex materials without performing extensive experimental testing. The anisotropy coefficients  $\hat{c}_{ij}^t$  and  $\hat{c}_{ij}''$  will therefore be determined from virtual testing using polycrystal plasticity theory. In addition to the lower cost than experiments, virtual testing allows for performing tests in any direction and material plane, i.e., virtual testing is not restricted by experimental limitations.

Each material is represented by an RVE, see Fig. 5, consisting of  $10 \times 10 \times 10$  elements, where each element represents a grain. This results in a total of 1000 grains in the RVE of the polycrystalline material. Periodic boundary conditions are applied to the nodes on the exterior boundaries to ensure periodicity. A convergence study was performed, where the number of elements per grain and the number of grains were varied. The details of that study are omitted here for brevity. It was found that this RVE contains a sufficiently large number of grains to predict the average stress state with adequate accuracy, and small enough to provide reasonable computational times. All elements/grains are given an initial orientation such that the ODF of the RVE is as close as possible to the ODF of the measured crystallographic texture for each alloy. The crystal orientations of the RVE are generated in the open source software DREAM.3D (Groeber and Jackson, 2014) by a stochastic iterative procedure.

The crystal plasticity model is implemented into a user material subroutine (VUMAT) for Abaqus/Explicit (Abaqus, 2014). An explicit integration scheme is utilised for time integration of the rate constitutive equations of single crystal plasticity (Zhang et al., 2014), along with explicit integration of the momentum equations. The grains are represented by linear eight-node elements with selective reduced integration (C3D8), i.e., reduced integration on the volumetric terms. The RVE is loaded with a strain rate of  $10^{-3} \text{ s}^{-1}$  in all simulations, and mass scaling is used to reduce the computational time. Throughout the simulations it is ensured that the response is quasi-static, i.e., that the kinetic energy is negligible.

Table 4 contains some of the crystal plasticity model parameters, which are common for a broad range of aluminium alloys from the literature (Khadyko et al., 2014, 2016b). These parameters are assumed constant for the materials at hand, while the parameters governing initial slip resistance and work hardening are dependent upon alloy and temper conditions. Note that a rather simple



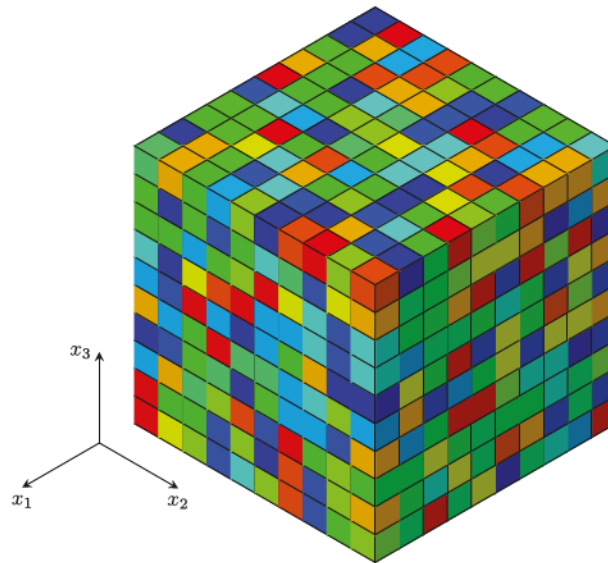


Fig. 5. Representative volume element (RVE) of a polycrystal used in the calibration of the yield surfaces.

Table 4  
Crystal plasticity parameters governing elasticity, rate sensitivity and latent hardening.

$\hat{\epsilon}_{11}$ (MPa)	$\hat{\epsilon}_{12}$ (MPa)	$\hat{\epsilon}_{44}$ (MPa)	$\dot{\gamma}_0$ (s <sup>-1</sup> )	$m$	$q_{\alpha\beta}$
106 430	60 350	28 210	0.010	0.005	1.0 if $\alpha = \beta$ 1.4 if $\alpha \neq \beta$

definition of the latent hardening matrix is used, with a single non-diagonal parameter. This choice could impact the response at large plastic deformations. In this paper, the crystal plasticity framework will only be used to determine the instance of initial yielding, i.e., to calibrate the yield surfaces. Thus, the current latent hardening matrix is deemed sufficiently accurate. The reader is referred to Khadyko et al. (2016a) for further details on latent hardening and plastic anisotropy evolution.

We define a global Cartesian coordinate system ( $x_1, x_2, x_3$ ) aligned with the principal axes of anisotropy of the extruded profile. The coordinate system is oriented so that ED is parallel to the  $x_1$  axis, TD is parallel to the  $x_2$  axis, and ND is parallel to the  $x_3$  axis. In the following, all stress and strain quantities are related to this coordinate system.

To include and study any effects of the strength and work hardening on the yield surfaces, the parameters controlling the slip resistance are fitted based on the experimental tests on smooth cylindrical specimens performed by Khadyko et al. (2014) and Khadyko (2018). The RVE is subjected to uniaxial tension along the  $x_2$  axis (TD), i.e., the same direction as the experiments. The non-linear optimisation software LS-OPT (Stander et al., 2015) is used together with Abaqus to calibrate the parameters controlling the slip resistance using experimental data up to diffuse necking. In the optimisation procedure, Abaqus supplies the stress-strain curve from the RVE to LS-OPT which calculates the mean squared error between the numerical and experimental stress-strain curves. Based on the optimisation algorithm the slip resistance parameters are adjusted to minimise the mean squared error in the next iteration. Within each iteration, LS-OPT runs 10 simulations simultaneously with Abaqus varying these parameters. In general, after 15–20

Table 5  
Crystal plasticity parameters governing initial slip resistance and work hardening.

Material	$\tau_0$ (MPa)	$\theta_{r1}$ (MPa)	$\eta$ (MPa)	$\theta_{r2}$ (MPa)	$\tau_2$ (MPa)
AA6060-O	10.5	301.0	13.1	49.9	13.5
AA6060-T7	54.5	207.9	19.3	0.0	0.0
AA6060-T6	72.2	81.5	16.5	0.0	0.0
AA6082.25-O	20.4	236.9	13.5	25.7	15.7
AA6082.25-T7	58.3	190.1	18.7	0.0	0.0
AA6082.25-T6	107.1	30.4	200.0	5.5	200.0
AA6082.50-O	13.6	262.3	12.5	55.6	17.0
AA6082.50-T7	78.7	175.1	16.1	0.0	0.0
AA6082.50-T6	123.0	13.0	199.2	8.1	190.7

iterations the mean squared error is reduced from 1–10 to approximately  $10^{-5}$  and further iterations will not reduce the error. One of these simulations with the RVE is completed in approximately 50–60 min utilising 4 threads on an Intel Xeon X5690 CPU. Table 5 contains the optimised slip resistance parameters for the different materials, valid up to diffuse necking. For further details regarding calibration of slip resistance parameters, the reader is referred to Khadyko et al. (2015).

With all the parameters of the crystal plasticity model identified, the RVE can be used to determine the yield surfaces of the nine materials. Barlat et al. (2005) proposed a series of experimental and numerical tests to be performed in order to determine the anisotropy coefficients  $\hat{c}_{ij}'$  and  $\hat{c}_{ij}''$ . These tests consist of uniaxial tension in seven different directions in the  $x_1 - x_2$  plane, i.e., uniaxial tension in  $15^\circ$  increments from the  $x_1$  axis to the  $x_2$  axis, and balanced biaxial tension in the  $x_1 - x_2$  plane. From these tests both the initial yield stress and the Lankford coefficients are used to calibrate the yield surface. In addition, the initial yield stress in simple shear in the  $x_2 - x_3$  and  $x_1 - x_3$  planes, and uniaxial tension tests oriented at  $45^\circ$  between the  $x_2$  and  $x_3$  axes, and between the  $x_1$  and  $x_3$  axes, are used. In order to perform tests at any angle from the principal axes of anisotropy of the material, the initial orientation of the RVE is rotated by an equal amount.

During the calibration process, it became clear that for some of the materials more tests were needed to get an accurate estimate of the yield surface. Particularly important were the plane-strain tension tests in the  $x_1 - x_2$  plane at  $0^\circ$  and  $90^\circ$  from the  $x_1$  axis. In addition, a plane-stress balanced biaxial strain test in the  $x_1 - x_2$  plane was included, i.e., where the strain rates in the two in-plane directions are equal and greater than zero, i.e.,  $\dot{\epsilon}_{11}/\dot{\epsilon}_{22} = 1$ . Note that this point coincides with that of balanced biaxial tension for an isotropic material. Also, five tests with different (negative) ratio between the strain rate along the  $x_1$  and  $x_2$  axes were included. These tests have the following strain-rate ratios:  $\dot{\epsilon}_{11}/\dot{\epsilon}_{22} = -2.00, -1.57, -1.00, -0.64$  and  $-0.50$ .

For each test and for every material, the volume-average Cauchy stress tensor is extracted at a volume-average plastic work corresponding to 0.2% plastic strain for uniaxial tension along the  $x_1$  axis, i.e., the reference direction. Further, the stress tensors for all the tests are normalised by the initial yield stress in uniaxial tension along the reference direction, and the Lankford coefficient is found by taking the average value from 90% to 100% of the same value of plastic work.

The yield surface is calibrated as follows. The normalised volume-average Cauchy stress tensors and the Lankford coefficients are used in the evaluation of an error function, see Barlat et al. (2005). This error function is a function of the equivalent stress, Equation (20), which depends on the anisotropy coefficients  $\hat{c}_{ij}'$  and  $\hat{c}_{ij}''$  and the yield surface exponent  $a$ . Note that the yield surface shape is assumed invariant of pressure, thus  $\phi = \varphi$  in Equation (19) during the calibration process. Further, the error function is minimised by varying these parameters with the global minimisation algorithm *basin-hopping* of the Scipy Python package (Scipy, 2017). The error function typically has several local minima, and therefore a global minimisation algorithm should be used. The generated yield surfaces for each material together with the predicted yield stresses by CP-FEM are depicted as projections in the  $x_1 - x_2$  plane in Fig. 6.

Although most of the stress points on the yield surface used in the calibration are located in the  $x_1 - x_2$  plane, the yield surfaces are not biased with respect to this plane. As both the crystal plasticity model and the Yld2004–18p yield function depend only on the deviatoric stress state, these points are equivalent to other points on the yield surface, e.g., uniaxial tension along the  $x_1$  axis is equivalent to balanced biaxial tension/compression in the  $x_2 - x_3$  plane. The strength differential effect is not accounted for by including non-Schmid effects in the crystal plasticity model, and does not affect the calibration of the yield surfaces.

Fig. 6 shows the differences between the yield surfaces and it is clear that while the yield surfaces are similar for the tempers of the same alloy, the difference between the alloys is considerable due to the crystallographic texture. The largest difference between tempers for the same alloy is seen for the AA6082.50 alloy as the contours of increasing normalised shear stress are different. This is also the alloy where the difference in maximum shear stress is the greatest between tempers.

Fig. 7 and Fig. 8 compare in turn the normalised yield stresses and Lankford coefficients as functions of the tensile direction, in the  $x_1 - x_2$  plane, for the different materials. The differences between tempers of the same alloy are seen more clearly in these figures, although the main trends are similar for the same alloy. The corresponding Yld2004–18p yield surface parameters are given in Table 6.

The main source of anisotropy is assumed to be the crystallographic texture (Engler and Randle, 2009). In the present study, effects of other microstructural features, such as the size and shape of grains and the precipitate structure, are thus neglected. We note that the calibrated yield surfaces are initial yield surfaces, and during extensive plastic deformation the texture and the anisotropy of the materials will evolve. The result is that the yield surface shape evolves accordingly and the initial yield surface deviates from the current yield surface of the material.

## 5.2. Phenomenological plasticity and work-hardening behaviour

The strength differential effect is described by the pressure-dependent yield criterion defined in Equation (19), where the pressure sensitivity is controlled by the parameter  $\alpha$ . The values of  $\alpha$  for the current materials are obtained from the experimental data and results presented in Holmen et al. (2017). These values are compiled in Table 7. The reader is referred to Holmen et al. (2017) for details on the parameter identification.

The remaining model parameters govern isotropic and kinematic hardening, work-hardening stagnation and permanent softening, are calibrated in a two step procedure. It is useful to express the parameters of the isotropic and kinematic hardening rules as

$$\theta_{Ri} = \kappa_i \theta_i, \quad \theta_{\chi i} = (1 - \kappa_i) \theta_i \quad (36)$$

$$Q_{Ri} = \kappa_i Q_i, \quad Q_{\chi i} = (1 - \kappa_i) Q_i \quad (37)$$

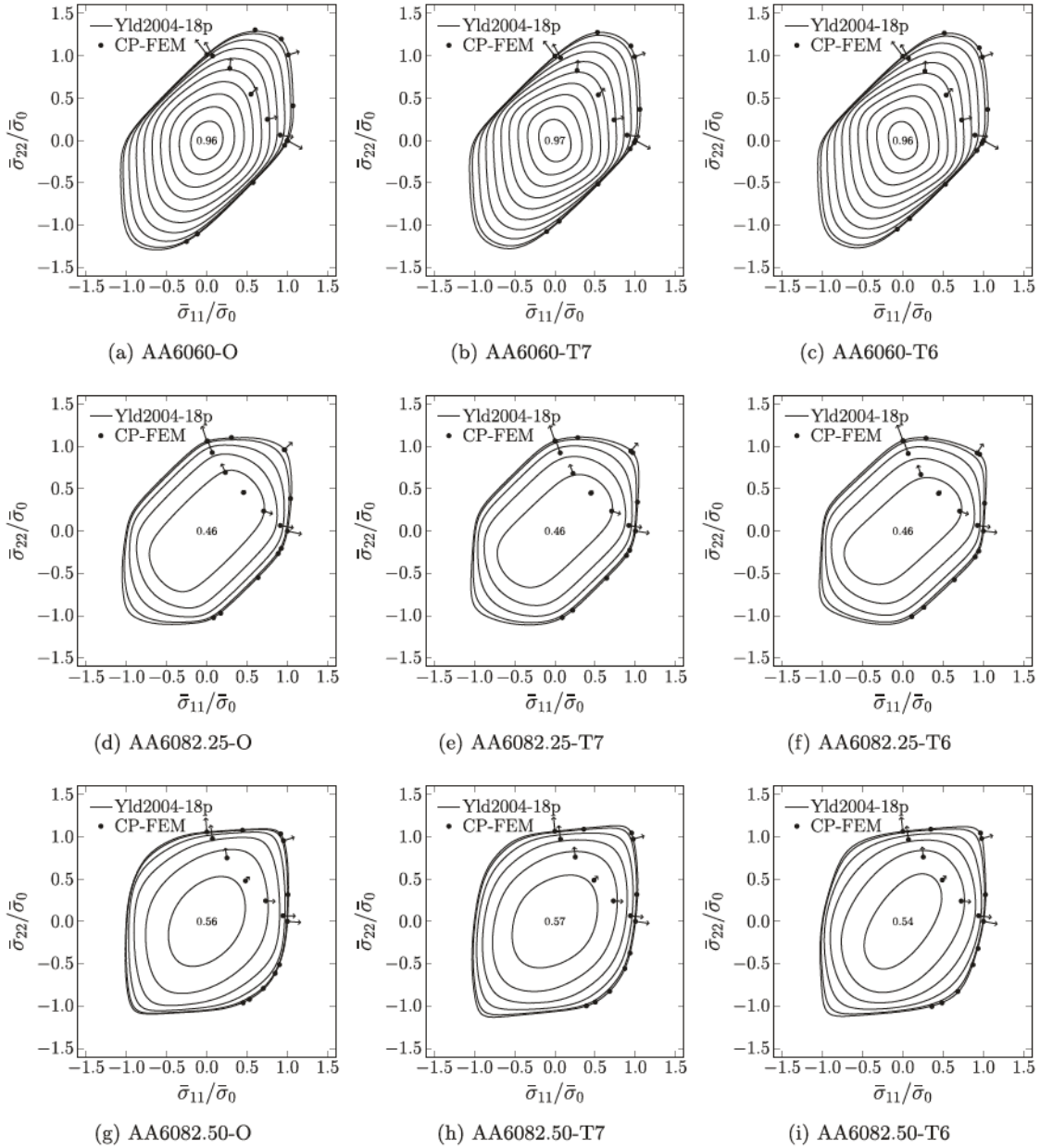


Fig. 6. Generated yield surfaces based on the CP-FEM, at a volume-average plastic work corresponding to 0.2% plastic strain along the reference direction, depicted in the  $x_1 - x_2$  (ED-TD) plane. Contours of the normalised shear stress  $\bar{\sigma}_{12}/\bar{\sigma}_0$  are plotted in 0.1 increments from zero, and the maximum value of  $\bar{\sigma}_{12}/\bar{\sigma}_0$  is shown in the centre. Arrows represent the projections of the direction of plastic flow predicted by the CP-FEM.

where there is no sum on  $i$  and it is assumed that the number of isotropic and kinematic hardening terms is the same, i.e.,  $N_V = N_\chi$ . A three-term hardening rule is adopted so that  $N_V = N_\chi = 3$ . The parameters  $Q_i$  and  $\theta_i$  define the work hardening of the material under monotonic loading, whereas  $\kappa_i$  define the partitioning into isotropic and kinematic hardening of the different hardening terms. This partitioning is possible because the isotropic and kinematic hardening rules give identical results in monotonic uniaxial tension.

In the first step, it is assumed that the work hardening is fully isotropic, i.e., all  $\kappa_i$  are equal to unity, and the parameters  $Q_i$  and  $\theta_i$  are identified using the stress-strain curves from monotonic tensile tests on smooth cylindrical specimens performed by Khadyko et al. (2014) and Khadyko (2018). In the second step, the stress-strain curves from the reversed loading tests subjected to 10% and 40% pre-compression (10% and 30% for the AA6060 alloy in temper O) are used to partition the work hardening into isotropic and

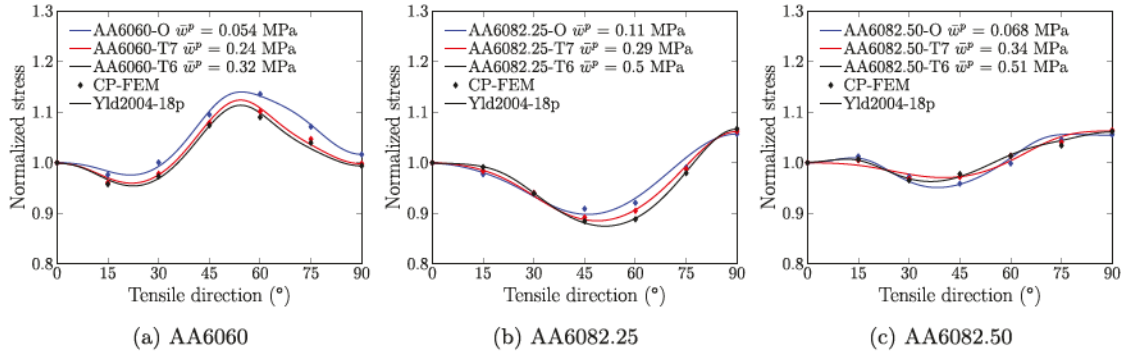


Fig. 7. Normalised yield stress versus tensile direction in uniaxial tension, from the CP-FEM and the generated yield surfaces, at a volume-average plastic work corresponding to 0.2% plastic strain along the reference direction.

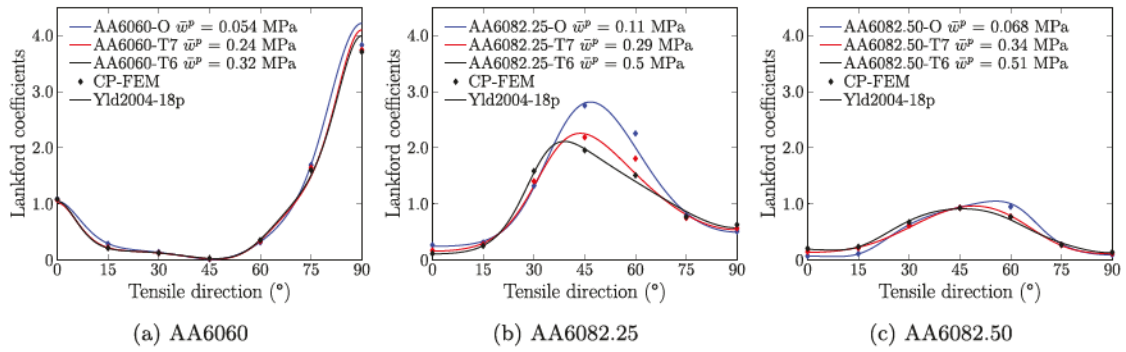


Fig. 8. Lankford coefficients versus tensile direction for uniaxial tension, from the CP-FEM and the generated yield surfaces, at a volume-average plastic work corresponding to 0.2% plastic strain along the reference direction.

Table 6  
Calibrated anisotropy coefficients and yield surface exponent for the Yld2004–18p yield criterion.

Material	AA6060			AA6082.25			AA6082.50		
	O	T7	T6	O	T7	T6	O	T7	T6
$\alpha$	9.2	11.4	11.8	18.9	13.6	13.5	17.0	14.5	12.5
$\hat{c}_{12}^{\prime}$	1.0000	1.0000	1.0000	1.0000	1.0000	1.0000	1.0000	1.0000	1.0000
$\hat{c}_{13}^{\prime}$	1.0000	1.0000	1.0000	1.0000	1.0000	1.0000	1.0000	1.0000	1.0000
$\hat{c}_{21}^{\prime}$	-0.7261	0.2604	-2.2769	0.6684	0.6898	0.6441	-0.3166	-3.3119	0.9218
$\hat{c}_{23}^{\prime}$	0.1009	0.4756	-0.4709	1.1443	1.0272	1.0412	2.5260	-1.0938	0.6785
$\hat{c}_{31}^{\prime}$	-0.1925	-2.2405	0.2555	0.5263	0.6059	0.6559	-0.5265	-3.6098	-0.5508
$\hat{c}_{32}^{\prime}$	-0.0950	-0.1944	0.2118	0.8230	0.8885	0.8653	-0.5163	-1.0424	0.8985
$\hat{c}_{44}^{\prime}$	-0.9592	0.1896	-0.1895	-1.0469	1.0120	0.9258	0.9885	1.0803	1.0859
$\hat{c}_{55}^{\prime}$	-1.2663	-0.1630	-0.1674	-1.0803	1.1697	1.4981	0.7676	-0.8979	0.8500
$\hat{c}_{66}^{\prime}$	-0.9536	1.0997	-1.0957	0.8995	0.9321	0.9452	1.1178	-0.6982	-0.8305
$\hat{c}_{12}^{\prime\prime}$	-0.0641	0.8676	1.1498	1.0868	0.7564	0.6093	1.1378	1.8762	0.4348
$\hat{c}_{13}^{\prime\prime}$	-1.0887	2.2273	-0.2049	1.4677	1.1787	0.9544	2.6320	1.5935	-0.0688
$\hat{c}_{21}^{\prime\prime}$	-1.3105	-0.5072	-1.5280	0.7687	0.8525	0.8362	0.3832	-2.3255	-0.3157
$\hat{c}_{23}^{\prime\prime}$	-1.5205	1.7280	-1.7423	1.1013	1.0114	1.0750	1.2385	0.2799	1.0286
$\hat{c}_{31}^{\prime\prime}$	-1.2515	-1.2435	-0.7779	0.9502	1.1155	1.1397	-1.9285	-3.0594	1.1692
$\hat{c}_{32}^{\prime\prime}$	1.0219	0.6461	-0.6487	0.6869	0.9250	0.9613	-0.5312	-0.8772	1.2030
$\hat{c}_{44}^{\prime\prime}$	0.1129	0.8948	0.9069	1.1840	1.2775	1.3740	0.8826	0.7526	0.8661
$\hat{c}_{55}^{\prime\prime}$	0.0064	1.2337	1.2410	1.0164	1.0073	0.7300	-0.8001	-0.6629	-0.6963
$\hat{c}_{66}^{\prime\prime}$	-0.3154	-0.1672	-0.1838	1.1146	1.1609	1.2299	0.4342	0.8519	0.7349



**Table 7**  
Pressure sensitivity parameter. From Holmen et al. (2017).

Material	$\beta$ (°)	$\alpha = \frac{1}{3}\tan\beta$
AA6060-O	0.7	0.004
AA6060-T7	1.7	0.010
AA6060-T6	2.2	0.013
AA6082.25-O	1.2	0.007
AA6082.25-T7	2.2	0.013
AA6082.25-T6	3.5	0.020
AA6082.50-O	0.9	0.005
AA6082.50-T7	2.5	0.015
AA6082.50-T6	3.6	0.021

kinematic contributions and to determine the parameters controlling work-hardening stagnation and permanent softening.

To determine the parameters  $Q_i$  and  $\theta_i$ , the smooth cylindrical tensile specimen used by Khadyko et al. (2014) is modelled in Abaqus/Standard. The phenomenological plasticity model described in Section 4.2 is implemented into a user material subroutine (UMAT) for Abaqus/Standard. A semi-implicit backward-Euler integration scheme is used to update the stress state for plastic loading steps. To ensure sufficient accuracy of the integration point values, substepping is employed (Dæhli et al., 2017). Isotropic elasticity is assumed with Young's modulus of  $E = 70000$  MPa and Poisson's ratio of  $\nu = 0.3$ . The plasticity model is used in simulations with the calibrated pressure-sensitive anisotropic yield surface and isotropic hardening. The finite element mesh of the smooth tensile specimen is shown in Fig. 9, with its tensile axis along the  $x_3$  axis (TD). Due to the orthotropic symmetry, only one-eighth of the specimen is modelled to reduce the computation time. Linear eight-node elements with selective reduced integration (C3D8) are used, where the dimension of the centre-most element is  $0.15 \times 0.15 \times 0.15$  mm<sup>3</sup>. Extensive testing with different element sizes showed that the selected mesh is appropriate for determining the hardening behaviour of the materials. The FE model in Abaqus is coupled to the non-linear optimisation software LS-OPT in the calibration procedure. The initial yield stress  $\sigma_0$  is found from the crystal plasticity model for uniaxial tension along the reference direction, i.e., the  $x_1$  axis (ED). The parameters  $Q_i$  and  $\theta_i$ , ( $i = 1,2,3$ ) are calibrated by minimising the mean squared error between the stress-strain curves to failure from the FE simulation and the experimental tests. The resulting initial yield stress and hardening parameters are given in Table 8. Note that the presence of voids is not accounted for during the calibration of the phenomenological plasticity model, and thus the work hardening of the materials is probably underestimated at large strains.

To determine the partitioning into isotropic and kinematic hardening and the parameters controlling work-hardening stagnation and permanent softening, the reversed loading tests subjected to 10% and 40% pre-compression are simulated. Fig. 10 shows the FE mesh of the diabolo-shaped specimen, and again only one-eighth of the specimen is modelled to reduce computational time. Symmetry boundary conditions are applied, and at the end of the specimen, boundary conditions to replicate conditions at the threaded section are enforced. Linear eight-node elements with selective-reduced integration (C3D8) are used in Abaqus/Standard, where the dimension of the centre-most element is  $0.12 \times 0.12 \times 0.12$  mm<sup>3</sup>. As before, the FE model is coupled to LS-OPT in the calibration procedure, and the mean squared error between the stress-strain curves of the FE simulation and the experimental tests is minimised by varying the relevant parameters:  $\kappa_1, \kappa_2, \kappa_3, c_p, k_r, c_r$  and  $q_r$ . The resulting parameters are given in Table 9 and Table 10.

### 5.3. Loading histories from the reversed loading tests

The FE model of the diabolo-shaped specimen in Fig. 10 is now subjected to the same load histories as applied in the reversed loading tests, using the phenomenological plasticity model with the calibrated parameter set. As before, the simulations are performed in Abaqus/Standard. Fig. 11 presents the stress-strain curves from the finite element simulations together with the

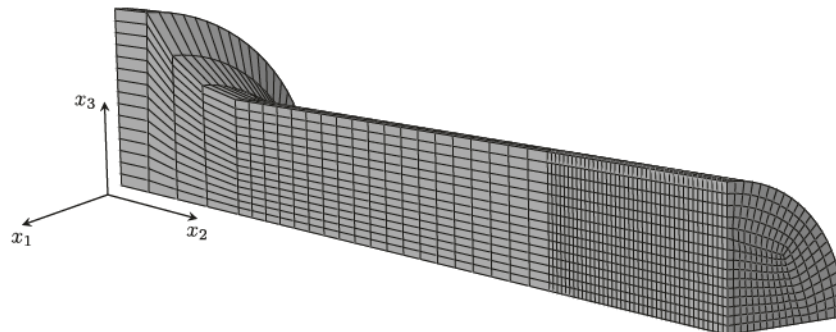


Fig. 9. Finite element mesh of the smooth cylindrical tensile specimen, with tensile axis along the  $x_3$  axis (TD).



**Table 8**  
Initial yield stress and parameters of the three-term hardening rule.

Material	$\sigma_0$ (MPa)	$\theta_1$ (MPa)	$Q_1$ (MPa)	$\theta_2$ (MPa)	$Q_2$ (MPa)	$\theta_3$ (MPa)	$Q_3$ (MPa)
AA6060-O	27.6	1844.8	34.7	400.5	28.8	83.5	91.5
AA6060-T7	124.6	1182.8	27.7	1094.8	28.1	39.6	726.9
AA6060-T6	170.8	549.2	19.9	476.3	17.8	70.0	124.9
AA6082.25-O	57.6	2661.3	44.6	382.2	32.6	120.8	91.0
AA6082.25-T7	163.6	1300.1	28.9	1301.2	40.7	52.3	232.9
AA6082.25-T6	299.5	470.5	28.5	485.0	29.8	50.0	279.4
AA6082.50-O	37.1	2009.9	39.3	233.6	30.9	208.2	69.5
AA6082.50-T7	189.9	1000.0	20.0	1366.5	41.1	29.3	153.5
AA6082.50-T6	284.1	8231.8	20.7	320.4	32.5	300.9	33.6

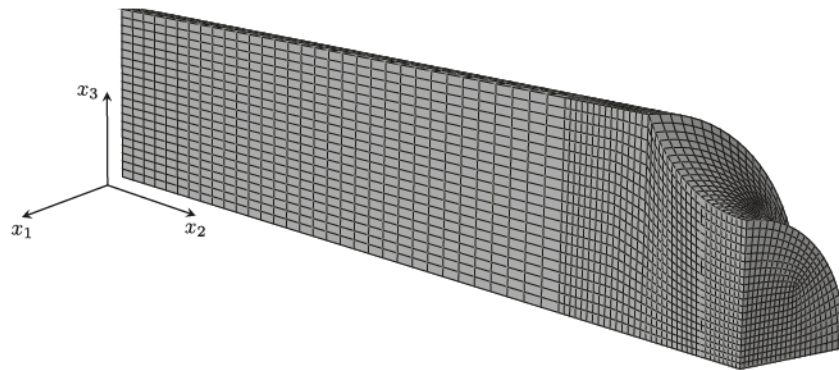


Fig. 10. Finite element mesh of the diabolo-shaped specimen, with tensile axis along the  $x_3$  axis (TD).

**Table 9**  
Parameters controlling the partitioning into isotropic and kinematic hardening.

Material	$\kappa_1$	$\kappa_2$	$\kappa_3$
AA6060-O	1.0000	0.4368	1.0000
AA6060-T7	0.3589	0.5986	1.0000
AA6060-T6	0.4751	0.8193	1.0000
AA6082.25-O	0.9304	0.2284	1.0000
AA6082.25-T7	0.6430	0.0000	1.0000
AA6082.25-T6	0.0000	0.0000	1.0000
AA6082.50-O	0.9418	0.0000	1.0000
AA6082.50-T7	0.4847	0.0000	1.0000
AA6082.50-T6	0.0000	0.3269	1.0000

**Table 10**  
Parameters governing work-hardening stagnation and permanent softening.

Material	$c_p$	$k_r$ (MPa)	$c_r$	$q_r$
AA6060-O	26.1	2164.8	12.3	2.82
AA6060-T7	13.9	1953.8	0.0	0.00
AA6060-T6	10.5	1441.5	0.0	0.00
AA6082.25-O	11.6	1127.3	32.4	0.27
AA6082.25-T7	7.1	1025.2	28.8	0.02
AA6082.25-T6	19.2	2688.1	6.9	2.90
AA6082.50-O	13.7	1262.1	24.9	0.72
AA6082.50-T7	7.2	1500.7	0.0	0.00
AA6082.50-T6	13.2	1414.1	0.0	0.00

experiments. Generally good agreement is observed between the experimental and numerical curves, and especially good agreement is found for the AA6082.25 alloy. For the two other alloys, small discrepancies are observed as the stress level in compression and in monotonic tension is slightly higher in magnitude in the simulations than in the experiments, except for the AA6060 alloy in temper O.

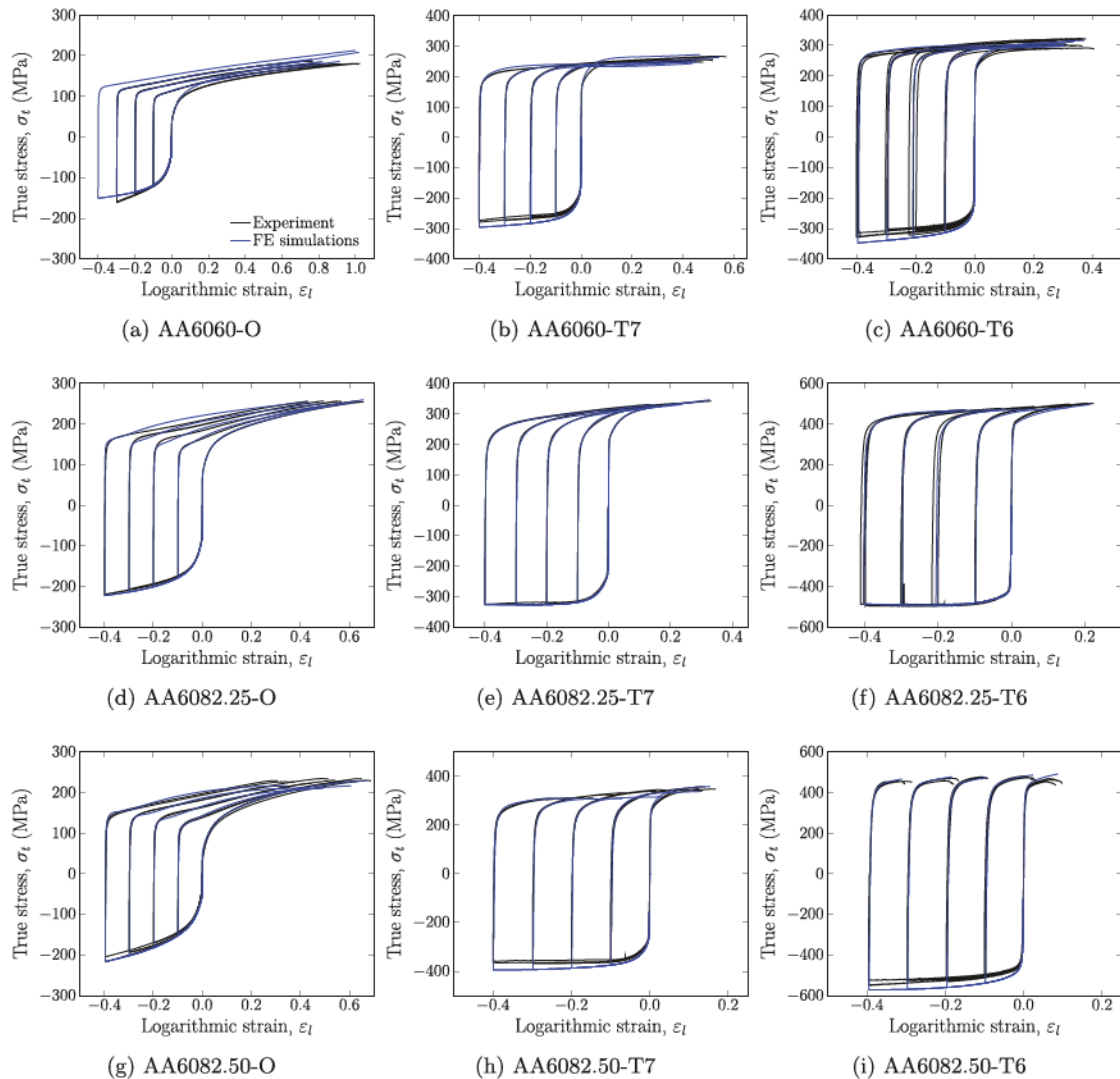


**Fig. 11.** Stress-strain curves for the three alloys in different tempers, from experiments (black curves) and finite element simulations (blue curves), until failure in the experiment. (For interpretation of the references to colour in this figure legend, the reader is referred to the Web version of this article.)

The deviations may come from inaccuracies in the calibrated yield surfaces, or the fact that the phenomenological model does not account for the evolution of the yield surface. During plastic deformation the crystallographic texture of the materials will evolve and affect the yield surface of the material and the plastic response of the specimen. From Fig. 4, it was observed that the AA6060 alloy developed a diamond-shaped fracture surface, which the phenomenological model is not fully able to recreate. This will yield inaccuracies, since the logarithmic strain measure is based on an elliptical cross-section area, as explained in Section 3.1. A discussion of this source of error is provided in Frodal et al. (2017). In addition, the strain path change model is not fully able to recreate the work-hardening stagnation observed for the alloys in temper O, as the experimental curves show that this transient appears to decrease for larger pre-compression levels. Also after the transient phase the resumed work-hardening rate deviates from that of the experiments for the alloys in temper O. This may be caused by the incorrectly described work-hardening stagnation behaviour as it would lead to an earlier localisation of deformation in the centre of the notch area. For the AA6082.50 alloy in temper T7, the permanent softening is overestimated for 10, 20 and 30% pre-compression, whereas it is well predicted for the 40% pre-compression curves used in the calibration process.

Fig. 12 shows the stress-strain curves for the AA6082.25 alloy in T7 temper, including finite element simulations with different hardening models. Here the importance of the strain path change model is revealed. It is seen that the simulations with either

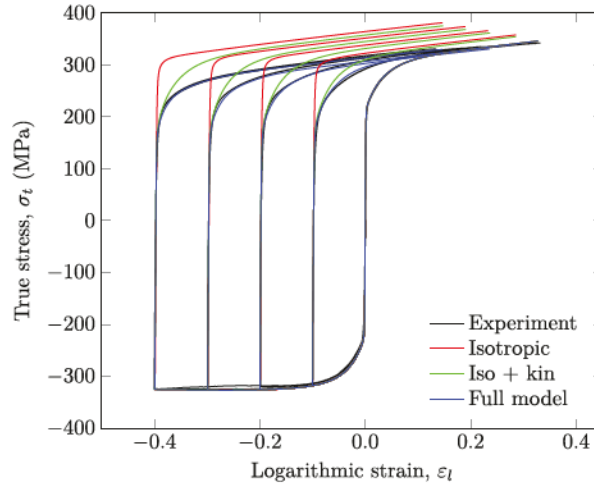


Fig. 12. Stress-strain curves for the AA6082.25 alloy in T7 temper, from experiments and finite element simulations with different hardening models. Note that the experimental (black) curves lie under the (blue) curves for the full model. (For interpretation of the references to colour in this figure legend, the reader is referred to the Web version of this article.)

isotropic hardening or combined isotropic and kinematic hardening do not capture the permanently reduced stress level in tension after load reversal. In contrast, the full model, involving all the parameters calibrated above, represents the stress level and the response of the specimen accurately, which is important when investigating failure.

The Lankford coefficients calculated from the finite element simulations are compiled in Table 11. Comparing the coefficients with the experimental values in Table 3, it is found that the coefficients for all tempers of the AA6082.25 alloy are in good agreement with the experimental values. For the two other alloys, the simulated Lankford coefficients typically overestimate the plastic anisotropy, with the exception of the AA6060 alloy in temper O and the AA6082.50 alloy in temper T6. Further, the numerical model does not capture the evolution of the Lankford coefficients, with increasing pre-compression as seen in the experiments. This indicates that the yield surface evolves with plastic deformation, affecting the response of the specimen.

The loading and deformation histories are then extracted from the critical element in the full model, i.e., the element where fracture is assumed to initiate. The critical element is assumed to be located in the centre of the specimen where the stress triaxiality is the highest at material failure. Due to the orthotropic material symmetry, the stress state of this element is already in the principal stress space. Following Dæhli et al. (2017), we can write the normal stress components on vector form as

$$\begin{bmatrix} \Sigma_{11} \\ \Sigma_{22} \\ \Sigma_{33} \end{bmatrix} = \Sigma_{eq}^{vm} \left[ \frac{2}{3} \begin{pmatrix} \cos\theta_L \\ \cos\left(\theta_L - \frac{2\pi}{3}\right) \\ \cos\left(\theta_L + \frac{2\pi}{3}\right) \end{pmatrix} + T \begin{pmatrix} 1 \\ 1 \\ 1 \end{pmatrix} \right] \tag{38}$$

where  $\Sigma_{eq}^{vm}$  is the equivalent von Mises stress,  $\theta_L$  is the deviatoric angle, and  $T$  is the stress triaxiality defined as

$$T = \frac{\Sigma_{kk}}{3\Sigma_{eq}^{vm}} \tag{39}$$

Table 11  
Calculated Lankford coefficients in tension, compression and in tension after pre-compression from the finite element model of the reversed loading tests.

Material	Tension	Compression	In tension after 10% pre-compression	In tension after 20% pre-compression	In tension after 30% pre-compression	In tension after 40% pre-compression
AA6060-O	1.04	0.96	0.93	0.92	0.90	0.94
AA6060-T7	1.67	1.59	1.52	1.48	1.50	1.54
AA6060-T6	1.62	1.59	1.49	1.43	1.43	1.43
AA6082.25-O	0.78	0.76	0.81	0.82	0.81	0.81
AA6082.25-T7	0.91	0.89	0.92	0.93	0.94	0.94
AA6082.25-T6	1.00	1.00	0.99	1.00	1.00	0.99
AA6082.50-O	0.25	0.26	0.30	0.33	0.35	0.38
AA6082.50-T7	0.30	0.29	0.35	0.41	0.44	0.44
AA6082.50-T6	0.52	0.49	0.55	0.57	0.61	0.62

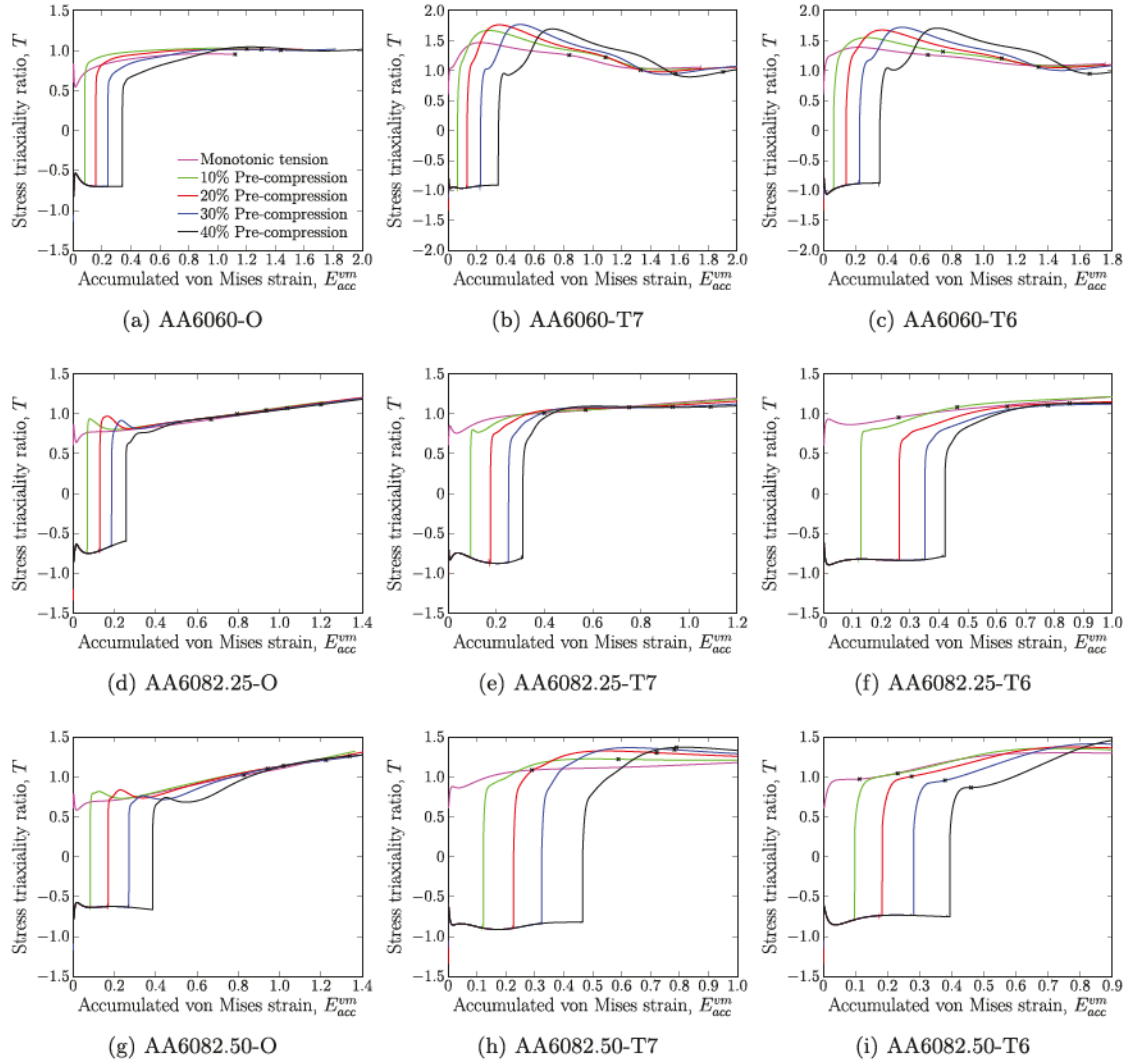


Fig. 13. Stress triaxiality ratio versus accumulated von Mises strain in the centre element from the reversed loading tests. The point corresponding to failure in the experiments is indicated with a cross.

Note that capital letters are now used for stress-related quantities to emphasise that they are the macroscopic quantities of the unit cell model in Section 5.4.

The ratios between the principal stress components are uniquely defined by the stress triaxiality ratio and the deviatoric angle. Thus, the non-proportional loading path that will be enforced on the unit cell model is uniquely defined by the stress triaxiality ratio and the deviatoric angle as functions of the accumulated von Mises strain, which is given by

$$E_{acc}^{vm} = \int_0^t \sqrt{\frac{2}{3} D_{ij}^d D_{ij}^d} dt \quad (40)$$

where  $D_{ij}^d$  is the deviatoric part of the rate of deformation tensor.

The stress triaxiality ratio and the deviatoric angle as functions of the accumulated von Mises strain from the critical element are shown in Fig. 13 and Fig. 14, respectively. The point corresponding to failure in the experiments is indicated with a cross. The plastic anisotropy, strength and work hardening of the materials are seen to have a great impact on the evolution of the triaxiality and the deviatoric angle, and are thus assumed also to affect the ductile failure. Also, the evolution after pre-compression is distinct from monotonic tension for a given material. The curves are different for each pre-compression level, caused by the change in specimen geometry and work hardening of the material. The reader should note here that a deviatoric angle of  $300^\circ$  and  $120^\circ$ , corresponds to a

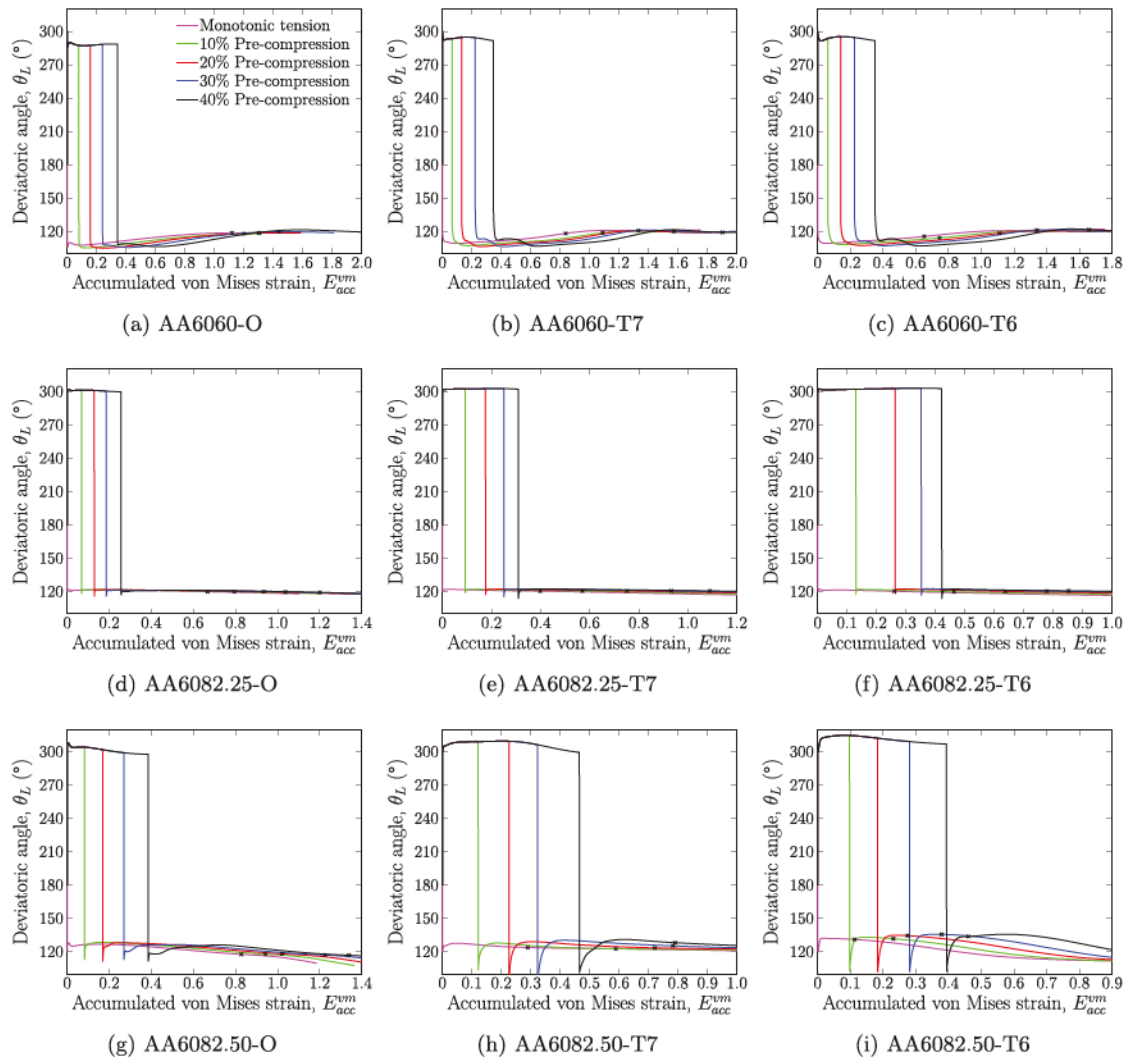


Fig. 14. Deviatoric angle versus accumulated von Mises strain in the centre element from the reversed loading tests. The point corresponding to failure in the experiments is indicated with a cross.

Lode parameter of +1 and -1, respectively.

#### 5.4. Unit cell modelling

To investigate possible fracture mechanisms involved during the reversed loading tests, unit cell simulations are conducted. The non-proportional loading paths extracted from the critical element in Section 5.3 are enforced on the unit cell. The unit cell is modelled with a rigid particle in the centre and a matrix material governed by the phenomenological plasticity model given in Section 4.2.

The material region defined by the critical element in Section 5.3 is now represented by the unit cell model, see Fig. 15a. Due to the orthotropic symmetry of the material and the stress and strain state of the material region, i.e., the orthotropic symmetry axes coincide with the principal directions of stress and strain, only one-eighth of the unit cell is modelled to reduce the computational time. Fig. 15b shows the FE mesh of the unit cell model used for the AA6082.50 alloy in temper O, with approximately 15 000 elements. The particle is modelled as an analytical rigid part in Abaqus/Standard, and is excluded from the figure since it has no mesh. The FE model consists of 5000 to 18 000 linear eight-node elements with selective-reduced integration (C3D8), where the number of elements used depends on the plastic anisotropy and ductility of the material at hand. A thorough mesh convergence study was conducted for each material, but these details are omitted here for brevity.



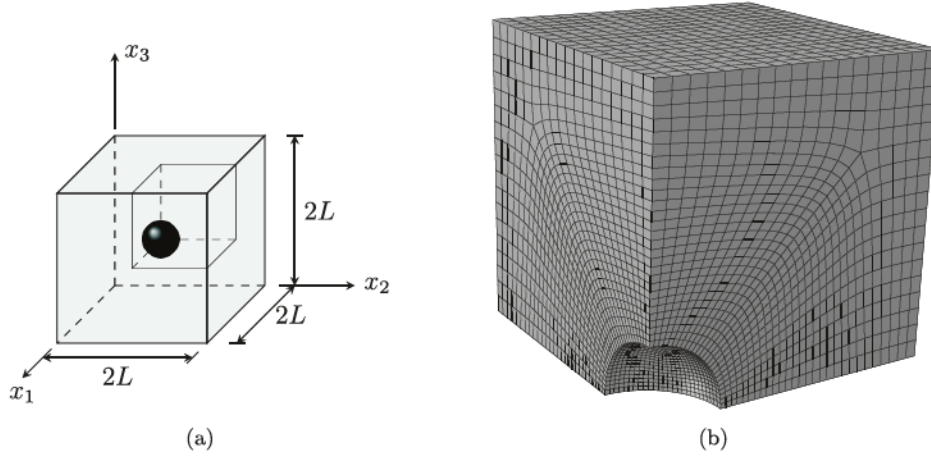


Fig. 15. (a) The unit cell model with dimensions  $2L \times 2L \times 2L$ , and (b) the finite element mesh of the one-eighth model, for the AA6082.50 alloy in temper O.

The dimensions of the unit cell are taken to be equal along the orthotropic symmetry axes, i.e.,  $L_1 = L_2 = L_3 = 2L$ , where  $L$  is the length of the one-eighth model, Fig. 15b. The rigid particle in the centre is spherical, i.e.,  $R_1 = R_2 = R_3 = R$ , with no cohesion to the matrix material. Hence, the unit cell model represents a uniform distribution of equally spaced, pre-nucleated voids with equally sized spherical particles inside, where we neglect any effects of initial void/particle shape, spatial distribution and debonding.

Periodicity is ensured by enforcing the exterior boundaries of the unit cell model to remain straight during deformation. A friction-less surface to surface contact formulation is used for the contact between the void surface and the analytical rigid particle. To impose the non-proportional loading history to the unit cell, non-linear kinematic constraints are used. Following Dæhli et al. (2016b, 2017), based on the work of Faleskog et al. (1998) and Kim et al. (2004) who introduced a technique for proportional loading of the unit cell, the principal stress ratios are introduced as

$$\psi_1 = \frac{\Sigma_{11}}{\Sigma_{\max}}, \quad \psi_2 = \frac{\Sigma_{22}}{\Sigma_{\max}}, \quad \psi_3 = \frac{\Sigma_{33}}{\Sigma_{\max}} \quad (41)$$

where  $\Sigma_{\max} = \max(\Sigma_{11}, \Sigma_{22}, \Sigma_{33})$ . Hence, by Equation (38), the principal stress ratios are uniquely defined by the stress triaxiality ratio and the deviatoric angle as functions of the accumulated von Mises strain, see Figs. 13 and 14.

The multi-point constraint (MPC) subroutine in Abaqus/Standard is used to impose the non-linear kinematic constraints to the unit cell model. The MPC subroutine is supplied with the principal stress ratios that are updated incrementally with the accumulated von Mises strain to enforce the non-proportional loading path to the unit cell model. For further details regarding the non-linear kinematic constraints, the reader is referred to Faleskog et al. (1998); Kim et al. (2004); Barsoum and Faleskog (2007); Cheng and Guo (2007); Vadillo and Fernández-Sáez (2009); Wong and Guo (2015); Liu et al. (2016) and Dæhli et al. (2017).

The initial void/particle volume fraction of the unit cell model is given by

$$f_0 = \frac{V_{v,0}}{V_{uc,0}} = \frac{\pi R^3}{6L^3} \quad (42)$$

where  $V_{v,0}$  and  $V_{uc,0}$  are the initial volume of the void/particle and the unit cell model, respectively. For each material  $f_0$  is calibrated to the monotonic tension test on the diabolo-shaped specimen. Thus,  $f_0$  is adjusted such that the point of coalescence in the unit cell model corresponds to the point of failure in the experimental tests under monotonic tension. This is achieved by making sure that the accumulated von Mises strains in the unit cell model at coalescence and the critical element at failure are equal. In the current work, we define coalescence as the point where the deformation mode of the unit cell model becomes uniaxial (Koplik and Needleman, 1988).

The calibrated value of  $f_0$  will here be bounded from above by the measured particle fractions of the materials. The measured fractions of primary particles are  $f_p = 0.0093$ ,  $f_p = 0.0120$  and  $f_p = 0.0139$  for the AA6060, AA6082.25 and AA6082.50 alloys, respectively (Frodal et al., 2017). The calibrated values of  $f_0$  are given in Table 12.

For the AA6082.25 in T6 temper and the AA6082.50 alloy in T7 and T6 temper,  $f_0$  is restricted by the measured particle fraction. In order for these materials to have coalescence of the unit cell corresponding to failure in the experiments subjected to monotonic tension, the calibrated values of  $f_0$  were 0.0320, 0.0265 and 0.1000 for the AA6082.25 alloy in T6 temper and the AA6082.50 alloy in T7 and T6 tempers, respectively. These high values of  $f_0$  indicate that other failure mechanisms and effects than those included in the unit cell model are present, e.g., effects of the large grain size for the AA6082.50 alloy, which reduce the material ductility (Frodal et al., 2017). Thus, for these materials the point of coalescence in the unit cell model will not coincide with failure in the experiments subjected to monotonic tension.

**Table 12**  
Initial void/particle volume fractions.

Material	$f_0$
AA6060-O	0.0015
AA6060-T7	0.0006
AA6060-T6	0.0022
AA6082.25-O	0.0025
AA6082.25-T7	0.0075
AA6082.25-T6	0.0120
AA6082.50-O	0.0078
AA6082.50-T7	0.0139
AA6082.50-T6	0.0139

For the other materials, a lower value of  $f_0$  than the measured particle fraction was found from the calibration, indicating that only a portion of the particles nucleate voids. By examining Tables 8 and 12 it is apparent that  $f_0$  varies with the strength of the material, i.e., a higher strength typically yields a higher value of  $f_0$ . It is reasonable to assume that this is linked to a higher void nucleation rate when the stress level is increased. For the AA6060 alloy, the calibrated value of  $f_0$  is greater for temper O than for temper T7 even though the latter has the higher strength. This is likely related to the significant differences observed in the stress triaxiality level, Fig. 13, the deviatoric angle, Fig. 14, and the work hardening of the different tempers for this alloy. Note that care should be taken when interpreting the results and microstructural input of the unit cell model, as this model represents complex materials in an idealised way.

### 5.5. Unit cell results

The unit cell model is now subjected to all the non-proportional loading paths given in Figs. 13 and 14, i.e., all pre-deformation levels for all the materials. Fig. 16 shows the response of the unit cell model in terms of the normalised von Mises stress versus the accumulated von Mises strain. The stress-strain curves obtained with the unit cell model are markedly different for the various alloy-temper combinations. However, the stress-strain curves for the three materials in O temper are similar. These materials have the greatest hardening and exhibit work-hardening stagnation after pre-compression.

For some of the materials, the stress level after pre-compression is lower than for monotonic tension, as clearly seen for the AA6060 alloy in T7 temper, due to the permanent softening of the material after load reversal. A softening effect is also observed in compression after approximately 20% pre-deformation for the AA6082.50 alloy in temper T7 and T6. This is caused by the low work hardening in combination with the shape of the yield surface for these materials, as the von Mises stress curves from the critical element of the diabolo-shaped specimen also exhibit the same trend. Thus, this is an effect of the metal plasticity as the stress state moves in stress space along the yield surface of the material.

Fig. 17 shows plots of the initial configuration and the configuration at the onset of void coalescence for the AA6082.25 alloy in temper O. Comparing the deformed configuration at the onset of coalescence after monotonic tension and after 40% pre-compression, it is apparent that the local matrix accumulated plastic strains are higher after pre-compression. Also the shape and size of the void are different after 40% pre-compression compared to monotonic tension.

Fig. 18 depicts the void growth in terms of the normalised void volume fraction versus the accumulated von Mises strain for the unit cell model, where the current void volume fraction is defined as

$$f = \frac{V_{uc} - V_m}{V_{uc}} \quad (43)$$

Here,  $V_{uc}$  is the current volume of the unit cell and  $V_m$  is the current volume of the matrix material, i.e., the sum of all integration point volumes. The void growth is distinct and evolves differently after pre-compression for the different materials. After pre-compression the growth rate tends to be higher than for monotonic tension. This is the case for all the materials except the AA6082.25 alloy in T6 temper, where the void growth rate appears to decrease with increasing pre-compression after load reversal. For the AA6060 alloy in temper T7 and T6, the initial growth rate after load reversal is lower for the unit cell subjected to 40% pre-compression than monotonic tension, but after some straining the growth rate increases beyond that observed for monotonic tension. The critical void volume fraction, i.e., the void volume fraction at coalescence, is seen to increase with increasing pre-compression for all the materials. The point corresponding to coalescence is indicated with a cross in the figures.

The evolution of the void and particularly the void aspect ratios  $R_1/R_2$  and  $R_3/R_2$  can be seen in Fig. 19. The void is prolate/oblate in the  $x_1$ - $x_2$  plane if the ratio  $R_1/R_2$  is less/greater than unity. Similarly, a value of  $R_3/R_2$  less/greater than unity implies a prolate/oblate void in the  $x_2$ - $x_3$  plane. The void aspect ratios have initial values equal to unity, i.e., a spherical void in the unit cell. The shape of the void for the unit cell subjected to monotonic tension evolves in the beginning of the deformation into a prolate spheroid for all the materials. As deformation continues and close to coalescence, the void becomes prolate along one of the material directions and oblate in the other for some of the materials. This is typical for the AA6060 and AA6082.50 alloys in T7 and T6 temper, while the other materials preserve the prolate void shape until coalescence.

During compression the void is seen to separate from the particle for some of the materials in one of the directions normal to the

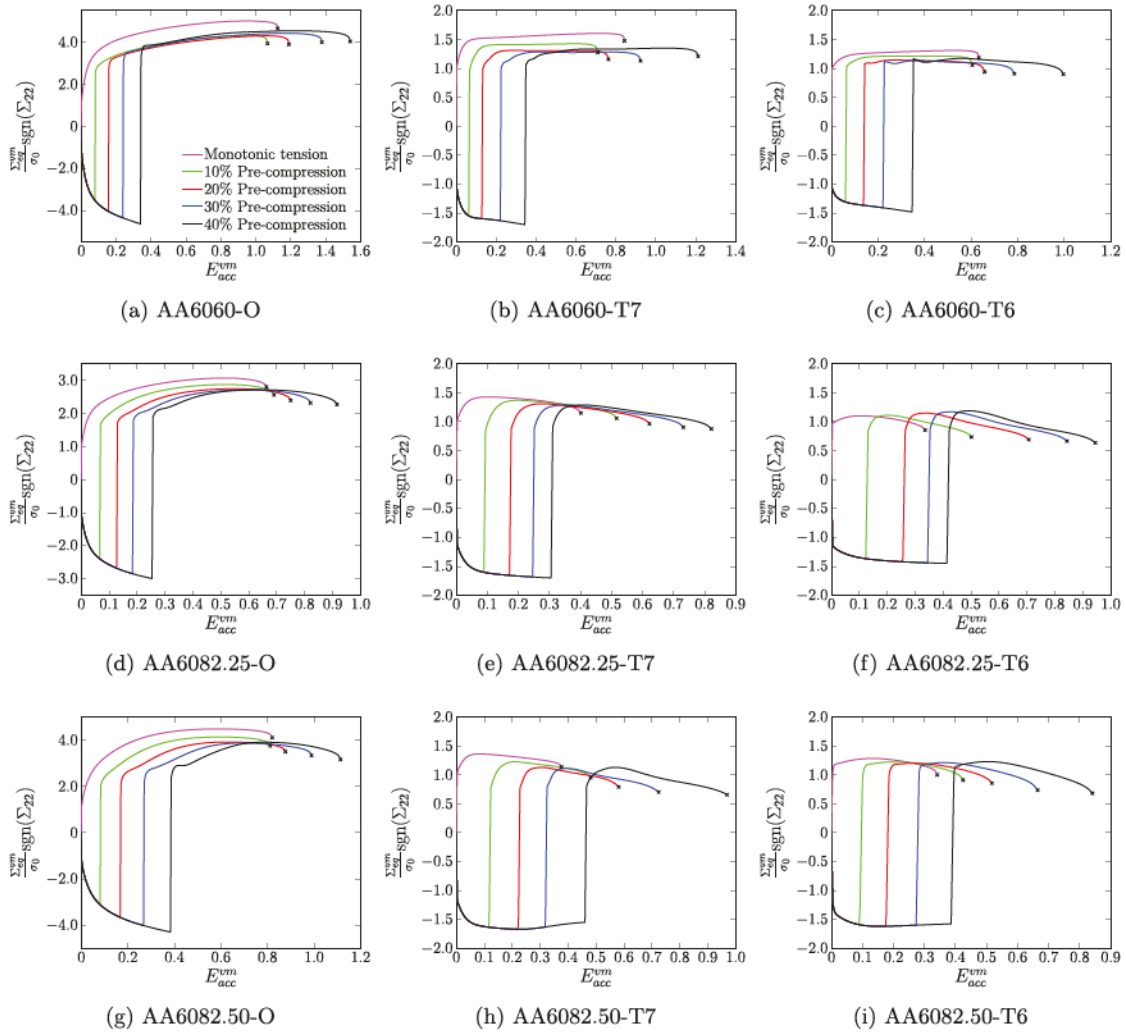


Fig. 16. Macroscopic stress-strain curves in terms of normalised von Mises stress and accumulated von Mises strain for the unit cell model. The point corresponding to coalescence is indicated with a cross.

compression axis (TD). This is observed for nearly all the materials except the AA6082.25 alloy in T7 and T6 temper. The amount of separation and when separation occurs are dependent upon the material. In particular, the AA6060 and AA6082.50 alloys in O temper are seen to exhibit separation from the beginning of the compression phase, as the void aspect ratio is greater than unity. In contrast, the AA6082.50 alloy in T7 and T6 temper only shows sign of separation after approximately 30% compression. After load reversal, the response is also different between alloys and from the response in monotonic tension. The materials exhibiting a prolate void shape along one material axis and an oblate void shape along the other axis for monotonic tension also exhibit this response after load reversal. This transition from a purely prolate shape to a combination of a prolate and oblate shape appears to occur after less deformation in tension after load reversal than for monotonic tension. The AA6060 and AA6082.50 alloys in temper T7 and T6 display a similar evolution of the void aspect ratio. The largest difference being that the oblate shape evolves along the  $x_3$  axis (ND) for the AA6060 alloy, while it evolves along the  $x_1$  axis (ED) for the AA6082.50 alloy. This is related to the anisotropy of these alloys, as the texture components of the Goss and the rotated cube texture for the AA6060 and AA6082.50 alloy, respectively, are related by a 90° rotation about the  $x_2$  axis (TD).

We can now relate the accumulated von Mises strain at coalescence in the unit cell to that of the critical element of the diabolo-shaped specimen. Thus, we can find the logarithmic strain at coalescence, as calculated from the cross-section area of the specimen. Fracture initiation in the specimen predicted by the unit cell can then be compared to the experimental results. Fig. 20 shows the failure strain and the relative failure strain versus pre-compression level for the experiments and the finite element analyses based on the unit cell simulations.



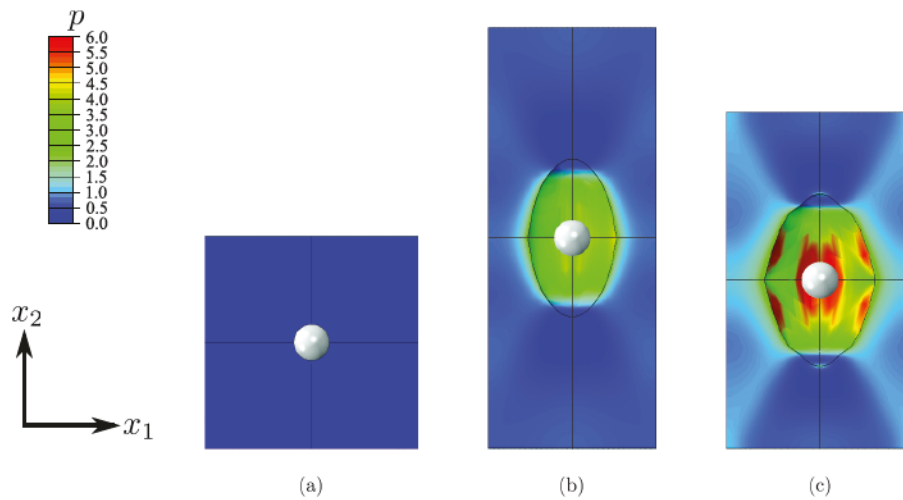


Fig. 17. Initial and deformed configuration plots of the unit cell model with fringes of matrix accumulated plastic strain for the AA6082.25 alloy in temper O, depicted in the  $x_1 - x_2$  (ED-TD) plane. (a) Initial configuration, (b) deformed configuration at onset of void coalescence after monotonic tension and (c) deformed configuration at the onset of void coalescence after 40% pre-compression. In the centre a (white) particle is shown.

Studying the results for the AA6060 alloy in Fig. 20, it is observed that the predicted relative failure strain decreases from 0 to 10% pre-compression for all the tempers, unlike in the experiments. Then, the predicted relative failure strain increases for further pre-compression for the AA6060 alloy in temper O, whereas it decreases until 20% pre-compression before it increases again for the AA6060 alloy in temper T7 and T6. It is clear that the applied unit cell model is incapable of predicting the large increase in the relative failure strain with increasing pre-compression as observed in the experiments. For the AA6060 alloy in temper O, the predictions are closer to the experimental results. This indicates that there are also other mechanisms involved in the fracture process than those included in the unit cell model that are particularly important for the T7 and T6 tempers of this alloy, see Section 6. Considering the results for the AA6082.25 alloy in Fig. 20, it is seen that the simulations predict an almost constant or a small increase in the relative failure strain with increasing pre-compression for all the tempers. A small increase is observed for the AA6082.25 alloy in temper T7 and T6, and the evolution predicted for the T6 temper is approximately equal to that observed in the experiments. The failure strain is higher in monotonic tension in the simulations than in the experiments for this material. This is because the initial void/particle fraction of the unit cell was restricted by the measured particle fraction for the AA6082.25 alloy in T6 temper and the AA6082.50 alloy in T7 and T6 tempers. Again this indicates that there are also other mechanisms involved in the fracture process, as will be discussed in Section 6. For the AA6082.50 alloy in Fig. 20, it is observed that the predicted relative failure strain is approximately constant for all the tempers with increasing pre-compression. This is in agreement with the experiments.

## 6. Discussion

From the experimental results presented in Fig. 2, significant differences are observed in the tensile ductility between the alloys and between the tempers within the same alloy. While the grain structure and anisotropy differ between the alloys, they are similar for the different tempers of the same alloy. In contrast, the strength and work-hardening behaviour depends markedly on the tempering and it transpires that these characteristics are important for the tensile ductility of an alloy. Fig. 3 clearly suggests that the ductility of the materials in monotonic tension depends upon their yield strength. Previous studies indicate that the failure strain decreases linearly with increasing yield strength for aluminium alloys with similar microstructures (Lloyd, 2003; Westermann et al., 2014; Pedersen et al., 2015; Hannard et al., 2016). In Fig. 2, pre-compression is found to either increase the tensile ductility compared to monotonic tension or to leave it approximately constant. In contrast, Bao and Treitler (2004) observed a decrease in the tensile ductility for an AA2024-T351 aluminium alloy with increasing pre-compression, and attributed the reduction in tensile ductility to particle fracture and an increased dislocation density after pre-compression. For an X65 steel, a decrease in tensile ductility has been observed after pre-compression as the failure mechanism may change from ductile to brittle (Kristoffersen et al., 2013).

For the AA6060 alloy in T7 and T6 temper, areas of intercrystalline fracture were observed on the fracture surface (Frodal et al., 2017). After pre-compression, the amount of intercrystalline fracture was found to decrease with increasing pre-compression, leading to an increase in the tensile ductility for these materials. On the other hand, intercrystalline fracture was not observed for the AA6060 alloy in temper O, and the amount of intercrystalline fracture for the AA6082.25 alloy was not seen to change after pre-compression. The precipitation free zones (PFZs) located adjacent to the grain boundaries are assumed to be the cause of intercrystalline fracture in these alloys (Lohne and Naess, 1979). In these weaker zones, the plastic deformation can localise, and crack initiation and growth may occur more easily (Dowling and Martin, 1976; Morgenerer et al., 2008; Khadyko et al., 2016b). A possible reason for the reduced amount of intercrystalline fracture in the AA6060 alloy in temper T7 and T6 after pre-compression is strengthening of the PFZs during

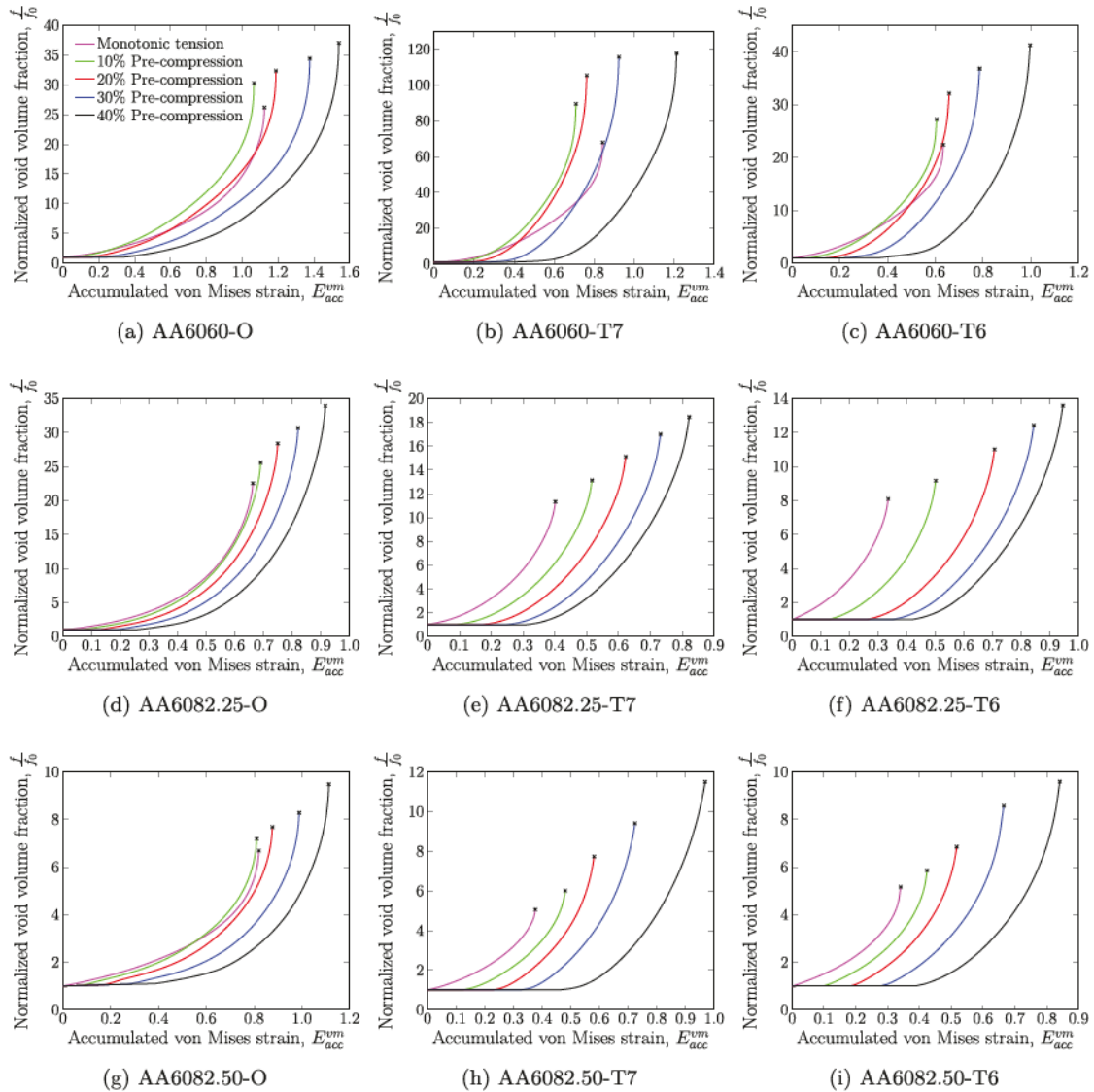


Fig. 18. Normalised void volume fraction versus the accumulated von Mises strain for the unit cell model. The point corresponding to coalescence is indicated with a cross.

compression (Christiansen et al., 2018).

When using polycrystal plasticity calculations to predict the yield surface of a material, the crystal plasticity model and the calibrated yield surface are in most cases not capable of precisely capturing all experimental observations, although good agreement has been obtained when more refined representations of the polycrystal aggregate are used (K. Zhang et al., 2015; H. Zhang et al., 2016). In the present study, the yield surfaces calibrated from crystal plasticity finite element simulations are deemed sufficiently accurate. The plastic anisotropy is generally overestimated for the AA6060 and AA6082.50 alloys, while the response of the AA6082.25 alloy is captured accurately, as seen by comparing Tables 3 and 11. However, this comparison gives only an indication on the performance of the calibrated yield surfaces, as more experimental tests are needed for a complete assessment. Although the main source of anisotropy is the crystallographic texture of a material (Engler and Randle, 2009), the grain morphology may have a noticeable effect (Delannay et al., 2009). The AA6060 alloy investigated here has a recrystallised, equi-axed grain structure and the RVE used in the crystal plasticity finite element simulations represents this morphology with reasonable accuracy. In contrast, the RVE gives a less accurate description of the fibrous grain structure for the AA6082.25 alloy, while the calibrated yield surfaces for this alloy appear to be more accurate based on the limited experimental validation. Using a higher resolution mesh could have resolved



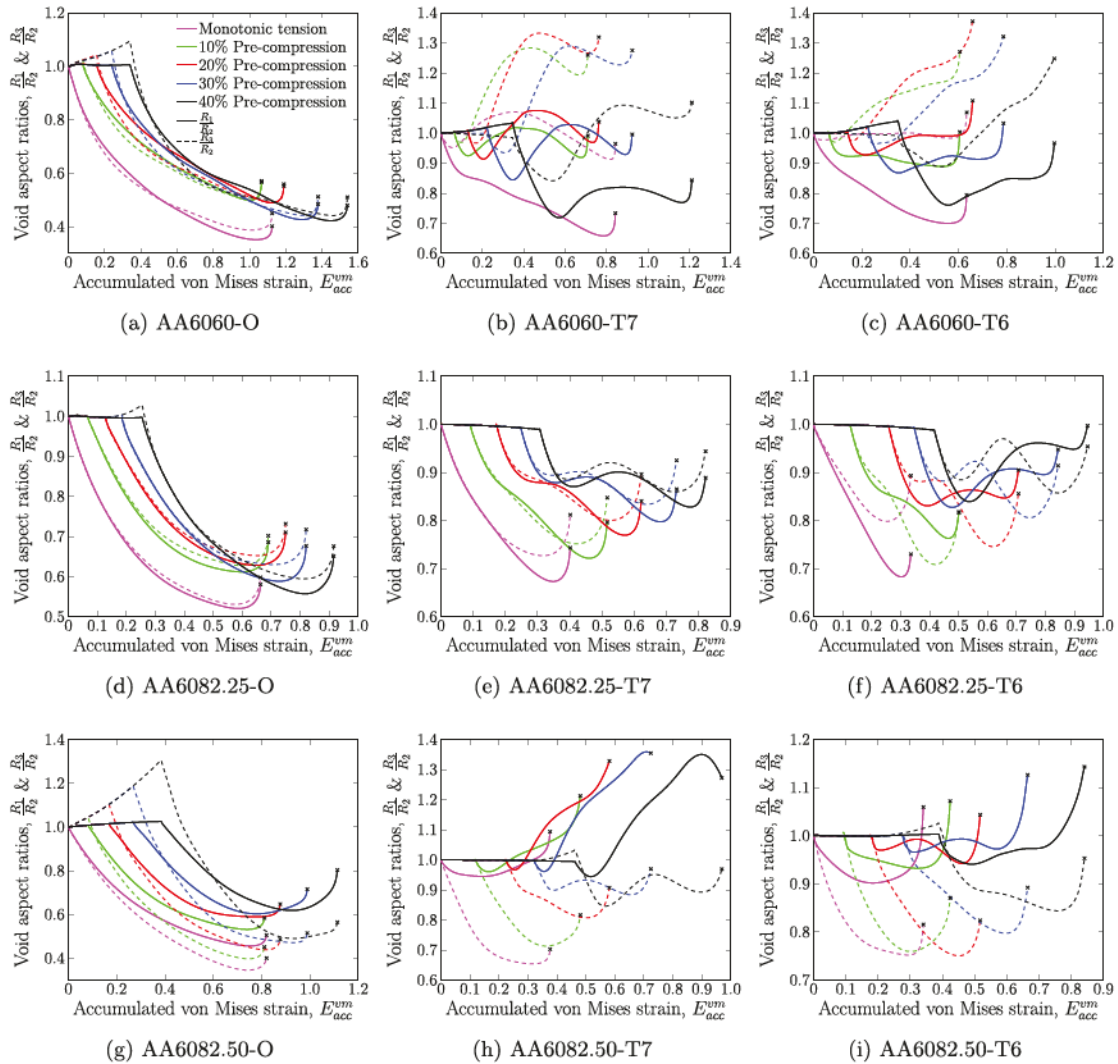


Fig. 19. Void aspect ratios versus the accumulated von Mises strain for the unit cell model. The point corresponding to coalescence is indicated with a cross.

the inter-grain gradients and given a more accurate description of the underlying microstructure, but at the cost of significantly increasing the computational time.

During plastic deformation the crystallographic texture in the deformed area of the specimens will evolve and affect the shape of the yield surface. Preliminary crystal plasticity finite element calculations of the materials suggest that during compression the cube texture component of the AA6060 and AA6082.25 alloys weakens. In contrast, the rotated cube texture of the AA6082.50 alloy strengthens during compression. In the subsequent tension stage, the trends are reversed and the texture of the AA6060 and AA6082.25 strengthens, whereas it weakens for the AA6082.50 alloy. Thus, when the strain is back to zero, the texture is similar to the initial texture of the alloy.

The strain path change model proposed by Mánik et al. (2015) captures the main effects of the strain reversal with reasonable accuracy, cf. Fig. 11. However, the model is incapable of describing the evolution of the work-hardening stagnation with increasing pre-compression observed for the alloys in temper O. It is seen in Fig. 12 that accurate modelling of the strain reversal effects is particularly important for the stress level after load-reversal and close to failure, which would otherwise be highly overestimated. An accurate description of the loading history and the void growth rate depends critically on the hardening behaviour (Lecarme et al., 2011).

In Figs. 13 and 14, differences in the loading histories are observed between the alloys and between the different tempers of the same alloy. This is clearly observed for the AA6060 alloy, as the stress triaxiality is significantly lower in magnitude for the O temper

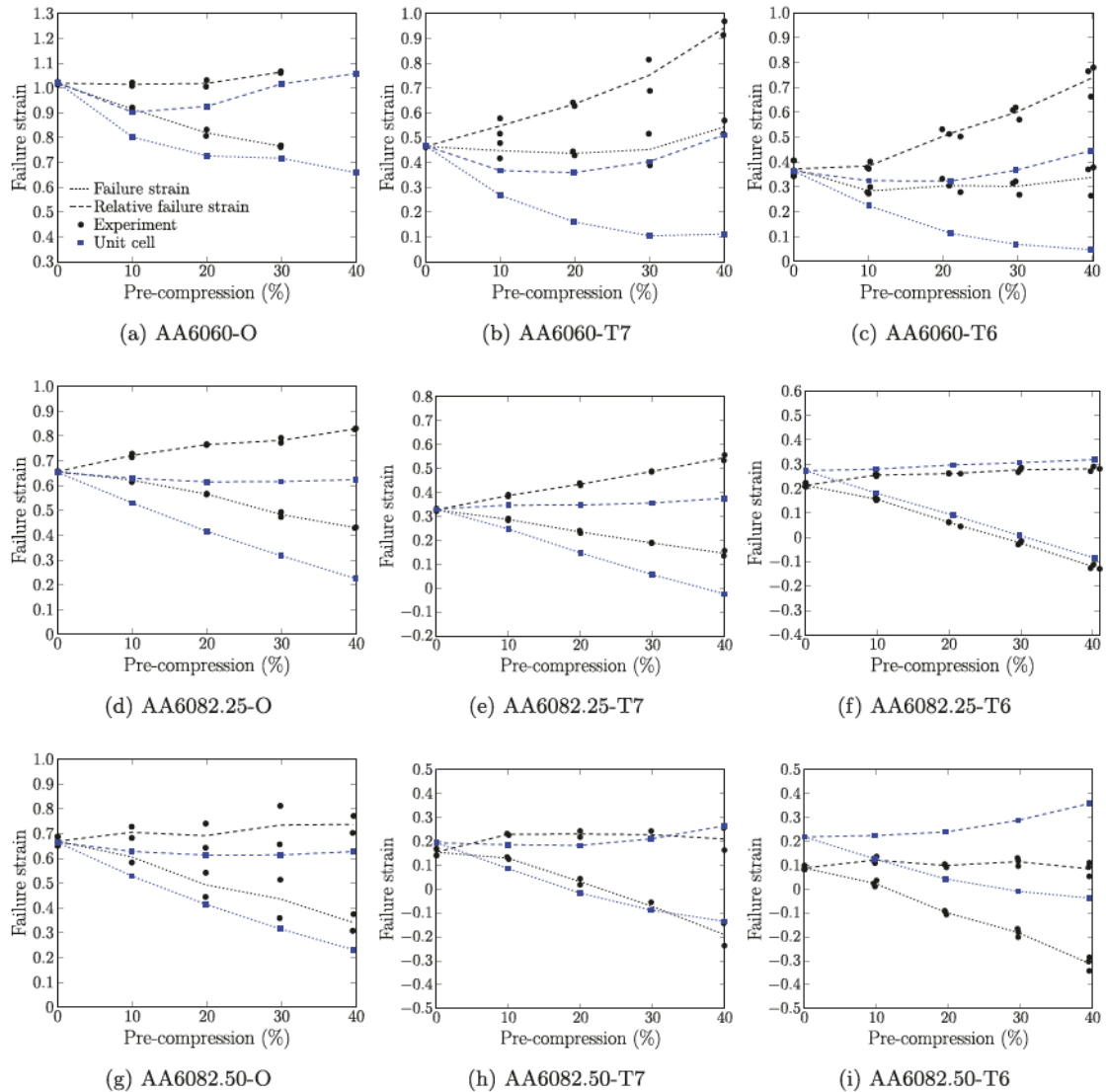


Fig. 20. Failure strain,  $\epsilon_f$ , and relative failure strain,  $\epsilon_r$ , versus pre-compression level from experiments and finite element analyses of unit cells. The relative failure strain is the strain to failure measured with respect to the compressed configuration.

than for the two other tempers. The triaxiality level is also lower for the other alloys in temper O, where the work hardening of the materials is the largest. Thus, the high work hardening of the O tempers reduces the triaxiality level and leads to an increased failure strain in monotonic tension. After pre-compression, the work-hardening stagnation observed for the alloys in temper O leads to plastic localisation and increased triaxiality. In addition, the compression of the specimen leads to a lower curvature of the neck, thus reducing the triaxiality after re-yielding in tension. It is reasonable to expect that the work-hardening stagnation reduces the failure strain, while the lower curvature of the neck after pre-compression has the opposite effect.

The loading history is also affected by the plastic anisotropy. For the stress triaxiality ratio, the effect of anisotropy seems to be as large as the effect of strength and work hardening. In contrast, the effect of anisotropy on the deviatoric angle appears to be even larger than that of the strength and work hardening. Thus, the anisotropy affects the location of yielding in stress space, as observed in the deviatoric plane. The anisotropy also affects the void aspect ratio, see Fig. 19, and for the materials with the highest strength and lowest work hardening the influence is seen to be the largest.

From the results of the unit cell simulations, see Fig. 20, it is found that the unit cell model predicts an almost constant tensile ductility after pre-compression. Albeit the strength, work hardening and anisotropy vary between the different materials, the failure mechanism described by the unit cell model is the same, namely growth and coalescence of a uniform distribution of pre-nucleated

voids with equally sized particles inside. The prediction of an almost constant tensile ductility matches the experimental observations for some of the materials. In addition, other physical mechanisms will play an important role in the ductile failure process. The large grains observed for the AA6082.50 alloy will have an effect on the strain to failure and are critical in the ductile failure process, as the large grains increase the likelihood of intercrystalline fracture and reduce the ductility of the alloy (Frodal et al., 2017).

The unit cell adopted in the present study represents materials consisting of a matrix and pre-nucleated voids with particles inside. In the actual materials, a combination of initial voids, with and without particles inside, and differently shaped particles, with and without cohesion to the matrix material, is observed (Frodal et al., 2017). During the extrusion process, primary particles have been observed to crack and debond from the matrix, leading to a diversity of pre-nucleated voids in the vicinity of particles. When the material is deformed in compression, voids without particles inside, voids in the vicinity of smaller particles and voids between cracked particles may shrink and close any gaps between the matrix and particle and between cracked particles. This delays the void growth in the subsequent tension stage and leads to increased tensile ductility.

Another effect not accounted for in the unit cell model is the influence of nucleation and debonding of the particle from the matrix material. During compression, the cohesion between the particle and matrix may increase or decrease depending on the underlying physical mechanisms present at the interface. The void growth rate in the unit cell model after load reversal was observed to be initially lower than that for monotonic tension for the AA6060 alloy in temper T7 and T6, see Fig. 18. If nucleation was accounted for, e.g., by including a cohesive zone between the matrix and particle, this would possibly reduce the nucleation rate after pre-compression and lead to an increase in the tensile ductility. In contrast, particles can crack during the compression phase and create new free surfaces where voids may grow during the tension stage (Bao and Treitler, 2004). This mechanism is more probable for the alloys with the highest strength, and the result is lower tensile ductility. A combination of all the above-mentioned mechanisms is probably in operation during the ductile failure process, and the importance of a certain mechanism will be different depending on the alloy and temper combination.

## 7. Concluding remarks

The influence of reversed loading on ductile failure for three aluminium alloys heat-treated to three different tempers was studied by conducting reversed loading experiments and finite element unit cell simulations. Diabolo-shaped specimens machined from extruded profiles were subjected to five different pre-compression levels and pulled to fracture in tension. The three aluminium alloys used herein, i.e., AA6060, AA6082.25 and AA6082.50, had different grain structure, grain size and crystallographic texture, and the strength and work hardening varied between the alloys and with the heat treatment. The strain to failure in monotonic tension was seen to decrease with increasing initial yield strength. After pre-compression, the tensile ductility is largely constant or exhibits a small increase for the majority of the materials, but for some materials a larger increase is observed with increasing pre-compression level. Here, tensile ductility is defined as the deformation capacity of a material after the pre-deformation.

The yield surfaces determined by crystal plasticity finite element simulations give a fair representation of the plastic anisotropy. For some of the materials the anisotropy is overestimated, but the adopted hierarchical modelling framework is nonetheless promising. The importance of a plasticity model accounting for transient and permanent effects after a strain reversal is demonstrated, as isotropic hardening or combined isotropic and kinematic hardening is not sufficient to describe the stress-strain curves observed experimentally after the strain reversal.

In general, the unit cell simulations predict a largely constant tensile ductility with pre-compression, and the strength, work hardening and anisotropy of the materials are found to have only a minor influence on the effect of pre-compression, i.e., only a minor effect is observed on the evolution of the relative failure strain with pre-compression. In contrast, the strength, work hardening and anisotropy have a larger influence on the deformation of the unit cell, and on the ductility in monotonic tension. Depending on the alloy and temper, other physical mechanisms that are not accounted for in the unit cell model can have a significant influence on the ductile failure process, e.g., inter-crystalline fracture induced by precipitate free zones along the grain boundaries. Inter-crystalline fracture is difficult to account for in the current unit cell framework and a localisation approach using imperfection analyses could be more appropriate to study this failure mechanism. Thus, further work will focus on simulations of the reversed loading experiments by imperfection analysis.

## Acknowledgements

The financial support of this work from the Centre for Advanced Structural Analysis (CASA), Project No. 237885, Centre for Research-based Innovation (CRI) at the Norwegian University of Science and Technology (NTNU), is gratefully acknowledged.

## References

- Abaqus, 2014. Version 6.14. Dassault Systemès Simulia Corporation. Providence, Rhode Island, USA.
- An, Y., Vegter, H., Carless, L., Lambriks, M., 2011. A novel yield locus description by combining the Taylor and the relaxed Taylor theory for sheet steels. *Int. J. Plast.* 27, 1758–1780.
- Aretz, H., 2008. A simple isotropic-distortional hardening model and its application in elastic–plastic analysis of localized necking in orthotropic sheet metals. *Int. J. Plast.* 24, 1457–1480.
- Aretz, H., Aegerter, J., Engler, O., 2010. Analysis of earing in deep drawn cups. *AIP Conference Proceedings* 1252, 417–424.
- Aretz, H., Barlat, F., 2013. New convex yield functions for orthotropic metal plasticity. *Int. J. Non Lin. Mech.* 51, 97–111.
- Armstrong, P.J., Frederick, C.O., 1966. A Mathematical Representation of the Multiaxial Bauschinger Effect. Technical Report. RD/B/N731, CEBG, Central Electricity



- Generating Board, Berkeley, UK.
- Bai, Y., Wierzbicki, T., 2008. A new model of metal plasticity and fracture with pressure and lode dependence. *Int. J. Plast.* 24, 1071–1096.
- Bao, Y., Treitler, R., 2004. Ductile crack formation on notched Al2024-T351 bars under compression-tension loading. *Mater. Sci. Eng., A* 384, 385–394.
- Barlat, F., Aretz, H., Yoon, J.W., Karabin, M.E., Brem, J.C., Dick, R.E., 2005. Linear transformation-based anisotropic yield functions. *Int. J. Plast.* 21, 1009–1039.
- Barlat, F., Grácio, J.J., Lee, M.G., Rauch, E.F., Vincze, G., 2011. An alternative to kinematic hardening in classical plasticity. *Int. J. Plast.* 27, 1309–1327.
- Barlat, F., Ha, J., Grácio, J.J., Lee, M.G., Rauch, E.F., Vincze, G., 2013. Extension of homogeneous anisotropic hardening model to cross-loading with latent effects. *Int. J. Plast.* 46, 130–142.
- Barlat, F., Lege, D.J., Brem, J.C., 1991. A six-component yield function for anisotropic materials. *Int. J. Plast.* 7, 693–712.
- Barlat, F., Vincze, G., Grácio, J.J., Lee, M.G., Rauch, E.F., Tomé, C.N., 2014. Enhancements of homogenous anisotropic hardening model and application to mild and dual-phase steels. *Int. J. Plast.* 58, 201–218.
- Barsoum, I., Faleskog, J., 2007. Rupture mechanisms in combined tension and shear—micromechanics. *Int. J. Solid Struct.* 44, 5481–5498.
- Basu, S., Benzerga, A.A., 2015. On the path-dependence of the fracture locus in ductile materials: Experiments. *Int. J. Solid Struct.* 71, 79–90.
- Bauschinger, J., 1881. Changes of the elastic limit and the modulus of elasticity on various metals. *Zivilingenieur* 27, 289–348.
- Benzerga, A.A., Besson, J., 2001. Plastic potentials for anisotropic porous solids. *Eur. J. Mech. A Solid* 20, 397–434.
- Benzerga, A.A., Surovik, D., Keralavarma, S.M., 2012. On the path-dependence of the fracture locus in ductile materials – analysis. *Int. J. Plast.* 37, 157–170.
- Bishop, J.F.W., Hill, R., 1951a. A theory of the plastic distortion of a polycrystalline aggregate under combined stresses. *Phil. Mag.* 42, 414–427.
- Bishop, J.F.W., Hill, R., 1951b. A theoretical derivation of the plastic properties of a polycrystalline face-centred metal. *Phil. Mag.* 42, 1298–1307.
- Bron, F., Besson, J., 2004. A yield function for anisotropic materials application to aluminum alloys. *Int. J. Plast.* 20, 937–963.
- Bulatov, V.V., Richmond, O., Glazov, M.V., 1999. An atomistic dislocation mechanism of pressure-dependent plastic flow in aluminum. *Acta Mater.* 47, 3507–3514.
- Cazacu, O., Barlat, F., 2001. Generalization of drucker's yield criterion to orthotropy. *Math. Mech. Solid* 6, 613–630.
- Cheng, L., Guo, T.F., 2007. Void interaction and coalescence in polymeric materials. *Int. J. Solid Struct.* 44, 1787–1808.
- Chien, W.Y., Pan, J., Tang, S.C., 2001. Modified anisotropic guron yield criterion for porous ductile sheet metals. *J. Eng. Mater. Technol.* 123, 409–416.
- Christiansen, E., Marioara, C.D., Marthinsen, K., Hopperstad, O.S., Holmestad, R., 2018. Lattice rotations in precipitate free zones in an Al-Mg-Si alloy. *Mater. Char.* 144, 522–531.
- Delannay, L., Melchior, M.A., Signorelli, J.W., Remacle, J.F., Kuwabara, T., 2009. Influence of grain shape on the planar anisotropy of rolled steel sheets – evaluation of three models. *Comput. Mater. Sci.* 45, 739–743.
- Dæhli, L.E.B., Børvik, T., Hopperstad, O.S., 2016a. Influence of loading path on ductile fracture of tensile specimens made from aluminium alloys. *Int. J. Solid Struct.* 88, 17–34.
- Dæhli, L.E.B., Faleskog, J., Børvik, T., Hopperstad, O.S., 2016b. Unit cell simulations and porous plasticity modelling for recrystallization textures in aluminium alloys. *Procedia Structural Integrity* 2, 2535–2542 21st European Conference on Fracture, ECF21, 20–24 June 2016, Catania, Italy.
- Dæhli, L.E.B., Faleskog, J., Børvik, T., Hopperstad, O.S., 2017. Unit cell simulations and porous plasticity modelling for strongly anisotropic fcc metals. *Eur. J. Mech. A Solid* 65, 360–383.
- Dowling, J.M., Martin, J.W., 1976. The influence of Mn additions on the deformation behaviour of an Al-Mg-Si alloy. *Acta Metall.* 24, 1147–1153.
- Drucker, D.C., Prager, W., 1952. Soil mechanics and plastic analysis or limit design. *Q. Appl. Math.* 10, 157–165.
- Eisenlohr, P., Diehl, M., Lebensohn, R.A., Roters, F., 2013. A spectral method solution to crystal elasto-viscoplasticity at finite strains. *Int. J. Plast.* 46, 37–53.
- Engler, O., Randle, V., 2009. Introduction to Texture Analysis: Macrotexture, Microtexture, and Orientation Mapping, second ed. CRC press, Taylor & Francis Group.
- Faleskog, J., Gao, X., Shih, C.F., 1998. Cell model for nonlinear fracture analysis – I. Micromechanics calibration. *Int. J. Fract.* 89, 355–373.
- Fourmeau, M., Børvik, T., Benallal, A., Lademo, O.G., Hopperstad, O.S., 2011. On the plastic anisotropy of an aluminium alloy and its influence on constrained multiaxial flow. *Int. J. Plast.* 27, 2005–2025.
- François, M., 2001. A plasticity model with yield surface distortion for non proportional loading. *Int. J. Plast.* 17, 703–717.
- Frederick, C.O., Armstrong, P.J., 2007. A mathematical representation of the multiaxial bauschinger effect. *Mater. A. T. High. Temp.* 24, 1–26.
- Freund, M., Shutov, A.V., Ihlemann, J., 2012. Simulation of distortional hardening by generalizing a uniaxial model of finite strain viscoplasticity. *Int. J. Plast.* 36, 113–129.
- Frodal, B.H., Pedersen, K.O., Børvik, T., Hopperstad, O.S., 2017. Influence of pre-compression on the ductility of AA6xxx aluminium alloys. *Int. J. Fract.* 206, 131–149.
- Gawad, J., Banabic, D., Bael, A.V., Comsa, D.S., Gologanu, M., Eyckens, P., Houtte, P.V., Roose, D., 2015. An evolving plane stress yield criterion based on crystal plasticity virtual experiments. *Int. J. Plast.* 75, 141–169.
- Groeber, M.A., Jackson, M.A., 2014. DREAM.3D: a digital representation environment for the analysis of microstructure in 3D. *Integrating Materials and Manufacturing Innovation* 3, 5.
- Grytten, F., Holmedal, B., Hopperstad, O.S., Børvik, T., 2008. Evaluation of identification methods for Yld2004-18p. *Int. J. Plast.* 24, 2248–2277.
- Ha, J., Lee, M.G., Barlat, F., 2013. Strain hardening response and modeling of EDDQ and DP780 steel sheet under non-linear strain path. *Mech. Mater.* 64, 11–26.
- Hannard, F., Pardoën, T., Maire, E., Bourlot, C.L., Mokso, R., Simar, A., 2016. Characterization and micromechanical modelling of microstructural heterogeneity effects on ductile fracture of 6xxx aluminium alloys. *Acta Mater.* 103, 558–572.
- Hasegawa, T., Yakou, T., Kocks, U.F., 1986. Forward and reverse rearrangements of dislocations in tangled walls. *Mater. Sci. Eng.* 81, 189–199.
- Hershey, A.V., 1954. The plasticity of an isotropic aggregate of anisotropic face-centered cubic crystals. *J. Appl. Mech.* 21, 241–249.
- Hill, R., 1948. A theory of the yielding and plastic flow of anisotropic metals. In: *Proceedings of the Royal Society of London A: Mathematical, Physical and Engineering Sciences*, vol. 193. pp. 281–297.
- Holmedal, B., Houtte, P.V., An, Y., 2008. A crystal plasticity model for strain-path changes in metals. *Int. J. Plast.* 24, 1360–1379.
- Holmen, J.K., Frodal, B.H., Hopperstad, O.S., Børvik, T., 2017. Strength differential effect in age hardened aluminum alloys. *Int. J. Plast.* 99, 144–161.
- Hosford, W.F., 1972. A generalized isotropic yield criterion. *J. Appl. Mech.* 39, 607–609.
- Hutchinson, J.W., 1976. Bounds and self-consistent estimates for creep of polycrystalline materials. In: *Proceedings of the Royal Society of London A: Mathematical, Physical and Engineering Sciences*, vol. 348. pp. 101–127.
- Iadicola, M.A., Foecke, T., Banovic, S.W., 2008. Experimental observations of evolving yield loci in biaxially strained AA5754-O. *Int. J. Plast.* 24, 2084–2101.
- Inal, K., Mishra, R.K., Cazacu, O., 2010. Forming simulation of aluminum sheets using an anisotropic yield function coupled with crystal plasticity theory. *Int. J. Solid Struct.* 47, 2223–2233.
- Kanjarla, A.K., Van Houtte, P., Delannay, L., 2010. Assessment of plastic heterogeneity in grain interaction models using crystal plasticity finite element method. *Int. J. Plast.* 26, 1220–1233.
- Karafilis, A.P., Boyce, M.C., 1993. A general anisotropic yield criterion using bounds and a transformation weighting tensor. *J. Mech. Phys. Solid* 41, 1859–1886.
- Keralavarma, S.M., Benzerga, A.A., 2010. A constitutive model for plastically anisotropic solids with non-spherical voids. *J. Mech. Phys. Solid* 58, 874–901.
- Keralavarma, S.M., Hoelscher, S., Benzerga, A.A., 2011. Void growth and coalescence in anisotropic plastic solids. *Int. J. Solid Struct.* 48, 1696–1710.
- Khadyko, M., 2018. Personal Communication. Structural Impact Laboratory (SIMLab), Norwegian University of Science and Technology (NTNU).
- Khadyko, M., Dumoulin, S., Børvik, T., Hopperstad, O.S., 2014. An experimental-numerical method to determine the work-hardening of anisotropic ductile materials at large strains. *Int. J. Mech. Sci.* 88, 25–36.
- Khadyko, M., Dumoulin, S., Børvik, T., Hopperstad, O.S., 2015. Simulation of large-strain behaviour of aluminium alloy under tensile loading using anisotropic plasticity models. *Comput. Struct.* 157, 60–75.
- Khadyko, M., Dumoulin, S., Cailletaud, G., Hopperstad, O.S., 2016a. Latent hardening and plastic anisotropy evolution in AA6060 aluminium alloy. *Int. J. Plast.* 76, 51–74.
- Khadyko, M., Marioara, C.D., Ringdalen, I.G., Dumoulin, S., Hopperstad, O.S., 2016b. Deformation and strain localization in polycrystals with plastically heterogeneous grains. *Int. J. Plast.* 86, 128–150.
- Khan, A.S., Huang, S., 1995. *Continuum Theory of Plasticity*. John Wiley & Sons.

- Khan, A.S., Kazmi, R., Pandey, A., Stoughton, T., 2009. Evolution of subsequent yield surfaces and elastic constants with finite plastic deformation. Part-I: a very low work hardening aluminum alloy (Al6061-T6511). *Int. J. Plast.* 25, 1611–1625.
- Khan, A.S., Pandey, A., Stoughton, T., 2010a. Evolution of subsequent yield surfaces and elastic constants with finite plastic deformation. Part II: a very high work hardening aluminum alloy (annealed 1100 Al). *Int. J. Plast.* 26, 1421–1431.
- Khan, A.S., Pandey, A., Stoughton, T., 2010b. Evolution of subsequent yield surfaces and elastic constants with finite plastic deformation. Part III: yield surface in tension–tension stress space (Al 6061–T 6511 and annealed 1100 Al). *Int. J. Plast.* 26, 1432–1441.
- Kim, J., Gao, X., Srivatsan, T.S., 2004. Modeling of void growth in ductile solids: effects of stress triaxiality and initial porosity. *Eng. Fract. Mech.* 71, 379–400.
- Kitayama, K., Tomé, C.N., Rauch, E.F., Grácio, J.J., Barlat, F., 2013. A crystallographic dislocation model for describing hardening of polycrystals during strain path changes. application to low carbon steels. *Int. J. Plast.* 46, 54–69.
- Kocks, U.F., Chandra, H., 1982. Slip geometry in partially constrained deformation. *Acta Metall.* 30, 695–709.
- Kohar, C.P., Bassani, J.L., Brahma, A., Muhammad, W., Mishra, R.K., Inal, K., 2017. A new multi-scale framework to incorporate microstructure evolution in phenomenological plasticity: theory, explicit finite element formulation, implementation and validation. *Int. J. Plast.* <https://doi.org/10.1016/j.ijplas.2017.08.006>.
- Koplik, J., Needleman, A., 1988. Void growth and coalescence in porous plastic solids. *Int. J. Solid Struct.* 24, 835–853.
- Kristoffersen, M., Børvik, T., Hopperstad, O.S., 2016. Using unit cell simulations to investigate fracture due to compression–tension loading. *Eng. Fract. Mech.* 162, 269–289.
- Kristoffersen, M., Børvik, T., Westermann, I., Langseth, M., Hopperstad, O.S., 2013. Impact against X65 steel pipes – an experimental investigation. *Int. J. Solid Struct.* 50, 3430–3445.
- Lebensohn, R.A., Kanjarla, A.K., Eisenlohr, P., 2012. An elasto-viscoplastic formulation based on fast fourier transforms for the prediction of micromechanical fields in polycrystalline materials. *Int. J. Plast.* 32–33, 59–69.
- Lebensohn, R.A., Tomé, C.N., 1993. A self-consistent anisotropic approach for the simulation of plastic deformation and texture development of polycrystals: application to zirconium alloys. *Acta Metall. Mater.* 41, 2611–2624.
- Lebensohn, R.A., Tomé, C.N., 1994. A self-consistent viscoplastic model: prediction of rolling textures of anisotropic polycrystals. *Mater. Sci. Eng., A* 175, 71–82.
- Lecarme, L., Tekoğlu, C., Pardo, T., 2011. Void growth and coalescence in ductile solids with stage III and stage IV strain hardening. *Int. J. Plast.* 27, 1203–1223.
- Lee, E.H., Stoughton, T.B., Yoon, J.W., 2017. A yield criterion through coupling of quadratic and non-quadratic functions for anisotropic hardening with non-associated flow rule. *Int. J. Plast.* 99, 120–143.
- Lee, J., Kim, D., Lee, Y.S., Bong, H.J., Barlat, F., Lee, M.G., 2015. Stress update algorithm for enhanced homogeneous anisotropic hardening model. *Comput. Methods Appl. Mech. Eng.* 286, 63–86.
- Legarth, B.N., Tvergaard, V., 2018. Effects of plastic anisotropy and void shape on full three-dimensional void growth. *J. Appl. Mech.* 85 051007.
- Li, F., Bate, P.S., 1991. Strain path change effects in cube textured aluminium sheet. *Acta Metall. Mater.* 39, 2639–2650.
- Liu, Z.G., Wong, W.H., Guo, T.F., 2016. Void behaviors from low to high triaxialities: transition from void collapse to void coalescence. *Int. J. Plast.* 84, 183–202.
- Lloyd, D.J., 2003. The scaling of the tensile ductile fracture strain with yield strength in Al alloys. *Scripta Mater.* 48, 341–344.
- Lohne, O., Naess, O.J., 1979. The effect of dispersoids and grain size on mechanical properties of AlMgSi alloys. In: Haasen, P., Gerold, V., Kosterz, G. (Eds.), *Strength of Metals and Alloys*. Pergamon, pp. 781–788.
- Lou, Y., Yoon, J.W., 2018. Anisotropic yield function based on stress invariants for BCC and FCC metals and its extension to ductile fracture criterion. *Int. J. Plast.* 101, 125–155.
- Luo, M., Rousselier, G., 2014. Modeling of large strain multi-axial deformation of anisotropic metal sheets with strength-differential effect using a reduced texture methodology. *Int. J. Plast.* 53, 66–89.
- Mánik, T., Holmedal, B., Hopperstad, O.S., 2015. Strain-path change induced transients in flow stress, work hardening and r-values in aluminum. *Int. J. Plast.* 69, 1–20.
- Marcadet, S.J., Mohr, D., 2015. Effect of compression–tension loading reversal on the strain to fracture of dual phase steel sheets. *Int. J. Plast.* 72, 21–43.
- Molinari, A., Canova, G.R., Ahzi, S., 1987. A self consistent approach of the large deformation polycrystal viscoplasticity. *Acta Metall.* 35, 2983–2994.
- Morgeneyer, T.F., Starink, M.J., Wang, S.C., Sinclair, I., 2008. Quench sensitivity of toughness in an Al alloy: direct observation and analysis of failure initiation at the precipitate-free zone. *Acta Mater.* 56, 2872–2884.
- Pandey, A., Khan, A.S., Kim, E.Y., Choi, S.H., Gnäupel-Herold, T., 2013. Experimental and numerical investigations of yield surface, texture, and deformation mechanisms in AA5754 over low to high temperatures and strain rates. *Int. J. Plast.* 41, 165–188.
- Papasidero, J., Doquet, V., Mohr, D., 2015. Ductile fracture of aluminum 2024-T351 under proportional and non-proportional multi-axial loading: Bao–Wierzbicki results revisited. *Int. J. Solid Struct.* 69, 459–474.
- Pedersen, K.O., Westermann, I., Furu, T., Børvik, T., Hopperstad, O.S., 2015. Influence of microstructure on work-hardening and ductile fracture of aluminium alloys. *Mater. Des.* 70, 31–44.
- Plunkett, B., Cazacu, O., Lebensohn, R.A., Barlat, F., 2007. Elastic-viscoplastic anisotropic modeling of textured metals and validation using the Taylor cylinder impact test. *Int. J. Plast.* 23, 1001–1021.
- Qin, J., Holmedal, B., Hopperstad, O.S., 2018. A combined isotropic, kinematic and distortional hardening model for aluminum and steels under complex strain-path changes. *Int. J. Plast.* 101, 156–169.
- Qin, J., Holmedal, B., Zhang, K., Hopperstad, O.S., 2017. Modeling strain-path changes in aluminum and steel. *Int. J. Solid Struct.* 117, 123–136.
- Raabe, D., Roters, F., 2004. Using texture components in crystal plasticity finite element simulations. *Int. J. Plast.* 20, 339–361.
- Saai, A., Dumoulin, S., Hopperstad, O.S., Lademo, O.G., 2013. Simulation of yield surfaces for aluminium sheets with rolling and recrystallization textures. *Comput. Mater. Sci.* 67, 424–433.
- Scipy, 2017. **Optimization and Root Finding, Scipy Version 1.0.0.** <https://docs.scipy.org/doc/scipy/reference/optimize.html>.
- Shutov, A.V., Ihlemann, J., 2012. A viscoplasticity model with an enhanced control of the yield surface distortion. *Int. J. Plast.* 39, 152–167.
- Shutov, A.V., Panhans, S., Kreifsig, R., 2011. A phenomenological model of finite strain viscoplasticity with distortional hardening. *ZAMM - Journal of Applied Mathematics and Mechanics/Z. Angew. Math. Mech.* 91, 653–680.
- Spitzig, W.A., Richmond, O., 1984. The effect of pressure on the flow stress of metals. *Acta Metall.* 32, 457–463.
- Stander, N., Roux, W., Basudhar, A., Eggleston, T., Goel, T., Craig, K., 2015. *LS-OPT User's Manual*. Livermore Software Technology Corporation, Livermore, California, USA.
- Steglich, D., Wafai, H., Besson, J., 2010. Interaction between anisotropic plastic deformation and damage evolution in Al 2198 sheet metal. *Eng. Fract. Mech.* 77, 3501–3518.
- Stout, M.G., Hecker, S.S., Bourcier, R., 1983. An evaluation of anisotropic effective stress-strain criteria for the biaxial yield and flow of 2024 aluminum tubes. *J. Eng. Mater. Technol.* 105, 242–249.
- Taylor, G.I., 1938. Plastic strain in metals. *J. Inst. Met.* 62, 307–324.
- Teodosiu, C., Hu, Z., 1995. Evolution of the intragranular microstructure at moderate and large strains: modelling and computational significance. Simulation of Materials Processing: theory, Methods and Applications. In: *Proceedings of the 5th International Conference on Numerical Methods in Industrial Forming Processes (NUMIFORM '95)*, vol. 5, pp. 173–182.
- Vadillo, G., Fernández-Sáez, J., 2009. An analysis of Gurson model with parameters dependent on triaxiality based on unitary cells. *Eur. J. Mech. A Solid.* 28, 417–427.
- Van Den Boogaard, T., Havinga, J., Belin, A., Barlat, F., 2016. Parameter reduction for the Yld2004-18p yield criterion. *Int. J. Material Form.* 9, 175–178.
- Van Houtte, P., 1982. On the equivalence of the relaxed Taylor theory and the bishop-hill theory for partially constrained plastic deformation of crystals. *Mater. Sci. Eng.* 55, 69–77.
- Van Houtte, P., 1988. A comprehensive mathematical formulation of an extended Taylor–Bishop–Hill model featuring relaxed constraints, the Renouard–Wintemberger theory and a strain rate sensitivity model. *Texture, Stress, Microstruct.* 8, 313–350.
- Van Houtte, P., Delannay, L., Kalidindi, S.R., 2002. Comparison of two grain interaction models for polycrystal plasticity and deformation texture prediction. *Int. J. Plast.* 18, 359–377.



- Voce, E., 1948. The relationship between stress and strain for homogeneous deformation. *J. Inst. Met.* 74, 537–562.
- Wang, D.A., Pan, J., Liu, S.D., 2004. An anisotropic guron yield criterion for porous ductile sheet metals with planar anisotropy. *Int. J. Damage Mech.* 13, 7–33.
- Wen, W., Borodachenkova, M., Tomé, C.N., Vincze, G., Rauch, E.F., Barlat, F., Grácio, J.J., 2015. Mechanical behavior of Mg subjected to strain path changes: experiments and modeling. *Int. J. Plast.* 73, 171–183.
- Wen, W., Borodachenkova, M., Tomé, C.N., Vincze, G., Rauch, E.F., Barlat, F., Grácio, J.J., 2016. Mechanical behavior of low carbon steel subjected to strain path changes: experiments and modeling. *Acta Mater.* 111, 305–314.
- Westermann, I., Pedersen, K.O., Furu, T., Børvik, T., Hopperstad, O.S., 2014. Effects of particles and solutes on strength, work-hardening and ductile fracture of aluminium alloys. *Mech. Mater.* 79, 58–72.
- Wong, W.H., Guo, T.F., 2015. On the energetics of tensile and shear void coalescences. *J. Mech. Phys. Solid.* 82, 259–286.
- Woodthorpe, J., Pearce, R., 1970. The anomalous behaviour of aluminium sheet under balanced biaxial tension. *Int. J. Mech. Sci.* 12, 341–347.
- Yoshida, F., Hamasaki, H., Uemori, T., 2013. A user-friendly 3D yield function to describe anisotropy of steel sheets. *Int. J. Plast.* 45, 119–139.
- Zhang, H., Diehl, M., Roters, F., Raabe, D., 2016. A virtual laboratory using high resolution crystal plasticity simulations to determine the initial yield surface for sheet metal forming operations. *Int. J. Plast.* 80, 111–138.
- Zhang, K., Holmedal, B., Hopperstad, O.S., Dumoulin, S., Gawad, J., Van Bael, A., Van Houtte, P., 2015. Multi-level modelling of mechanical anisotropy of commercial pure aluminium plate: crystal plasticity models, advanced yield functions and parameter identification. *Int. J. Plast.* 66, 3–30.
- Zhang, K., Hopperstad, O.S., Holmedal, B., Dumoulin, S., 2014. A robust and efficient substepping scheme for the explicit numerical integration of a rate-dependent crystal plasticity model. *Int. J. Numer. Methods Eng.* 99, 239–262.
- Zhang, Z.L., Skallerud, B., 2010. Void coalescence with and without prestrain history. *Int. J. Damage Mech.* 19, 153–174.

# PART 3

Bjørn Håkon Frodal, David Morin, Tore Børvik,  
Odd Sture Hopperstad

## **On the effect of plastic anisotropy, strength and work hardening on the tensile ductility of aluminium alloys**

Submitted for possible journal publication.

© 2019. This manuscript version is made available under the CC-BY-NC-ND 4.0  
license <http://creativecommons.org/licenses/by-nc-nd/4.0/>

# On the effect of plastic anisotropy, strength and work hardening on the tensile ductility of aluminium alloys

Bjørn Håkon Frodal<sup>a,b,\*</sup>, David Morin<sup>a,b</sup>, Tore Børvik<sup>a,b</sup>, Odd Sture Hopperstad<sup>a,b</sup>

<sup>a</sup>*Structural Impact Laboratory (SIMLab), Department of Structural Engineering, Norwegian University of Science and Technology (NTNU), NO-7491, Trondheim, Norway*

<sup>b</sup>*Centre for Advanced Structural Analysis (CASA), NTNU, NO-7491, Trondheim, Norway*

---

## Abstract

The influence of plastic anisotropy, strength and work hardening on ductile failure is studied by nonlinear finite element simulations and strain localization analyses of tensile tests in different material orientations. Three aluminium alloys with different grain structure and crystallographic texture, heat-treated to three conditions giving rise to different strength and work-hardening behaviours, are considered. The anisotropic yield surfaces of the alloys, obtained by the crystal plasticity finite element method, are used in the numerical simulations of ductile failure in the tensile tests. In addition, a yield surface for an isotropic material is included for comparison. These yield surfaces are combined with three flow stress curves representative for the different heat-treatments, resulting in a range of relevant model materials with different plastic anisotropy, strength and work hardening used in the numerical investigations. Finite element simulations of tensile tests in seven in-plane directions are carried out, i.e., 0°, 15°, 30°, 45°, 60°, 75° and 90° to the reference direction, and the non-proportional loading histories are used in the subsequent strain localization analyses. Plastic anisotropy is found to have a marked influence on the tensile ductility and to induce fracture anisotropy. The shape and extension of the regions of localized plastic flow in the finite element simulations vary with tensile direction for the anisotropic materials. In agreement with previous experimental evidence, the strain localization analyses predict a variation of the failure strain with tensile direction that appears to correlate with the variation of the Lankford coefficient, indicating that the fracture anisotropy is closely linked to the plastic anisotropy. The strain localization analyses predict a higher ductility for materials with lower strength and higher work hardening, as these features lead to a more distributed plastic deformation and a stress state with a lower stress triaxiality in the neck. This redistribution of plastic deformation makes the tensile specimen less prone to localization and ductile failure. The influence of strength and work hardening is further found to depend on the plastic anisotropy.

*Keywords:* Ductile failure, Strain localization, Anisotropy, Work hardening, Porous plasticity

---

## 1. Introduction

The thermo-mechanical processing of metals influences microstructural characteristics such as the grain structure and the crystallographic texture, and determines the plastic behaviour of these materials. As a result, extruded profiles, rolled plates and other formed structural components typically exhibit plastic anisotropy. The strength of the plastic anisotropy varies, and is mostly governed by the crystallographic texture (Engler and Randle, 2009). Using crystal plasticity theory, which accounts for the crystallographic texture of materials, the yielding and plastic flow of metals are well described (Zhang et al., 2015, 2016).

---

\*Corresponding author

Email address: bjorn.h.frodal@ntnu.no (Bjørn Håkon Frodal)



## Nomenclature

### Symbols

$\sigma$	Cauchy stress tensor	$\varepsilon_l$	Logarithmic strain
$\dot{\lambda}$	Plastic multiplier	$\varphi$	Equivalent stress
$\dot{\mathbf{q}}$	Non-uniformity rate vector	$\xi$	Strain rate ratio
$\dot{p}$	Equivalent plastic strain rate	$A$	Cross-section area
$\mathbf{C}^t$	Material tangent stiffness tensor	$a$	Yield surface exponent
$\mathbf{D}$	Rate-of-deformation tensor	$A_0$	Initial cross-section area
$\mathbf{F}$	Deformation gradient tensor	$D$	Cross-section diameter
$\mathbf{I}$	Second-order identity tensor	$E, \nu$	Elastic coefficients
$\mathbf{L}$	Velocity gradient tensor	$F$	Measured force
$\mathbf{N}$	Nominal stress tensor	$f$	Void volume fraction
$\mathbf{n}$	Unit normal vector to imperfection band	$f_0$	Initial void volume fraction
$\mathbf{R}$	Rotation tensor	$L$	Lode parameter
$\Phi$	Yield function	$p$	Equivalent plastic strain
$\phi, \theta$	Localization band angles	$p_f$	Local equivalent failure strain
$\phi_0, \theta_0$	Initial localization band angles	$Q_i, \theta_i$	Isotropic hardening parameters
$\sigma_0$	Initial yield stress	$q_i$	Tvergaard parameters
$\sigma_t$	True stress	$S'_k, S''_l$	Principal values of transformed tensors
$\sigma_I, \sigma_{II}, \sigma_{III}$	Ordered principal stresses	$T$	Stress triaxiality ratio
$\sigma_M$	Matrix flow stress	<b>Abbreviations</b>	
$\sigma_h$	Hydrostatic stress	ED	Extrusion/reference direction
$\sigma_{vm}$	von Mises equivalent stress	ND	Normal/thickness direction
$\varepsilon_f$	Macroscopic failure strain	TD	Transverse direction

10 Numerical simulations of materials with crystal plasticity are in general computational expensive, and phenomenological plasticity models are thus preferred when relatively large structural components are considered. These models may include an anisotropic yield function, typically incorporating one or several linear transformations of the stress tensor (Barlat et al., 2005), which is calibrated from either a large number of experimental tests (Fourmeau et al., 2011) or crystal plasticity simulations (Zhang et al., 2015, 2016; Frodal et al., 2019).

15 The process of ductile fracture includes nucleation, growth and coalescence of microscopic voids at second-phase particles or inclusions, and depends markedly on the local stress state and microstructural characteristics in a complex way (Pineau et al., 2016). In turn, the local stress state is governed by the yielding and plastic flow of the material, and it follows that the strength and work hardening of a material can influence the ductility measured in an experimental test. If the material exhibits plastic anisotropy because of the thermo-mechanical processing, the measured ductility could also depend on the direction of  
20 loading. For aluminium alloys, experiments show that the tensile ductility decreases with increasing yield stress (Lloyd, 2003; Westermann et al., 2014; Pedersen et al., 2015; Hannard et al., 2016) and is markedly influenced also by plastic anisotropy (Fourmeau et al., 2013; Khadyko et al., 2019). Numerical simulations

indicate that this variation in tensile ductility is partially due to differences in the deformation and local stress state within the neck region of the tensile specimen, as a higher yield strength is typically associated with reduced work hardening (Dæhli et al., 2016). A higher stress level may also accelerate void nucleation at second-phase particles or inclusions (Pineau et al., 2016).

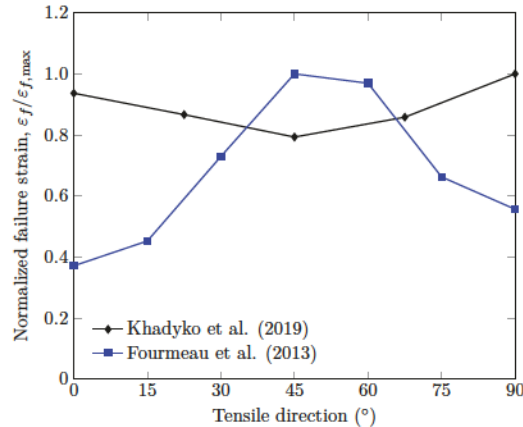


Figure 1: Normalized failure strain versus tensile direction obtained from tensile tests on a recrystallized AA6063 alloy (Khadyko et al., 2019) and a non-recrystallized AA7075 alloy (Fourmeau et al., 2013) with different crystallographic textures.

There are three main sources of anisotropic fracture behaviour in metals: *plastic anisotropy*, which primarily stems from the crystallographic texture, *morphological anisotropy*, which originates from the shape and preferred orientation of particles and voids, and *topological anisotropy*, which is a result of the spatial distribution of particles and voids. Experimental evidence from tensile tests on smooth axisymmetric specimens (Fourmeau et al., 2013) and flat rectangular specimens (Khadyko et al., 2019) indicates that the fracture anisotropy observed for some aluminium alloys correlates with the plastic flow anisotropy as expressed by the Lankford coefficients. In Figure 1, fracture anisotropy (i.e., that the failure strain varies with tensile direction) is illustrated for a recrystallized alloy with recrystallization texture (AA6063 (Khadyko et al., 2019)) and a fibrous, non-recrystallized alloy with deformation texture (AA7075 (Fourmeau et al., 2013)). Whereas the fracture anisotropy is significant for both materials, the variation of the fracture strain with tensile direction is opposite for the two alloys.

The orientation of second-phase particles relative to the loading direction has also been observed to induce fracture anisotropy, as particles can be more prone to crack formation along a certain direction (Agarwal et al., 2002). Based on unit cell simulations, Keralavarma et al. (2011) showed that the void aspect ratio can significantly affect the overall ductility. More recently, Legarth and Tvergaard (2018) performed three-dimensional unit cell simulations investigating the three sources of anisotropic failure. They found that the presence of plastic anisotropy amplifies the predictions obtained for different initial void shapes, and that there was a clear interaction between the effects of plastic anisotropy, void shape and void spacing. Also experimentally, the arrangement of second-phase particles has been observed to have an effect on the failure process as well as the fracture anisotropy (Hannard et al., 2018).

Use of unit cell simulations is an attractive way of studying the mechanisms of ductile fracture, as information of the local deformation fields can be employed to get a more profound understanding of the growth and coalescence of voids. In the unit cell modelling framework, ductile failure is usually assumed to correspond to the onset of void coalescence. However, strain localization is often a strong indicator for imminent ductile failure, as plastic deformation and damage evolution localize in a narrow region prior to failure initiation. Based on unit cell simulations, Tekoğlu et al. (2015) showed that depending on the stress triaxiality, strain localization occurs simultaneously or prior to void coalescence. Thus, the strain

localization phenomenon can be considered as an indicator for ductile failure.

55 The imperfection band approach to localization analysis, first proposed by Marciniak and Kuczyński (1967) for plane stress states, and later extended by Rice (1976) to a general and rigorous formulation, can be applied to study and predict the initiation of ductile failure. A material with an imperfection is considered where the properties are slightly different inside the imperfection compared to the rest of the material. When the material is subjected to loading, deformation tends to concentrate inside the imperfection and this tendency promotes localization of deformation in the material. The imperfection is taken in the form of a planar band, and the stress and strain fields inside and outside of the band are homogeneous but different. Localization by loss of ellipticity occurs when the strain rate becomes infinite inside the imperfection band. To trigger loss of ellipticity, the imperfection band must incorporate a softening mechanism (Rudnicki and Rice, 1975) in the case of associated plastic flow, and this is usually achieved by use of a porous plasticity 65 model describing the constitutive behaviour inside the band. The material outside the band is described either by metal plasticity or porous plasticity. The imperfection band approach has recently been used in several studies, and good quantitative agreement is observed both with unit cell simulations (Morin et al., 2018a, 2019) and experimental tests (Gruben et al., 2017; Morin et al., 2018b, 2019). Whereas several studies have used unit cell simulations to investigate void growth and coalescence in anisotropic materials 70 (Keralavarma et al., 2011; Dæhli et al., 2017a; Legarth and Tvergaard, 2018; Frodal et al., 2019), localization analyses with finite element-based unit cells have so far only been performed for isotropic materials (Barsoum and Faleskog, 2007, 2011; Dunand and Mohr, 2014; Dæhli et al., 2017b; Guo and Wong, 2018). Using these computationally expensive finite element models to perform strain localization analyses for anisotropic solids is still difficult even with modern computers. A large number of localization band orientations has to be 75 investigated within a three-dimensional setup for each load case and results in prohibitive computational times.

In this study, the influence of plastic anisotropy, strength and work hardening on ductile failure in tension is investigated numerically by use of the strain localization theory. Experimental data from tension tests on three extruded aluminium alloys obtained in previous studies (Khadyko et al., 2014; Frodal et al., 2019) are 80 used as backdrop for the numerical study. These alloys have different grain structure and crystallographic texture, and were solution heat-treated and artificially aged to three conditions giving different strength and work-hardening behaviour. The anisotropic yield surfaces of the alloys were obtained by crystal plasticity simulations. With these experimental data as a backdrop, a set of fictitious, but relevant, aluminium materials are designed that exhibit different combinations of strength, work hardening and plastic anisotropy. 85 Finite element simulations of tensile tests on smooth axisymmetric specimens are performed for each of these materials in seven in-plane directions, i.e.,  $0^\circ$ ,  $15^\circ$ ,  $30^\circ$ ,  $45^\circ$ ,  $60^\circ$ ,  $75^\circ$  and  $90^\circ$  to the reference direction. Subsequently, the non-proportional loading histories from the finite element simulations are used in strain localization analyses to predict ductile failure of the tensile specimens, and thus to investigate the effect of plastic anisotropy, strength and work hardening on the tensile ductility. In order to incorporate the plastic 90 anisotropy of the materials, the porous plasticity model proposed by Dæhli et al. (2017a), incorporating the anisotropic yield criterion Yld2004-18p (Barlat et al., 2005), is applied in all simulations. Plastic anisotropy is found to have a marked influence on the tensile ductility and to induce fracture anisotropy. The localization analyses predict a failure strain that appears to correlate with the Lankford coefficient, i.e., the fracture anisotropy seems to be closely related to the plastic flow anisotropy. Lower strength and higher work- 95 hardening rate lead to more distributed plastic deformation and a stress state with lower stress triaxiality in the neck, which makes the tensile specimen less prone to localization and ductile failure.

## 2. Experimental background

The tensile ductility of the aluminium alloys AA6060, AA6082.25 and AA6082.50 has been examined experimentally in previous studies (Khadyko et al., 2014; Frodal et al., 2019). These alloys were provided by 100 Hydro Aluminium as extruded rectangular profiles, with a thickness of 10 mm and a width of 83 mm, from which tensile specimens were machined. The specimens were solution heat-treated and artificially aged to three different tempers, namely temper O (annealed), temper T7 (overaged) and temper T6 (peak strength).

The three aluminium alloys have different grain structure and crystallographic texture (Frodal et al., 2017) leading to different plastic anisotropy (Frodal et al., 2019). The AA6060 alloy has a recrystallized grain structure comprising equi-axed grains, and exhibits a cube texture with a minor Goss component. A typical fibrous, non-recrystallized grain structure is observed for the AA6082.25 alloy, which has a cube texture with orientations along the  $\beta$ -fibre. The AA6082.50 alloy has recrystallized grain structure with large elongated grains and a rotated cube texture (Frodal et al., 2017). For further details about the materials, the reader is referred to Khadyko et al. (2014) and Frodal et al. (2017, 2019).

Axisymmetric tensile specimens, see Figure 2, were used to determine the work-hardening response and ductile failure properties of the materials (Khadyko et al., 2014; Frodal et al., 2019). All of the specimens were oriented along the transverse direction (TD) of the extruded profile. A displacement-controlled test machine with a constant cross-head velocity of 1.2 mm/min was used to perform the tests. During testing, the force and diameters along the extrusion direction (ED) and thickness direction (ND) of the minimum cross-section of the specimen were continuously measured until fracture using a load cell and an in-house measuring system (Frodal et al., 2017), respectively.

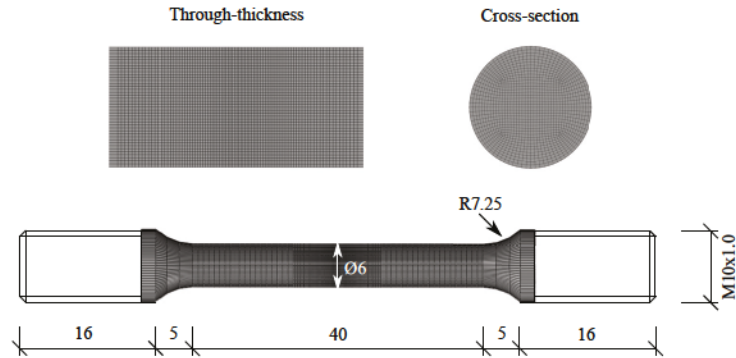


Figure 2: Axisymmetric tensile specimen with the finite element mesh. The through-thickness and cross-section mesh are shown from the centre of the specimen. Dimensions are in mm.

The current area of the specimen can be estimated by

$$A = \frac{\pi}{4} D_1 D_3 \quad (1)$$

where  $D_1$  and  $D_3$  are the measured diameters in ED and ND, respectively. The true stress over the minimum cross-section area is

$$\sigma_t = \frac{F}{A} \quad (2)$$

where  $F$  is the measured force. Assuming plastic incompressibility and negligible elastic strains, the logarithmic (or true) strain is given by

$$\varepsilon_l = \ln \left( \frac{A_0}{A} \right) \quad (3)$$

where  $A_0$  is the initial cross-section area of the specimen. It is important to note that  $\sigma_t$  and  $\varepsilon_l$  represent average values over the minimum cross-section area of the specimen.

Figure 3 presents the true stress-strain curves from the tensile tests in TD plotted up to the point of failure, where marked differences between the behaviour of the different alloy and temper combinations can be observed. Note that failure is here defined as the point of maximum true stress, and an abrupt decrease in the stress level is observed after this point. The strength and work hardening of the different tempers of the same alloy are distinct. In general, the O tempers have the highest work hardening, but the lowest strength. The T6 tempers have the lowest work hardening and the highest strength, while the T7 tempers



130 are between the O and T6 tempers when it comes to strength and work hardening, see also Section 3.2. Comparing the alloys, the strength clearly vary between them, and also the work hardening is different. Typically, the strength of the two AA6082 alloys for the same temper is similar and higher than for the AA6060 alloy. The only exception is for the O temper, where the AA6082.25 alloy has higher strength than the two other alloys.

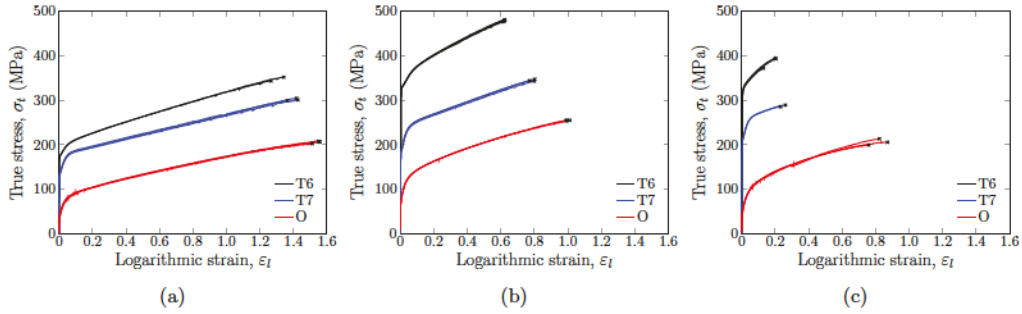


Figure 3: True stress-strain curves from tension tests of the aluminium alloys (a) AA6060 , (b) AA6082.25, and (c) AA6082.50 in tempers T6, T7 and O. All tests were performed with tensile direction along TD of the extruded profile. The data is taken from Khadyko et al. (2014) and Frodal et al. (2017, 2019).

135 Comparing the point of failure for the various alloy-temper combinations, makes it apparent that the AA6060 alloy is by far the most ductile alloy and the O temper is the most ductile temper for each alloy. Even the least ductile temper of the AA6060 alloy, i.e, the T6 temper, has a much higher failure strain than all of the tempers of the two AA6082 alloys. Comparing the two AA6082 alloys, it is observed that the AA6082.25 alloy has, in general, a higher failure strain than the AA6082.50 alloy, for the same temper.

140 The lower ductility observed for the AA6082.50 alloy can be linked to the grain structure for this alloy, see Section 5.

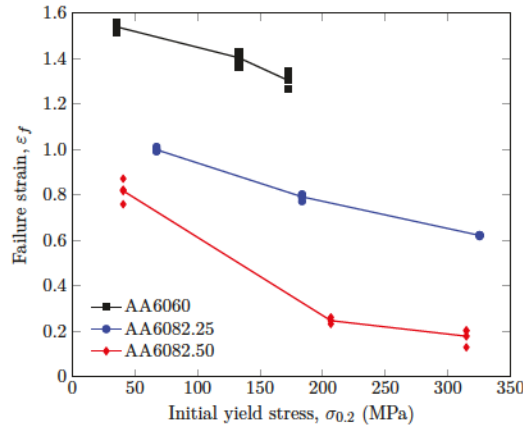


Figure 4: Failure strain in tension versus initial yield stress at 0.2% plastic strain for the three alloys in different tempers.

Figure 4 shows the average failure strain from the tensile tests in TD versus the initial yield stress at 0.2% plastic strain. It is clearly visible that the magnitude of the failure strain, and thus the ductility of the materials, vary with yield strength. Examining Figure 4, the difference between the alloys becomes evident

145 as the curves representing the failure strain for each alloy is displaced relative to each other. In previous



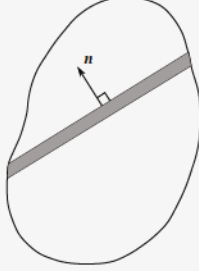
studies on various aluminium alloys, it has been found that the failure strain tends to decrease linearly with increasing yield strength for similar microstructure (Lloyd, 2003; Westermann et al., 2014; Pedersen et al., 2015; Hannard et al., 2016).

### 3. Numerical methods

#### 150 3.1. Strain localization theory

The strain localization theory is used herein to investigate the influence of strength, work hardening and plastic anisotropy on the tensile failure of ductile materials. At moderate stress triaxialities, localization has been found to occur simultaneously as void coalescence (Tekoğlu et al., 2015) and can thus be useful in predicting incipient ductile failure. In this study, the imperfection band approach proposed by Rice (1976) is used. This method considers a material consisting of two homogeneous regions, which are separated by a thin planar imperfection band, and subjected to an overall uniform deformation. The constitutive equations inside and outside of the imperfection band are allowed to be different, with the requirement that equilibrium and compatibility conditions are enforced across the band. A brief overview of the governing equations of the imperfection band approach is given in Box 1. The reader is referred to Rice (1976), Needleman and Rice (1978), and Morin et al. (2018a,b) for further details.

Box 1: Overview of the strain localization analyses (Morin et al., 2018a)<sup>1</sup>

<ul style="list-style-type: none"> <li>• Continuing equilibrium: <math>\mathbf{n} \cdot \dot{\mathbf{N}}_b = \mathbf{n} \cdot \dot{\mathbf{N}}_o</math> (4)</li> <li>• Constitutive equations outside the band: <math>\dot{\mathbf{N}}_o = \mathbf{C}_o^t : \mathbf{L}_o</math> (5)</li> <li>• Constitutive equations inside the band: <math>\dot{\mathbf{N}}_b = \mathbf{C}_b^t : \mathbf{L}_b</math> (6)</li> <li>• Equation system for the non-uniformity rate vector <math>\dot{\mathbf{q}}</math>: <math>(\mathbf{n} \cdot \mathbf{C}_b^t \cdot \mathbf{n}) \cdot \dot{\mathbf{q}} = \mathbf{n} \cdot (\mathbf{C}_o^t - \mathbf{C}_b^t) : \mathbf{L}_o</math> (7)</li> </ul>		<ul style="list-style-type: none"> <li>• Compatibility: <math>\mathbf{L}_b = \mathbf{L}_o + \dot{\mathbf{q}} \otimes \mathbf{n}</math> (8)</li> <li>• Band orientation in updated configuration: <math>\mathbf{n} = \begin{bmatrix} \cos \phi \\ \cos \theta \sin \phi \\ \sin \theta \sin \phi \end{bmatrix}</math> (9)</li> <li>• Localization conditions: <math>\det(\mathbf{n} \cdot \mathbf{C}_b^t \cdot \mathbf{n}) = 0</math> (10) <math>\xi = \sqrt{\frac{\mathbf{D}_b : \mathbf{D}_b}{\mathbf{D}_o : \mathbf{D}_o}} \rightarrow \infty</math> (11)</li> </ul>
---	---	--

160 While this method does not impose any restrictions on the constitutive equations of the material inside or outside the imperfection band, the same approach as in Nahshon and Hutchinson (2008), Gruben et al. (2017), and Morin et al. (2018a,b, 2019) is used in the current work. A porous plasticity model is used to represent the material inside and outside of the imperfection band. It is assumed that any voiding mechanism occurring outside of the band is negligible and that the porosity here is zero ( $f = 0$ ), whereas inside the band an imperfection is introduced by pre-existing voids ( $f_0 > 0$ ). For moderate stress triaxialities, this is usually an appropriate assumption (Xue et al., 2010, 2013; Westermann et al., 2014). Note that also other types of imperfections can be included both inside and outside the band, e.g., void nucleation (Morin et al., 2018a,b, 2019) and void softening in shear (Nahshon and Hutchinson, 2008; Morin et al., 2018a) can be introduced in the constitutive equations.

170 An overview of the porous plasticity model used herein is given in Box 2. The heuristic modification of the Gurson (1977) model proposed by Dæhli et al. (2017a) and applied by Morin et al. (2018b) is used in the current study. This extension introduces the equivalent stress of the Yld2004-18p yield function (Barlat et al., 2005) into the constitutive equations, in order to include anisotropic yielding and plastic flow. For

<sup>1</sup>Note that in Morin et al. (2019), there is a typo in Equation (26) and (27). The correct expressions are here given in Equation (5) and (6) of Box 1.

Box 2: Overview of the porous plasticity model (Dæhli et al., 2017a).

<ul style="list-style-type: none"> <li>• Corotational formulation:  <math>\dot{\boldsymbol{\sigma}} = \mathbf{R}^T \cdot \boldsymbol{\sigma} \cdot \mathbf{R} \quad \wedge \quad \dot{\mathbf{D}} = \mathbf{R}^T \cdot \mathbf{D} \cdot \mathbf{R}</math> (12)</li> </ul>	<ul style="list-style-type: none"> <li>• Isotropic work hardening:  <math>\sigma_M = \sigma_0 + \sum_{i=1}^3 Q_i \left( 1 - \exp \left( -\frac{\theta_i}{Q_i} p \right) \right)</math> (17)</li> </ul>
<ul style="list-style-type: none"> <li>• Additive decomposition of strain rate:  <math>\dot{\mathbf{D}} = \dot{\mathbf{D}}^e + \dot{\mathbf{D}}^p</math> (13)</li> </ul>	<ul style="list-style-type: none"> <li>• Associated flow rule:  <math>\dot{\mathbf{D}}^p = \lambda \frac{\partial \Phi}{\partial \boldsymbol{\sigma}}</math> (18)</li> </ul>
<ul style="list-style-type: none"> <li>• Generalized Hooke's law on rate form:  <math>\dot{\boldsymbol{\sigma}} = \frac{E}{1+\nu} \dot{\mathbf{D}}^e + \frac{E}{3(1-2\nu)} \text{tr}(\dot{\mathbf{D}}^e) \mathbf{I}</math> (14)</li> </ul>	<ul style="list-style-type: none"> <li>• Equivalent plastic strain:  <math>p = \int_0^t \dot{p} d\bar{t} = \int_0^t \frac{\dot{\boldsymbol{\sigma}} : \dot{\mathbf{D}}^p}{(1-f) \sigma_M} d\bar{t}</math> (19)</li> </ul>
<ul style="list-style-type: none"> <li>• Yield function:  <math>\Phi = \left( \frac{\varphi(\dot{\boldsymbol{\sigma}})}{\sigma_M} \right)^2 + 2q_1 f \cosh \left( \frac{q_2 \text{tr}(\dot{\boldsymbol{\sigma}})}{2\sigma_M} \right) - 1 - q_3 f^2 \leq 0</math> (15)</li> </ul>	<ul style="list-style-type: none"> <li>• Evolution of void volume fraction:  <math>\dot{f} = (1-f) \text{tr}(\dot{\mathbf{D}}^p)</math> (20)</li> </ul>
<ul style="list-style-type: none"> <li>• Equivalent stress:  <math>\varphi(\dot{\boldsymbol{\sigma}}) = \left( \frac{1}{4} \sum_{k=1}^3 \sum_{l=1}^3  S_k' - S_l'' ^a \right)^{\frac{1}{a}}</math> (16)</li> </ul>	<ul style="list-style-type: none"> <li>• Loading-unloading conditions:  <math>\Phi \leq 0, \quad \dot{\lambda} \geq 0, \quad \dot{\lambda} \Phi = 0</math> (21)</li> </ul>

175 zero porosity, the yield criterion reduces to the original Yld2004-18p yield function (Barlat et al., 2005). The porous plasticity model introduces material softening inside the imperfection band, which triggers loss of ellipticity of the governing equations, i.e., strain localization. When an associated flow rule is adopted, material softening is required for loss of ellipticity to occur (Rudnicki and Rice, 1975) and thus for the localization conditions (Box 1) to be met for reasonable stress levels.

180 The strain localization theory by the imperfection band approach has been implemented in a stand-alone Fortran programme, as described in detail by Morin et al. (2018a). The porous plasticity model has been implemented into a user material subroutine (UMAT) for Abaqus/Standard (Abaqus, 2014). To ensure sufficiently accuracy of the integration point values, sub-stepping is employed (Dæhli et al., 2017a).

### 3.2. Finite element analyses

185 The imperfection band analyses are driven by loading histories extracted from finite element analyses of tensile tests. The axisymmetric tensile specimen is modelled in Abaqus/Standard, and the finite element mesh is presented in Figure 2. Linear eight-node solid elements with selective reduced integration (C3D8) are used. The dimensions of the elements located in the centre of the specimen are  $0.10 \times 0.15 \times 0.15 \text{ mm}^3$ , with the shortest element length along the tensile direction.

190 The material behaviour of the tensile specimen is defined by the porous plasticity model described in Box 2. When running the finite element simulations of the tensile tests, the initial porosity is set to zero ( $f_0 = 0$ ), thus reducing the model to the anisotropic Yld2004-18p plasticity model (Barlat et al., 2005) with isochoric plastic flow. Isotropic elasticity is assumed with a Young's modulus of  $E = 70000 \text{ MPa}$  and a Poisson's ratio of  $\nu = 0.3$ , which are relevant values for aluminium alloys.

195 In order to study the effect of plastic anisotropy on the tensile ductility, typical yield surfaces for textured aluminium alloys are employed in the simulations. The AA6060 and AA6082.25 alloys have typical recrystallization and deformation texture, respectively, whereas the AA6082.50 alloy has a typical texture of an alloy with large recrystallized grains, see Section 2. In addition, the yield surface of an isotropic alloy with random texture is included for comparison. To emphasise that the yield surfaces from these alloys in the following will be combined with flow stress curves that do not belong to the respective alloy, we will consider 200 the alloys as model materials and rename them accordingly. The model materials are thus denoted alloy A, B, C and D with yield surface belonging to alloy AA6060, AA6082.25 AA6082.50 and an isotropic material, respectively. The yield surfaces of the model materials are presented in Figure 5 depicted in the ED-TD plane. It is apparent that the yield surfaces for the alloys are distinct due to the crystallographic texture.

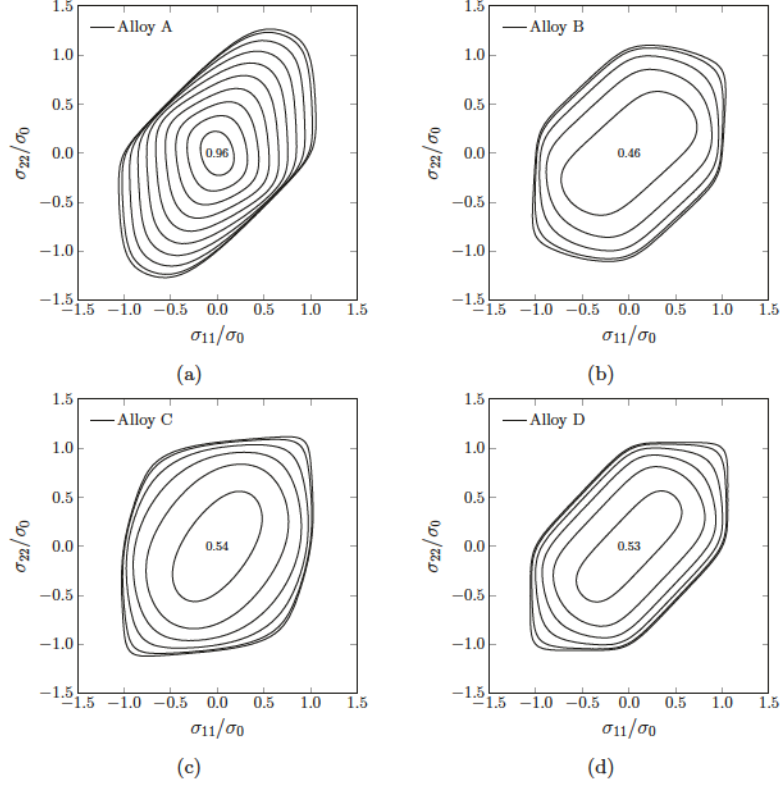


Figure 5: Yield surfaces depicted in the ED-TD plane for (a) alloy A (AA6060), (b) alloy B (AA6082.25), (c) alloy C (AA6082.50), and (d) alloy D (isotropic). Contours of increasing normalized shear stress are plotted in 0.1 increments, with the maximum value in the centre.

205 These anisotropic yield surfaces have previously been found by Frodal et al. (2019) using crystal plasticity  
 finite element analyses. The yield surface of the isotropic material (alloy D) is given by the Yld2004-18p  
 yield function with all anisotropy coefficients equal to one, thus reducing it to an isotropic high-exponent  
 yield function. The exponents of the selected anisotropic yield surfaces are approximately 12. Thus, to limit  
 210 the influence of the yield surface curvature on the imperfection band analyses, as studied by Dæhli et al.  
 (2017b), the exponent of the isotropic material is set to  $a = 12$ . The list of anisotropy parameters is omitted  
 in this paper, and the reader is referred to Frodal et al. (2019) for further details.

Figure 6 presents the normalized yield stresses and Lankford coefficients as function of the tensile direction  
 in the ED-TD plane obtained with the selected yield surfaces. The  $0^\circ$  direction is along ED, and is taken as  
 the reference direction in this study, while the  $90^\circ$  direction is along TD of the extruded profile. Both the  
 215 values and the variation of the normalized yield stresses and Lankford coefficients are markedly different for  
 the anisotropic yield surfaces. The two curves appear to exhibit the opposite trend for a given anisotropic  
 yield surface, i.e., when the normalized yield stress has a maximum/minimum, the Lankford coefficient tends  
 to have a minimum/maximum.

In order to study the influence of strength and work hardening on ductile failure, selected work-hardening  
 220 curves typical for aluminium alloys will be used. The selected work-hardening behaviour is taken from the  
 AA6082.25 alloy artificially aged to the three conditions given in Section 2. The work-hardening rule

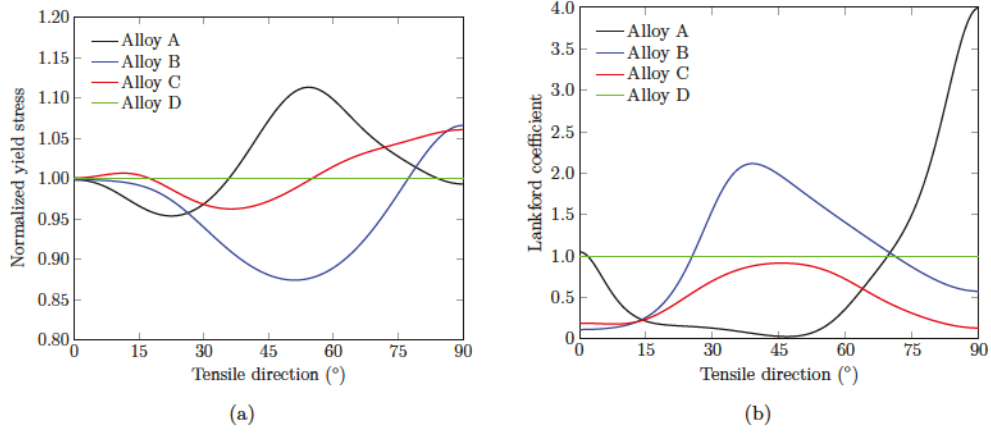


Figure 6: (a) Normalized yield stress and (b) Lankford coefficient versus tensile direction for uniaxial tension in the ED-TD plane obtained with the four selected yield surfaces.

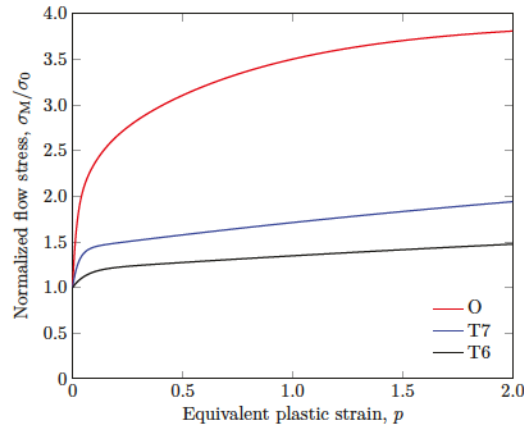


Figure 7: Normalized flow stress curves representing the work-hardening behaviours used in the numerical study.

defined in Box 2 was calibrated using an optimization procedure in Frodal et al. (2019). Figure 7 presents the normalized flow stress curves and displays the large difference in work hardening between the three tempers. The corresponding initial yield stress and work-hardening parameters are given in Table 1.

Table 1: Initial yield stress and work-hardening parameters (Frodal et al., 2019).

Temper	$\sigma_0$ (MPa)	$\theta_1$ (MPa)	$Q_1$ (MPa)	$\theta_2$ (MPa)	$Q_2$ (MPa)	$\theta_3$ (MPa)	$Q_3$ (MPa)
O	57.6	2661.3	44.6	382.2	32.6	120.8	91.0
T7	163.6	1300.1	28.9	1301.2	40.7	52.3	232.9
T6	299.5	470.5	28.5	485.0	29.8	50.0	279.4

225

In the following, the simulation procedure consists of finite element analyses of the tensile tests in seven



in-plane directions, i.e.,  $0^\circ$ ,  $15^\circ$ ,  $30^\circ$ ,  $45^\circ$ ,  $60^\circ$ ,  $75^\circ$  and  $90^\circ$  with respect to the reference direction (ED). Strain localization theory will be used to predict the logarithmic failure strain in each simulation of a tensile test, see Section 3.3. Note that only initiation of failure is predicted by using the strain localization theory in the post-processing of the finite element simulation results.

### 230 3.3. Localization analyses

When performing the imperfection band analyses, the material inside the band is described by the porous plasticity model in Box 2 with an initial porosity of  $f_0 = 0.005$ , while outside, the porosity is set to zero as in the finite element simulations. This value of  $f_0$ , which is a reasonable value for aluminium alloys (Westermann et al., 2014), is chosen for all the materials in order to isolate the effects of strength, work  
235 hardening and plastic anisotropy on the failure strain. The porous plasticity parameters by Tvergaard (1981) are here given standard values of  $q_1 = 1.5$ ,  $q_2 = 1.0$  and  $q_3 = q_1^2$ , but could alternatively be calibrated for each combination of yield surface and flow stress curve, as done by Dæhli et al. (2017a).

The location of ductile failure initiation is not known a priori, but it is reasonable to assume that failure is first encountered within the neck of the tensile specimen. Accordingly, all elements within this region are  
240 examined for strain localization using the imperfection band approach as described in Box 1. The numerical procedure is as follows (Morin et al., 2018b):

1. The deformation gradient  $\mathbf{F}(t)$  of each element within the neck region is calculated based on the nodal displacements and the isoparametric shape functions.
2. An imperfection analysis is run for each of these elements based on the extracted deformation gradient  
245  $\mathbf{F}(t)$  for a large number of band orientations defined by  $\phi_0 \in [0, \pi]$  and  $\theta_0 \in [0, 2\pi]$ , using a domain reduction method as described in Morin et al. (2018a).
3. For each element, a local failure strain  $p_f$  is calculated as the minimum over all band orientations of the equivalent plastic strain outside the imperfection band at loss of ellipticity inside the band.
4. Using the relationship between the local equivalent plastic strain  $p$  of the elements and the macroscopic logarithmic strain  $\varepsilon_l$  from the finite element simulation of the specimen, the macroscopic failure strain  
250  $\varepsilon_f$  corresponding to localization within the actual element is found.
5. The actual logarithmic failure strain corresponds to the minimum value of  $\varepsilon_f$  over the neck region and its position is assumed to be the location of failure initiation.

For further details on the numerical procedure the reader is referred to Morin et al. (2018b, 2019). In  
255 the subsequent sections, the localization band will refer to the band for which loss of ellipticity occurs first in the critical element, thus the band giving the lowest macroscopic failure strain  $\varepsilon_f$ .

## 4. Numerical results

### 4.1. Macroscopic behaviour

Figure 8 presents the true stress-strain curves from the finite element analyses of the tensile tests along  
260 the reference direction (ED). All of the materials represented by the yield surfaces in Figure 5 are shown with the three work-hardening behaviours, and are plotted until failure predicted by the imperfection band approach. It is evident that both the plastic anisotropy and the strength and work hardening have a pronounced effect on the failure strain, whereas the stress-strain curves are almost identical between the different yield surfaces in the reference direction. In the other tensile directions, variations are observed as  
265 the yield stress varies with tensile direction according to the plastic anisotropy defined by the yield surface, see Figure 6a. Note that, although the macroscopic stress-strain curves are indistinguishable, the local stress state varies with the plastic anisotropy, see Section 4.2.

In Figure 9a, the predicted failure strain is plotted against the initial yield stress for all materials. The effect of strength and work hardening is seen to vary with the plastic anisotropy. For the lowest strength

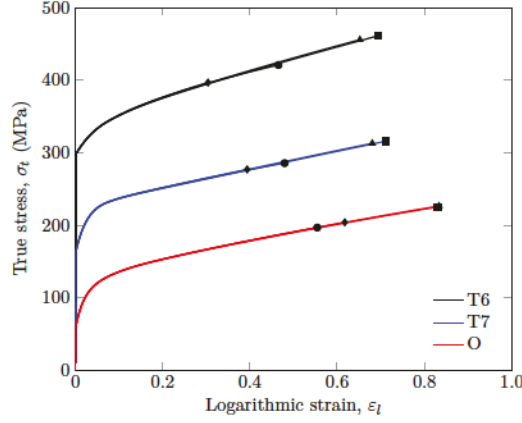


Figure 8: True stress-strain curves from the finite element analyses of the tensile tests along the reference direction (ED), where the curves are plotted until failure as predicted by the strain localization theory for each material. The location of predicted failure, is shown with the corresponding symbols used in Figure 9: (■) alloy A, (●) alloy B, (◆) alloy C, (▲) alloy D.

270 and highest work hardening (temper O), alloys A and D have approximately the same failure strain, which is significantly higher than the failure strains of alloys B and C. In this temper, alloy B has somewhat lower ductility than alloy C. For higher strength and lower work hardening (tempers T6 and T7), however, alloys B and C switch position, and the failure strain becomes clearly lower for alloy C than for alloy B. The difference in ductility between alloys A and D remains small in tempers T6 and T7, but alloy A has  
 275 somewhat higher ductility than alloy D. Thus, the decrease in failure strain with increasing strength and decreasing work hardening depends markedly upon the plastic anisotropy.

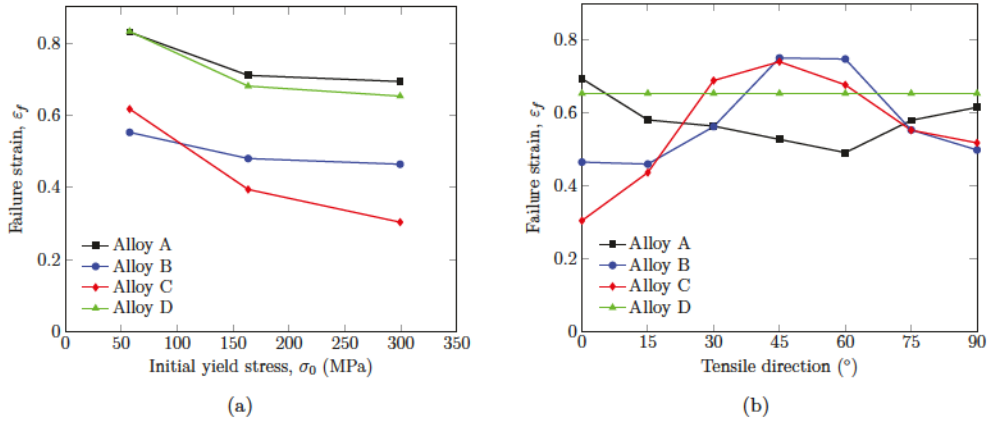


Figure 9: (a) Failure strain versus initial yield stress for loading along the reference direction (ED), and (b) failure strain versus tensile direction in the ED-TD plane for the alloys with the temper T6 work hardening.

Figure 9b presents the failure strain versus the tensile direction in the ED-TD plane for the alloys with the temper T6 work hardening, i.e., the highest strength and lowest work hardening. The failure strain of the anisotropic materials varies significantly with the tensile direction, while for the isotropic alloy (alloy  
 280 D) the failure strain is constant. The failure strain, and thus the tensile ductility of alloy A, is the greatest

in ED ( $0^\circ$  direction), whereas alloys B and C have the highest ductility when loaded in the  $45^\circ$  direction. The lowest failure strain is observed in the  $60^\circ$ ,  $15^\circ$  and  $0^\circ$  directions for alloys A, B, and C, respectively. Comparing the variation of the failure strain in Figure 9b with the variation of the Lankford coefficient in Figure 6b, it is found that these two characteristics experience to some extent the same trends. The predicted variation of the failure strain with tensile direction also resembles experimental observations from the literature reproduced in Figure 1. The predictions for alloy A exhibit the same trend as the experimental data for the AA6063 alloy in Khadyko et al. (2019), and the experimental findings in Fourmeau et al. (2013) for a AA7075 alloy are similar to the predictions for alloy B. These alloys have similar grain structure and crystallographic texture to those presented in Figure 1.

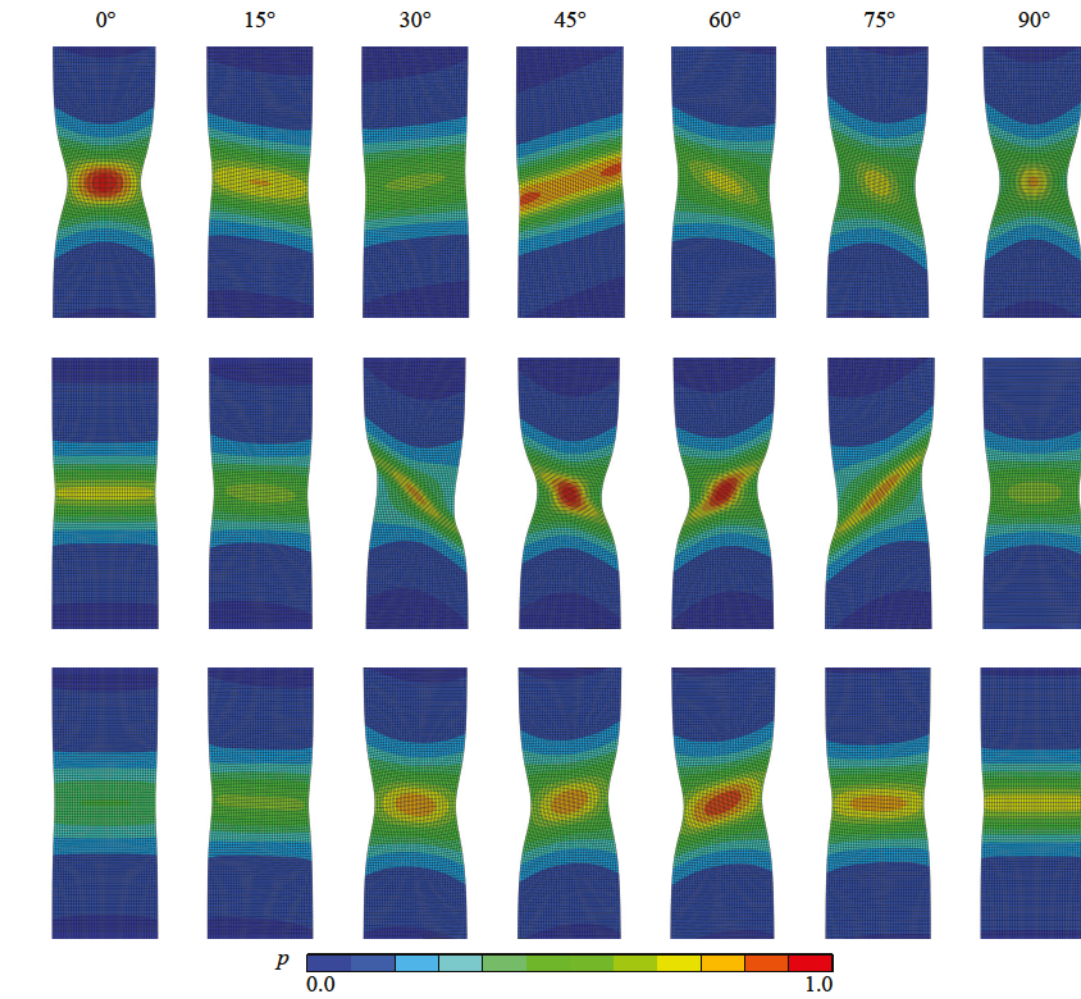


Figure 10: Deformed configuration of the tensile specimen at failure (as predicted by the imperfection band analysis) depicted in the ED-TD plane as obtained from the simulations of tensile tests in different directions with respect to the reference direction (ED): (top) alloy A, (middle) alloy B, and (bottom) alloy C, with work hardening according to temper T6. Contours of the equivalent plastic strain are shown on the deformed meshes.

290 Plots of the deformed configuration of the tensile specimen at failure predicted by the imperfection band analyses are shown in Figure 10, as obtained in the finite element simulations of the tensile tests in different directions with respect to the reference direction (ED). Regions of localized plastic flow is observed in the centre of the specimen. The shape of these regions is defined by the plastic anisotropy as described by the yield surface. Between the materials, different deformation modes are seen, and the level of equivalent plastic strain at failure varies between the materials and with the tensile direction. For the tests along ED and TD, the region of localized plastic flow is symmetric about the material axes due to the orthotropic sample symmetry, whereas in the other directions the localized region develops at an angle to the loading axis. These deformation modes lead to different shapes of fractured specimens, varying between cup-and-cone to slant shear fracture modes due to the anisotropic plastic flow. The deformed shapes obtained here for alloy B are similar to the fracture modes observed experimentally by Fourmeau et al. (2013). In addition to plastic anisotropy, material inhomogeneities, e.g., the arrangement of second-phase particles, can contribute to the ductile failure process and affect the fracture path (Hannard et al., 2018). Failure initiation, as predicted by the strain localization theory, is observed to occur in the region of the highest equivalent plastic strain, and for alloys B, C and D, failure initiates in the centre for all loading directions. For alloy A, failure initiates in the centre for all loading directions with the 45° direction as an exception. In this loading direction, failure initiation occurs further towards the specimen periphery.

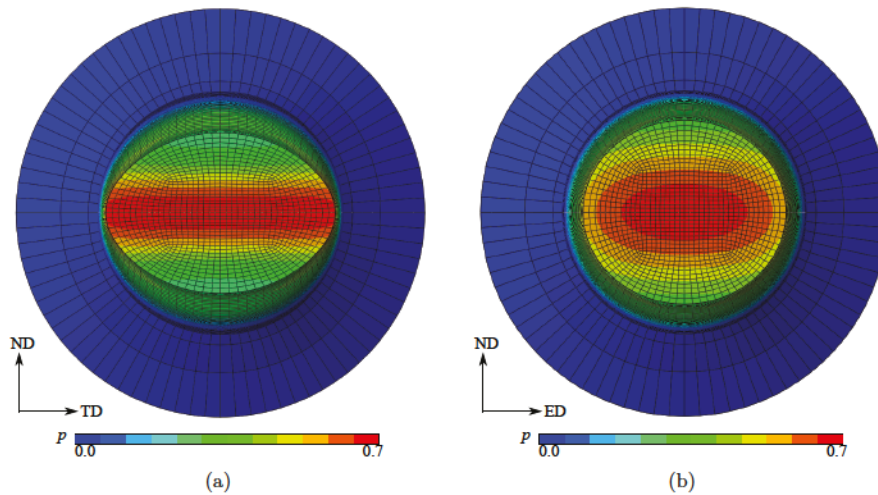


Figure 11: Minimum cross-section at failure (as predicted by the imperfection band analysis) of alloy B with the temper T6 work hardening showing contours of the equivalent plastic strain for simulations of tensile tests in the: (a) 0° direction, and (b) 90° direction.

Figure 11 depicts contour plots of the equivalent plastic strain on the minimum cross-section of the tensile tests in the 0° and 90° directions for alloy B in temper T6. The equivalent plastic strain is observed to be more localized in the centre of the specimen in the 0° direction, which is linked to the very low value of the Lankford coefficient in this direction, see Figure 6b. In the 90° direction, the Lankford coefficient is markedly higher and this contributes to distribute the plastic strain more uniformly across the specimen's cross-section, which is positive for the tensile ductility. As a result, alloy B has a slightly higher failure strain in the 90° direction than in the 0° direction, see Figure 9b, even though the stress level is higher in the 90° direction, see Figure 6a. The effect of plastic flow on ductility will be further discussed in the next section—and in particular in connection with Figure 14.



#### 4.2. Microscopic behaviour

In this section, we look more closely into the microscopic behaviour of the critical element in the neck region of the tensile specimen, i.e., the location of failure initiation. Relevant quantities both inside and outside of the imperfection band are investigated in order to further interpret the effects of strength, work hardening and plastic anisotropy on strain localization. It is therefore useful to define certain stress invariants, such as the stress triaxiality ratio and Lode parameter to be used in the following. The stress triaxiality ratio is defined as

$$T = \frac{\sigma_h}{\sigma_{vm}} \quad (22)$$

where  $\sigma_h = \frac{1}{3}\text{tr}(\boldsymbol{\sigma})$  is the hydrostatic stress and  $\sigma_{vm} = \sqrt{\frac{3}{2}\boldsymbol{\sigma}' : \boldsymbol{\sigma}'}$  is the von Mises equivalent stress,  $\boldsymbol{\sigma}'$  being the stress deviator. The Lode parameter is defined as

$$L = \frac{2\sigma_{II} - \sigma_I - \sigma_{III}}{\sigma_I - \sigma_{III}} \quad (23)$$

where  $\sigma_I \geq \sigma_{II} \geq \sigma_{III}$  are the ordered principal stresses. Note that the Lode parameter is  $L = -1$  for generalized axisymmetric tension,  $L = 0$  for generalized shear, and  $L = +1$  for generalized axisymmetric compression.

Figure 12 presents quantities from the imperfection band analyses obtained inside and outside of the critical imperfection band in the simulations of the tensile tests in the reference direction (ED) for alloys A, B, C and D in temper T6. The normalized von Mises stress, inside and outside the band, together with the normalized void volume fraction inside the band, are plotted against the logarithmic strain in Figure 12a. The von Mises stress is similar outside of the band for all alloys, whereas inside the band the material experiences porosity induced softening before localization occurs. Initially, the evolution of the porosity is similar for all materials, but with straining the porosity inside the band grows differently depending on the material and thus the plastic anisotropy. As shown in Figure 9, alloys A and C have respectively the highest and lowest failure strain for this configuration. Softening is seen to occur earlier for alloy C than for the other alloys, owing to the rapid increase of the porosity at a lower value of the logarithmic strain in the neck. The stress triaxiality is plotted against the logarithmic strain in Figure 12b. After necking, the stress triaxiality increases with straining, but with a higher rate inside the imperfection band than outside, and strain softening inside the band coincides with a rapid increase of the stress triaxiality. Compared with the other alloys, alloy C has higher stress triaxiality both outside and inside the band for all strains, which explains the lower ductility. An earlier rapid increase of the stress triaxiality inside the band is seen for the alloys with the lowest ductility, namely alloys B and C. The equivalent plastic strain  $p$  inside and outside of the critical imperfection band is plotted in Figure 12c as a function of the logarithmic strain  $\varepsilon_l$  over the neck. Outside of the imperfection band, the equivalent plastic strain evolves similarly for all alloys, whereas inside the evolution differs. The material inside the band experiences a higher equivalent plastic strain rate than outside to compensate for the porosity-induced softening, which occurs at different strain levels for the four materials. Figure 12d displays the Lode parameter  $L$  inside and outside of the imperfection band as a function of the logarithmic strain  $\varepsilon_l$  over the neck. It is apparent that the stress state drifts from generalized tension ( $L = -1$ ) towards generalized shear ( $L = 0$ ) inside the imperfection band, as also observed by Morin et al. (2018a,b). The stress state is also observed to differ slightly from generalized tension outside of the imperfection band due to the plastic anisotropy. For the materials with the lowest ductility, e.g., alloy C, the stress state inside of the band is observed to change rapidly from generalized tension towards generalized shear at a lower logarithmic strain than for the more ductile materials, e.g., alloy A.

In Figure 13 the same quantities as in Figure 12 are shown, but here the simulations of the tension tests in the reference direction (ED) for alloy A in tempers O, T7 and T6 are addressed. The trends seen in Figure 13 are representative for the other alloys as well. The porosity is seen to grow the fastest for the T6 temper and the slowest for the O temper, i.e., a higher work hardening leads to a lower growth rate of the porosity as a function of the logarithmic strain over the neck of the tensile specimen, see Figure 13a. In the simulations for the O temper, the stress triaxiality increases with a clearly lower rate than for the other two tempers with higher strength and lower work hardening, see Figure 13b. Thus, for a given logarithmic



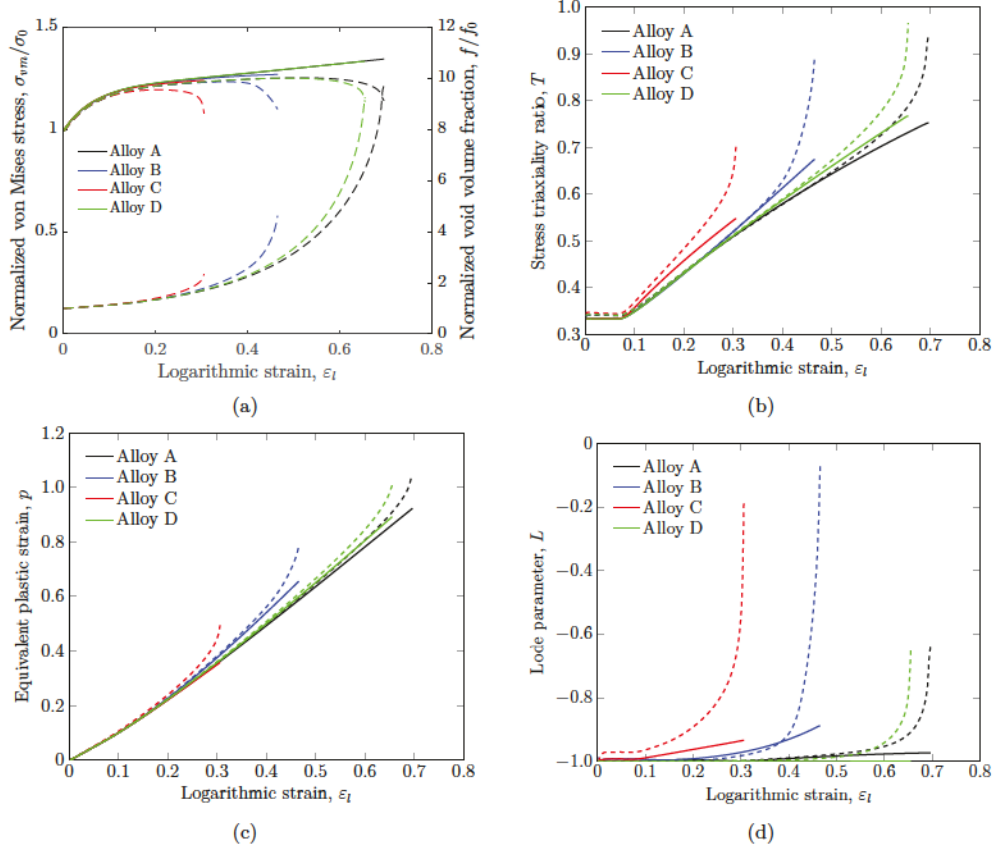


Figure 12: Local behaviour in the regions inside (dashed lines) and outside (solid lines) of the imperfection band for the materials with work hardening according to temper T6 loaded along ED: (a) normalized von Mises stress and normalized void volume fraction, (b) stress triaxiality ratio, (c) equivalent plastic strain, and (d) Lode parameter versus logarithmic strain over the neck.

strain after necking, the stress triaxiality is definitely the lowest for the O temper, which is partly the reason for the higher tensile ductility. The stress triaxiality ratio is found to be higher close to localization for the T6 temper than for the T7 temper, both inside and outside of the imperfection band. From Figure 13c it is evident that the lower strength and higher work hardening of the O temper lead to a more gradual increase in the equivalent plastic strain as the logarithmic strain over the neck increases compared with the T6 and T7 tempers. The higher work hardening contributes to distribute the plastic deformation more evenly throughout the cross-section of the tensile specimen, which delays the formation of a neck and thus plastic localization. Albeit not as apparent, the equivalent plastic strain inside and outside of the imperfection band evolves faster for the T6 temper than for the T7 temper. As seen in Figure 13d, the stress state appears to drift earlier from generalized tension towards generalized shear for tempers T6 and T7 than for temper O due to the higher strength and lower work hardening. It seems as if the plastic anisotropy might have a stronger impact on the stress state within the neck region for a material with lower work hardening.

Figure 14 presents the microscopic behaviour of alloy B in temper T6 from simulations of the tension tests in the  $0^\circ$ ,  $45^\circ$ , and  $90^\circ$  directions. In agreement with Figure 6a, the von Mises stress level is clearly

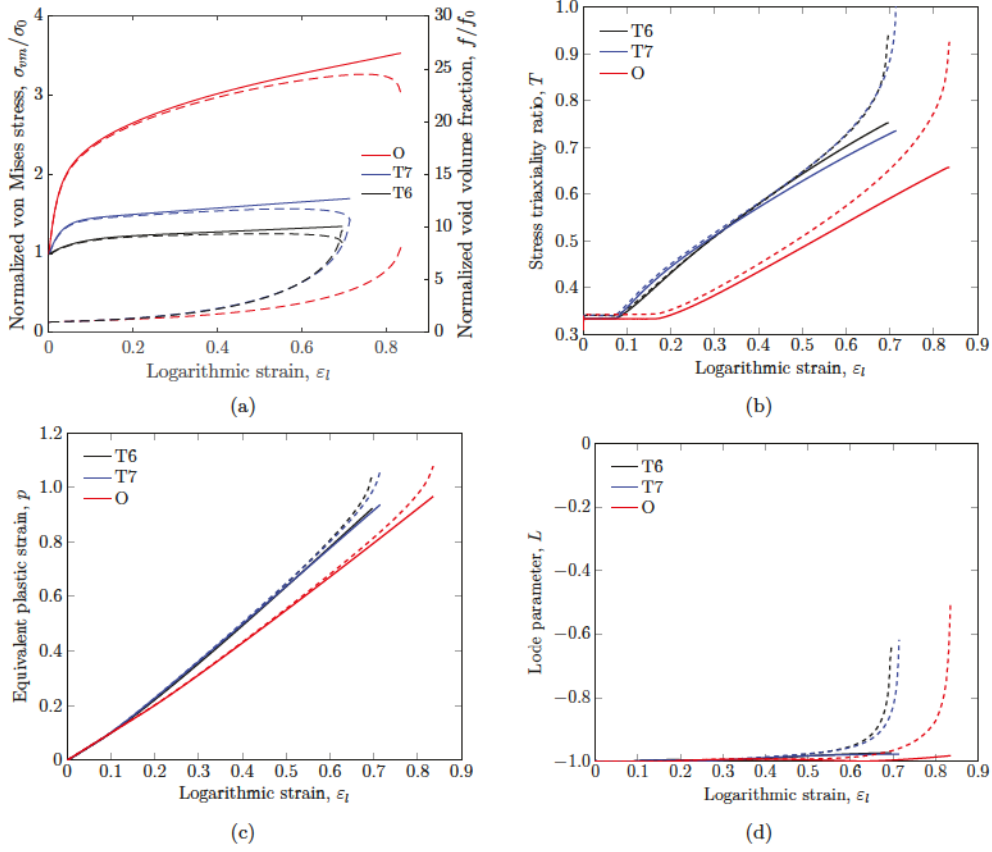


Figure 13: Local behaviour in the regions inside (dashed lines) and outside (solid lines) of the imperfection band for alloy A with the three different flow stress curves loaded along ED: (a) normalized von Mises stress and normalized void volume fraction, (b) stress triaxiality ratio, (c) equivalent plastic strain, and (d) Lode parameter versus logarithmic strain over the neck.

different in the three directions, see Figure 14a. The evolution of the porosity is also different in the three directions, where the void growth is the slowest in the  $45^\circ$  direction, which has the lowest von Mises stress. Initially, the void growth is lower in the  $0^\circ$  direction than in the  $90^\circ$  direction, but this changes in the final stage before localization. From Figure 14b, it can be observed that the triaxiality level inside the imperfection band at a given logarithmic strain over the neck is higher in the  $0^\circ$  direction with the lowest ductility. Outside the band, the  $90^\circ$  direction has a slightly lower triaxiality level than the  $45^\circ$  direction, and the  $0^\circ$  direction is also here the direction with the highest triaxiality level. In the  $45^\circ$  direction, the equivalent plastic strain rate is lower than in the other directions, see Figure 14c. This indicates that the plastic deformation is more dispersed over the specimen's cross-section, which is favourable to prevent strain localization. Again, the stress state is seen to drift from generalized tension ( $L = -1$ ) towards generalized shear ( $L = 0$ ) inside of the imperfection band, and the drift occurs first in the  $0^\circ$  direction exhibiting the lowest ductility. Also outside the band the Lode parameter is seen to evolve differently for different tensile directions due to the plastic anisotropy as defined by the yield surface.

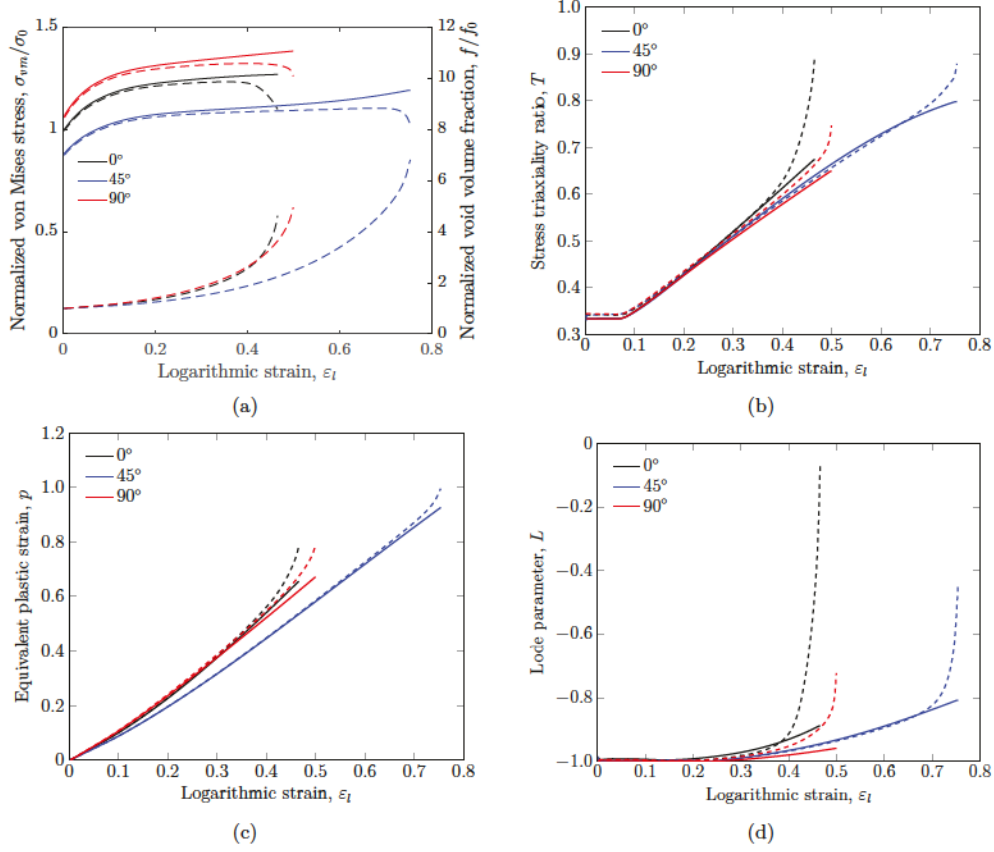


Figure 14: Local behaviour in the regions inside (dashed lines) and outside (solid lines) of the imperfection band for alloy B with temper T6 work hardening loaded in the ED-TD plane: (a) normalized von Mises stress and normalized void volume fraction, (b) stress triaxiality ratio, (c) equivalent plastic strain, and (d) Lode parameter versus logarithmic strain.

## 5. Discussion

390 The failure predictions presented in Figure 9 obtained in the strain localization analyses are found to capture the trends observed experimentally. In agreement with the experimental data in Figure 4, the localization analyses in Figure 9a give a lower failure strain for a material with a higher strength and lower work hardening. Also, the failure strain is observed to vary with plastic anisotropy and the influence of strength and work hardening is different depending on the alloy. Albeit good agreement is achieved between  
395 the numerical and experimental trends, there are certain mechanisms not included in the numerical study that can have a substantial effect on the failure strain. For instance, in the experiments for the AA6060 and AA6082.25 alloys, the difference in the failure strain between the O and T7 tempers and the T7 and T6 tempers is similar, but numerically a smaller difference is observed between the T7 and T6 tempers. A reasonable explanation for this finding is that the stress level for the T6 temper is sufficiently high to  
400 make void nucleation a more important mechanism for damage evolution (Pineau et al., 2016), which is not captured by the porous plasticity model used herein, considering only growth of pre-existing voids. For the AA6082.50 alloy, a large decrease in the failure strain between the O and T7 tempers is observed

experimentally. This finding and the lower overall ductility observed for the AA6082.50 alloy can be linked to the grain structure, as the large grains of this alloy increase the amount of intercrystalline fracture and reduce the tensile ductility (Frodal et al., 2017).

Although plastic anisotropy related to the crystallographic texture can lead to variations in the failure strain both between alloys and with tensile direction as seen in the numerical study, other sources of anisotropy can influence the ductile failure process and affect the fracture anisotropy. Even materials exhibiting nearly isotropic yielding and plastic flow can exhibit fracture anisotropy because of morphological or topological anisotropy caused by the shape, orientation and spatial distribution of voids and particles (Hannard et al., 2018). As investigated by Agarwal et al. (2002), the combination of loading direction and orientation of particles can affect the particle cracking process, and thus void nucleation by particle cracking can introduce anisotropic effects. Also the spatial distribution of particles and clusters can influence the void coalescence process and lead to fracture anisotropy (Hannard et al., 2018). It has also been shown by unit cell analyses that the void aspect ratio can significantly affect the overall ductility (Keralavarma et al., 2011) and that plastic anisotropy can amplify this effect (Legarth and Tvergaard, 2018).

It was quite apparent from Figure 10 that the plastic anisotropy has an influence on the fracture mode of the specimen, as the shape and extension of the regions of localized plastic flow vary with tensile direction for the anisotropic materials. The variation in shape of the regions can change the failure mode from cup-and-cone failure to slant shear failure depending on the plastic anisotropy and loading direction. These failure modes are typically observed experimentally for anisotropic materials (Chen et al., 2011; Fourmeau et al., 2013). This was also recently studied by Benzerga et al. (2019), who showed that anisotropic plasticity can effectively trigger shear bands and cause failure of ductile materials.

From the strain localization analyses, it was evident that the stress states in the regions inside and outside of the imperfection band depend on the plastic anisotropy of alloys A, B, and C, see Figure 12. The stress state inside of the imperfection band was seen to be strongly affected by the plastic anisotropy and this has a great influence on the failure strain. Higher work-hardening rate is favourable for delaying failure as it delays necking and distributes the plastic deformation over a wider area of the specimen's cross-section. This will in turn affect the local stress state inside the specimen so that, e.g., the stress triaxiality is reduced for a given value of the logarithmic strain over the neck, cf. Figure 13.

The failure strain varies with tensile direction for anisotropic materials and the plastic anisotropy of alloy B was found to affect the stress state both inside and outside of the imperfection band, see Figure 14. A lower stress level was observed to give an increase in the ductility, but also the value of the Lankford coefficient affects the ductility, since it governs the distribution of the plastic deformation across the specimen cross-section. A Lankford coefficient close to unity will distribute the plastic deformations more uniformly and thus be positive for the ductility, cf. Figure 11. Albeit a lower stress level, caused by the anisotropy in yield stress, appears to increase the ductility, the effect of the stress triaxiality and Lode parameter seems to be even greater. As an example, in the simulations of the tensile tests of alloy B, the stress level is lower in the  $0^\circ$  direction than in the  $90^\circ$  direction, but even so the ductility is lower in the former direction. The reason for the lower ductility in the  $0^\circ$  direction is that the stress triaxiality and the Lode parameter evolve in a favourable way for localization, which is more important than the lower stress level.

## 6. Concluding remarks

Three aluminium alloys with different grain structure and crystallographic texture, solution heat-treated and artificially aged to three conditions giving different strength and work-hardening behaviours, were considered in the study. Previous experiments on these materials had shown that the tensile ductility of the alloys decreased with higher strength and lower work hardening, and the ductility was different depending on the plastic anisotropy.

The influence of plastic anisotropy, strength and work hardening on ductile failure was studied by non-linear finite element simulations and strain localization analyses of tensile tests in various directions. The anisotropic yield surfaces of the aluminium alloys, previously obtained by the crystal plasticity finite element method, were used to construct a set of model materials. These yield surfaces and an isotropic yield surface



were combined with three flow stress curves representative for the different heat-treatments. Thus, a total of 12 model materials, with different plastic anisotropy, strength and work hardening were constructed and used in the numerical investigations. Finite element simulations of tensile tests on smooth axisymmetric specimens were conducted in seven in-plane directions, and the deformation gradient history extracted from the numerical simulations were used to drive the strain localization analyses.

Plastic anisotropy was found to have a marked influence on the tensile ductility and to induce fracture anisotropy. The shape and extension of the regions of localized plastic flow in the finite element simulations varied with tensile direction for the anisotropic materials. The highly deformed regions were found to vary in shape so that the failure mode changes from cup-and-cone failure to slant shear failure depending on the loading direction and plastic anisotropy. In agreement with experimental evidence from the literature (Fourmeau et al., 2013; Khadyko et al., 2019), the strain localization analyses predicted a variation of the failure strain with tensile direction that appears to correlate with the variation of the Lankford coefficient, thus indicating that the fracture anisotropy is closely linked to the plastic anisotropy for these aluminium alloys.

The strain localization analyses predict a higher ductility for materials with lower strength and higher work hardening, as these features lead to a more distributed plastic deformation and a stress state with a lower stress triaxiality in the neck. The redistribution of plastic deformation due to the high work hardening makes the tensile specimen less prone to localization and ductile failure. The influence of strength and work hardening on the tensile ductility is also found to depend on the plastic anisotropy.

## Acknowledgements

The financial support of this work from the Centre for Advanced Structural Analysis (CASA), Project No. 237885, Centre for Research-based Innovation (CRI) at the Norwegian University of Science and Technology (NTNU), is gratefully acknowledged.

## References

- Abaqus, 2014. Version 6.14. Dassault Systemès Simulia Corporation. Providence, Rhode Island, USA.
- Agarwal, H., Gokhale, A.M., Graham, S., Horstemeyer, M.F., 2002. Anisotropy of intermetallic particle cracking damage evolution in an Al-Mg-Si base wrought aluminum alloy under uniaxial compression. *Metallurgical and Materials Transactions A* 33, 3443–3448.
- Barlat, F., Aretz, H., Yoon, J., Karabin, M., Brem, J., Dick, R., 2005. Linear transformation-based anisotropic yield functions. *International Journal of Plasticity* 21, 1009 – 1039.
- Barsoum, I., Faleskog, J., 2007. Rupture mechanisms in combined tension and shear—micromechanics. *International Journal of Solids and Structures* 44, 5481 – 5498.
- Barsoum, I., Faleskog, J., 2011. Micromechanical analysis on the influence of the lode parameter on void growth and coalescence. *International Journal of Solids and Structures* 48, 925 – 938.
- Benzerga, A.A., Thomas, N., Herrington, J.S., 2019. Plastic flow anisotropy drives shear fracture. *Scientific Reports* 9, 1425.
- Chen, J., Madi, Y., Morgeneyer, T.F., Besson, J., 2011. Plastic flow and ductile rupture of a 2198 Al–Cu–Li aluminum alloy. *Computational Materials Science* 50, 1365 – 1371.
- Dæhli, L.E.B., Børvik, T., Hopperstad, O.S., 2016. Influence of loading path on ductile fracture of tensile specimens made from aluminium alloys. *International Journal of Solids and Structures* 88, 17 – 34.
- Dæhli, L.E.B., Faleskog, J., Børvik, T., Hopperstad, O.S., 2017a. Unit cell simulations and porous plasticity modelling for strongly anisotropic FCC metals. *European Journal of Mechanics - A/Solids* 65, 360 – 383.
- Dæhli, L.E.B., Morin, D., Børvik, T., Hopperstad, O.S., 2017b. Influence of yield surface curvature on the macroscopic yielding and ductile failure of isotropic porous plastic materials. *Journal of the Mechanics and Physics of Solids* 107, 253 – 283.
- Dunand, M., Mohr, D., 2014. Effect of lode parameter on plastic flow localization after proportional loading at low stress triaxialities. *Journal of the Mechanics and Physics of Solids* 66, 133 – 153.
- Engler, O., Randle, V., 2009. *Introduction to texture analysis: microtexture, microtexture, and orientation mapping*. Second ed., CRC press, Taylor & Francis Group.
- Fourmeau, M., Børvik, T., Benallal, A., Hopperstad, O.S., 2013. Anisotropic failure modes of high-strength aluminium alloy under various stress states. *International Journal of Plasticity* 48, 34 – 53.
- Fourmeau, M., Børvik, T., Benallal, A., Lademo, O.G., Hopperstad, O.S., 2011. On the plastic anisotropy of an aluminium alloy and its influence on constrained multiaxial flow. *International Journal of Plasticity* 27, 2005 – 2025.
- Frodal, B.H., Dæhli, L.E.B., Børvik, T., Hopperstad, O.S., 2019. Modelling and simulation of ductile failure in textured aluminium alloys subjected to compression-tension loading. *International Journal of Plasticity* 118, 36 – 69.

- 505 Frodal, B.H., Pedersen, K.O., Børvik, T., Hopperstad, O.S., 2017. Influence of pre-compression on the ductility of AA6xxx aluminium alloys. *International Journal of Fracture* 206, 131–149.
- Gruben, G., Morin, D., Langseth, M., Hopperstad, O.S., 2017. Strain localization and ductile fracture in advanced high-strength steel sheets. *European Journal of Mechanics - A/Solids* 61, 315 – 329.
- Guo, T.F., Wong, W.H., 2018. Void-sheet analysis on macroscopic strain localization and void coalescence. *Journal of the Mechanics and Physics of Solids* 118, 172 – 203.
- 510 Gurson, A.L., 1977. Continuum theory of ductile rupture by void nucleation and growth: Part I—Yield criteria and flow rules for porous ductile media. *Journal of Engineering Materials and Technology* 99, 2–15.
- Hannard, F., Pardoën, T., Maire, E., Bourlot, C.L., Mokso, R., Simar, A., 2016. Characterization and micromechanical modelling of microstructural heterogeneity effects on ductile fracture of 6xxx aluminium alloys. *Acta Materialia* 103, 558 – 572.
- 515 Hannard, F., Simar, A., Maire, E., Pardoën, T., 2018. Quantitative assessment of the impact of second phase particle arrangement on damage and fracture anisotropy. *Acta Materialia* 148, 456 – 466.
- Keralavarma, S.M., Hoelscher, S., Benzerga, A.A., 2011. Void growth and coalescence in anisotropic plastic solids. *International Journal of Solids and Structures* 48, 1696 – 1710.
- 520 Khadyko, M., Dumoulin, S., Børvik, T., Hopperstad, O.S., 2014. An experimental–numerical method to determine the work-hardening of anisotropic ductile materials at large strains. *International Journal of Mechanical Sciences* 88, 25 – 36.
- Khadyko, M., Morin, D., Børvik, T., Hopperstad, O.S., 2019. Tensile ductility of extruded aluminium alloy AA6063 in different tempers. *Materials Science and Engineering: A* 744, 500 – 511.
- Legarth, B.N., Tvergaard, V., 2018. Effects of plastic anisotropy and void shape on full three-dimensional void growth. *Journal of Applied Mechanics* 85, 051007.
- 525 Lloyd, D.J., 2003. The scaling of the tensile ductile fracture strain with yield strength in Al alloys. *Scripta Materialia* 48, 341 – 344.
- Marciniak, Z., Kuczyński, K., 1967. Limit strains in the processes of stretch-forming sheet metal. *International Journal of Mechanical Sciences* 9, 609 – 620.
- 530 Morin, D., Dæhli, L.E.B., Børvik, T., Benallal, A., Hopperstad, O.S., 2019. Numerical study of ductile failure under non-proportional loading. *European Journal of Mechanics - A/Solids* 74, 221 – 241.
- Morin, D., Fourmeau, M., Børvik, T., Benallal, A., Hopperstad, O.S., 2018b. Anisotropic tensile failure of metals by the strain localization theory: An application to a high-strength aluminium alloy. *European Journal of Mechanics - A/Solids* 69, 99 – 112.
- 535 Morin, D., Hopperstad, O.S., Benallal, A., 2018a. On the description of ductile fracture in metals by the strain localization theory. *International Journal of Fracture* 209, 27–51.
- Nahshon, K., Hutchinson, J.W., 2008. Modification of the gurson model for shear failure. *European Journal of Mechanics - A/Solids* 27, 1 – 17.
- Needleman, A., Rice, J.R., 1978. Limits to ductility set by plastic flow localization. *Mechanics of Sheet Metal Forming: Material Behavior and Deformation Analysis*, 237–267.
- 540 Pedersen, K.O., Westermann, I., Furu, T., Børvik, T., Hopperstad, O.S., 2015. Influence of microstructure on work-hardening and ductile fracture of aluminium alloys. *Materials & Design* 70, 31 – 44.
- Pineau, A., Benzerga, A.A., Pardoën, T., 2016. Failure of metals I: Brittle and ductile fracture. *Acta Materialia* 107, 424 – 483.
- 545 Rice, J.R., 1976. Localization of plastic deformation. In: *14th International Congress of Theoretical and Applied Mechanics*, 207 – 220.
- Rudnicki, J.W., Rice, J.R., 1975. Conditions for the localization of deformation in pressure-sensitive dilatant materials. *Journal of the Mechanics and Physics of Solids* 23, 371 – 394.
- Tekoğlu, C., Hutchinson, J.W., Pardoën, T., 2015. On localization and void coalescence as a precursor to ductile fracture. *Philosophical Transactions of the Royal Society A: Mathematical, Physical and Engineering Sciences* 373, 20140121.
- 550 Tvergaard, V., 1981. Influence of voids on shear band instabilities under plane strain conditions. *International Journal of Fracture* 17, 389–407.
- Westermann, I., Pedersen, K.O., Furu, T., Børvik, T., Hopperstad, O.S., 2014. Effects of particles and solutes on strength, work-hardening and ductile fracture of aluminium alloys. *Mechanics of Materials* 79, 58 – 72.
- 555 Xue, Z., Faleskog, J., Hutchinson, J.W., 2013. Tension-torsion fracture experiments – Part II: Simulations with the extended Gurson model and a ductile fracture criterion based on plastic strain. *International Journal of Solids and Structures* 50, 4258 – 4269.
- Xue, Z., Pontin, M.G., Zok, F.W., Hutchinson, J.W., 2010. Calibration procedures for a computational model of ductile fracture. *Engineering Fracture Mechanics* 77, 492 – 509.
- 560 Zhang, H., Diehl, M., Roters, F., Raabe, D., 2016. A virtual laboratory using high resolution crystal plasticity simulations to determine the initial yield surface for sheet metal forming operations. *International Journal of Plasticity* 80, 111 – 138.
- Zhang, K., Holmedal, B., Hopperstad, O.S., Dumoulin, S., Gawad, J., Van Bael, A., Van Houtte, P., 2015. Multi-level modelling of mechanical anisotropy of commercial pure aluminium plate: Crystal plasticity models, advanced yield functions and parameter identification. *International Journal of Plasticity* 66, 3 – 30.



# PART 4

Bjørn Håkon Frodal, Emil Christiansen, Ole Runar Myhr,  
Odd Sture Hopperstad

**The role of quench rate on the plastic flow and  
fracture of three aluminium alloys with different  
grain structure and texture**

To be submitted for journal publication.



This paper is awaiting publication and is not included in NTNU Open



# Appendices



## **A Single crystal plasticity model**

In the following, a report for the implementation and verification of the rate-dependent single crystal plasticity model used in Part 2 of the thesis is presented.





---

## Implementation and Verification of a Rate-Dependent Single Crystal Plasticity Model

---

SIMLab Crystal Mechanics model - Hypoelastic formulation  
SCMM-Hypo  
Version 1.0.0

*Bjørn Håkon Frodal*

Faculty of Engineering  
Department of Structural Engineering  
SIMLab - Structural Impact Laboratory  
CASA - Centre for Advanced Structural Analysis

July 1, 2019

### **Abstract**

In this report, a rate dependent single crystal plasticity model has been implemented in a standalone code and as user-defined material subroutines in the commercial finite element code Abaqus. A standalone code for polycrystals has also been implemented using the full constraint (FC) Taylor approach. A forward Euler method is used to integrate the response of the single crystal in time using a hypoelastic formulation of the constitutive relation. The hypoelastic model was compared to a hyperelastic model and another hypoelastic model in simple shear for four different initial orientations. For two of the orientations, the response of the hypoelastic model agreed with the hyperelastic model, but for the other two orientations, differences were observed for large strains, whereas the results from the two hypoelastic models agreed.

# Contents

Abstract	i
Contents	ii
<b>1 Introduction</b>	<b>1</b>
<b>2 Theoretical Framework</b>	<b>2</b>
2.1 Crystalline Materials	2
2.2 Kinematics of Single Crystals	2
2.3 Rate Dependent Single Crystal Plasticity	4
2.4 Work-Hardening	5
2.4.1 The Extended Voce Hardening Model	5
2.4.2 The Hardening Model by Kalidindi et al.	6
2.5 Crystal Orientation	6
<b>3 Algorithm and Implementation</b>	<b>8</b>
3.1 Forward Euler Method	8
3.1.1 Substepping	8
3.1.2 Numerical Integration	8
3.2 Implementation	10
3.2.1 Standalone Code for Single Crystal Plasticity (Fortran Program)	10
3.2.2 Standalone Code for Polycrystal Plasticity (FC-Taylor Program)	10
3.2.3 Material Subroutine for Abaqus Explicit (VUMAT)	12
3.2.4 Material Subroutine for Abaqus Standard (UMAT)	13
<b>4 Verification</b>	<b>14</b>
4.1 Single Crystal Response	14
4.1.1 Simple Shear	15
4.1.2 Hypo- vs. Hyper-elastic	18
4.2 Polycrystal Response	19
<b>5 Concluding Remarks</b>	<b>22</b>
References	24
<b>A Appendix</b>	<b>25</b>
A.1 Slip Systems for FCC Crystals	25
A.2 von Mises Equivalent Stress	25
A.3 von Mises Equivalent Plastic Strain	25
<b>B User Input/Output</b>	<b>27</b>
B.1 Subroutine Input	27
B.2 Solution-Dependent State Variables	27
B.3 FC-Taylor Input	28

# 1 | Introduction

In this report, a rate dependent single crystal plasticity model has been implemented in a standalone code and as user-defined material subroutines in the commercial finite element code Abaqus (Abaqus, 2014). Using the full-constraint (FC) Taylor approach, a standalone code for polycrystals has also been implemented. A forward Euler method (Hopperstad and Børvik, 2016) is used to integrate the response of the single crystal in time using a hypoelastic formulation of the constitutive relation. The hypoelastic rate dependent crystal plasticity model will at the end be compared to a hyperelastic crystal plasticity model based on a forward Euler scheme proposed by Grujic and Batchu (2002), and another hypoelastic model by Zhang et al. (2014).

The report will first give a brief overview of the theoretical framework of single crystal plasticity along with definitions used in the following. Then, give an overview of the algorithm and implementation of the model and further verify and compare the hypoelastic model to the hyperelastic model. Further, the FC-Taylor program is demonstrated and compared to results from crystal plasticity simulations with the finite element method (CP-FEM).

The input parameters and solution-dependent variables for the user-defined material subroutine implemented are found in the Appendix along with parameters for the FC-Taylor program.



## 2 | Theoretical Framework

In this Chapter, the theoretical framework for single crystal plasticity will be outlined and is the basis for the next chapters. The reader is referred to Khan and Huang (1995), Belytschko et al. (2014), and Hopperstad and Børvik (2016) for further theory.

### 2.1 Crystalline Materials

There exist many atomistic structures that materials can possess. Most metals have an organized crystal structure forming a crystal lattice that extends in all directions. Some crystal structures commonly found in metals are face-centred cubic (FCC), body-centred cubic (BCC) and hexagonal close packing (HCP) (Buehler, 2008). Figure 2.1 displays these crystal structures. Most materials found in nature are not perfect single crystalline materials, and most metals such as aluminium are polycrystalline materials. They are composed of several crystals connected at the grain boundaries.

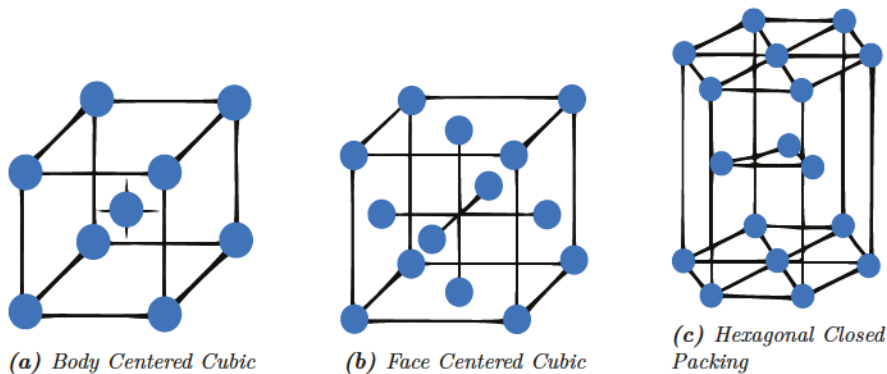


**Figure 2.1:** Overview of different crystal structures, displaying (a) BCC, (b) FCC and (c) HCP crystal structure.

Dislocations are the main mechanism for plastic deformation in a crystalline material. In the single crystal plasticity model outlined in the following chapters, plastic deformation is assumed to occur by plastic slip on certain crystallographic slip systems. These slip systems are given by the crystal structure and are defined for an FCC structure in Appendix A.1. The report will further only consider FCC materials although the crystal plasticity model presented in the following sections is also valid for other crystal structures.

### 2.2 Kinematics of Single Crystals

In this section the mathematical foundation for the kinematics of single crystals will be established. The plastic deformation is assumed to occur via plastic slip on certain crystallographic slip systems,  $\alpha$ , defined by a slip normal,  $\mathbf{n}^{(\alpha)}$  and a slip direction,  $\mathbf{m}^{(\alpha)}$ . The number of slip systems is given by the crystal structure and is  $n_s = 12$  for an FCC crystal. In the following the elastic deformations are assumed to be small, while the plastic deformations and rotations can

be finite. The velocity gradient,  $\mathbf{L}$ , can be decomposed into a symmetric and a skew-symmetric part as

$$L_{ij} = D_{ij} + W_{ij} = \frac{\partial v_i}{\partial x_j} \quad (2.1)$$

where  $\mathbf{D}$  is the symmetric rate of deformation tensor,  $\mathbf{W}$  is the skew-symmetric spin tensor,  $\mathbf{v}$  is the velocity field and  $\mathbf{x}$  is the position vector in the current configuration. The velocity gradient can be additively decomposed into an elastic and a plastic part

$$L_{ij} = L_{ij}^e + L_{ij}^p \quad (2.2)$$

where  $\blacksquare^e$  will in the following denote any elastic quantity and  $\blacksquare^p$  any plastic quantity. It follows from the above equations that the rate of deformation tensor and the spin tensor can be additively decomposed into an elastic and a plastic part

$$D_{ij} = D_{ij}^e + D_{ij}^p, \quad W_{ij} = W_{ij}^e + W_{ij}^p \quad (2.3)$$

Using the fact that plastic slip occurs on certain slip systems, the plastic part of the velocity gradient can be written as

$$L_{ij}^p = \sum_{\alpha=1}^{n_s} \dot{\gamma}^{(\alpha)} m_i^{(\alpha)} n_j^{(\alpha)} = \sum_{\alpha=1}^{n_s} \dot{\gamma}^{(\alpha)} S_{ij}^{(\alpha)} \quad (2.4)$$

where  $\dot{\gamma}^{(\alpha)}$  is the plastic shear strain rate on slip system  $\alpha$ , and the Schmid tensor  $\mathbf{S}^{(\alpha)} = \mathbf{m}^{(\alpha)} \otimes \mathbf{n}^{(\alpha)}$  has been introduced. The plastic rate of deformation tensor and the plastic spin tensor are then given by the symmetric and skew-symmetric part of the plastic velocity gradient, respectively

$$D_{ij}^p = \frac{1}{2} \sum_{\alpha=1}^{n_s} \dot{\gamma}^{(\alpha)} (S_{ij}^{(\alpha)} + S_{ji}^{(\alpha)}), \quad W_{ij}^p = \frac{1}{2} \sum_{\alpha=1}^{n_s} \dot{\gamma}^{(\alpha)} (S_{ij}^{(\alpha)} - S_{ji}^{(\alpha)}) \quad (2.5)$$

The crystal lattice is assumed to rotate with the elastic spin  $\mathbf{W}^e$ , i.e., the slip normals and the slip directions rotate with the elastic spin, which contains spin from rigid body rotation and spin from elastic deformations

$$\dot{m}_i^{(\alpha)} = W_{ij}^e m_j^{(\alpha)}, \quad \dot{n}_i^{(\alpha)} = W_{ij}^e n_j^{(\alpha)} \quad (2.6)$$

It is convenient to define a co-rotational coordinate system that rotates with the crystal lattice, which will be free of rigid body rotations. Then the rotation tensor,  $\mathfrak{R}$ , describing this rotation, will evolve according to the evolution law

$$\dot{\mathfrak{R}}_{ij} = W_{ik}^e \mathfrak{R}_{kj}, \quad \mathfrak{R}_{ik} \mathfrak{R}_{jk} = \mathfrak{R}_{ki} \mathfrak{R}_{kj} = \delta_{ij} \quad (2.7)$$

The rotation tensor is an orthogonal tensor and the co-rotational basis system,  $\hat{\mathbf{e}}_i$ , is related to the global or fixed basis,  $\mathbf{e}_i$ , as

$$\hat{\mathbf{e}}_i = \mathfrak{R} \cdot \mathbf{e}_i \quad (2.8)$$

In the following  $\hat{\blacksquare}$  will denote a quantity given in the co-rotational coordinate system w.r.t  $\mathfrak{R}$ . The components of the slip normals and slip directions in the co-rotated coordinate system are related to the components of the slip normals and the slip directions in the global coordinate system as

$$m_i^{(\alpha)} = \mathfrak{R}_{ij} \hat{m}_j^{(\alpha)}, \quad n_i^{(\alpha)} = \mathfrak{R}_{ij} \hat{n}_j^{(\alpha)} \quad \Rightarrow \quad S_{ij}^{(\alpha)} = \mathfrak{R}_{ik} \hat{S}_{kl}^{(\alpha)} \mathfrak{R}_{jl} \quad (2.9)$$

where the components of the slip normals and slip directions are constant in the lattice frame, i.e., the co-rotational coordinate system, and thus also the Schmid tensor components. The components of the rate of deformation tensor in the global and co-rotated coordinate systems are related by

$$D_{ij} = \mathfrak{R}_{ik} \hat{D}_{kl} \mathfrak{R}_{jl} \quad (2.10)$$

### 2.3 Rate Dependent Single Crystal Plasticity

Schmid's law states that plastic slip will occur on a certain slip system when the magnitude of the resolved shear stress on the slip plane given by its normal,  $\mathbf{n}^{(\alpha)}$ , and along the slip direction,  $\mathbf{m}^{(\alpha)}$ , reaches a critical value, i.e.,

$$|\tau^{(\alpha)}| \geq \tau_c^{(\alpha)} \Rightarrow \text{Plastic slip} \quad (2.11)$$

where  $\tau^{(\alpha)}$  is the resolved shear stress and  $\tau_c^{(\alpha)}$  is the critical resolved shear stress also called the slip resistance on slip system  $\alpha$ . The resolved shear stress,  $\tau^{(\alpha)}$  is given by

$$\tau^{(\alpha)} = n_i^{(\alpha)} \sigma_{ij} m_j^{(\alpha)} = \sigma_{ij} S_{ij}^{(\alpha)} = \hat{\sigma}_{ij} \hat{S}_{ij}^{(\alpha)} = \frac{1}{2} \hat{\sigma}_{ij} (\hat{S}_{ij}^{(\alpha)} + \hat{S}_{ji}^{(\alpha)}) \quad (2.12)$$

where the Schmid tensor has been used and the fact that the Cauchy stress tensor is symmetric.

To circumvent the Taylor ambiguity (see e.g. Hopperstad and Børvik, 2016) present for rate independent crystal plasticity and to accommodate that most metals are rate sensitive, a rate dependent crystal plasticity (RDCP) formulation will be used in the present work. The plastic shear rate on slip system  $\alpha$  is here given by the constitutive relation

$$\dot{\gamma}^{(\alpha)} = \dot{\gamma}_0 \left| \frac{\tau^{(\alpha)}}{\tau_c^{(\alpha)}} \right|^{\frac{1}{m}} \text{sgn}(\tau^{(\alpha)}) \quad (2.13)$$

where  $\dot{\gamma}_0$  is a reference slip rate,  $m$  is the instantaneous strain rate sensitivity and  $\text{sgn}(x)$  is defined as

$$\text{sgn}(x) = \begin{cases} +1 & \text{if } x > 0 \\ 0 & \text{if } x = 0 \\ -1 & \text{if } x < 0 \end{cases} \quad (2.14)$$

For the case of RDCP a yield condition does not exist, i.e., plastic slip takes place for  $|\tau^{(\alpha)}| > 0$ , but for small rate sensitivities,  $m$ , the plastic shear rate will be negligible when  $|\tau^{(\alpha)}| < \tau_c^{(\alpha)}$ . Then Schmid's law, given by Equation 2.11, is approximately satisfied.

During plastic deformation, the single crystal will work-harden due to accumulation of dislocations, i.e., the critical resolved shear stress will evolve due to plastic deformation. The evolution of the critical resolved shear stress is here given by

$$\dot{\tau}_c^{(\alpha)} = \sum_{\beta=1}^{n_s} h_{\alpha\beta} |\dot{\gamma}^{(\beta)}| \quad (2.15)$$

where  $h_{\alpha\beta}$  is the instantaneous strain hardening matrix, see Section 2.4 for further details.

In the co-rotational coordinate system, the rate form of the generalized Hooke's law can be expressed as

$$\dot{\hat{\sigma}}_{ij} = \hat{C}_{ijkl} \hat{D}_{kl}^e \quad (2.16)$$

where the forth-order elasticity tensor  $\hat{C}_{ijkl}$  is assumed invariant of plastic deformation and is constant in the co-rotational lattice frame. The elasticity tensor  $\hat{C}_{ijkl}$  accounts for the elastic anisotropy of the crystal, and will in the following be described by three independent elastic constants. In numerical implementations it is convenient to introduce matrix notation, thus

transforming Equation 2.16 into

$$\begin{bmatrix} \dot{\hat{\sigma}}_{11} \\ \dot{\hat{\sigma}}_{22} \\ \dot{\hat{\sigma}}_{33} \\ \dot{\hat{\sigma}}_{12} \\ \dot{\hat{\sigma}}_{23} \\ \dot{\hat{\sigma}}_{31} \end{bmatrix} = \begin{bmatrix} \hat{c}_{11} & \hat{c}_{12} & \hat{c}_{12} & 0 & 0 & 0 \\ \hat{c}_{12} & \hat{c}_{11} & \hat{c}_{12} & 0 & 0 & 0 \\ \hat{c}_{12} & \hat{c}_{12} & \hat{c}_{11} & 0 & 0 & 0 \\ 0 & 0 & 0 & \hat{c}_{44} & 0 & 0 \\ 0 & 0 & 0 & 0 & \hat{c}_{44} & 0 \\ 0 & 0 & 0 & 0 & 0 & \hat{c}_{44} \end{bmatrix} \begin{bmatrix} \hat{D}_{11}^e \\ \hat{D}_{22}^e \\ \hat{D}_{33}^e \\ 2\hat{D}_{12}^e \\ 2\hat{D}_{23}^e \\ 2\hat{D}_{31}^e \end{bmatrix} \quad (2.17)$$

where  $\hat{c}_{11}$ ,  $\hat{c}_{12}$  and  $\hat{c}_{44}$  are the independent elastic constants.

The plastic dissipation for the RDCP model is given by

$$\mathfrak{D}_p = \sigma_{ij} D_{ij}^p = \hat{\sigma}_{ij} \hat{D}_{ij}^p = \sum_{\alpha=1}^{n_s} \tau^{(\alpha)} \dot{\gamma}^{(\alpha)} = \sum_{\alpha=1}^{n_s} \dot{\gamma}_0 \left| \tau^{(\alpha)} \right| \left| \frac{\tau^{(\alpha)}}{\tau_c^{(\alpha)}} \right|^{\frac{1}{m}} \geq 0 \quad (2.18)$$

where it is easily seen that the plastic dissipation is non-negative for non-negative reference slip rates.

## 2.4 Work-Hardening

The work-hardening of the single crystal is given by Equation 2.15, where the instantaneous strain hardening matrix,  $h_{\alpha\beta}$ , describes the hardening behaviour. This matrix can be divided into a latent hardening matrix,  $q_{\alpha\beta}$ , and a single slip hardening rate,  $\Theta_\beta$  as

$$h_{\alpha\beta} = q_{\alpha\beta} \Theta_\beta \quad (\text{no sum on } \beta) \quad (2.19)$$

Here, the latent hardening matrix will control the degree of latent hardening on a slip system, i.e., how much slip system  $\alpha$  is hardened due to slip on system  $\beta$ .

To describe the single slip hardening rate, two different models will be introduced in the present work: one model based on an extended Voce hardening rule (Saai et al., 2013) and another model after Kalidindi et al. (1992).

### 2.4.1 The Extended Voce Hardening Model

Here the latent hardening matrix is given by (Saai et al., 2013)

$$[q_{\alpha\beta}] = \begin{bmatrix} 1 & \text{if } \alpha = \beta \\ q & \text{if } \alpha \neq \beta \end{bmatrix} \quad (2.20)$$

where  $q$  is the latent hardening coefficient with a typical value of  $q = 1.4$ .

The accumulated plastic shear strain,  $\Gamma$ , is introduced as

$$\Gamma = \int_0^t \sum_{\alpha=1}^{n_s} \left| \dot{\gamma}^{(\alpha)} \right| dt \quad (2.21)$$

The relation between the critical resolved shear stress and the accumulated plastic shear strain is given by the extended Voce hardening rule as

$$\tau_c^{(\beta)} = \tau_c(\Gamma) = \tau_{c0} + \sum_{k=1}^{n_V} \tau_k \left( 1 - \exp\left(-\frac{\theta_k}{\tau_k} \Gamma\right) \right) \quad (2.22)$$

where  $\tau_{c0}$  is the initial critical resolved shear stress,  $\tau_k$  is the saturated value for hardening term  $k$ ,  $\theta_k$  is the initial hardening rate for term  $k$ , and  $n_V$  is the number of hardening terms set equal to two in the present work. The single slip hardening rate,  $\Theta_\beta$ , is then derived by taking the derivative of Equation 2.22 with respect to  $\Gamma$

$$\Theta_\beta = \Theta(\Gamma) = \frac{d\tau_c(\Gamma)}{d\Gamma} = \sum_{k=1}^{n_V} \theta_k \exp\left(-\frac{\theta_k}{\tau_k} \Gamma\right) \quad (2.23)$$

Note that the single slip hardening rate,  $\Theta_\beta = \Theta$ , is equal for all slip systems  $\beta$ .

#### 2.4.2 The Hardening Model by Kalidindi et al.

Here the latent hardening matrix is given by (Kalidindi et al., 1992)

$$[q_{\alpha\beta}] = \begin{bmatrix} \mathbf{A} & q\mathbf{A} & q\mathbf{A} & q\mathbf{A} \\ q\mathbf{A} & \mathbf{A} & q\mathbf{A} & q\mathbf{A} \\ q\mathbf{A} & q\mathbf{A} & \mathbf{A} & q\mathbf{A} \\ q\mathbf{A} & q\mathbf{A} & q\mathbf{A} & \mathbf{A} \end{bmatrix}, \quad \mathbf{A} = \begin{bmatrix} 1 & 1 & 1 \\ 1 & 1 & 1 \\ 1 & 1 & 1 \end{bmatrix} \quad (2.24)$$

where  $q$  is the latent hardening coefficient with the typical value of  $q = 1.4$ . The slip systems  $\{1,2,3\}$ ,  $\{4,5,6\}$ ,  $\{7,8,9\}$  and  $\{10,11,12\}$ , given in Appendix A.1, are coplanar. The latent hardening rate for coplanar slip systems is taken to be equal to the self-hardening rate.

The single slip hardening rate,  $\Theta_\beta$ , is introduced as a function of the critical resolved shear stress on slip system  $\beta$  as

$$\Theta_\beta = \Theta\left(\tau_c^{(\beta)}\right) = h_0 \left(1 - \frac{\tau_c^{(\beta)}}{\tau_s}\right)^a \quad (2.25)$$

where  $h_0$  is the initial hardening rate,  $a$  is a slip system hardening parameter and  $\tau_s$  is the saturation value of  $\tau_c^{(\beta)}$ .

## 2.5 Crystal Orientation

The single crystal is not always oriented such that its local orientation is aligned with the global coordinate system. In a polycrystal the individual crystals can have different orientations, and the orientation of the different crystals is defined by the transformation matrix

$$[a_{ij}] = \begin{bmatrix} \cos \varphi_1 \cos \varphi_2 - \sin \varphi_1 \sin \varphi_2 \cos \Phi & \sin \varphi_1 \cos \varphi_2 + \cos \varphi_1 \sin \varphi_2 \cos \Phi & \sin \varphi_2 \sin \Phi \\ -\cos \varphi_1 \sin \varphi_2 - \sin \varphi_1 \cos \varphi_2 \cos \Phi & -\sin \varphi_1 \sin \varphi_2 + \cos \varphi_1 \cos \varphi_2 \cos \Phi & \cos \varphi_2 \sin \Phi \\ \sin \varphi_1 \sin \Phi & -\cos \varphi_1 \sin \Phi & \cos \Phi \end{bmatrix}$$

where  $0 \leq \varphi_1 \leq 2\pi$ ,  $0 \leq \Phi \leq \pi$ ,  $0 \leq \varphi_2 \leq 2\pi$  are the Bunge definition of the Euler angles, representing a rotation in 3D-space. Engler and Randle (2010) defines the rotations as

$\varphi_1$  about the  $z$ -direction, transforming the  $y$ -direction into  $y'$ -direction and the  $x$ -direction into  $x'$ -direction

$\Phi$  about the  $x'$ -direction (in its new orientation)

$\varphi_2$  about the  $z''$ -direction (in its new orientation)

In the present work the initial condition to the rotation tensor,  $\mathfrak{R}$ , will be given by

$$\mathfrak{R}_{ij,0} = a_{ji} \left(\varphi_1^0, \Phi^0, \varphi_2^0\right) \quad (2.26)$$



where  $\{\varphi_1^0, \Phi^0, \varphi_2^0\}$  are the initial values of the Euler angles. While the evolution of the Euler angles,  $\{\varphi_1, \Phi, \varphi_2\}$ , can be calculated by solving for the Euler angles in the following relation

$$a_{ji}(\varphi_1, \Phi, \varphi_2) = \mathfrak{R}_{ij} \quad (2.27)$$

Note that  $\mathfrak{R}$  is the transpose of the transformation matrix  $\mathbf{a}$ , defined above.

## 3 | Algorithm and Implementation

### 3.1 Forward Euler Method

#### 3.1.1 Substepping

In the present work, the forward Euler method given in Section 8.2.8 of Hopperstad and Børvik (2016) is used to integrate the constitutive equations of the RDCP model. The forward Euler method is an explicit method and only conditionally stable, i.e., if the time step used, exceeds a critical time step,  $\Delta t_{crit}$ , the solution will diverge. It is therefore convenient to impose a constraint on the time step allowed, to ensure a converged solution. In practice, instability is detected when,  $\max(\dot{\gamma}^{(\alpha)}\Delta t) = \max(\Delta\gamma^{(\alpha)}) \geq \Delta\gamma_{crit}$  (Zhang et al., 2014), where  $\Delta\gamma_{crit}$  is a critical shear strain increment determined empirically. Thus  $\max(\Delta\gamma^{(\alpha)})$  must be less than or equal to  $\Delta\gamma_{crit}$  for a converged solution.

Since the plastic part of the rate of deformation tensor,  $D_{ij}^p$ , is linearly dependent on the shear strain rates,  $\dot{\gamma}^{(\alpha)}$ , a similar constraint can be formulated on the plastic strain increments,  $\Delta\varepsilon_{ij}^p = D_{ij}^p\Delta t$ . Assuming that the elastic strain increments,  $\Delta\varepsilon_{ij}^e = D_{ij}^e\Delta t$ , are negligible, a constraint can be formulated by use of the total strain increment,  $\Delta\varepsilon_{ij} = D_{ij}\Delta t$  as

$$\|\Delta\varepsilon\| = \sqrt{\Delta\varepsilon_{ij}\Delta\varepsilon_{ij}} \leq \Delta\varepsilon_{crit} \quad (3.1)$$

where  $\Delta\varepsilon_{crit}$  is a critical strain increment. To satisfy Equation 3.1, the incremental step can be divided into  $n_{sub}$  number of substeps.

$$n_{sub} = \left\lceil \frac{\|\Delta\varepsilon\|}{\Delta\varepsilon_{sub}} \right\rceil \quad (3.2)$$

where  $\Delta\varepsilon_{sub}$  is a substep increment such that  $\Delta\varepsilon_{sub} \leq \Delta\varepsilon_{crit}$  and  $\text{ceiling}(x) = \lceil x \rceil$  is the smallest integer greater than or equal to  $x$ . The velocity gradient is assumed constant during the time step  $\Delta t$ .

#### 3.1.2 Numerical Integration

In this section a slightly modified version of the integration algorithm given in Section 8.2.8 of Hopperstad and Børvik (2016) will be outlined, as to include the primitive substepping algorithm given in Section 3.1.1. The input to the material update algorithm will be the quantities  $\sigma_{ij,n}$ ,  $\Gamma_n$ ,  $\tau_{c,n}^{(\alpha)}$  and  $\mathfrak{R}_{ij,n}$  determined from the previous step. The velocity gradient is assumed constant and equal to  $L_{ij,n+1/2} = \frac{1}{2}(L_{ij,n} + L_{ij,n+1})$  during the time step  $\Delta t_{n+1} = t_{n+1} - t_n$ . The incremental strain and rotation tensors are then calculated as  $\Delta\varepsilon_{ij,n+1} = D_{ij,n+1/2}\Delta t_{n+1}$  and  $\Delta\omega_{ij,n+1} = W_{ij,n+1/2}\Delta t_{n+1}$ , in the global coordinate system. The slip systems defined by the slip normal,  $\mathbf{n}^{(\alpha)}$ , and the slip direction,  $\mathbf{m}^{(\alpha)}$ , have constant components in the co-rotational coordinate system, given in Appendix A.1 for FCC crystals.

1. Based on Equation 2.10, transform  $\sigma_{ij,n}$  into the co-rotational coordinate system using the rotation tensor,  $\mathfrak{R}_{ij,n}$  at  $t_n$

$$\hat{\sigma}_{ij,n} = \mathfrak{R}_{mi,n}\sigma_{ml,n}\mathfrak{R}_{lj,n}$$

2. Calculate the number of substeps based on Equation 3.2

$$n_{sub} = \left\lceil \frac{\sqrt{\Delta\varepsilon_{ij,n+1}\Delta\varepsilon_{ij,n+1}}}{\Delta\varepsilon_{sub}} \right\rceil$$

3. Calculate the incremental strain and rotation tensors used in the substep, along with the time increment associated with each substep

$$\delta\varepsilon_{ij,k+1} = \frac{\Delta\varepsilon_{ij,n+1}}{n_{sub}}, \quad \delta\omega_{ij,k+1} = \frac{\Delta\omega_{ij,n+1}}{n_{sub}}, \quad \delta t_{k+1} = \frac{\Delta t_{n+1}}{n_{sub}}$$

- Loop over all the substeps,  $k = 0, \dots, n_{sub} - 1$
- Transform  $\delta\varepsilon_{ij,k+1}$  into the co-rotational coordinate system using the rotation tensor,  $\mathfrak{R}_{ij,k}$  at  $t_n + k\delta t_{k+1}$

$$\delta\hat{\varepsilon}_{ij,k+1} = \mathfrak{R}_{mi,k}\delta\varepsilon_{ml,k+1}\mathfrak{R}_{lj,k} \quad (3.3)$$

- Calculate the resolved shear stresses at  $t_n + k\delta t_{k+1}$  using Equation 2.12

$$\tau_k^{(\alpha)} = \hat{\sigma}_{ij,k}\hat{S}_{ij}^{(\alpha)}$$

- Estimate the shear strain increments, using the shear strain rates at  $t_n + k\delta t_{k+1}$ , Equation 2.13

$$\delta\gamma_{k+1}^{(\alpha)} \approx \delta t_{k+1}\dot{\gamma}_k^{(\alpha)} = \delta t_{k+1}\dot{\gamma}_0 \left| \frac{\tau_k^{(\alpha)}}{\tau_{c,k}^{(\alpha)}} \right|^{\frac{1}{m}} \text{sgn}(\tau_k^{(\alpha)})$$

- Based on Equation 2.5, calculate the incremental plastic strains and rotations during the time step  $\delta t_{k+1}$  in the co-rotated coordinate system

$$\delta\hat{\varepsilon}_{ij,k+1}^p = \frac{1}{2} \sum_{\alpha=1}^{n_s} \delta\gamma_{k+1}^{(\alpha)} \left( \hat{S}_{ij}^{(\alpha)} + \hat{S}_{ji}^{(\alpha)} \right), \quad \delta\hat{\omega}_{ij,k+1}^p = \frac{1}{2} \sum_{\alpha=1}^{n_s} \delta\gamma_{k+1}^{(\alpha)} \left( \hat{S}_{ij}^{(\alpha)} - \hat{S}_{ji}^{(\alpha)} \right)$$

- Update the Cauchy stress tensor in the co-rotated coordinate system, based on the rate form of the generalized Hooke's law, Equation 2.16

$$\hat{\sigma}_{ij,k+1} = \hat{\sigma}_{ij,k} + \delta\hat{\sigma}_{ij,k+1} = \hat{\sigma}_{ij,k} + \hat{C}_{ijml} \left( \delta\hat{\varepsilon}_{ml,k+1} - \delta\hat{\varepsilon}_{ml,k+1}^p \right)$$

- Update the critical resolved shear stresses based on Equation 2.15

$$\tau_{c,k+1}^{(\alpha)} = \tau_{c,k}^{(\alpha)} + \sum_{\beta=1}^{n_s} h_{\alpha\beta,k} \left| \delta\gamma_{k+1}^{(\beta)} \right|$$

where  $h_{\alpha\beta,k}$  is  $h_{\alpha\beta}(\Gamma_k)$  for the extended Voce hardening rule and  $h_{\alpha\beta}(\tau_{c,k}^{(\beta)})$  for the hardening model after Kalidindi et al. (1992), see Section 2.4.

- Update the accumulated plastic shear strain, based on Equation 2.21

$$\Gamma_{k+1} = \Gamma_k + \sum_{\alpha=1}^{n_s} \left| \delta\gamma_{k+1}^{(\alpha)} \right|$$

- Calculate the incremental elastic rotation during the time step  $\delta t_{k+1}$  in the global coordinate system

$$\delta\omega_{ij,k+1}^e = \delta\omega_{ij,k+1} - \mathfrak{R}_{im,k}\delta\hat{\omega}_{ml,k+1}^p\mathfrak{R}_{jl,k}$$

- Update the rotation tensor,  $\mathfrak{R}$ , using a 2<sup>nd</sup> order update of Equation 2.7

$$\mathfrak{R}_{ij,k+1} = \left( \delta_{im} - \frac{1}{2}\delta\omega_{im,k+1}^e \right)^{-1} \left( \delta_{ml} + \frac{1}{2}\delta\omega_{ml,k+1}^e \right) \mathfrak{R}_{lj,k}$$

- End substep loop  $\Rightarrow$  update variables, i.e.,  $\Gamma_{n+1} = \Gamma_{k+1}$ ,  $\tau_{c,n+1}^{(\alpha)} = \tau_{c,k+1}^{(\alpha)}$ ,  $\mathfrak{R}_{ij,n+1} = \mathfrak{R}_{ij,k+1}$  and  $\hat{\sigma}_{ij,n+1} = \hat{\sigma}_{ij,k+1}$ .

4. Transform the Cauchy stress tensor into the global coordinate system

$$\sigma_{ij,n+1} = \mathfrak{R}_{im,n+1}\hat{\sigma}_{ml,n+1}\mathfrak{R}_{jl,n+1}$$

## 3.2 Implementation

The forward Euler algorithm given above has been used to implement the hypoelastic formulation of the rate dependent single crystal plasticity model given in Section 2.3. The algorithm has been implemented in a standalone code for single crystal plasticity, a standalone code for polycrystal plasticity, and as user-defined material subroutines (VUMAT & UMAT) in Abaqus Explicit & Abaqus Standard.

### 3.2.1 Standalone Code for Single Crystal Plasticity (Fortran Program)

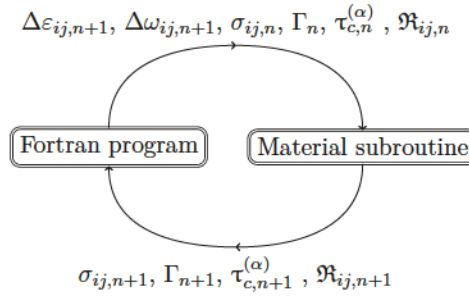


*Figure 3.1*

The Fortran program calls the material subroutine, Figure 3.1, with the strain and rotation increments  $\Delta\varepsilon_{ij,n+1}$  and  $\Delta\omega_{ij,n+1}$ , the Cauchy stress tensor components  $\sigma_{ij,n}$  and the state variables  $\Gamma_n, \tau_{c,n}^{(\alpha)}$  and  $\mathfrak{R}_{ij,n}$ . Then the material subroutine updates the stress tensor components and the state variables according to the forward Euler algorithm, see Section 3.1.2, and the output variables are written to a file.

### 3.2.2 Standalone Code for Polycrystal Plasticity (FC-Taylor Program)

Here, a full-constraint (FC) Taylor program has been implemented using the material subroutine of the single crystal plasticity model, in Section 3.2.1, to describe the material behaviour of polycrystals. To represent the material volume, a user-defined number of grains with different

sizes/weights and orientations are taken as input to the program. In addition, material parameters of the single crystal plasticity model are needed as input. The Taylor hypothesis is enforced, as the individual grains experience the same deformation. Thus, compatibility is fulfilled but stress equilibrium is violated.

Every grain is given an initial orientation and a corresponding weight by the user, where the volume fraction of grain  $i$  is taken as

$$f_i = \frac{v_i}{\sum_{k=1}^{N_g} v_k} \quad (3.4)$$

where  $v_i$  is the weight of grain  $i$ , and  $N_g$  is the total number of grains/orientations. Then, the volume-average Cauchy stress tensor  $\sigma$  of the polycrystal is defined as

$$\sigma = \sum_{k=1}^{N_g} f_k \sigma_k \quad (3.5)$$

where  $\sigma_k$  is the Cauchy stress tensor of grain  $k$ . The volume-average plastic work per unit volume  $w^p$  is defined as

$$w^p = \sum_{k=1}^{N_g} f_k w_k^p = \sum_{k=1}^{N_g} f_k \left( \int_0^t \left( \sum_{\alpha=1}^{n_s} \tau_k^{(\alpha)} \dot{\gamma}_k^{(\alpha)} \right) dt \right) = \int_0^t \left( \sum_{k=1}^{N_g} \sum_{\alpha=1}^{n_s} f_k \tau_k^{(\alpha)} \dot{\gamma}_k^{(\alpha)} \right) dt \quad (3.6)$$

where  $w_k^p$  is the plastic work per unit volume of grain  $k$ ,  $\tau_k^{(\alpha)}$  is the resolved shear stress and  $\dot{\gamma}_k^{(\alpha)}$  is the shear strain rate on slip system  $\alpha$  of grain  $k$ .

The FC-Taylor program is able to generate discrete yield surface data by generating as evenly distributed stress points as possible for a user-defined amount of plastic work per unit volume  $w_c^p$ . Here, plastic incompressibility is given by the single crystal plasticity model, and the plastic rate of deformation tensor has five independent components. To generate these stress points, the direction of plastic deformation is distributed on the surface of a hypercube, i.e., 5-dimensional cube and projected onto the surface of a hypersphere. The directions on the hypercube are evenly distributed but when transformed to the hypersphere, points are distributed with an increased density around corners of the hypercube. This will result in stress points condensed on the yield surface where the gradient of the yield surface changes most rapidly, see Section 4.2.

A contraction of the plastic rate of deformation tensor  $\mathbf{D}^p$  into a five-dimensional vector  $\mathbf{d}$  is performed as in Van Houtte (1988), and Grytten et al. (2008). Assuming negligible elastic deformations, the rate of deformation tensor can be expressed as

$$D_{11} = \frac{\sqrt{3}+3}{6}d_1 + \frac{\sqrt{3}-3}{6}d_2 \quad (3.7a)$$

$$D_{22} = \frac{\sqrt{3}-3}{6}d_1 + \frac{\sqrt{3}+3}{6}d_2 \quad (3.7b)$$

$$D_{33} = -\frac{\sqrt{3}}{3}d_1 - \frac{\sqrt{3}}{3}d_2 \quad (3.7c)$$

$$D_{12} = \frac{\sqrt{2}}{2}d_3 \quad (3.7d)$$

$$D_{23} = \frac{\sqrt{2}}{2}d_4 \quad (3.7e)$$

$$D_{31} = \frac{\sqrt{2}}{2}d_5 \quad (3.7f)$$



The user can choose to generate stress points in the full deviatoric stress space or a state of plane stress. For plane stress,  $d_4 = d_5 = 0$ . The total number of points to be generated on the surface of the hyper-cubes are

- Full stress space

$$N_\sigma = 10 (n_{pts} - 2)^4 + 40 (n_{pts} - 2)^3 + 80 (n_{pts} - 2)^2 + 80 (n_{pts} - 2) + 32 \quad (3.8)$$

- Plane stress

$$N_\sigma = 6 (n_{pts} - 2)^2 + 12 (n_{pts} - 2) + 8 \quad (3.9)$$

where  $n_{pts} \geq 2$  is the resolution of the grid along each axis of the hyper-cubes taken as input from the user. In addition, centrosymmetry can be assumed or not based on input from the user, i.e., if centrosymmetry is assumed, for each stress point  $\sigma$  there is an indistinguishable point  $-\sigma$ . Thus, if centrosymmetry is assumed, only deformation states where  $D_{11} \geq 0$  are considered, and the deformation states to be generated are thus reduced.

### 3.2.3 Material Subroutine for Abaqus Explicit (VUMAT)

The material subroutine written for the Fortran program needs some modification to work with Abaqus Explicit. While the Fortran program supplied tensor components in the global coordinate system, Abaqus Explicit supplies strain increments, relative rotation increments and Cauchy stress components in a co-rotated coordinate system. This co-rotated coordinate system differs from the co-rotated coordinate system of the single crystal defined earlier.

The co-rotated coordinate system used in Abaqus Explicit is rotated according to the rotation tensor  $\mathbf{R}$ , where  $\mathbf{F} = \mathbf{R}\mathbf{U}$  is the deformation gradient and  $\mathbf{U}$  is the right stretch tensor. Abaqus Explicit supplies the material subroutine with the components of the deformation gradient and the components of the right stretch tensor components in the global coordinate system, at  $n$  and  $n + 1$ .

To update the stress tensor and the state variables, the strain and rotation tensor increments in the co-rotational coordinate system w.r.t  $\mathfrak{R}$  is needed. Let tensor components given in the co-rotated coordinate system w.r.t  $\mathbf{R}$  be denoted  $\blacksquare$ . Now either the strain increments  $\Delta \bar{\epsilon}_{ij,n+1}$  and the relative rotation increments  $\Delta t_{n+1}(\bar{W}_{ij,n+1/2} - \bar{\Omega}_{ij,n+1/2})$ , where  $\Omega_{ij} = \dot{R}_{im}R_{jm}$  can be transformed in to the global coordinate system, or the strain and rotation increments can be calculated from  $\mathbf{F}$ . In the present work, the second approach using  $\mathbf{F}$  will be used.

The relation between the velocity gradient,  $\mathbf{L}$ , and the deformation gradient,  $\mathbf{F}$ , is given by

$$L_{ij} = \dot{F}_{im}F_{mj}^{-1} \quad (3.10)$$

Based on a first order Taylor expansion of  $\dot{F}_{ij}$  we get

$$\dot{F}_{ij,n+1} = \dot{F}_{ij,n} = \frac{1}{\Delta t_{n+1}} (F_{ij,n+1} - F_{ij,n}) \quad (3.11)$$

, i.e., forward Euler and backward Euler yields the same approximation. Now, the velocity gradient at the half step can be approximated as

$$L_{ij,n+1/2} = \frac{2}{\Delta t_{n+1}} (F_{im,n+1} - F_{im,n}) (F_{mj,n+1} + F_{mj,n})^{-1} \quad (3.12)$$

and the rate of deformation and spin tensors at the half step follow by taking the symmetric and skew-symmetric parts, respectively. Then the incremental strain and rotation tensors are

calculated,  $\Delta\varepsilon_{ij,n+1} = D_{ij,n+1/2}\Delta t_{n+1}$  and  $\Delta\omega_{ij,n+1} = W_{ij,n+1/2}\Delta t_{n+1}$  in the global coordinate system, respectively, and further transformed into the co-rotated coordinate system w.r.t.  $\mathfrak{R}$ .

Abaqus Explicit supplies the Cauchy stress tensor components in the co-rotated coordinate system w.r.t.  $\mathbf{R}$ , and they need to be rotated into the co-rotated coordinate system w.r.t.  $\mathfrak{R}$ , i.e.,

$$\hat{\sigma}_{ij,n} = \mathfrak{R}_{mi,n}\sigma_{ml,n}\mathfrak{R}_{lj,n} = \mathfrak{R}_{mi,n}R_{mp,n}\bar{\sigma}_{pq,n}R_{lq,n}\mathfrak{R}_{lj,n} \quad (3.13)$$

Then the numerical integration scheme given in Section 3.1.2 is used to update the Cauchy stress tensor and the solution dependent variables. Finally, the new Cauchy stress tensor components is transformed in to the co-rotated coordinate system w.r.t.  $\mathbf{R}$  as

$$\bar{\sigma}_{ij,n+1} = R_{mi,n+1}\sigma_{ml,n+1}R_{lj,n+1} = R_{mi,n+1}\mathfrak{R}_{mp,n+1}\hat{\sigma}_{pq,n+1}\mathfrak{R}_{lq,n+1}R_{lj,n+1} \quad (3.14)$$

and given to Abaqus Explicit.

### 3.2.4 Material Subroutine for Abaqus Standard (UMAT)

For Abaqus Standard (Implicit) the incremental strain and rotation tensors are calculated in the same way as for Abaqus Explicit using the deformation gradient  $\mathbf{F}$ , see Section 3.2.3. In Abaqus Standard the Cauchy stress tensor has already been rotated to account for rigid body motion in the increment before the subroutine is called, thus the stress tensor needs to be rotated back to the global coordinate system in a similar way as for Abaqus Explicit. In the UMAT the rotation increment is given, and the utility subroutine *ROTSIG* available in Abaqus standard is used to rotate the stress tensor. Then, the numerical integration scheme given in Section 3.1.2 is used to update the Cauchy stress tensor and the solution dependent variables, but unlike as for Abaqus Explicit the stress tensor components are delivered to Abaqus Standard in the global coordinate system.

In addition, to the updated Cauchy stress tensor components and the solution dependent variables, the material tangent modulus  $\partial\Delta\sigma/\partial\Delta\varepsilon$  must be returned in the subroutine. Here, two alternatives are implemented; (i) the elastic tangent modulus and (ii) the consistent material tangent modulus. The elastic tangent modulus should be used with the quasi-Newton solution technique of the Abaqus standard solver. The quasi-Newton solution technique in Abaqus uses the BFGS method (Broyden, 1970; Fletcher, 1970; Goldfarb, 1970; Shanno, 1970) which improves the approximations of the material tangent, with each iteration, that satisfies a secant condition. This method is computationally inexpensive (Matthies and Strang, 1979), and can give good results where the material tangent is fairly well-conditioned (Abaqus, 2014). The consistent tangent modulus should be used with the Newton-Raphson solution technique of the Abaqus solver to obtain quadratic convergence when the estimate of the solution is within the radius of convergence of the algorithm (Abaqus, 2014).

The elastic tangent modulus is easily calculated based on the elastic constants of the elasticity tensor  $\hat{C}_{ijkl}$ , see Equation (2.17). Thus, little computational effort is devoted to this part. The consistent tangent modulus is found by calling the subroutine several times, using the numerical integration scheme in Section 3.1.2, with various perturbations of the strain increment. Hence, this method is more computationally expensive than returning an elastic tangent modulus. In general, the convergence rate of the quasi-Newton algorithm is lower than that for the Newton-Raphson solution technique, but the BFGS method used with the quasi-Newton algorithm improves the rate of convergence. It is here recommended to use the option of an elastic tangent modulus with the quasi-Newton algorithm.

## 4 | Verification

In this section, the response of the hypoelastic crystal plasticity model given in the preceding chapters will be compared to a hyperelastic crystal plasticity model implemented in LS-DYNA by Dumoulin et al. (2009). The hyperelastic crystal plasticity model is integrated using an algorithm based on a forward Euler scheme proposed by Grujicic and Batchu (2002). The LS-DYNA simulations in the following were performed by Khadyko (2016).

### 4.1 Single Crystal Response

In this section, the four initial crystal orientations given in Table 4.1 will be used to verify the hypoelastic crystal plasticity model.

*Table 4.1: Initial crystal orientations.*

Orientation	$\varphi_1^0$	$\Phi^0$	$\varphi_2^0$
1	0°	0°	0°
2	45°	0°	0°
3	129.2315°	114.0948°	333.4349°
4	206.5651°	114.0948°	50.76848°

Orientation 1 is such that the x-, y- and z-axis of the global coordinate system coincide with the [100], [010] and [001] directions of the crystal, respectively. This orientation is also called the Cube orientation. Orientation 2 is a 45° rotation of the crystal about the z-axis, a rotated Cube orientation. Orientation 3 is such that the slip direction of the first slip system, see Appendix A.1, is oriented along the x-direction and the slip normal is oriented along the y-direction in the global coordinate system. Orientation 4 is the Euler angles that give an initial rotation tensor to be the transpose of the initial rotation tensor for orientation 3, i.e.,  $\mathfrak{R}_{ij,0}^{(4)} = \mathfrak{R}_{ji,0}^{(3)}$ .

To study the single crystal response the set of material parameters from Khadyko et al. (2014) given in Table 4.2 is used. The work-hardening model after Kalidindi et al. (1992) is used for the verification of the single crystal plasticity model.

*Table 4.2: Crystal plasticity material parameters. From Khadyko et al. (2014).*

$\hat{c}_{11}$	$\hat{c}_{12}$	$\hat{c}_{44}$	$\dot{\gamma}_0$	$m$	$\tau_{c0}$	$q$	$h_0$	$\tau_s$	$a$
[MPa]	[MPa]	[MPa]	[s <sup>-1</sup> ]		[MPa]		[MPa]	[MPa]	
106430	60350	28210	0.010	0.005	46.73	1.4	411.25	104.02	1.354

The single crystal is modelled using a single eight-node element with reduced integration in Abaqus and LS-DYNA for the hypoelastic and hyperelastic models, respectively. The standalone code is also used for comparison. The single crystals will be subjected to simple shear depicted in Figure 4.1. In the initial configuration, the element is a cube with side lengths 1mm.

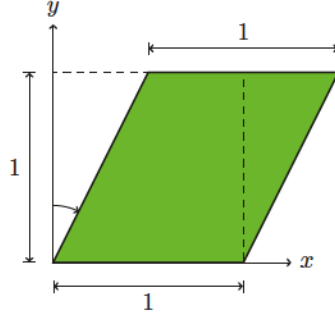


**Figure 4.1:** Deformation mode applied to the single crystal, initial configuration dashed and deformed configuration filled, dimensions in millimetres.

#### 4.1.1 Simple Shear

In the standalone code, the simple shear deformation is given by a constant shearing rate. The strain increments and rotation increments are given such that the deformation is equivalent to giving the top edge of the cube in Figure 4.1 a constant velocity of  $v = 0.01\text{mm/s}$  over a loading time of 100s. In both Abaqus and LS-DYNA the top edge is given an almost constant velocity, over a loading time of 100s. The velocity of the top edge is for Abaqus and LS-DYNA defined as

$$v(t) = \begin{cases} 0.01 (6t^5 - 15t^4 + 10t^3) & \text{for } 0 \leq t < 1 \\ 0.01 & \text{for } 1 \leq t \leq 100 \end{cases} \quad (4.1)$$

This is done to avoid large accelerations in the beginning of the step, as the cube is initially stationary. In addition, mass scaling is used to reduce computational time in Abaqus Explicit and LS-DYNA.

The results from the analyses are extracted and curves for the equivalent von Mises stress versus equivalent von Mises plastic strain will be compared in the following. See Appendix A.2 and A.3 for the definitions of the equivalent von Mises stress and the equivalent von Mises plastic strain, respectively.

Figure 4.2 presents the response curves for simple shear of the crystals with four different initial orientations. It is clear that the responses of the hypoelastic model obtained with the standalone code and Abaqus Explicit/Standard are almost identical. For orientation 1 and 4, the hypoelastic and the hyperelastic models agree and the response is nearly identical, also the components of the Cauchy stress tensor agree. For orientations 2 and 3 the response of the hypoelastic model deviates from the hyperelastic model at large plastic strains.

Let us look at the crystal with orientation 3. Here, the crystal is aligned such that only slip system 1 should be active during plastic deformation, i.e.,  $\tau^{(\alpha)} \approx \tau_c^{(\alpha)}$  for  $\alpha = 1$  and  $\tau^{(\alpha)} < \tau_c^{(\alpha)}$  for  $\alpha \neq 1$ . In the RDCP model, this results in shear strain rates as

$$\dot{\gamma}^{(\alpha)} \approx \begin{cases} \dot{\gamma}_0 & \text{for } \alpha = 1 \\ 0 & \text{for } \alpha \neq 1 \end{cases}$$

Since the slip direction and the slip normal are aligned along the x- and y-direction, respectively, we get the Schmid tensor  $\mathbf{S}^{(1)} = \mathbf{m}^{(1)} \otimes \mathbf{n}^{(1)} = \mathbf{e}_1 \otimes \mathbf{e}_2$  for slip system 1. Based on Equation 2.5, the plastic rate of deformation and plastic spin tensors can be calculated as

$$\mathbf{D}^p \approx \frac{1}{2} \dot{\gamma}_0 (\mathbf{e}_1 \otimes \mathbf{e}_2 + \mathbf{e}_2 \otimes \mathbf{e}_1), \quad \mathbf{W}^p \approx \frac{1}{2} \dot{\gamma}_0 (\mathbf{e}_1 \otimes \mathbf{e}_2 - \mathbf{e}_2 \otimes \mathbf{e}_1)$$

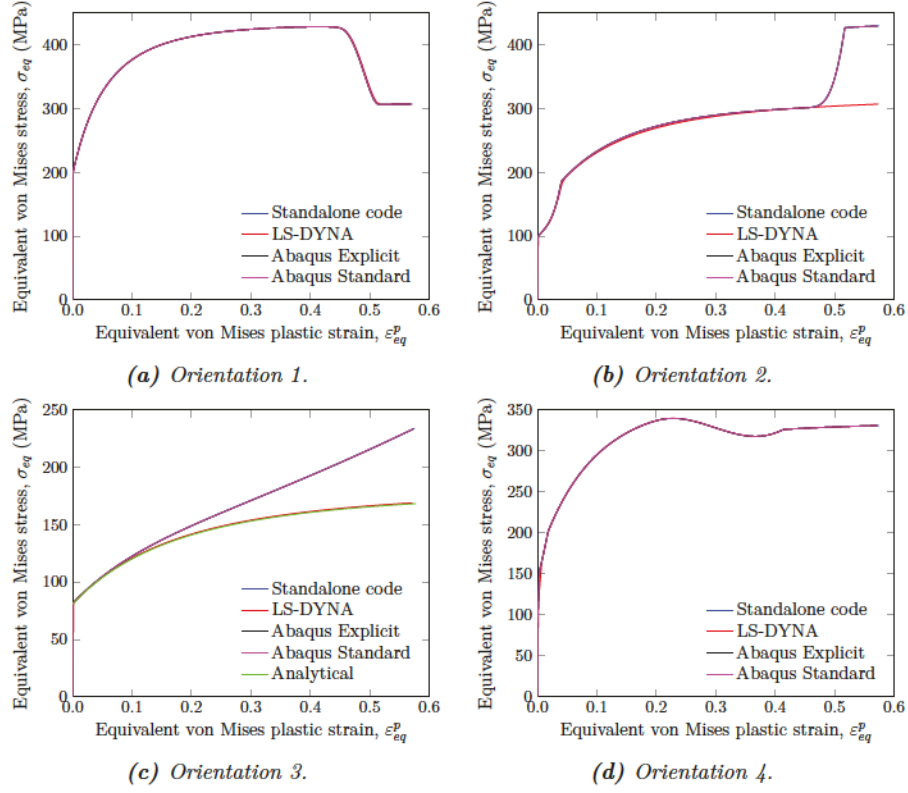


**Figure 4.2:** Single crystal response for the four initial orientations given in Table 4.1, subjected to simple shear.

The total rate of deformation and spin tensors given by the simple shear deformation are of the same form

$$\mathbf{D} = \frac{1}{2} \dot{\gamma}_{12} (\mathbf{e}_1 \otimes \mathbf{e}_2 + \mathbf{e}_2 \otimes \mathbf{e}_1), \quad \mathbf{W} = \frac{1}{2} \dot{\gamma}_{12} (\mathbf{e}_1 \otimes \mathbf{e}_2 - \mathbf{e}_2 \otimes \mathbf{e}_1)$$

where  $\dot{\gamma}_0$  is exchanged for  $\dot{\gamma}_{12}$ . The elastic parts are thus given by

$$\mathbf{D}^e \approx \frac{1}{2} (\dot{\gamma}_{12} - \dot{\gamma}_0) (\mathbf{e}_1 \otimes \mathbf{e}_2 + \mathbf{e}_2 \otimes \mathbf{e}_1), \quad \mathbf{W}^e \approx \frac{1}{2} (\dot{\gamma}_{12} - \dot{\gamma}_0) (\mathbf{e}_1 \otimes \mathbf{e}_2 - \mathbf{e}_2 \otimes \mathbf{e}_1)$$

Now assuming that the elastic deformations are negligible, i.e.,  $\mathbf{D}^e \approx 0$ , we get  $\dot{\gamma}_{12} \approx \dot{\gamma}_0$ , which also results in  $\mathbf{W}^e \approx 0$ . Based on Equation 2.7 and the above assumptions, the lattice frame should not change for this orientation and deformation mode, i.e.,  $\dot{\mathfrak{R}} \approx 0$ .

Based on the above assumptions one can establish a non-linear first-order differential equation for the resolved shear stress on slip system 1. The evolution of the critical resolved shear stress on slip system 1 can be expressed as

$$\dot{\tau}_c^{(1)} = h_{11} |\dot{\gamma}^{(1)}| = h_0 \left( 1 - \frac{\tau_c^{(1)}}{\tau_s} \right)^a \dot{\gamma}^{(1)}$$

Let us denote  $\tau = \tau^{(1)} = \sigma_{ij} S_{ij}^{(1)} = \sigma_{12} = \sigma_{21} \approx \tau_c^{(1)}$ . Exchanging  $\tau_c^{(1)}$  with  $\tau$  in the above evolution equation yields

$$\dot{\tau} = h_0 \dot{\gamma}_0 \left( 1 - \frac{\tau}{\tau_s} \right)^a \quad (4.2)$$



For this orientation with the above assumptions, the only non-zero components of the Cauchy stress tensor are  $\sigma_{12} = \sigma_{21} = \tau$  such that the equivalent von Mises stress  $\sigma_{eq} = \sqrt{3} |\tau|$ . The rate of the equivalent von Mises plastic strain rate can be expressed as  $\dot{\varepsilon}_{eq}^p = \frac{1}{\sqrt{3}} |\dot{\gamma}^{(1)}| = \frac{1}{\sqrt{3}} \dot{\gamma}_0$ . Integrating Equation 4.2 for  $a \neq 1$  gives

$$\tau(t) = \tau_s - \tau_s \left[ \frac{(a-1)h_0\dot{\gamma}_0}{\tau_s} t + \left(1 - \frac{\tau_{c0}}{\tau_s}\right)^{1-a} \right]^{\frac{1}{1-a}} \quad (4.3)$$

Utilising the expressions for the von Mises equivalent stress and plastic strain rate, the analytical solution plotted in Figure 4.2(c) is obtained.

For the implemented models the elastic strains are small but not all exactly zero, thus the lattice frame will be subject to a small rotation. Also, since the models do not have a yield surface, plastic slip will occur for  $\tau^{(\alpha)} \neq 0$ . Both the hyperelastic and the hypoelastic models presents a small rotation of the lattice in this orientation. This is seen as the Euler angles will slightly alter during deformation in this orientation.

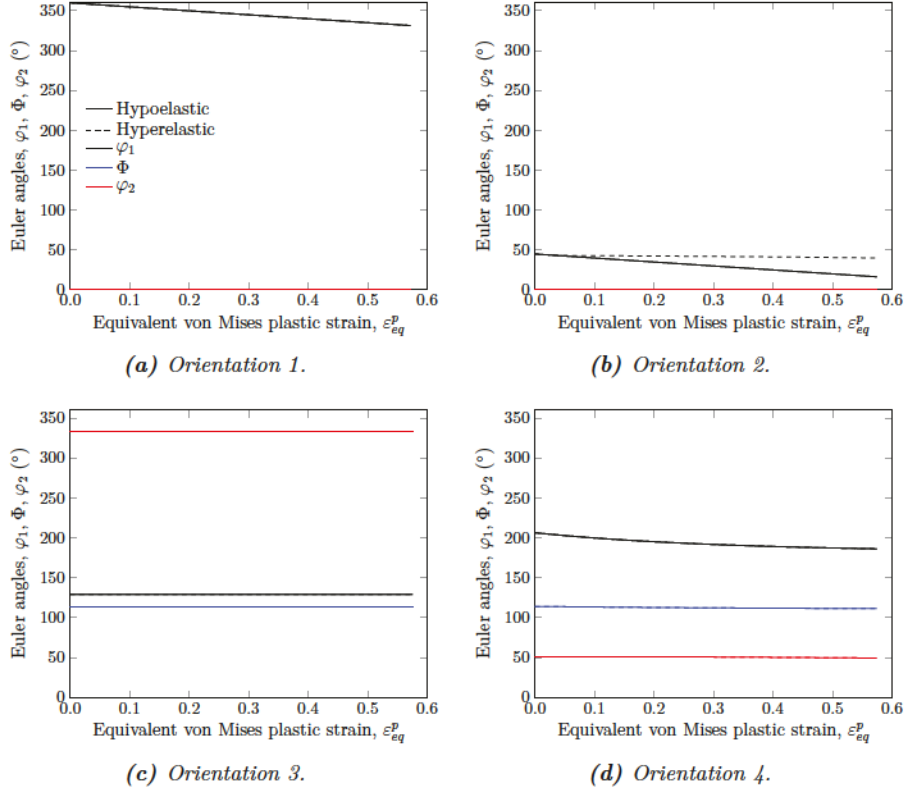


**Figure 4.3:** Evolution of the crystal orientation, for simple shear.

Figure 4.3(c) presents the evolution of the Euler angles during deformation of the crystal with initial orientation 3. From Figure 4.3(c) the Euler angles do not appear to change, but looking more closely at the curves, a small rotation of the crystal can be observed. The hyperelastic and hypoelastic models predict the same rotation of the crystal. The change of the Euler angles  $\Phi$  and  $\varphi_2$  is negligible, but the change of  $\varphi_1$  is around  $0.1^\circ$ . Due to this rotation of the crystal, the

deformation cannot be represented by slip along only one slip system. Thus more slip systems need to be activated or the cube needs to be elastically deformed to accommodate the rotation. From Figure 4.2(c) it appears as the hypoelastic model is affected by the small rotation, unlike the hyperelastic model.

In the following the input to the hypoelastic model is varied and the response is compared to the response of the hyperelastic model for orientation 3, seen in Figure 4.2(c). If the initial configuration is instead given by the Euler angles  $\varphi_1^0 = 129.3315$ ,  $\Phi^0 = 114.0948$  and  $\varphi_2^0 = 333.4349$ . This orientation is almost equal to orientation 3, with the only difference being  $\varphi_1$  which is  $0.1^\circ$  greater. The resulting response is equal to the hyperelastic response, see Figure 4.4. Thus, this orientation is clearly unstable and variations in the response are merely a numerical artefact.

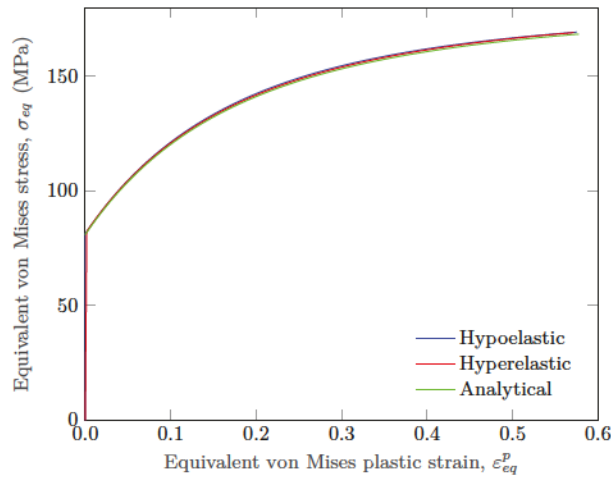


**Figure 4.4:** Single crystal response with initial orientation 3 for the hyperelastic model and  $\varphi_1^0 = 129.3315$ ,  $\Phi^0 = 114.0948$  and  $\varphi_2^0 = 333.4349$  for the hypoelastic model.

For initial orientation 1, 3 and 4, the evolution of the Euler angles for the hypoelastic model is identical to the hyperelastic model, seen in Figure 4.3, whereas the evolution of the Euler angles for the hypoelastic model deviates from the hyperelastic model for orientation 2. The Euler angles  $\Phi$  and  $\varphi_2$  are equal for the two models, but  $\varphi_1$  deviates. For the hypoelastic model, the evolution of  $\varphi_1$  appears linear and the change of  $\varphi_1$  appears to be equal to the change seen for orientation 1. For the hyperelastic model,  $\varphi_1$  evolves similar to the hypoelastic model at small plastic strains, but for increasing plastic strain the rate of change of  $\varphi_1$  decreases, unlike the hypoelastic model.

#### 4.1.2 Hypo- vs. Hyper-elastic

In order to further assess the differences observed between the hyperelastic and the hypoelastic models, the hypoelastic implementation of Zhang et al. (2014) was tested as well. The results are compared in Figure 4.5. The response of the two hypoelastic models agrees for all the orientations.

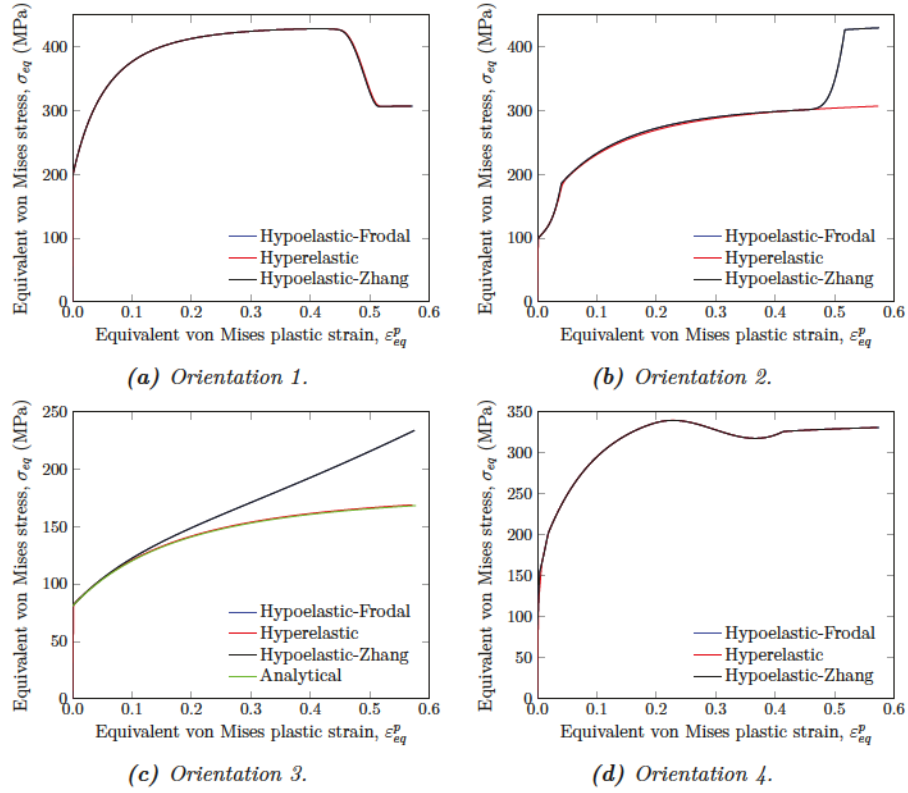


**Figure 4.5:** Single crystal response for the four initial orientations given in Table 4.1, subjected to simple shear.

## 4.2 Polycrystal Response

In this section, the predictive capabilities of the FC-Taylor program are compared to simulations performed by Frodal et al. (2019) using crystal plasticity with the finite element method (CP-FEM). For details concerning the representative volume element (RVE) and of the CP-FEM the reader is referred to Frodal et al. (2019). The same parameters governing elasticity, rate sensitivity and latent hardening as in Table 4.2 are used, whereas the parameters governing initial slip resistance and work-hardening are given in Table 4.3. The three aluminium alloys AA6060, AA6082.25 and AA6082.50 are investigated.

**Table 4.3:** Crystal plasticity parameters governing initial slip resistance and work hardening. From Frodal et al. (2019).

Alloy	$\tau_0$ (MPa)	$\theta_{\tau_1}$ (MPa)	$\tau_1$ (MPa)	$\theta_{\tau_2}$ (MPa)	$\tau_2$ (MPa)
AA6060	72.2	81.5	16.5	0.0	0.0
AA6082.25	107.1	30.4	200.0	5.5	200.0
AA6082.50	123.0	13.0	199.2	8.1	190.7

For the stress space points generated by the FC-Taylor program, the same values of plastic work per unit volumes as in the CP-FEM simulations are used. Hence,  $w_c^p = 0.32$  MPa,  $w_c^p = 0.50$

MPa, and  $w_c^p = 0.51$  MPa have been used for the AA6060, AA6082.25 and AA6082.50 alloys, respectively. These values correspond to the point of 0.2% plastic strain in uniaxial tension along the extrusion direction. The imposed strain rate is set to  $\dot{\epsilon} = 0.001$ , and the stress points have been generated using  $n_{pts} = 20$ . Plane stress is assumed and the number of generated stress points is  $N_\sigma = 2168$ . Note that the yield surfaces generated in Frodal et al. (2019) are valid for the full stress space.

The microstructure has been represented by the number of measured grains by the EBSD measurements of the alloys reported by Frodal et al. (2017). Hence, a total of 2611, 25512 and 1565 grains with the corresponding area fractions as weights were used for the AA6060, AA6082.25 and AA6082.50 alloys, respectively. Figure 4.6 displays the generated stress points with the FC-Taylor program together with the stress points generated by CP-FEM. The contour of the Yld2004-18p (Barlat et al., 2005) yield surface at zero shear stress is also depicted. The yield surface was calibrated to the CP-FEM data.

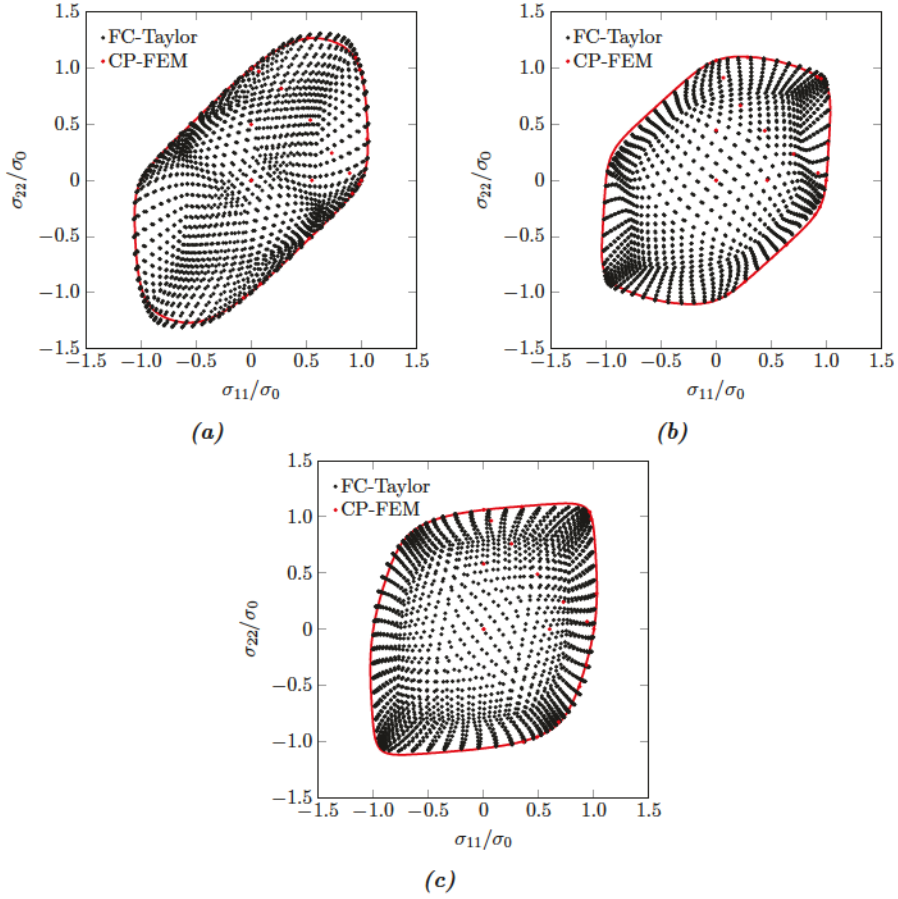


**Figure 4.6:** Stress points generated by the FC-Taylor program and compared to CP-FEM. Points are projected to the ED-TD ( $x_1 - x_2$ ) plane. The red line shows the calibrated yield surface from the CP-FEM at zero shear stress.

The overall shapes of the yield surfaces are captured with reasonable accuracy by the FC-Taylor program, but some deviations are observed. At some points along the periphery of the yield

surface, the stress points generated by the FC-Taylor program are outside of the yield surface generated by CP-FEM. The initial yield stress in uniaxial tension along ED deviates as well, for the FC-Taylor program the predicted values are  $\sigma_0 = 173.7$  MPa,  $\sigma_0 = 311.0$  MPa, and  $\sigma_0 = 301.0$  MPa for the AA6060, AA6082.25 and AA6082.50 alloys, respectively. In contrast, the predicted initial yield stresses with CP-FEM are  $\sigma_0 = 170.2$  MPa,  $\sigma_0 = 291.5$  MPa, and  $\sigma_0 = 287.6$  MPa for the AA6060, AA6082.25 and AA6082.50 alloys, respectively. Thus, the FC-Taylor program overestimates the predicted yield stresses at 0.2% plastic strain in uniaxial tension along the extrusion direction, and the error depends on the crystallographic texture of the alloy.

Albeit, the FC-Taylor approach is not as precise as the CP-FEM since stress equilibrium across grains is violated, the computational time is much lower for the FC-Taylor method, i.e., a stress point is calculated in just a few seconds. Thus, the FC-Taylor approach can be a nice starting point when determining a yield surface for an alloy.



## 5 | Concluding Remarks

In this report, a hypoelastic single crystal plasticity model has been implemented in a standalone code and as user-defined material subroutines in Abaqus Explicit and Abaqus Standard along with a standalone code for polycrystal analysis using the FC-Taylor approach. The hypoelastic model has been compared to a hyperelastic model and another hypoelastic model, by subjecting a cube to simple shear. Four different initial orientations of the single crystal were studied and differences were seen between the hypoelastic and hyperelastic models for some of the orientations.

For initial orientation 1 and 4, the response was nearly identical, but for orientation 2 and 3, the response deviated for large plastic strains. The response of the hypoelastic model was seen to be sensitive to the small rotation for initial orientation 3. For a change of  $\Delta\varphi_1 = 0.1^\circ$  from initial orientation 3, the response became identical to the hyperelastic model. For initial orientation 2, the rotation of the crystal lattice for the hypoelastic model deviated from the hyperelastic model. The implementation of the hypoelastic model herein agreed with the implementation of the hypoelastic model of Zhang et al. (2014).

In polycrystal simulations, the instabilities encountered with the hypoelastic models in simple shear are unlikely to be achieved. The plastic behaviour in polycrystals will activate several slip systems in a grain and the aggregate of crystals will stabilize the response. The FC-Taylor approach gives a good estimate of the yield surface of aluminium alloys and is generally a good method for qualitative studies of polycrystals.

### Acknowledgement

Dr. Mikhail Khadyko is gratefully acknowledged for performing the simulations of the hyperelastic model in LS-DYNA and discussions of the crystal plasticity models. Dr. Stephane Dumoulin is thanked for discussions and help with the implementation of the crystal plasticity model, and associate professor David Morin is thanked for help with the implementation of the model in Abaqus Standard.

## References

- Abaqus (2014). Abaqus documentation, version 6.14. Dassault Systèmes Simulia.
- Barlat, F., Aretz, H., Yoon, J. W., Karabin, M. E., Brem, J. C., and Dick, R. E. (2005). Linear transformation-based anisotropic yield functions. *International Journal of Plasticity*, 21(5):1009 – 1039.
- Belytschko, T., Liu, W. K., Moran, B., and Elkhodary, K. (2014). *Nonlinear finite elements for continua and structures*. John Wiley & Sons, second edition.
- Broyden, C. G. (1970). The Convergence of a Class of Double-rank Minimization Algorithms: 2. The New Algorithm. *IMA Journal of Applied Mathematics*, 6(3):222–231.
- Buehler, M. J. (2008). *Atomistic Modeling of Materials Failure*. Springer.
- Dumoulin, S., Hopperstad, O., and Berstad, T. (2009). Investigation of integration algorithms for rate-dependent crystal plasticity using explicit finite element codes. *Computational Materials Science*, 46(4):785 – 799.
- Engler, O. and Randle, V. (2010). *Introduction to Texture Analysis: Macrotexture, Microtexture, and Orientation Mapping*. CRC press, second edition.
- Fletcher, R. (1970). A new approach to variable metric algorithms. *The Computer Journal*, 13(3):317–322.
- Frodal, B. H., Dæhli, L. E. B., Børvik, T., and Hopperstad, O. S. (2019). Modelling and simulation of ductile failure in textured aluminium alloys subjected to compression-tension loading. *International Journal of Plasticity*.
- Frodal, B. H., Pedersen, K. O., Børvik, T., and Hopperstad, O. S. (2017). Influence of pre-compression on the ductility of aa6xxx aluminium alloys. *International Journal of Fracture*, 206(2):131–149.
- Goldfarb, D. (1970). A family of variable-metric methods derived by variational means. *Mathematics of computation*, 24(109):23–26.
- Grujicic, M. and Batchu, S. (2002). Crystal plasticity analysis of earing in deep-drawn OFHC copper cups. *Journal of Materials Science*, 37(4):753–764.
- Grytten, F., Holmedal, B., Hopperstad, O. S., and Børvik, T. (2008). Evaluation of identification methods for Yld2004-18p. *International Journal of Plasticity*, 24(12):2248 – 2277.
- Hopperstad, O. S. and Børvik, T. (2016). Lecture Notes - Materials Mechanics. NTNU.
- Kalidindi, S., Bronkhorst, C., and Anand, L. (1992). Crystallographic texture evolution in bulk deformation processing of FCC metals. *Journal of the Mechanics and Physics of Solids*, 40(3):537 – 569.
- Khadyko, M. (2016). Private communication.
- Khadyko, M., Dumoulin, S., Børvik, T., and Hopperstad, O. (2014). An experimental–numerical method to determine the work-hardening of anisotropic ductile materials at large strains. *International Journal of Mechanical Sciences*, 88:25 – 36.

- Khan, A. S. and Huang, S. (1995). *Continuum theory of plasticity*. John Wiley & Sons.
- Matthies, H. and Strang, G. (1979). The solution of nonlinear finite element equations. *International Journal for Numerical Methods in Engineering*, 14(11):1613–1626.
- Saai, A., Dumoulin, S., Hopperstad, O., and Lademo, O.-G. (2013). Simulation of yield surfaces for aluminium sheets with rolling and recrystallization textures. *Computational Materials Science*, 67:424 – 433.
- Shanno, D. F. (1970). Conditioning of quasi-newton methods for function minimization. *Mathematics of computation*, 24(111):647–656.
- Van Houtte, P. (1988). A comprehensive mathematical formulation of an extended taylor–bishop–hill model featuring relaxed constraints, the renouard–wintenberger theory and a strain rate sensitivity model. *Texture, Stress, and Microstructure*, 8:313–350.
- Zhang, K., Hopperstad, O., Holmedal, B., and Dumoulin, S. (2014). A robust and efficient substepping scheme for the explicit numerical integration of a rate-dependent crystal plasticity model. *International Journal for Numerical Methods in Engineering*, 99(4):239–262.

# A | Appendix

## A.1 Slip Systems for FCC Crystals

**Table A.1:** Slip system directions and plane normals w.r.t. an orthonormal basis associated with the lattice for an FCC crystal. From Belytschko et al. (2014).

Slip system, $\alpha$	Direction, $\hat{\mathbf{m}}^{(\alpha)}$	Plane, $\hat{\mathbf{n}}^{(\alpha)}$
1	$\frac{1}{\sqrt{2}} \begin{bmatrix} -1 & 0 & 1 \end{bmatrix}$	$\frac{1}{\sqrt{3}} \begin{bmatrix} 1 & 1 & 1 \end{bmatrix}$
2	$\frac{1}{\sqrt{2}} \begin{bmatrix} -1 & 1 & 0 \end{bmatrix}$	$\frac{1}{\sqrt{3}} \begin{bmatrix} 1 & 1 & 1 \end{bmatrix}$
3	$\frac{1}{\sqrt{2}} \begin{bmatrix} 0 & -1 & 1 \end{bmatrix}$	$\frac{1}{\sqrt{3}} \begin{bmatrix} 1 & 1 & 1 \end{bmatrix}$
4	$\frac{1}{\sqrt{2}} \begin{bmatrix} 0 & 1 & 1 \end{bmatrix}$	$\frac{1}{\sqrt{3}} \begin{bmatrix} -1 & -1 & 1 \end{bmatrix}$
5	$\frac{1}{\sqrt{2}} \begin{bmatrix} -1 & 1 & 0 \end{bmatrix}$	$\frac{1}{\sqrt{3}} \begin{bmatrix} -1 & -1 & 1 \end{bmatrix}$
6	$\frac{1}{\sqrt{2}} \begin{bmatrix} 1 & 0 & 1 \end{bmatrix}$	$\frac{1}{\sqrt{3}} \begin{bmatrix} -1 & -1 & 1 \end{bmatrix}$
7	$\frac{1}{\sqrt{2}} \begin{bmatrix} 1 & 0 & 1 \end{bmatrix}$	$\frac{1}{\sqrt{3}} \begin{bmatrix} -1 & 1 & 1 \end{bmatrix}$
8	$\frac{1}{\sqrt{2}} \begin{bmatrix} 1 & 1 & 0 \end{bmatrix}$	$\frac{1}{\sqrt{3}} \begin{bmatrix} -1 & 1 & 1 \end{bmatrix}$
9	$\frac{1}{\sqrt{2}} \begin{bmatrix} 0 & -1 & 1 \end{bmatrix}$	$\frac{1}{\sqrt{3}} \begin{bmatrix} -1 & 1 & 1 \end{bmatrix}$
10	$\frac{1}{\sqrt{2}} \begin{bmatrix} 0 & 1 & 1 \end{bmatrix}$	$\frac{1}{\sqrt{3}} \begin{bmatrix} 1 & -1 & 1 \end{bmatrix}$
11	$\frac{1}{\sqrt{2}} \begin{bmatrix} 1 & 1 & 0 \end{bmatrix}$	$\frac{1}{\sqrt{3}} \begin{bmatrix} 1 & -1 & 1 \end{bmatrix}$
12	$\frac{1}{\sqrt{2}} \begin{bmatrix} -1 & 0 & 1 \end{bmatrix}$	$\frac{1}{\sqrt{3}} \begin{bmatrix} 1 & -1 & 1 \end{bmatrix}$

## A.2 von Mises Equivalent Stress

The von Mises equivalent stress is defined as

$$\sigma_{eq} = \sqrt{\frac{3}{2} \sigma'_{ij} \sigma'_{ij}} = \sqrt{\frac{1}{2} [(\sigma_{11} - \sigma_{22})^2 + (\sigma_{22} - \sigma_{33})^2 + (\sigma_{33} - \sigma_{11})^2] + 3\sigma_{12}^2 + 3\sigma_{23}^2 + 3\sigma_{31}^2}$$

where

$$\sigma'_{ij} = \sigma_{ij} - \frac{1}{3} \sigma_{kk} \delta_{ij}$$

## A.3 von Mises Equivalent Plastic Strain

The von Mises equivalent plastic strain is defined as

$$\varepsilon_{eq}^p = \int_0^t \sqrt{\frac{2}{3} D_{ij}^p D_{ij}^p} dt$$

Numerically this is integrated as

$$\varepsilon_{eq,n+1}^p = \varepsilon_{eq,n}^p + \sqrt{\frac{2}{3} \Delta \varepsilon_{ij,n+1}^p \Delta \varepsilon_{ij,n+1}^p} \quad (\text{A.1})$$



## B | User Input/Output

### B.1 Subroutine Input

*Table B.1: Input to the material subroutines.*

Property number	Material Input
1	Elastic constant, $\hat{c}_{11}$
2	Elastic constant, $\hat{c}_{12}$
3	Elastic constant, $\hat{c}_{44}$
4	Reference slip rate, $\dot{\gamma}_0$
5	Instantaneous strain rate sensitivity, $m$
6	Initial critical resolved shear stress, $\tau_{c0}$
7	Latent hardening coefficient, $q$
8	Texture flag (1=Euler angles from material card, 2=Euler angles from history card)
9	Initial Euler angle, $\varphi_1^0$ in degree
10	Initial Euler angle, $\Phi^0$ in degree
11	Initial Euler angle, $\varphi_2^0$ in degree
12	Hardening flag (1 for Voce or 2 for Kalidindi et al. (1992))
13	Hardening parameter, $h_0$ or $\theta_1$ depending on hflag
14	Hardening parameter, $\tau_s$ or $\tau_1$ depending on hflag
15	Hardening parameter, $a$ or $\theta_2$ depending on hflag
16	Hardening parameter, 0.0 or $\tau_2$
17	Tangent operator flag (1=Elastic tangent operator, 2=Consistent tangent operator)

Note that the Tangent operator flag, property number 17, is only used for Abaqus Standard, and the Quasi-Newton solution technique should be used when the Elastic tangent operator is selected. The Quasi-Newton solution technique is located under the step settings in the Abaqus CAE.

Note also that the last Hardening parameter, property number 16, should be put to 0.0 when the Kalidindi et al. (1992) hardening model is used with Abaqus Standard.

### B.2 Solution-Dependent State Variables

*Table B.2: Solution-dependent state variables.*

Variable number	Solution dependent variable
1-3	Euler angles $\varphi_1$ , $\Phi$ and $\varphi_2$
4-12	Components of the rotation tensor $\mathfrak{R}$
13-24	Critical resolved shear stresses $\tau_c^{(\alpha)}$
25	Accumulated plastic shear strain $\Gamma$
26	Equivalent von Mises stress $\sigma_{eq}$
27	Equivalent von Mises plastic strain $\varepsilon_{eq}^p$
28	Number of sub-steps in the current time step $n_{sub}$

Note that the components of the rotation tensor  $\mathfrak{R}$  are stored as;  $\mathfrak{R}_{11}, \mathfrak{R}_{21}, \mathfrak{R}_{31}, \mathfrak{R}_{12}, \mathfrak{R}_{22}, \mathfrak{R}_{32}, \mathfrak{R}_{13}, \mathfrak{R}_{23}, \mathfrak{R}_{33}$ , and the critical resolved shear stresses  $\tau_c^{(\alpha)}$  are stored as;  $\tau_c^{(1)}, \tau_c^{(2)}, \dots, \tau_c^{(12)}$ .

### B.3 FC-Taylor Input

**Table B.3:** Material input to the FC-Taylor program.

Property number	Material Input
1	Elastic constant, $\hat{c}_{11}$
2	Elastic constant, $\hat{c}_{12}$
3	Elastic constant, $\hat{c}_{44}$
4	Reference slip rate, $\dot{\gamma}_0$
5	Instantaneous strain rate sensitivity, $m$
6	Initial critical resolved shear stress, $\tau_{c0}$
7	Latent hardening coefficient, $q$
8	Hardening flag (1 for Voce or 2 for Kalidindi et al. (1992))
9	Hardening parameter, $h_0$ or $\theta_1$ depending on hflag
10	Hardening parameter, $\tau_s$ or $\tau_1$ depending on hflag
11	Hardening parameter, $a$ or $\theta_2$ depending on hflag
12	Hardening parameter, 0.0 or $\tau_2$

**Table B.4:** Deformation state and other input to the FC-Taylor program.

Property number	Input
1	Plane stress flag (1 for plane stress, 0 for full stress space)
2	Centrosymmetry flag (1 for centrosymmetry, else 0)
3	Resolution of the strain rate grid, $n_{pts}$
4	Imposed strain rate, $\dot{\epsilon}$
5	Plastic work per unit volume to extract stress points, $w_c^p$
6	Number of threads/cores to utilize <sup>1</sup> , $n_{cpu}$

**Table B.5:** Microstructure input to the FC-Taylor program.

Property number	Input
1	Initial Euler angles, $\varphi_1^{(k)}$ in degree, for $k = 1, \dots, N_g$
2	Initial Euler angles, $\Phi^{(k)}$ in degree, for $k = 1, \dots, N_g$
3	Initial Euler angles, $\varphi_2^{(k)}$ in degree, for $k = 1, \dots, N_g$
4	Orientation weight, $v_k$ , for $k = 1, \dots, N_g$

<sup>1</sup>if  $n_{cpu} = 0$ , then  $n_{cpu}$  will be set to the number of threads/cores of the CPU.



**DEPARTMENT OF STRUCTURAL ENGINEERING  
NORWEGIAN UNIVERSITY OF SCIENCE AND TECHNOLOGY**

N-7491 TRONDHEIM, NORWAY  
Telephone: +47 73 59 47 00

"Reliability Analysis of Structural Systems using Nonlinear Finite Element Methods",  
C. A. Holm, 1990:23, ISBN 82-7119-178-0.

"Uniform Stratified Flow Interaction with a Submerged Horizontal Cylinder",  
Ø. Arntsen, 1990:32, ISBN 82-7119-188-8.

"Large Displacement Analysis of Flexible and Rigid Systems Considering  
Displacement-Dependent Loads and Nonlinear Constraints",  
K. M. Mathisen, 1990:33, ISBN 82-7119-189-6.

"Solid Mechanics and Material Models including Large Deformations",  
E. Levold, 1990:56, ISBN 82-7119-214-0, ISSN 0802-3271.

"Inelastic Deformation Capacity of Flexurally-Loaded Aluminium Alloy Structures",  
T. Welo, 1990:62, ISBN 82-7119-220-5, ISSN 0802-3271.

"Visualization of Results from Mechanical Engineering Analysis",  
K. Aamnes, 1990:63, ISBN 82-7119-221-3, ISSN 0802-3271.

"Object-Oriented Product Modeling for Structural Design",  
S. I. Dale, 1991:6, ISBN 82-7119-258-2, ISSN 0802-3271.

"Parallel Techniques for Solving Finite Element Problems on Transputer Networks",  
T. H. Hansen, 1991:19, ISBN 82-7119-273-6, ISSN 0802-3271.

"Statistical Description and Estimation of Ocean Drift Ice Environments",  
R. Korsnes, 1991:24, ISBN 82-7119-278-7, ISSN 0802-3271.

"Properties of concrete related to fatigue damage: with emphasis on high strength  
concrete",  
G. Petkovic, 1991:35, ISBN 82-7119-290-6, ISSN 0802-3271.

"Turbidity Current Modelling",  
B. Brørs, 1991:38, ISBN 82-7119-293-0, ISSN 0802-3271.

"Zero-Slump Concrete: Rheology, Degree of Compaction and Strength. Effects of  
Fillers as Part Cement-Replacement",  
C. Sørensen, 1992:8, ISBN 82-7119-357-0, ISSN 0802-3271.

"Nonlinear Analysis of Reinforced Concrete Structures Exposed to Transient Loading",  
K. V. Høiseith, 1992:15, ISBN 82-7119-364-3, ISSN 0802-3271.

"Finite Element Formulations and Solution Algorithms for Buckling and Collapse  
Analysis of Thin Shells",  
R. O. Bjærum, 1992:30, ISBN 82-7119-380-5, ISSN 0802-3271.

"Response Statistics of Nonlinear Dynamic Systems",  
J. M. Johnsen, 1992:42, ISBN 82-7119-393-7, ISSN 0802-3271.

"Digital Models in Engineering. A Study on why and how engineers build and operate  
digital models for decision support",  
J. Høyte, 1992:75, ISBN 82-7119-429-1, ISSN 0802-3271.

"Sparse Solution of Finite Element Equations",  
A. C. Damhaug, 1992:76, ISBN 82-7119-430-5, ISSN 0802-3271.

"Some Aspects of Floating Ice Related to Sea Surface Operations in the Barents Sea",  
S. Løset, 1992:95, ISBN 82-7119-452-6, ISSN 0802-3271.

"Modelling of Cyclic Plasticity with Application to Steel and Aluminium Structures",  
O. S. Hopperstad, 1993:7, ISBN 82-7119-461-5, ISSN 0802-3271.

"The Free Formulation: Linear Theory and Extensions with Applications to Tetrahedral  
Elements  
with Rotational Freedoms",  
G. Skeie, 1993:17, ISBN 82-7119-472-0, ISSN 0802-3271.

"Høyfast betongs motstand mot piggedekkslitasje. Analyse av resultater fra prøving i  
Veisliter'n",  
T. Tveter, 1993:62, ISBN 82-7119-522-0, ISSN 0802-3271.

"A Nonlinear Finite Element Based on Free Formulation Theory for Analysis of  
Sandwich Structures",  
O. Aamlid, 1993:72, ISBN 82-7119-534-4, ISSN 0802-3271.

"The Effect of Curing Temperature and Silica Fume on Chloride Migration and Pore  
Structure of High Strength Concrete",  
C. J. Hauck, 1993:90, ISBN 82-7119-553-0, ISSN 0802-3271.

"Failure of Concrete under Compressive Strain Gradients",  
G. Markeset, 1993:110, ISBN 82-7119-575-1, ISSN 0802-3271.

"An experimental study of internal tidal amphidromes in Vestfjorden",  
J. H. Nilsen, 1994:39, ISBN 82-7119-640-5, ISSN 0802-3271.



"Structural analysis of oil wells with emphasis on conductor design",  
H. Larsen, 1994:46, ISBN 82-7119-648-0, ISSN 0802-3271.

"Adaptive methods for non-linear finite element analysis of shell structures",  
K. M. Okstad, 1994:66, ISBN 82-7119-670-7, ISSN 0802-3271.

"On constitutive modelling in nonlinear analysis of concrete structures",  
O. Fyrileiv, 1994:115, ISBN 82-7119-725-8, ISSN 0802-3271.

"Fluctuating wind load and response of a line-like engineering structure with emphasis  
on motion-induced wind forces",  
J. Bogunovic Jakobsen, 1995:62, ISBN 82-7119-809-2, ISSN 0802-3271.

"An experimental study of beam-columns subjected to combined torsion, bending and  
axial actions",  
A. Aalberg, 1995:66, ISBN 82-7119-813-0, ISSN 0802-3271.

"Scaling and cracking in unsealed freeze/thaw testing of Portland cement and silica  
fume concretes",  
S. Jacobsen, 1995:101, ISBN 82-7119-851-3, ISSN 0802-3271.

"Damping of water waves by submerged vegetation. A case study of laminaria  
hyperborea",  
A. M. Dubi, 1995:108, ISBN 82-7119-859-9, ISSN 0802-3271.

"The dynamics of a slope current in the Barents Sea",  
Sheng Li, 1995:109, ISBN 82-7119-860-2, ISSN 0802-3271.

"Modellering av delmaterialenes betydning for betongens konsistens",  
Ernst Mørtzell, 1996:12, ISBN 82-7119-894-7, ISSN 0802-3271.

"Bending of thin-walled aluminium extrusions",  
Birgit Søvik Opheim, 1996:60, ISBN 82-7119-947-1, ISSN 0802-3271.

"Material modelling of aluminium for crashworthiness analysis",  
Torodd Berstad, 1996:89, ISBN 82-7119-980-3, ISSN 0802-3271.

"Estimation of structural parameters from response measurements on submerged  
floating tunnels",  
Rolf Magne Larssen, 1996:119, ISBN 82-471-0014-2, ISSN 0802-3271.

"Numerical modelling of plain and reinforced concrete by damage mechanics",  
Mario A. Polanco-Loria, 1997:20, ISBN 82-471-0049-5, ISSN 0802-3271.

"Nonlinear random vibrations - numerical analysis by path integration methods",  
Vibeke Moe, 1997:26, ISBN 82-471-0056-8, ISSN 0802-3271.

“Numerical prediction of vortex-induced vibration by the finite element method”,  
Joar Martin Dalheim, 1997:63, ISBN 82-471-0096-7, ISSN 0802-3271.

“Time domain calculations of buffeting response for wind sensitive structures”,  
Ketil Aas-Jakobsen, 1997:148, ISBN 82-471-0189-0, ISSN 0802-3271.

"A numerical study of flow about fixed and flexibly mounted circular cylinders",  
Trond Stokka Meling, 1998:48, ISBN 82-471-0244-7, ISSN 0802-3271.

“Estimation of chloride penetration into concrete bridges in coastal areas”,  
Per Egil Steen, 1998:89, ISBN 82-471-0290-0, ISSN 0802-3271.

“Stress-resultant material models for reinforced concrete plates and shells”,  
Jan Arve Øverli, 1998:95, ISBN 82-471-0297-8, ISSN 0802-3271.

“Chloride binding in concrete. Effect of surrounding environment and concrete composition”,  
Claus Kenneth Larsen, 1998:101, ISBN 82-471-0337-0, ISSN 0802-3271.

“Rotational capacity of aluminium alloy beams”,  
Lars A. Moen, 1999:1, ISBN 82-471-0365-6, ISSN 0802-3271.

“Stretch Bending of Aluminium Extrusions”,  
Arild H. Clausen, 1999:29, ISBN 82-471-0396-6, ISSN 0802-3271.

“Aluminium and Steel Beams under Concentrated Loading”,  
Tore Tryland, 1999:30, ISBN 82-471-0397-4, ISSN 0802-3271.

"Engineering Models of Elastoplasticity and Fracture for Aluminium Alloys",  
Odd-Geir Lademo, 1999:39, ISBN 82-471-0406-7, ISSN 0802-3271.

"Kapasitet og duktilitet av dybelforbindelser i trekonstruksjoner",  
Jan Siem, 1999:46, ISBN 82-471-0414-8, ISSN 0802-3271.

“Etablering av distribuert ingeniørarbeid; Teknologiske og organisatoriske erfaringer fra en norsk ingeniørbedrift”,  
Lars Line, 1999:52, ISBN 82-471-0420-2, ISSN 0802-3271.

“Estimation of Earthquake-Induced Response”,  
Símon Ólafsson, 1999:73, ISBN 82-471-0443-1, ISSN 0802-3271.

“Coastal Concrete Bridges: Moisture State, Chloride Permeability and Aging Effects”  
Ragnhild Holen Relling, 1999:74, ISBN 82-471-0445-8, ISSN 0802-3271.

”Capacity Assessment of Titanium Pipes Subjected to Bending and External Pressure”,  
Arve Bjørset, 1999:100, ISBN 82-471-0473-3, ISSN 0802-3271.

“Validation of Numerical Collapse Behaviour of Thin-Walled Corrugated Panels”,  
Håvar Ilstad, 1999:101, ISBN 82-471-0474-1, ISSN 0802-3271.

“Strength and Ductility of Welded Structures in Aluminium Alloys”,  
Miroslaw Matusiak, 1999:113, ISBN 82-471-0487-3, ISSN 0802-3271.

“Thermal Dilation and Autogenous Deformation as Driving Forces to Self-Induced Stresses in High Performance Concrete”,  
Øyvind Bjøntegaard, 1999:121, ISBN 82-7984-002-8, ISSN 0802-3271.

“Some Aspects of Ski Base Sliding Friction and Ski Base Structure”,  
Dag Anders Moldestad, 1999:137, ISBN 82-7984-019-2, ISSN 0802-3271.

"Electrode reactions and corrosion resistance for steel in mortar and concrete",  
Roy Antonsen, 2000:10, ISBN 82-7984-030-3, ISSN 0802-3271.

"Hydro-Physical Conditions in Kelp Forests and the Effect on Wave Damping and Dune Erosion. A case study on Laminaria Hyperborea",  
Stig Magnar Løvås, 2000:28, ISBN 82-7984-050-8, ISSN 0802-3271.

"Random Vibration and the Path Integral Method",  
Christian Skaug, 2000:39, ISBN 82-7984-061-3, ISSN 0802-3271.

"Buckling and geometrical nonlinear beam-type analyses of timber structures",  
Trond Even Eggen, 2000:56, ISBN 82-7984-081-8, ISSN 0802-3271.

”Structural Crashworthiness of Aluminium Foam-Based Components”,  
Arve Grønsund Hanssen, 2000:76, ISBN 82-7984-102-4, ISSN 0809-103X.

“Measurements and simulations of the consolidation in first-year sea ice ridges, and some aspects of mechanical behaviour”,  
Knut V. Høyland, 2000:94, ISBN 82-7984-121-0, ISSN 0809-103X.

”Kinematics in Regular and Irregular Waves based on a Lagrangian Formulation”,  
Svein Helge Gjosund, 2000-86, ISBN 82-7984-112-1, ISSN 0809-103X.

”Self-Induced Cracking Problems in Hardening Concrete Structures”,  
Daniela Bosnjak, 2000-121, ISBN 82-7984-151-2, ISSN 0809-103X.

"Ballistic Penetration and Perforation of Steel Plates",  
Tore Børvik, 2000:124, ISBN 82-7984-154-7, ISSN 0809-103X.

"Freeze-Thaw resistance of Concrete. Effect of: Curing Conditions, Moisture Exchange and Materials",  
Terje Finnerup Rønning, 2001:14, ISBN 82-7984-165-2, ISSN 0809-103X

"Structural behaviour of post tensioned concrete structures. Flat slab. Slabs on ground",  
Steinar Trygstad, 2001:52, ISBN 82-471-5314-9, ISSN 0809-103X.

"Slipforming of Vertical Concrete Structures. Friction between concrete and slipform panel",  
Kjell Tore Fosså, 2001:61, ISBN 82-471-5325-4, ISSN 0809-103X.

"Some numerical methods for the simulation of laminar and turbulent incompressible flows",  
Jens Holmen, 2002:6, ISBN 82-471-5396-3, ISSN 0809-103X.

"Improved Fatigue Performance of Threaded Drillstring Connections by Cold Rolling",  
Steinar Kristoffersen, 2002:11, ISBN: 82-421-5402-1, ISSN 0809-103X.

"Deformations in Concrete Cantilever Bridges: Observations and Theoretical Modelling",  
Peter F. Takács, 2002:23, ISBN 82-471-5415-3, ISSN 0809-103X.

"Stiffened aluminium plates subjected to impact loading",  
Hilde Giæver Hildrum, 2002:69, ISBN 82-471-5467-6, ISSN 0809-103X.

"Full- and model scale study of wind effects on a medium-rise building in a built up area",  
Jónas Thór Snæbjörnsson, 2002:95, ISBN82-471-5495-1, ISSN 0809-103X.

"Evaluation of Concepts for Loading of Hydrocarbons in Ice-infested water",  
Arnor Jensen, 2002:114, ISBN 82-417-5506-0, ISSN 0809-103X.

"Numerical and Physical Modelling of Oil Spreading in Broken Ice",  
Janne K. Økland Gjosteen, 2002:130, ISBN 82-471-5523-0, ISSN 0809-103X.

"Diagnosis and protection of corroding steel in concrete",  
Franz Pruckner, 2002:140, ISBN 82-471-5555-4, ISSN 0809-103X.

"Tensile and Compressive Creep of Young Concrete: Testing and Modelling",  
Dawood Atrushi, 2003:17, ISBN 82-471-5565-6, ISSN 0809-103X.

"Rheology of Particle Suspensions. Fresh Concrete, Mortar and Cement Paste with Various Types of Lignosulfonates",  
Jon Elvar Wallevik, 2003:18, ISBN 82-471-5566-4, ISSN 0809-103X.

"Oblique Loading of Aluminium Crash Components",  
Aase Reyes, 2003:15, ISBN 82-471-5562-1, ISSN 0809-103X.

"Utilization of Ethiopian Natural Pozzolans",  
Surafel Ketema Desta, 2003:26, ISSN 82-471-5574-5, ISSN:0809-103X.

“Behaviour and strength prediction of reinforced concrete structures with discontinuity regions”, Helge Brå, 2004:11, ISBN 82-471-6222-9, ISSN 1503-8181.

“High-strength steel plates subjected to projectile impact. An experimental and numerical study”, Sumita Dey, 2004:38, ISBN 82-471-6282-2 (printed version), ISBN 82-471-6281-4 (electronic version), ISSN 1503-8181.

“Alkali-reactive and inert fillers in concrete. Rheology of fresh mixtures and expansive reactions.”

Bård M. Pedersen, 2004:92, ISBN 82-471-6401-9 (printed version), ISBN 82-471-6400-0 (electronic version), ISSN 1503-8181.

“On the Shear Capacity of Steel Girders with Large Web Openings”.

Nils Christian Hagen, 2005:9 ISBN 82-471-6878-2 (printed version), ISBN 82-471-6877-4 (electronic version), ISSN 1503-8181.

”Behaviour of aluminium extrusions subjected to axial loading”.

Østen Jensen, 2005:7, ISBN 82-471-6873-1 (printed version), ISBN 82-471-6872-3 (electronic version), ISSN 1503-8181.

”Thermal Aspects of corrosion of Steel in Concrete”.

Jan-Magnus Østvik, 2005:5, ISBN 82-471-6869-3 (printed version), ISBN 82-471-6868 (electronic version), ISSN 1503-8181.

”Mechanical and adaptive behaviour of bone in relation to hip replacement.” A study of bone remodelling and bone grafting.

Sébastien Muller, 2005:34, ISBN 82-471-6933-9 (printed version), ISBN 82-471-6932-0 (electronic version), ISSN 1503-8181.

“Analysis of geometrical nonlinearities with applications to timber structures”.

Lars Wollebæk, 2005:74, ISBN 82-471-7050-5 (printed version), ISBN 82-471-7019-1 (electronic version), ISSN 1503-8181.

“Pedestrian induced lateral vibrations of slender footbridges”.

Anders Rönnquist, 2005:102, ISBN 82-471-7082-5 (printed version), ISBN 82-471-7081-7 (electronic version), ISSN 1503-8181.

“Initial Strength Development of Fly Ash and Limestone Blended Cements at Various Temperatures Predicted by Ultrasonic Pulse Velocity”.

Tom Ivar Fredvik, 2005:112, ISBN 82-471-7105-8 (printed version), ISBN 82-471-7103-1 (electronic version), ISSN 1503-8181.

“Behaviour and modelling of thin-walled cast components”.

Cato Dørum, 2005:128, ISBN 82-471-7140-6 (printed version), ISBN 82-471-7139-2 (electronic version), ISSN 1503-8181.



- “Behaviour and modelling of selfpiercing riveted connections”,  
Raffaele Porcaro, 2005:165, ISBN 82-471-7219-4 (printed version), ISBN 82-471-7218-6 (electronic version), ISSN 1503-8181.
- ”Behaviour and Modelling og Aluminium Plates subjected to Compressive Load”,  
Lars Rønning, 2005:154, ISBN 82-471-7169-1 (printed version), ISBN 82-471-7195-3 (electronic version), ISSN 1503-8181.
- ”Bumper beam-longitudinal system subjected to offset impact loading”,  
Satyanarayana Kokkula, 2005:193, ISBN 82-471-7280-1 (printed version), ISBN 82-471-7279-8 (electronic version), ISSN 1503-8181.
- “Control of Chloride Penetration into Concrete Structures at Early Age”,  
Guofei Liu, 2006:46, ISBN 82-471-7838-9 (printed version), ISBN 82-471-7837-0 (electronic version), ISSN 1503-8181.
- “Modelling of Welded Thin-Walled Aluminium Structures”,  
Ting Wang, 2006:78, ISBN 82-471-7907-5 (printed version), ISBN 82-471-7906-7 (electronic version), ISSN 1503-8181.
- ”Time-variant reliability of dynamic systems by importance sampling and probabilistic analysis of ice loads”,  
Anna Ivanova Olsen, 2006:139, ISBN 82-471-8041-3 (printed version), ISBN 82-471-8040-5 (electronic version), ISSN 1503-8181.
- “Fatigue life prediction of an aluminium alloy automotive component using finite element analysis of surface topography”,  
Sigmund Kyrre Ås, 2006:25, ISBN 82-471-7791-9 (printed version), ISBN 82-471-7791-9 (electronic version), ISSN 1503-8181.
- ”Constitutive models of elastoplasticity and fracture for aluminium alloys under strain path change”,  
Dasharatha Achani, 2006:76, ISBN 82-471-7903-2 (printed version), ISBN 82-471-7902-4 (electronic version), ISSN 1503-8181.
- “Simulations of 2D dynamic brittle fracture by the Element-free Galerkin method and linear fracture mechanics”,  
Tommy Karlsson, 2006:125, ISBN 82-471-8011-1 (printed version), ISBN 82-471-8010-3 (electronic version), ISSN 1503-8181.
- “Penetration and Perforation of Granite Targets by Hard Projectiles”,  
Chong Chiang Seah, 2006:188, ISBN 82-471-8150-9 (printed version), ISBN 82-471-8149-5 (electronic version), ISSN 1503-8181.

“Deformations, strain capacity and cracking of concrete in plastic and early hardening phases”,

Tor Arne Hammer, 2007:234, ISBN 978-82-471-5191-4 (printed version), ISBN 978-82-471-5207-2 (electronic version), ISSN 1503-8181.

“Crashworthiness of dual-phase high-strength steel: Material and Component behaviour”, Venkatapathi Tarigopula, 2007:230, ISBN 82-471-5076-4 (printed version), ISBN 82-471-5093-1 (electronic version), ISSN 1503-8181.

“Fibre reinforcement in load carrying concrete structures”,

Åse Lyslo Døssland, 2008:50, ISBN 978-82-471-6910-0 (printed version), ISBN 978-82-471-6924-7 (electronic version), ISSN 1503-8181.

“Low-velocity penetration of aluminium plates”,

Frøde Grytten, 2008:46, ISBN 978-82-471-6826-4 (printed version), ISBN 978-82-471-6843-1 (electronic version), ISSN 1503-8181.

“Robustness studies of structures subjected to large deformations”,

Ørjan Fyllingen, 2008:24, ISBN 978-82-471-6339-9 (printed version), ISBN 978-82-471-6342-9 (electronic version), ISSN 1503-8181.

“Constitutive modelling of morsellised bone”,

Knut Birger Lunde, 2008:92, ISBN 978-82-471-7829-4 (printed version), ISBN 978-82-471-7832-4 (electronic version), ISSN 1503-8181.

“Experimental Investigations of Wind Loading on a Suspension Bridge Girder”,

Bjørn Isaksen, 2008:131, ISBN 978-82-471-8656-5 (printed version), ISBN 978-82-471-8673-2 (electronic version), ISSN 1503-8181.

“Cracking Risk of Concrete Structures in The Hardening Phase”,

Guomin Ji, 2008:198, ISBN 978-82-471-1079-9 (printed version), ISBN 978-82-471-1080-5 (electronic version), ISSN 1503-8181.

“Modelling and numerical analysis of the porcine and human mitral apparatus”,

Victorien Emile Prot, 2008:249, ISBN 978-82-471-1192-5 (printed version), ISBN 978-82-471-1193-2 (electronic version), ISSN 1503-8181.

“Strength analysis of net structures”,

Heidi Moe, 2009:48, ISBN 978-82-471-1468-1 (printed version), ISBN 978-82-471-1469-8 (electronic version), ISSN 1503-8181.

“Numerical analysis of ductile fracture in surface cracked shells”,

Espen Berg, 2009:80, ISBN 978-82-471-1537-4 (printed version), ISBN 978-82-471-1538-1 (electronic version), ISSN 1503-8181.

“Subject specific finite element analysis of bone – for evaluation of the healing of a leg lengthening and evaluation of femoral stem design”,  
Sune Hansborg Pettersen, 2009:99, ISBN 978-82-471-1579-4 (printed version), ISBN 978-82-471-1580-0 (electronic version), ISSN 1503-8181.

“Evaluation of fracture parameters for notched multi-layered structures”,  
Lingyun Shang, 2009:137, ISBN 978-82-471-1662-3 (printed version), ISBN 978-82-471-1663-0 (electronic version), ISSN 1503-8181.

“Modelling of Dynamic Material Behaviour and Fracture of Aluminium Alloys for Structural Applications”  
Yan Chen, 2009:69, ISBN 978-82-471-1515-2 (printed version), ISBN 978-82-471-1516-9 (electronic version), ISSN 1503-8181.

“Nanomechanics of polymer and composite particles”  
Jianying He 2009:213, ISBN 978-82-471-1828-3 (printed version), ISBN 978-82-471-1829-0 (electronic version), ISSN 1503-8181.

“Mechanical properties of clear wood from Norway spruce”  
Kristian Berbom Dahl 2009:250, ISBN 978-82-471-1911-2 (printed version) ISBN 978-82-471-1912-9 (electronic version), ISSN 1503-8181.

“Modeling of the degradation of TiB<sub>2</sub> mechanical properties by residual stresses and liquid Al penetration along grain boundaries”  
Micol Pezzotta 2009:254, ISBN 978-82-471-1923-5 (printed version) ISBN 978-82-471-1924-2 (electronic version) ISSN 1503-8181.

“Effect of welding residual stress on fracture”  
Xiabo Ren 2010:77, ISBN 978-82-471-2115-3 (printed version) ISBN 978-82-471-2116-0 (electronic version), ISSN 1503-8181.

“Pan-based carbon fiber as anode material in cathodic protection system for concrete structures”  
Mahdi Chini 2010:122, ISBN 978-82-471-2210-5 (printed version) ISBN 978-82-471-2213-6 (electronic version), ISSN 1503-8181.

“Structural Behaviour of deteriorated and retrofitted concrete structures”  
Irina Vasililjeva Sæther 2010:171, ISBN 978-82-471-2315-7 (printed version) ISBN 978-82-471-2316-4 (electronic version) ISSN 1503-8181.

“Prediction of local snow loads on roofs”  
Vivian Meløysund 2010:247, ISBN 978-82-471-2490-1 (printed version) ISBN 978-82-471-2491-8 (electronic version) ISSN 1503-8181.

“Behaviour and modelling of polymers for crash applications”  
Virgile Delhayé 2010:251, ISBN 978-82-471-2501-4 (printed version) ISBN 978-82-471-2502-1 (electronic version) ISSN 1503-8181.

“Blended cement with reduced CO<sub>2</sub> emission – Utilizing the Fly Ash-Limestone Synergy”,  
Klaartje De Weerd 2011:32, ISBN 978-82-471-2584-7 (printed version) ISBN 978-82-471-2584-4 (electronic version) ISSN 1503-8181.

“Chloride induced reinforcement corrosion in concrete” Concept of critical chloride content – methods and mechanisms.  
Ueli Angst 2011:113, ISBN 978-82-471-2769-9 (printed version) ISBN 978-82-471-2763-6 (electronic version) ISSN 1503-8181.

“A thermo-electric-Mechanical study of the carbon anode and contact interface for Energy savings in the production of aluminium”.  
Dag Herman Andersen 2011:157, ISBN 978-82-471-2859-6 (printed version) ISBN 978-82-471-2860-2 (electronic version) ISSN 1503-8181.

“Structural Capacity of Anchorage Ties in Masonry Veneer Walls Subjected to Earthquake”. The implications of Eurocode 8 and Eurocode 6 on a typical Norwegian veneer wall.  
Ahmed Mohamed Yousry Hamed 2011:181, ISBN 978-82-471-2911-1 (printed version) ISBN 978-82-471-2912-8 (electronic ver.) ISSN 1503-8181.

“Work-hardening behaviour in age-hardenable Al-Zn-Mg(-Cu) alloys”.  
Ida Westermann , 2011:247, ISBN 978-82-471-3056-8 (printed ver.) ISBN 978-82-471-3057-5 (electronic ver.) ISSN 1503-8181.

“Behaviour and modelling of selfpiercing riveted connections using aluminium rivets”.  
Nguyen-Hieu Hoang, 2011:266, ISBN 978-82-471-3097-1 (printed ver.) ISBN 978-82-471-3099-5 (electronic ver.) ISSN 1503-8181.

“Fibre reinforced concrete”.  
Sindre Sandbakk, 2011:297, ISBN 978-82-471-3167-1 (printed ver.) ISBN 978-82-471-3168-8 (electronic ver) ISSN 1503:8181.

“Dynamic behaviour of cablesupported bridges subjected to strong natural wind”.  
Ole Andre Øiseth, 2011:315, ISBN 978-82-471-3209-8 (printed ver.) ISBN 978-82-471-3210-4 (electronic ver.) ISSN 1503-8181.

“Constitutive modeling of solargrade silicon materials”  
Julien Cochard, 2011:307, ISBN 978-82-471-3189-3 (printed ver.) ISBN 978-82-471-3190-9 (electronic ver.) ISSN 1503-8181.

“Constitutive behavior and fracture of shape memory alloys”  
Jim Stian Olsen, 2012:57, ISBN 978-82-471-3382-8 (printed ver.) ISBN 978-82-471-3383-5 (electronic ver.) ISSN 1503-8181.

“Field measurements in mechanical testing using close-range photogrammetry and digital image analysis”

Egil Fagerholt, 2012:95, ISBN 978-82-471-3466-5 (printed ver.) ISBN 978-82-471-3467-2 (electronic ver.) ISSN 1503-8181.

“Towards a better understanding of the ultimate behaviour of lightweight aggregate concrete in compression and bending”

Håvard Nedrelid, 2012:123, ISBN 978-82-471-3527-3 (printed ver.) ISBN 978-82-471-3528-0 (electronic ver.) ISSN 1503-8181.

“Numerical simulations of blood flow in the left side of the heart”

Sigrid Kaarstad Dahl, 2012:135, ISBN 978-82-471-3553-2 (printed ver.) ISBN 978-82-471-3555-6 (electronic ver.) ISSN 1503-8181.

“Moisture induced stresses in glulam”

Vanessa Angst-Nicollier, 2012:139, ISBN 978-82-471-3562-4 (printed ver.) ISBN 978-82-471-3563-1 (electronic ver.) ISSN 1503-8181.

“Biomechanical aspects of distraction osteogenesis”

Valentina La Russa, 2012:250, ISBN 978-82-471-3807-6 (printed ver.) ISBN 978-82-471-3808-3 (electronic ver.) ISSN 1503-8181.

“Ductile fracture in dual-phase steel. Theoretical, experimental and numerical study”

Gaute Gruben, 2012:257, ISBN 978-82-471-3822-9 (printed ver.) ISBN 978-82-471-3823-6 (electronic ver.) ISSN 1503-8181.

“Damping in Timber Structures”

Nathalie Labonnote, 2012:263, ISBN 978-82-471-3836-6 (printed ver.) ISBN 978-82-471-3837-3 (electronic ver.) ISSN 1503-8181.

“Biomechanical modeling of fetal veins: The umbilical vein and ductus venosus bifurcation”

Paul Roger Leinan, 2012:299, ISBN 978-82-471-3915-8 (printed ver.) ISBN 978-82-471-3916-5 (electronic ver.) ISSN 1503-8181.

“Large-Deformation behaviour of thermoplastics at various stress states”

Anne Serine Ognedal, 2012:298, ISBN 978-82-471-3913-4 (printed ver.) ISBN 978-82-471-3914-1 (electronic ver.) ISSN 1503-8181.

“Hardening accelerator for fly ash blended cement”

Kien Dinh Hoang, 2012:366, ISBN 978-82-471-4063-5 (printed ver.) ISBN 978-82-471-4064-2 (electronic ver.) ISSN 1503-8181.

“From molecular structure to mechanical properties”

Jianyang Wu, 2013:186, ISBN 978-82-471-4485-5 (printed ver.) ISBN 978-82-471-4486-2 (electronic ver.) ISSN 1503-8181.



“Experimental and numerical study of hybrid concrete structures”

Linn Grepstad Nes, 2013:259, ISBN 978-82-471-4644-6 (printed ver.) ISBN 978-82-471-4645-3 (electronic ver.) ISSN 1503-8181.

“Mechanics of ultra-thin multi crystalline silicon wafers”

Saber Saffar, 2013:199, ISBN 978-82-471-4511-1 (printed ver.) ISBN 978-82-471-4513-5 (electronic ver.) ISSN 1503-8181.

“Through process modelling of welded aluminium structures”

Anizahyati Alisibramulisi, 2013:325, ISBN 978-82-471-4788-7 (printed ver.) ISBN 978-82-471-4789-4 (electronic ver.) ISSN 1503-8181.

“Combined blast and fragment loading on steel plates”

Knut Gaarder Rakvåg, 2013:361, ISBN978-82-471-4872-3 (printed ver.) ISBN 978-82-4873-0 (electronic ver.) ISSN 1503-8181.

“Characterization and modelling of the anisotropic behaviour of high-strength aluminium alloy”

Marion Fourmeau, 2014:37, ISBN 978-82-326-0008-3 (printed ver.) ISBN 978-82-326-0009-0 (electronic ver.) ISSN 1503-8181.

“Behaviour of threaded steel fasteners at elevated deformation rates”

Hemming Fransplass, 2014:65, ISBN 978-82-326-0054-0 (printed ver.) ISBN 978-82-326-0055-7 (electronic ver.) ISSN 1503-8181.

“Sedimentation and Bleeding”

Ya Peng, 2014:89, ISBN 978-82-326-0102-8 (printed ver.) ISBN 978-82-326-0103-5 (electric ver.) ISSN 1503-8181.

“Impact against X65 offshore pipelines”

Martin Kristoffersen, 2014:362, ISBN 978-82-326-0636-8 (printed ver.) ISBN 978-82-326-0637-5 (electronic ver.) ISSN 1503-8181.

“Formability of aluminium alloy subjected to prestrain by rolling”

Dmitry Vysochinskiy, 2014:363., ISBN 978-82-326-0638-2 (printed ver.) ISBN 978-82-326-0639-9 (electronic ver.) ISSN 1503-8181.

“Experimental and numerical study of Yielding, Work-Hardening and anisotropy in textured AA6xxx alloys using crystal plasticity models”

Mikhail Khadyko, 2015:28, ISBN 978-82-326-0724-2 (printed ver.) ISBN 978-82-326-0725-9 (electronic ver.) ISSN 1503-8181.

“Behaviour and Modelling of AA6xxx Aluminium Alloys Under a Wide Range of Temperatures and Strain Rates”

Vincent Vilamosa, 2015:63, ISBN 978-82-326-0786-0 (printed ver.) ISBN 978-82-326-0787-7 (electronic ver.) ISSN 1503-8181.

“A Probabilistic Approach in Failure Modelling of Aluminium High Pressure Die-Castings”

Octavian Knoll, 2015:137, ISBN 978-82-326-0930-7 (printed ver.) ISBN 978-82-326-0931-4 (electronic ver.) ISSN 1503-8181.

“Ice Abrasion on Marine Concrete Structures”

Egil Møen, 2015:189, ISBN 978-82-326-1034-1 (printed ver.) ISBN 978-82-326-1035-8 (electronic ver.) ISSN 1503-8181.

“Fibre Orientation in Steel-Fibre-Reinforced Concrete”

Giedrius Zirgulis, 2015:229, ISBN 978-82-326-1114-0 (printed ver.) ISBN 978-82-326-1115-7 (electronic ver.) ISSN 1503-8181.

“Effect of spatial variation and possible interference of localised corrosion on the residual capacity of a reinforced concrete beam”

Mohammad Mahdi Kioumarsi, 2015:282, ISBN 978-82-326-1220-8 (printed ver.) ISBN 978-82-1221-5 (electronic ver.) ISSN 1503-8181.

“The role of concrete resistivity in chloride-induced macro-cell corrosion”

Karla Horbostel, 2015:324, ISBN 978-82-326-1304-5 (printed ver.) ISBN 978-82-326-1305-2 (electronic ver.) ISSN 1503-8181.

“Flowable fibre-reinforced concrete for structural applications”

Elena Vidal Sarmiento, 2015:335, ISBN 978-82-326-1324-3 (printed ver.) ISBN 978-82-326-1325-0 (electronic ver.) ISSN 1503-8181.

“Development of chushed sand for concrete production with microproportioning”

Rolands Cepuritis, 2016:19, ISBN 978-82-326-1382-3 (printed ver.) ISBN 978-82-326-1383-0 (electronic ver.) ISSN 1503-8181.

“Withdrawal properties of threaded rods embedded in glued-laminated timber elements”

Haris Stamatopoulos, 2016:48, ISBN 978-82-326-1436-3 (printed ver.) ISBN 978-82-326-1437-0 (electronic ver.) ISSN 1503-8181.

“An Experimental and numerical study of thermoplastics at large deformation”

Marius Andersen, 2016:191, ISBN 978-82-326-1720-3 (printed ver.) ISBN 978-82-326-1721-0 (electronic ver.) ISSN 1503-8181.

“Modeling and Simulation of Ballistic Impact”

Jens Kristian Holmen, 2016:240, ISBN 978-82-326-1818-7 (printed ver.) ISBN 978-82-326-1819-4 (electronic ver.) ISSN 1503-8181.

“Early age crack assessment of concrete structures”

Anja B. Estensen Klausen, 2016:256, ISBN 978-82-326-1850-7 (printed ver.) ISBN 978-82-326-1851-4 (electronic ver.) ISSN 1503-8181.

“Uncertainty quantification and sensitivity analysis for cardiovascular models”

Vinzenz Gregor Eck, 2016:234, ISBN 978-82-326-1806-4 (printed ver.) ISBN 978-82-326-1807-1 (electronic ver.) ISSN 1503-8181.

“Dynamic behaviour of existing and new railway catenary systems under Norwegian conditions”

Petter Røe Nåvik, 2016:298, ISBN 978-82-326-1935-1 (printed ver.) ISBN 978-82-326-1934-4 (electronic ver.) ISSN 1503-8181.

“Mechanical behaviour of particle-filled elastomers at various temperatures”

Arne Ilseng, 2016:295, ISBN 978-82-326-1928-3 (printed ver.) ISBN 978-82-326-1929-0 (electronic ver.) ISSN 1503-8181.

“Nanotechnology for Anti-Icing Application”

Zhiwei He, 2016:348, ISBN 978-82-326-2038-8 (printed ver.) ISBN 978-82-326-2019-5 (electronic ver.) ISSN 1503-8181.

“Conduction Mechanisms in Conductive Adhesives with Metal-Coated Polymer Spheres”

Sigurd Rolland Pettersen, 2016:349, ISBN 978-326-2040-1 (printed ver.) ISBN 978-82-326-2041-8 (electronic ver.) ISSN 1503-8181.

“The interaction between calcium lignosulfonate and cement”

Alessia Colombo, 2017:20, ISBN 978-82-326-2122-4 (printed ver.) ISBN 978-82-326-2123-1 (electronic ver.) ISSN 1503-8181.

“Behaviour and Modelling of Flexible Structures Subjected to Blast Loading”

Vegard Aune, 2017:101, ISBN 978-82-326-2274-0 (printed ver.) ISBN 978-82-326-2275-7 (electronic ver.) ISSN 1503-8181.

“Behaviour of steel connections under quasi-static and impact loading”

Erik Løhre Grimsmo, 2017:159, ISBN 978-82-326-2390-7 (printed ver.) ISBN 978-82-326-2391-4 (electronic ver.) ISSN 1503-8181.

“An experimental and numerical study of cortical bone at the macro and Nano-scale”

Masoud Ramenzanzadehkoldeh, 2017:208, ISBN 978-82-326-2488-1 (printed ver.) ISBN 978-82-326-2489-8 (electronic ver.) ISSN 1503-8181.

“Optoelectrical Properties of a Novel Organic Semiconductor: 6,13-Dichloropentacene”

Mao Wang, 2017:130, ISBN 978-82-326-2332-7 (printed ver.) ISBN 978-82-326-2333-4 (electronic ver.) ISSN 1503-8181.

“Core-shell structured microgels and their behavior at oil and water interface”

Yi Gong, 2017:182, ISBN 978-82-326-2436-2 (printed ver.) ISBN 978-82-326-2437-9 (electronic ver.) ISSN 1503-8181.

“Aspects of design of reinforced concrete structures using nonlinear finite element analyses”

Morten Engen, 2017:149, ISBN 978-82-326-2370-9 (printed ver.) ISBN 978-82-326-2371-6 (electronic ver.) ISSN 1503-8181.

“Numerical studies on ductile failure of aluminium alloys”

Lars Edvard Dæhli, 2017:284, ISBN 978-82-326-2636-6 (printed ver.) ISBN 978-82-326-2637-3 (electronic ver.) ISSN 1503-8181.

“Modelling and Assessment of Hydrogen Embrittlement in Steels and Nickel Alloys”

Haiyang Yu, 2017:278, ISBN 978-82-326-2624-3 (printed ver.) ISBN 978-82-326-2625-0 (electronic ver.) ISSN 1503-8181.

“Network arch timber bridges with light timber deck on transverse crossbeams”

Anna Weronika Ostrycharczyk, 2017:318, ISBN 978-82-326-2704-2 (printed ver.) ISBN 978-82-326-2705-9 (electronic ver.) ISSN 1503-8181.

“Splicing of Large Glued Laminated Timber Elements by Use of Long Threaded Rods”

Martin Cepelka, 2017:320, ISBN 978-82-326-2708-0 (printed ver.) ISBN 978-82-326-2709-7 (electronic ver.) ISSN 1503-8181.

“Thermomechanical behaviour of semi-crystalline polymers: experiments, modelling and simulation”

Joakim Johnsen, 2017:317, ISBN 978-82-326-2702-8 (printed ver.) ISBN 978-82-326-2703-5 (electronic ver.) ISSN 1503-8181.

“Small-Scale Plasticity under Hydrogen Environment”

Kai Zhao, 2017:356, ISBN 978-82-326-2782-0 (printed ver.) ISBN 978-82-326-2783-7 (electronic ver.) ISSN 1503-8181.

“Risk and Reliability Based Calibration of Structural Design Codes”

Michele Baravalle, 2017:342, ISBN 978-82-326-2752-3 (printed ver.) ISBN 978-82-326-2753-0 (electronic ver.) ISSN 1503-8181.

“Dynamic behaviour of floating bridges exposed to wave excitation”

Knut Andreas Kvåle, 2017:365, ISBN 978-82-326-2800-1 (printed ver.) ISBN 978-82-326-2801-8 (electronic ver.) ISSN 1503-8181.

“Dolomite calcined clay composite cement – hydration and durability”

Alisa Lydia Machner, 2018:39, ISBN 978-82-326-2872-8 (printed ver.) ISBN 978-82-326-2873-5 (electronic ver.) ISSN 1503-8181.

“Modelling of the self-excited forces for bridge decks subjected to random motions: an experimental study”

Bartosz Siedziako, 2018:52, ISBN 978-82-326-2896-4 (printed ver.) ISBN 978-82-326-2897-1 (electronic ver.) ISSN 1503-8181.

“A probabilistic-based methodology for evaluation of timber facade constructions”  
Klodian Gradeci, 2018:69, ISBN 978-82-326-2928-2 (printed ver.) ISBN 978-82-326-2929-9 (electronic ver.) ISSN 1503-8181.

“Behaviour and modelling of flow-drill screw connections”  
Johan Kolstø Sønstabø, 2018:73, ISBN 978-82-326-2936-7 (printed ver.) ISBN 978-82-326-2937-4 (electronic ver.) ISSN 1503-8181.

“Full-scale investigation of the effects of wind turbulence characteristics on dynamic behavior of long-span cable-supported bridges in complex terrain”  
Aksel Fenerci, 2018 100, ISBN 9978-82-326-2990-9 (printed ver.) ISBN 978-82-326-2991-6 (electronic ver.) ISSN 1503-8181.

“Modeling and simulation of the soft palate for improved understanding of the obstructive sleep apnea syndrome”  
Hongliang Liu, 2018:101, ISBN 978-82-326-2992-3 (printed ver.) ISBN 978-82-326-2993-0 (electronic ver.) ISSN 1503-8181.

“Long-term extreme response analysis of cable-supported bridges with floating pylons subjected to wind and wave loads”.  
Yuwang Xu, 2018:229, ISBN 978-82-326-3248-0 (printed ver.) ISBN 978-82-326-3249-7 (electronic ver.) ISSN 1503-8181.

“Reinforcement corrosion in carbonated fly ash concrete”  
Andres Belda Revert, 2018:230, ISBN 978-82-326-3250-3 (printed ver.) ISBN 978-82-326-3251-0 (electronic ver.) ISSN 1503-8181.

“Direct finite element method for nonlinear earthquake analysis of concrete dams including dam-water-foundation rock interaction”  
Arnkjell Løkke, 2018:252, ISBN 978-82-326-3294-7 (printed ver.) ISBN 978-82-326-3295-4 (electronic ver.) ISSN 1503-8181.

“Electromechanical characterization of metal-coated polymer spheres for conductive adhesives”  
Molly Strimbeck Bazilchuk, 2018:295, ISBN 978-82-326-3380-7 (printed. ver.) ISBN 978-82-326-3381-4 (electrical ver.) ISSN 1503-8181.

“Determining the tensile properties of Artic materials and modelling their effects on fracture”  
Shengwen Tu, 2018:269, ISBN 978-82-326-3328-9 (printed ver.) ISBN 978-82-326-3329-6 (electronic ver.) ISSN 1503-8181.

“Atomistic Insight into Transportation of Nanofluid in Ultra-confined Channel”  
Xiao Wang, 2018:334, ISBN978-82-326-3456-9 (printed ver.) ISBN 978-82-326-3457-6 (electronic ver.) ISSN 1503-8181.



“An experimental and numerical study of the mechanical behaviour of short glass-fibre reinforced thermoplastics”.

Jens Petter Henrik Holmstrøm, 2019:79, ISBN 978-82-326-3760-7 (printed ver.) ISBN 978-82-326-3761-4 (electronic ver.) ISSN 1503-8181.

“Uncertainty quantification and sensitivity analysis informed modeling of physical systems”

Jacob Sturdy, 2019:115, ISBN 978-82-326-3828-4 (printed ver.) ISBN 978-82-326-3829-1 (electric ver.) ISSN 1503-8181.

“Load model of historic traffic for fatigue life estimation of Norwegian railway bridges”

Gunnstein T. Frøseth, 2019:73, ISBN 978-82-326-3748-5 (printed ver.) ISBN 978-82-326-3749-2 (electronic ver.) ISSN 1503-8181.

“Force identification and response estimation in floating and suspension bridges using measured dynamic response”

Øyvind Wiig Petersen, 2019:88, ISBN 978-82-326-3778-2 (printed ver.) ISBN 978-82-326-3779-9 (electronic ver.) ISSN 1503-8181.

“Consistent crack width calculation methods for reinforced concrete elements subjected to 1D and 2D stress states”

Reignard Tan, 2019:147, ISBN 978-82-326-3892-5 (printed ver.) ISBN 978-82-326-3893-2 (electronic ver.) ISSN 1503-8181.

“Nonlinear static and dynamic isogeometric analysis of slender spatial and beam type structures”

Siv Bente Raknes, 2019:181, ISBN 978-82-326-3958-8 (printed ver.) ISBN 978-82-326-3959-5 (electronic ver.) ISSN 1503-8181.

“Experimental study of concrete-ice abrasion and concrete surface topography modification”

Guzel Shamsutdinova, 2019:182, ISBN 978-82-326-3960-1 (printed ver.) ISBN 978-82-326-3961-8 (electronic ver.) ISSN 1503-8181.

“Wind forces on bridge decks using state-of-the art FSI methods”

Tore Andreas Helgedagsrud, 2019:180, ISBN 978-82-326-3956-4 (printed ver.) ISBN 978-82-326-3957-1 (electronic ver.) ISSN 1503-8181.

“Numerical Study on Ductile-to-Brittle Transition of Steel and its Behavior under Residual Stresses”

Yang Li, 2019:227, ISBN 978-82-326-4050-8 (printed ver.) ISBN 978-82-326-4015-5 (electronic ver.) ISSN 1503-8181.